Influence of the flow exchanges between streets and a city block during urban floods: Laboratory experiments under steady and unsteady flow conditions

M.A. Mejia Morales

N°d'ordre NNT : 2022LYSEI042

THESE de DOCTORAT DE L'UNIVERSITE DE LYON
opérée au sein de
L'INSTITUT NATIONAL DES SCIENCES APPLIQUEES DE LYON

Ecole Doctorale N° 162
Mécanique, Energétique, Génie Civil, Acoustique - MEGA

Spécialité/ discipline de doctorat :
Mécanique des Fluides

Soutenue publiquement le 23/05/2022, par :
Miguel Angel Mejía Morales

Influence of the flow exchanges between streets and a city block during urban floods

Laboratory experiments under steady and unsteady flow conditions

---

Devant le jury composé de :

MACCHIONE Francesco	Professeur, Università della Calabria	Rapporteur
GOMEZ Manuel	Professeur, Universitat Politècnica de Catalunya	Rapporteur
JODEAU Magali	Docteur, EDF - Laboratoire d'hydraulique Saint-Venant	Examinatrice
DEWALS Benjamin	Professeur, Université de Liège	Examinateur
PROUST Sébastien	Chercheur HDR, INRAE UR Riverly	Directeur de thèse
MIGNOT Emmanuel	Maitre de conférence HDR, INSA Lyon	Co-directeur de thèse
PAQUIER André	IGPEF, INRAE UR Riverly	Encadrant

Département FEDORA – INSA Lyon - Ecoles Doctorales

SIGLE	ECOLE DOCTORALE	NOM ET COORDONNEES DU RESPONSABLE
CHIMIE	**CHIMIE DE LYON** **https://www.edchimie-lyon.fr** Sec. : Renée EL MELHEM Bât. Blaise PASCAL, 3e étage secretariat@edchimie-lyon.fr	**M. Stéphane DANIELE** C2P2-CPE LYON-UMR 5265 Bâtiment F308, BP 2077 43 Boulevard du 11 novembre 1918 69616 Villeurbanne **directeur@edchimie-lyon.fr**
E.E.A.	**ÉLECTRONIQUE, ÉLECTROTECHNIQUE, AUTOMATIQUE** **https://edeea.universite-lyon.fr** Sec. : Stéphanie CAUVIN Bâtiment Direction INSA Lyon Tél : 04.72.43.71.70 secretariat.edeea@insa-lyon.fr	**M. Philippe DELACHARTRE** INSA LYON Laboratoire CREATIS Bâtiment Blaise Pascal, 7 avenue Jean Capelle 69621 Villeurbanne CEDEX Tél : 04.72.43.88.63 **philippe.delachartre@insa-lyon.fr**
E2M2	**ÉVOLUTION, ÉCOSYSTÈME, MICROBIOLOGIE, MODÉLISATION** **http://e2m2.universite-lyon.fr** Sec. : Bénédicte LANZA Bât. Atrium, UCB Lyon 1 Tél : 04.72.44.83.62 secretariat.e2m2@univ-lyon1.fr	**Mme Sandrine CHARLES** Université Claude Bernard Lyon 1 UFR Biosciences Bâtiment Mendel 43, boulevard du 11 Novembre 1918 69622 Villeurbanne CEDEX **sandrine.charles@univ-lyon1.fr**
EDISS	**INTERDISCIPLINAIRE SCIENCES-SANTÉ** **http://ediss.universite-lyon.fr** Sec. : Bénédicte LANZA Bât. Atrium, UCB Lyon 1 Tél : 04.72.44.83.62 secretariat.ediss@univ-lyon1.fr	**Mme Sylvie RICARD-BLUM** Institut de Chimie et Biochimie Moléculaires et Supramoléculaires (ICBMS) - UMR 5246 CNRS - Université Lyon 1 Bâtiment Raulin - 2ème étage Nord 43 Boulevard du 11 novembre 1918 69622 Villeurbanne Cedex Tél : +33(0)4 72 44 82 32 **sylvie.ricard-blum@univ-lyon1.fr**
INFOMATHS	**INFORMATIQUE ET MATHÉMATIQUES** **http://edinfomaths.universite-lyon.fr** Sec. : Renée EL MELHEM Bât. Blaise PASCAL, 3e étage Tél : 04.72.43.80.46 infomaths@univ-lyon1.fr	**M. Hamamache KHEDDOUCI** Université Claude Bernard Lyon 1 Bât. Nautibus 43, Boulevard du 11 novembre 1918 69 622 Villeurbanne Cedex France Tél : 04.72.44.83.69 **hamamache.kheddouci@univ-lyon1.fr**
Matériaux	**MATÉRIAUX DE LYON** **http://ed34.universite-lyon.fr** Sec. : Yann DE ORDENANA Tél : 04.72.18.62.44 yann.de-ordenana@ec-lyon.fr	**M. Stéphane BENAYOUN** Ecole Centrale de Lyon Laboratoire LTDS 36 avenue Guy de Collongue 69134 Ecully CEDEX Tél : 04.72.18.64.37 **stephane.benayoun@ec-lyon.fr**
MEGA	**MÉCANIQUE, ÉNERGÉTIQUE, GÉNIE CIVIL, ACOUSTIQUE** **http://edmega.universite-lyon.fr** Sec. : Stéphanie CAUVIN Tél : 04.72.43.71.70 Bâtiment Direction INSA Lyon mega@insa-lyon.fr	**M. Jocelyn BONJOUR** INSA Lyon Laboratoire CETHIL Bâtiment Sadi-Carnot 9, rue de la Physique 69621 Villeurbanne CEDEX **jocelyn.bonjour@insa-lyon.fr**
ScSo	**ScSo*** **https://edsciencessociales.universite-lyon.fr** Sec. : Mélina FAVETON INSA : J.Y. TOUSSAINT Tél : 04.78.69.77.79 melina.faveton@univ-lyon2.fr	**M. Christian MONTES** Université Lumière Lyon 2 86 Rue Pasteur 69365 Lyon CEDEX 07 **christian.montes@univ-lyon2.fr**

*ScSo : Histoire, Géographie, Aménagement, Urbanisme, Archéologie, Science politique, Sociologie, Anthropologie

To my wife,
to my parents and sister
and to my grandparents,
especially Josefina and Susana,
who sadly passed away during the course of these years

Acknowledgements

First of all, I would like to express my gratitude to my three supervisors: **André Paquier**, because I arrived at INRAE and I had the opportunity to apply for this PhD thanks to the internship that he supervised, also for his teachings, his availability whenever I needed his help and for his kindness; **Emmanuel Mignot** for his willingness to help, always being available and his constant encouragement during these years, which helped me to continue through some tough periods and finish this project; and **Sébastien Proust**, for his advice and help throughout these years, as well as for the various discussions we had during these years, on scientific issues, but also on topics related to French culture, among other interesting topics.

I really thank the technical team of the Hydraulics Laboratory at INRAE Lyon, **Alexis Buffet**, **Adrien Bonnefoy**, **Darius Sigaud** and especially **Fabien Tollet**, for their patience and all the help I received to successfully carry out the various experimental campaigns. I would also like to thank the INRAE RiverLy team, for their support and warmth, especially **Jérôme Le Coz**, for all his help for the use of the Fudaa LSPIV software, and **Benoît Camenen**, for his advice and feedback during the various thesis committees. A special thanks also to my doctoral student friends at INRAE, who gave me a friendly welcome and helped me to be incorporated into the team, especially **Yassine Kaddi** and **Matteo Darienzo**.

My great gratitude to the members of the jury, the reviewers, **Prof. Manuel Gómez** and **Prof. Francesco Macchione**, for their comments and advice on this manuscript, as well as for the effort to travel a long way to be present at the defence of this thesis. To the examiner, **Dr. Magali Jodeau**, for accepting, reviewing the manuscript and being present at the defence of this thesis, and to the jury president, **Prof. Benjamin Dewals**, for accepting and travelling a long way to be present in the thesis defence, as well as for his multiple suggestions and advice throughout the DEUFI project meetings.

I would also like to thank **Nicolas Rivière** and **Gislain Lipeme**, for being part of my thesis committee, for their comments and advice over these years.

Finally, my greatest gratitude to my wife, **Rocío**, for all her support and patience, which immensely contributed to successfully accomplish my PhD, as well as for all the effort she has made to be together in this adventure. Likewise to my parents, **Vicente** and **Beatriz**, and my sister, **Angélica**, for all their support and for keeping me in their thoughts despite the physical distance.

Abstract

The increasing occurrence of urban flooding in recent years demands a more accurate flood hazard assessment (flow depth and velocity) and the associated risk to property and people. This assessment must be based on a detailed understanding of the hydrodynamic processes, particularly on a local scale (at street or at city block). In this context, the aim of the thesis work was to study the lateral flow exchanges between a city block and streets during a urban flood, based on laboratory experiments. The latter were carried out under steady and unsteady flow conditions. The investigation area was limited to a single city block and its adjacent streets, considering the mechanisms that affect the capability of the city block to convey and store floodwaters. Three key issues were then addressed to quantify the influence on flow depth, velocity and discharge in the streets and within the city block: (*i*) by varying the magnitude of the conveyance porosity of the block; (*ii*) by varying the distribution of the conveyance porosity of the block; and (*iii*) by varying the storage capacity of the block. Firstly, it was found that in the streets surrounding the block, the velocity and flow depth can vary significantly when considering the conveyance and storage of floodwater in the block. Within the block, the most impacted flow parameter is the number and size of horizontal secondary flow cells. Secondly, it was found that the inflow hydrograph unsteadiness has a strong influence on the flood flow characteristics, as well as on the floodwater volume stored within the block. Finally, the flood risk to pedestrians, which is both velocity and flow depth related, increases locally when considering the conveyance and storage within the city block.

RÉSUMÉ

L'augmentation du nombre d'inondations urbaines au cours des dernières années incite à évaluer de manière précise l'aléa hydraulique (hauteur et vitesse de l'eau) et le risque associé pour les biens et les personnes. Cette évaluation doit s'appuyer sur une compréhension fine des processus hydrodynamiques en jeu notamment à une échelle locale (celle de la rue ou d'un bloc de bâtiments). Dans ce contexte, le travail de thèse a eu pour but d'étudier les échanges latéraux d'eau entre un bloc de bâtiments et les rues à proximité du bloc lors d'une inondation en ville, en s'appuyant sur des expériences de laboratoire. Ces dernières ont été réalisées dans des conditions d'écoulement stationnaire et instationnaire. La zone d'investigation a été limitée à un seul bloc de bâtiments et à ses rues adjacentes, en considérant les mécanismes qui affectent la capacité du bloc à convoyer et à stocker les flux d'inondation. Trois points clés ont ensuite été abordés pour quantifier l'influence sur la hauteur, la vitesse et le débit d'écoulement dans les rues et à l'intérieur du bloc de bâtiments: (*i*) en faisant varier la magnitude de la porosité de convoyage du bloc; (*ii*) en faisant varier la distribution de la porosité de convoyage du bloc; et (*iii*) en faisant varier la capacité de stockage du bloc. Premièrement, on a constaté que, dans les rues entourant le bloc, la vitesse et la hauteur de l'eau peuvent varier considérablement si l'on tient compte du passage et du stockage des eaux de ruissellement à travers le bloc. À l'intérieur du bloc, le paramètre d'écoulement le plus impacté est le nombre et la taille des cellules d'écoulement secondaires horizontales. Deuxièmement, il a été constaté que l'instationnarité de l'hydrogramme du débit entrant a une forte influence sur les caractéristiques des flux d'inondation, ainsi que sur le volume

d'eau stocké dans le bloc. Enfin, le risque d'inondation pour les piétons, qui est à la fois lié à la vitesse et à la hauteur de l'eau, augmente localement en tenant compte du passage et du stockage à l'intérieur du bloc de bâtiments.

RÉSUMÉ ÉTENDU

Contexte

Depuis de nombreuses années et actuellement, les inondations font partie des catastrophes naturelles les plus répandues dans le monde, selon CRED and UNDRR (2020). En outre, l'occurrence signalée des inondations au fil du temps est en nette augmentation, de même que le coût économique associé. Selon le sixième rapport d'évaluation du groupe d'experts intergouvernemental sur l'évolution du climat (IPCC), il est prévu que les inondations provoquées par les pluies (par exemple, les crues soudaines et les inondations urbaines) devraient augmenter dans le monde entier au cours des prochaines années.

Dans les agglomérations urbaines, le nombre de personnes touchées et les dommages causés par les inondations sont particulièrement importants, principalement en raison de la forte densité de population et de la valeur des biens. Selon United Nations et al. (2019), le nombre de personnes vivant dans des zones urbaines dans le monde entier est en augmentation, et on estime que, d'ici 2050, deux tiers de la population mondiale vivront dans ces zones. Par conséquent, l'amélioration de la compréhension des inondations urbaines est devenue une question extrêmement importante dans le monde entier.

Néanmoins, l'étude des inondations urbaines constitue un défi majeur en raison de la grande variabilité des schémas d'écoulement et des éléments urbains qui interagissent avec l'écoulement, c'est-à-dire les bâtiments, les véhicules stationnés, le mobilier urbain, les espaces souterrains (par exemple, le réseau de métro, le réseau d'égouts). Parmi tous ces

éléments, les bâtiments sont la principale caractéristique d'un milieu urbain, et bien qu'ils aient des caractéristiques différentes, ils ont aussi des éléments en commun tels que des fenêtres, des portes, des portails et d'autres installations pour y accéder, il s'agit donc de structures poreuses.

Dans les zones à forte densité urbaine, les bâtiments sont souvent regroupés en blocs de bâtiments (Figure 1.4). Ces blocs disposent d'espaces intérieurs ouverts et vides (par exemple, jardins, cours, parkings, sous-sols), ainsi que des zones d'accès (ouvertures dans les façades) à ces espaces à travers les bâtiments (par exemple, portes, passages). Lors d'une inondation, l'eau peut donc accéder à l'intérieur des blocs de bâtiments par ces ouvertures et, en outre, être stockée dans les espaces internes vides. Par conséquent, un bloc urbain peut être caractérisé par ces deux propriétés: sa propriété à *convoyer* l'eau à travers les ouvertures dans les murs (porosité de convoyage, ψ) et sa propriété à *stocker* l'eau dans les espaces internes vides (capacité de stockage, ϕ).

Parmi les outils utilisés pour étudier les inondations urbaines, la modélisation numérique est la méthode la plus utilisée, notamment pour résoudre les équations bidimensionnelles (2D) des eaux peu profondes moyennées en hauteur (par exemple, Mignot et al., 2006; Soares-Frazão et al., 2008; Guinot, 2012; Bazin et al., 2017). Dans ces modèles 2D, différentes approches ont été développées pour incorporer les bâtiments et/ou des blocs et prendre en compte leurs effets. Cependant, les modèles numériques doivent être calibrés et validés, et le manque d'informations détaillées et fiables provenant d'inondations réelles représente un inconvénient à cet effet (Macchione et al., 2019). Un autre outil utilisé pour l'étude des inondations urbaines est la modélisation expérimentale, utile pour l'étude d'écoulements complexes dans des conditions contrôlées, ainsi que comme outil de référence pour la calibration des modèles numériques. Néanmoins, la plupart des études expérimentales sur les inondations urbaines considèrent les bâtiments ou les blocs de bâtiments comme des structures non poreuses à travers lesquelles l'eau ne peut pas entrer (par exemple, Ishigaki, 2003; Araud et al., 2014; Finaud-Guyot et al., 2018). Par conséquent, les données de validation des modèles physiques reproduisant l'intrusion de l'écoulement à l'intérieur des bâtiments ou des blocs urbains font encore défaut, même si des améliorations récentes ont été apportées.

Objectif

L'objectif de cette recherche est d'obtenir des données quantitatives sur l'influence que les échanges de flux de crue entre un bloc de bâtiments poreux et les rues ont sur le risque d'inondation.

Ce faisant, trois questions clés ont été abordées, en tenant compte des propriétés susmentionnées d'un bloc de bâtiments:

- *Question clé 1.* Quelle est l'influence de la variation de *l'ampleur de la porosité de convoyage* du bloc de bâtiments, ψ, sur les caractéristiques de l'écoulement?
- *Question clé 2.* Quelle est l'influence de la variation de la *distribution de la porosité de convoyage* du bloc de bâtiments, ψ, sur les caractéristiques de l'écoulement?
- *Question clé 3.* Quelle est l'influence de la variation de la *capacité de stockage* du bloc de bâtiments, ϕ, sur les caractéristiques de l'écoulement?

La porosité de convoyage du bloc, ψ, est définie ici comme la longueur totale des ouvertures dans le mur, divisée par la longueur totale du mur (Figure 1.5.A). La capacité de stockage, ϕ, est définie comme la surface horizontale vide à l'intérieur du bloc de bâtiments, divisée par la surface horizontale totale du bloc (Figure 1.5.B).

Méthodologie

Pour atteindre les objectifs, trois campagnes expérimentales sont menées, une pour chaque question clé abordée. Pour l'étude des deux premières questions clés, les expériences sont réalisées dans des conditions d'écoulement stationnaire. Pour la troisième question clé, les expériences sont menées dans des conditions d'écoulement stationnaire et instationnaire.

Les expériences ont été effectuées sur la Maquette Urbaine pour l'etude du Risque d'Inondation (MURI). Il s'agit d'une plate-forme rectangulaire basculante de 5,4 m de long et 3,8 m de large, qui représente un quartier urbain (Figure 3.1). Il comprend trois rues longitudinales (alignée avec l'axe x), croisant trois rues transversales (alignée avec l'axe y), toutes d'une largeur de 0,15 m, délimitées par seize blocs de bâtiments rectangulaires (Figure 3.2).

Pour le présent travail de doctorat, MURI est adapté en réduisant la zone d'étude à 5,4 m (axe des x)× 3,2 m (axe des y), c'est-à-dire en se concentrant sur un seul bloc de bâtiments et sur les quatre rues environnantes, respectivement intitulées, *amont, aval, droite et gauche* (voir la Figure 3.4). La pente du fond du modèle dans le sens longitudinal, $S_{0,x}$, est fixée à 0,12%, et la pente dans le sens transversal, $S_{0,y}$, est égale à zéro. Le bloc de bâtiments étudié comporte trois ouvertures disponibles le long de chaque mur (qui représentent les zones d'accès à l'intérieur du bloc), soit un total de douze ouvertures (voir la Figure 3.3).

Porosité de convoyage, ψ

Pour l'étude de la porosité de convoyage du bloc, ψ (questions clés 1 et 2), les expériences sont réalisées dans des conditions d'écoulement stationnaire et de régime fluvial. Le dispositif expérimental considère deux entrées de débit, provenant des voies droite et gauche. Le débit total entrant, $Q_{in,T} = 6.5\,\mathrm{l\,s^{-1}}$, est divisé en $Q_{in,1} = 4.5\,\mathrm{l\,s^{-1}}$ ($\approx$ 70% of $Q_{in,T}$), et $Q_{in,2} = 2.0\,\mathrm{l\,s^{-1}}$ ($\approx 30\%$ of $Q_{in,T}$), comme le montre la Figure 3.4.A. L'eau quitte le dispositif expérimental par quatre sorties, une à chaque rue (Sorties 1, 2, 3 et 4, dans les rues droite, gauche, aval et amont, respectivement). A chaque sortie, il y a un seuil, les hauteurs des seuils, w, sont fixées pour assurer une hauteur d'eau plus élevée dans la rue de droite que dans la rue de gauche, favorisant un écoulement transversal à travers le bloc poreux.

Pour l'étude de *l'ampleur de la porosité de convoyage* (question clé 1) huit cas d'étude avec différentes porosités de convoyage sont considérés, tous avec une porosité de convoyage symétrique dans les murs en face, c'est-à-dire la même valeur le long des murs en amont et en aval, et la même le long des murs à droite et à gauche. Un cas de référence est considéré, C00-00, qui comprend un bloc urbain non poreux, c'est-à-dire $\psi = 0$ dans toutes les murs (Figure 4.1, croquis A). Un cas extrême opposé est considéré, C100-100, où ψ est égal à 100% dans tous les murs du bloc, donc sans le bloc, qui représente une configuration urbaine d'une place de la ville (Figure 4.1, croquis B). Entre ces deux cas, une petite valeur de ψ (une seule ouverture le long d'un mur de bloc) et une grande valeur de ψ (trois ouvertures le long d'un mur de bloc) sont tous deux étudiés avec six cas présentant la même porosité de convoyage le long des murs de blocs face à face. Le long des murs de blocs orientés dans la direction x, C00-04 et 00-12 (Figure 4.1, croquis C et D), orientés dans la direction y, C06-00 et C19-00 (Figure 4.1, croquis E et F), et enfin dans les deux directions, C06-04 et C19-12 (Figure 4.1,

croquis G et H).

Pour l'étude de la *distribution de la porosité de convoyage* (question clé 2) six cas sont étudiés, avec la même ampleur de la porosité de convoyage le long du périmètre du bloc de bâtiments, quatre ouvertures au total, mais avec une distribution différente. Le premier, le cas C06-04 est un cas expérimental déjà étudié dans la question clé 1, qui répond aux caractéristiques requises pour l'étude de la question clé 2, il est donc considéré ici aussi. Les cas RL08 et R04L12 comprennent une porosité de convoyage le long de murs de blocs face à face, dans les murs de droite et de gauche. Cependant, pour le cas RL08, la magnitude de la porosité de convoyage est symétrique, c'est-à-dire, même valeur de ψ sur les deux murs face à face (deux ouvertures dans chaque mur, Figure 4.14.A), tandis que dans R04L12, elle est asymétrique, ψ est trois fois plus élevée dans le mur de gauche que dans le mur de droite (une ouverture dans le mur de droite et trois ouvertures dans le mur de gauche, Figure 4.14.B). Pour le cas D13R08, il y a une porosité de convoyage dans les murs adjacentes du bloc, à droite et en aval (deux ouvertures dans les deux murs, voir Figure 4.14.C). Dans les deux derniers cas, U06R12 et D06L12, ψ est concentré dans une région spécifique du bloc, dans la zone des murs amont/droite pour U06R12 (Figure 4.14.D) et dans la zone des murs aval/gauche pour D06L12 (Figure 4.14.E).

Capacité de stockage, ϕ

Pour l'étude de la capacité de stockage du bloc, ϕ (question clé 3), les expériences sont réalisées dans des conditions d'écoulement stationnaire et instationnaire. Pour un meilleur contrôle du débit d'entrée pendant les essais d'écoulement instationnaire, ainsi que pour diminuer l'incertitude des instruments de mesure, une seule entrée d'écoulement est considérée dans ce dispositif expérimental. L'eau arrive par l'entrée de la rue droite et est évacuée par les quatre rues de sortie (droite, gauche, amont et aval). Pour éviter tout effet de remous dans les écoulements instationnaires, aucun seuil n'a été placé aux sorties des rues (Figure 3.5.A), ce qui donne des conditions de sortie libre. Dans cette variante du dispositif expérimental, une seule ouverture est incluse dans chaque mur latéral du bloc de bâtiments poreux. En outre, pour modifier l'espace occupé à l'intérieur du bloc, un bâtiment non poreux de surface décroissante est installé ici (Figure 3.5).

Pour les expériences dans des conditions d'écoulement instationnaire, trois hydrogrammes

d'entrée ont été considérés (Figure 5.1.A). Ils présentent le même débit de pointe ($Q_{pk} \approx 5\,\mathrm{l\,s^{-1}}$) mais des caractéristiques différentes, c'est-à-dire, le temps de montée, T_r, le temps de descente, T_f, et le volume total d'eau de crue distribué, V (Figure 5.1.B). Toutes les caractéristiques des trois hydrogrammes d'entrée sont listées dans le Table 5.1. Dans des conditions d'écoulement stationnaire, cinq débits d'entrée ont également été étudiées, Q_{in}= 1, 2, 3, 4 and $5\,\mathrm{l\,s^{-1}}$, pour comparaison avec les tests dans des conditions d'écoulement instationnaire.

Techniques de mesure et traitement des données

Pour caractériser l'écoulement des crues dans la zone urbaine, les mesures combinent les débits d'entrée et de sortie, la hauteur et la vitesse de l'eau dans les rues et dans le bloc de bâtiments. Cependant, la manière dont ces paramètres sont collectés et traités diffère selon qu'il s'agit d'un écoulement stationnaire ou instationnaire. Dans les écoulements stationnaires, pour un débit d'entrée donné, des résultats fiables sont obtenus en mesurant chaque paramètre sur une certaine période de temps, donc toutes les valeurs présentées sont des *valeurs moyennes dans le temps*. Pour les écoulements instationnaires, un hydrogramme d'entrée est injecté et répliqué un certain nombre de fois, en mesurant chaque paramètre pendant toute la durée de toutes les répliques de l'hydrogramme, donc les valeurs présentées sont des *valeurs moyennes d'ensemble*.

Les débits de sortie sont mesurées avec des débitmètres électromagnétiques, et chaque débit d'entrée est réglé indépendamment avec un système automatique de vanne-débitmètre (Figure 3.4.B). Pour chaque débitmètre, des tests de convergence ont été effectués afin de déterminer la durée d'acquisition nécessaire dans des conditions d'écoulement stationnaire. Il a été constaté que ce temps est de 400 s (Figure 3.6). Pour déterminer le nombre approprié de répétitions de l'hydrogramme d'entrée dans des conditions d'écoulement instationnaire et obtenir ainsi la convergence de l'hydrogramme d'entrée moyenné par l'ensemble, l'hydrogramme a été injecté 200 fois. Il a été constaté que le nombre de répliques de l'hydrogramme d'entrée nécessaire est de 50 (Figure 3.8).

Le champ 2D de la hauteur d'eau, d, est obtenu à l'aide d'un capteur de distance à ultrasons (US), voir la Figure 3.9. Pour définir la durée d'acquisition appropriée de chaque mesure locale de la hauteur de l'eau dans des conditions d'écoulement stationnaire, la convergence temporelle du signal US est évaluée en effectuant treize mesures indépendantes de

la hauteur de l'eau en divers endroits (dans les rues, à l'intérieur du pâté de maisons et dans des zones spécifiques présentant des fluctuations importantes de la hauteur de l'eau, comme les carrefours). Cette durée a été définie comme étant de 50 secondes (Figure 3.10). Pour estimer le nombre minimum de répétitions nécessaires à la convergence des hauteurs d'eau moyennes d'ensemble pour les écoulements instationnaires, on suit la même procédure que pour l'hydrogramme d'entrée moyen d'ensemble. Le nombre minimum de répliques requis pour la convergence du limnigramme moyenné d'ensemble est de 50 (Figure 3.13).

La vitesse d'écoulement dans la colonne d'eau est mesurée en utilisant un vélocimètre acoustique à effet Doppler (ADV) avec une sonde à visée latérale (Figure 3.14). Ces mesures ont été effectuées uniquement en écoulement instationnaire. Afin de définir la durée d'acquisition appropriée, la convergence temporelle des données de vitesse ADV est testée en mesurant la vitesse d'écoulement à quatorze endroits de la zone d'étude (huit dans les rues et six dans le bloc, voir Table 3.1). En général, la convergence est obtenue plus tôt dans les rues qu'à l'intérieur du pâté de maisons (Figure 3.15). Par conséquent, deux durées d'acquisition appropriées sont proposées pour le calcul des vitesses moyennes dans le temps (U_x, U_y), 100 s dans les rues et 200 s à l'intérieur du pâté de maisons. Ces vitesses sont utilisées pour le calcul du débit dans les rues.

La vitesse de surface, dans les rues et dans le bloc, est mesurée à l'aide de la Large Scale Particle Image Velocimetry technique (LSPIV), pour les écoulements stationnaires et instationnaires (Figure 3.17). Afin d'évaluer la durée d'enregistrement vidéo appropriée pour la technique LSPIV, des essais de convergence sont établis en enregistrant à une fréquence de 25 fps le champ de vitesse de surface. Pour les expériences dans des conditions d'écoulement stationnaire, un temps de 60 s s'est avéré suffisant pour la convergence des vitesses de surface moyennes (Figure 3.18). Pour les expériences dans des conditions d'écoulement instationnaire, un temps de 2 s est considéré, ce qui semble être un bon compromis entre une fréquence d'échantillonnage suffisamment élevée (50 images) et une estimation convergente de la de la vitesse moyenne de la surface variant dans le temps (Figure 3.21).

Modèle à échelle distordue

Afin de transférer les données mesurées et estimées de l'échelle du modèle à l'échelle du prototype réel, la similitude de Froude a été utilisée, $Fr_M = Fr_P$. Un modèle distordu

a également été considéré, c'est-à-dire que le rapport d'échelle horizontal, λ_{xy}, diffère du rapport d'échelle vertical, λ_z. Le rapport d'échelle horizontal considéré est $\lambda_{xy} = 50$, tandis que le rapport d'échelle vertical diffère entre les expériences pour étudier la porosité de convoyage et la capacité de stockage. Pour le premier, $\lambda_z = 10$, et pour le second $\lambda_z = 30$.

Résultats

Porosité de convoyage, ψ

On constate que l'ampleur de la porosité de convoyage a une faible influence sur la distribution spatiale des hauteurs d'eau. Dans les rues entourant le bloc, la différence moyenne de hauteur d'eau (par rapport au cas de référence) est d'environ 1,5%, et la différence maximale de 12% (Figure 4.4). Cependant, comme ces variations de hauteur d'eau se produisent localement, à proximité des ouvertures, on constate que la distribution de la porosité de convoyage affecte significativement la localisation de ces variations (Figure 4.16). Elle est toujours plus importante dans la rue par laquelle le flux du bloc est évacué (c'est-à-dire la rue en aval). Lorsqu'on s'éloigne du bloc de bâtiments (c'est-à-dire dans le tronçon de rue non adjacent au bloc), l'influence de l'ampleur et de la distribution de la porosité de convoyage est beaucoup plus faible, avec une différence maximale mesurée d'environ 3% (par rapport au cas de référence). Il faut noter que la hauteur d'eau peut fortement varier de part et d'autre d'un mur de bloc, c'est-à-dire entre le bloc et la rue : de -14% (hauteur d'eau plus faible dans la rue) à 10% (hauteur d'eau plus élevée dans la rue), voir la Figure 4.3. Ce résultat remet en question les pratiques courantes qui consistent à considérer que le niveau d'eau dans le bâtiment est égal à celui de la rue adjacente pour estimer les dommages potentiels d'un scénario d'inondation.

L'impact de la porosité de convoyage est beaucoup plus significatif sur la vitesse globale locale et les débits dans les rues entourant le bloc (changements dans le débit jusqu'à 70% par rapport au cas de référence), voir la Figure 4.10. A l'intérieur du bloc, la valeur et la distribution de la porosité ont une influence significative sur le schéma d'écoulement. Le nombre et la taille des cellules de recirculation sont principalement déterminés par l'ampleur et l'emplacement des débits d'échange entrants et sortants entre la rue et le bloc (voir la Figure 4.12). Cependant, lorsqu'on s'éloigne du bloc, l'influence de la porosité est limitée,

comme cela a été observé pour les hauteurs d'eau, et pourrait donc être négligée.

Au sein du bloc urbain, la variation de la hauteur d'eau entre les différents cas est minime lorsque l'ampleur et la distribution de la porosité changent (des variations de l'ordre de 3% ont été trouvées). A l'inverse, les vitesses sont largement affectées, principalement parce qu'elles sont exarcerbées par les jets d'eau entrant dans le bloc. Les vitesses d'écoulement augmentent alors lorsque la porosité de convoyage est située sur les murs du bloc adjacent à la rue à débit prédominant (c'est-à-dire la rue avec le plus grand débit), voir la Figure 4.12. Par conséquent, l'ampleur de la porosité de convoyage et sa distribution ont un impact majeur sur les vitesses et les schémas d'écoulement dans le bloc.

Enfin, les variations de l'ampleur et de la distribution de la porosité de convoyage ne modifient le risque d'inondation pour les piétons que localement, à proximité des ouvertures, à la fois dans les rues et dans le bloc de bâtiments (Voir la Figure 4.13).

Capacité de stockage, ϕ

On constate que l'augmentation de la capacité de stockage du bloc, ϕ, atténue le débit de pointe (Q_{pk}) global de la région amont à la région aval de la zone urbaine, avec une réduction maximale du débit de pointe de 10% (voir le graphique *Global outflow hydrograph* de la Figure 5.5). Cependant, ϕ peut également augmenter le débit dans certaines rues, jusqu'à 14% est observé dans cette étude (voir le graphique *Outflow hydrograph 4* de la Figure 5.5). À l'inverse, le décalage temporel entre les débits de pointe de l'hydrogramme du débit entrant et du débit sortant global n'est pas significativement impacté. La capacité de stockage a également réduit la hauteur maximale de l'eau dans la plupart des rues, jusqu'à 13% pour les rues de gauche et d'aval (voir la Figure 5.7) et d'environ 15% dans le bloc de bâtiments. L'impact sur la vitesse de surface dans la rue droite reste limité à 4%, cependant, pour la rue gauche, l'augmentation de ϕ augmente la vitesse maximale de surface, d'environ 20% lorsque ϕ passe de 0,5 à 1 (Figure 5.9). A l'intérieur du bloc de bâtiments, une légère augmentation de la vitesse est constatée (7%) à la valeur de capacité de stockage la plus élevée (c'est-à-dire $\phi = 1$). Dans cette zone, on observe plusieurs cellules d'écoulement de recirculation, dont le nombre et la taille sont déterminés par la distance entre les murs du bloc et les murs du bâtiment non poreux (Figure 5.10). Avec les modifications de la hauteur et de la vitesse de l'eau, principalement sur la rue de gauche, en raison de l'augmentation de

la capacité de stockage, le risque pour les piétons augmente dans cette zone (Figure 5.11). Dans le bloc, il y a une augmentation du niveau de risque dans quelques zones lorsque la capacité de stockage augmente (Figure 5.12).

L'influence de l'instationnarité de l'hydrogramme d'entrée, α_r, est assez notable. Parmi les trois hydrogrammes d'entrée testés, les résultats pour les deux hydrogrammes ayant la même valeur α_r ($\sim$2,2) sont très similaires et différents de ceux de l'hydrogramme d'entrée avec un degré d'nstationnarité plus élevé (H.SLS, avec $\alpha_r = 4,49$). Pour une valeur plus élevée de α_r, l'atténuation du débit de pointe global est plus importante: de 5% lorsque $\alpha_r = 2,2$ à 10% lorsque $\alpha_r = 4,49$ (voir le graphique *Global outflow hydrograph* de la Figure 5.5). Les variations des hauteurs d'eau maximales, dans les rues entourant le bloc, par rapport au cas de référence, sont plus importantes pour la valeur α_r la plus élevée (sauf dans la rue droite où elles sont identiques) et dans des sens différents, c'est-à-dire que pour $\alpha_r = 2,2$ les hauteurs d'eau maximales augmentent dans la plupart des cas, alors que pour $\alpha_r = 4,49$ dans tous les cas les hauteurs d'eau maximales diminuent (voir la Figure 5.7).

Enfin, les résultats pour les écoulements instationnaires diffèrent à certains égards de ceux des écoulements stationnaires. Les hauteurs d'eau étaient dans la plupart des cas plus importantes pour les écoulements stationnaires dans les rues et à l'intérieur du bloc, jusqu'à 30% (voir la Figure 5.7 et la Figure 5.8). La vitesse maximale de surface était plus faible dans la plupart des cas pour les écoulements stationnaires: dans la rue gauche, jusqu'à 25% et dans le bloc de bâtiments, jusqu'à 20%. Le risque d'inondation évalué pour les piétons a varié, dans certains cas le niveau de risque était plus élevé en cas d'écoulement instationnaire ($\phi = 0,5$ et 0,75), dans d'autres en cas d'écoulement stationnaire ($\phi = 0,9$) et il était à peu près le même pour $\phi = 1$ (voir la Figure 5.12).

Conclusions

L'influence de la porosité de convoyage sur les caractéristiques des eaux de crue est plus importante que celle de la capacité de stockage. On observe également que cette influence est plus importante sur les vitesses d'écoulement que sur les hauteurs d'eau, dans les rues et à l'intérieur du bloc.

La distribution de la porosité de convoyage a une grande influence sur le débit à travers le bloc de bâtiments, et donc aussi sur les caractéristiques d'écoulement dans les rues et à

l'intérieur du bloc. Il a été observé dans cette recherche que cette influence peut faire passer le débit à travers le bloc de moins de 1% du débit total entrant dans le district urbain à 10%, simplement en changeant la distribution des ouvertures le long des murs du bloc. Les débits les plus élevés dans le bloc sont observés dans les cas où les ouvertures dans les murs du bloc font face à la direction de l'écoulement de la crue, tandis que les débits les plus faibles sont observés lorsque les ouvertures sont dans les murs opposés.

Le degré d'instationnarité de la crue (hydrogramme d'entrée) a un fort impact sur le volume d'eau qui est stocké dans le bloc, et par conséquent sur les caractéristiques d'écoulement dans les rues et le bloc.

Enfin, au vu des différents impacts observés sur les caractéristiques d'écoulement dus aux échanges de débits latéraux entre les rues et le bloc de bâtiments lors d'une inondation, on constate qu'il y a également un impact considérable sur l'estimation du risque d'inondation. Par conséquent, il est fortement recommandé de considérer les effets d'un bloc urbain poreux pour une évaluation plus fiable des risques d'inondation.

CONTENTS

Nomenclature

A_b	horizontal surface covered by the non-porous building within the city block
A_B	total horizontal surface within the city block
b	street width
d	flow depth
d_{bs}	base flow depth
d_{pk}	peak flow depth
DF	debris factor
Fr	Froude number
h_s	height of the subject
l	clearance between the block walls and the non-porous building
$L_{B,x}$	length of a block side wall aligned with the $x-$axis
$L_{B,y}$	length of a block side wall aligned with the $y-$axis
M_0	force per unit width of the flood flow
m_s	mass of the subject
PN	product number
Q	discharge
Q_{in}	inflow discharge
Q_{out}	outflow discharge
Q_{pk}	peak discharge
Q_{st}	street discharge
Re	Reynolds number
S	rising speed of the free-surface
$S_{0,x}$	bed slope along $x-$axis
$S_{0,y}$	bed slope along $y-$axis
t	time
T	hydrograph total duration
T_d	stage hydrograph rising time
T_f	inflow hydrograph falling time

T_r inflow hydrograph rising time

U velocity magnitude

U_b bulk velocity

U_{bs} base flow velocity

U_c convection velocity of turbulent eddies

U_{pk} peak flow velocity

U_s surface velocity

U_x time-averaged velocity along $x-$axis

U_y time-averaged velocity along $y-$axis

U_z time-averaged velocity along $z-$axis

u_x instantaneous velocity along $x-$axis

u_y instantaneous velocity along $y-$axis

u_z instantaneous velocity along $z-$axis

V total floodwater volume dispatched by the inflow hydrograph

V_r floodwater volume dispatched by the inflow hydrograph during the rising stage

w weir height

x, y, z global coordinates, in longitudinal, transverse and vertical directions, respectively

x^*, y^*, z^* local coordinates, in longitudinal, transverse and vertical directions, respectively

Greek letters

α unsteadiness parameter

θ_v mobility parameter

λ_{xy} scale ratio in the horizontal plane xy

λ_z scale ratio in the vertical direction z

μ friction coefficient for vehicle stability in flood flows

ϕ city block storage capacity

ψ city block conveyance porosity

CHAPTER 1

INTRODUCTION

1.1 General context

During summer 2021, several European cities were affected by extreme weather events. Among these, the most severe occurred in cities in Belgium and Germany (see Figure 1.1), where floods affected thousands of people and resulted in more than 200 casualties. Over the same summer in China, heavy rainfall caused flooding in several cities in Henan province, resulting in more than 300 fatalities. The estimated cost of the damage in Belgium an Germany was around 20 billion USD and about 30 billion USD in China (source: International Disaster Database, EM-DAT). Worldwide, for the same year we find more or less severe cases of flooding. According to the EM-DAT, 206 flood events were reported around the world in 2021, for an estimated damage cost of at least 70 billion US dollars.

Nevertheless, 2021 was not an atypical year, full of extreme weather events. For many years and nowadays, flooding has been, among the most prevalent natural disasters worldwide, as shown in Figure 1.2, for the period 2000-2019 (flooding accounted for 44% of all natural disasters according to CRED and UNDRR, 2020). Moreover, the reported occurrence of flood events over time has a clear increase, along with the economic cost involved (see Figure 1.3), which can be partly attributed to the improved reporting, the increase in population, the expansion of urban areas and to rising assets property values (Kundzewicz

FIGURE 1.1. Left: Flooding in the city of Liège, Belgium, during the summer of 2021. Rigt: Bad Münstereifel downtown, just after the summer flooding in 2021. Source: Deutsche Welle (www.dw.com).

et al., 2014). However, there is also evidence that climate change is altering various factors affecting flooding, e.g. precipitation frequency and intensity, snow cover, snowmelt, soil moisture, etc. According to the Sixth Assessment Report by the Intergovernmental Panel on Climate Change (IPCC), it is projected that in the coming decades continued alteration of these factors could lead to increased rainfall-generated flooding (e.g. flash flooding and urban flooding) in several areas of the planet.

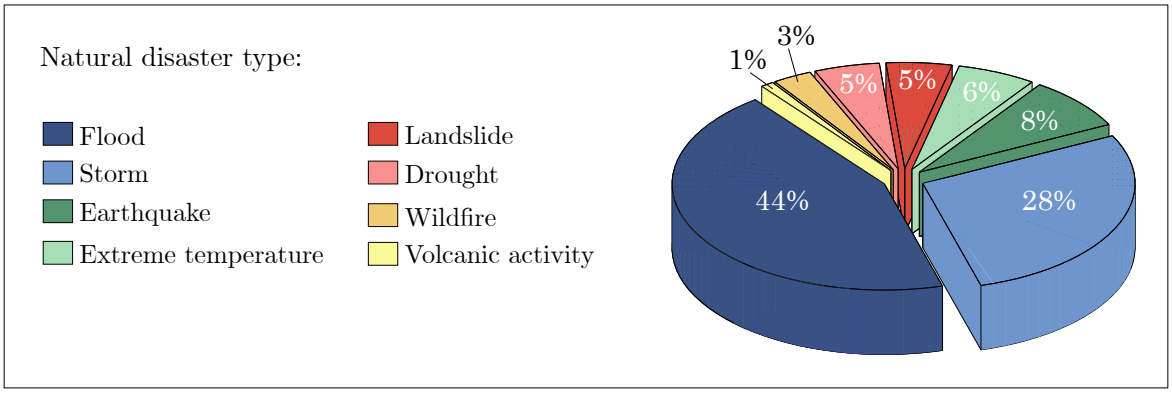

FIGURE 1.2. Percentage of occurrence of natural disasters worldwide by disaster type from 2000 to 2019, according to CRED and UNDRR (2020).

In urban settlements, the number of people affected and damages caused by flooding are particularly significant, mainly because of the high population density and value of assets. According to United Nations et al. (2019), the number of people living in urban areas worldwide is increasing, and it is estimated that, by 2050, two thirds of the world's population will be living in these areas. Moreover, in low-income countries, where the infrastructure is not adequate for mitigation and protection, floods often cause irreparable damage and suffering to the inhabitants, which could revert years of progress in poverty reduction and

development (Rentschler and Salhab, 2020). Therefore, improving the understanding of such flood events has become an extremely important issue worldwide.

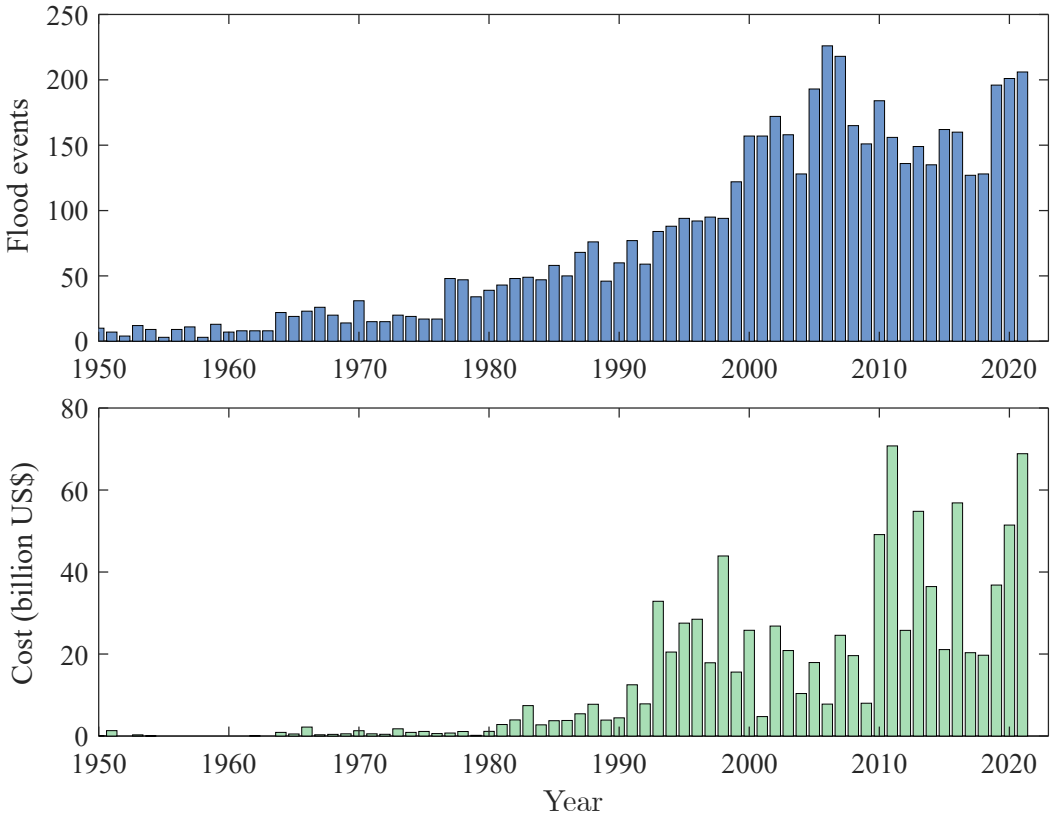

FIGURE 1.3. Worldwide reported flooding events and the damage cost caused by them, from 1950 to the present. Source: EM-DAT, CRED.

Nonetheless, investigating urban floods is a major challenge because of the high variability of flow patterns and urban elements that interact with the flow, i.e., buildings, parked vehicles, street furniture, underground spaces (e.g., metro network, sewerage network). Among all these elements, buildings are the main feature of an urban environment, and although they have different characteristics, they also have elements in common such as windows, doors, gates and other facilities to access them. Hence, buildings are porous structures, because floodwaters can pass through these facilities. In addition, in areas with high urban density, buildings are often gathered in city blocks[1] (see Figure 1.4), where part of the floodwater volume can be stored in interior open spaces (e.g., gardens, courtyards, parking lots, basements), which can then modify the characteristics of the flood flows in the area (e.g. flow depths, velocities, discharge distribution, etc.).

Among the tools used to study urban flooding, numerical modelling is the most widely

[1] A city block is the smallest group of buildings that is surrounded by streets.

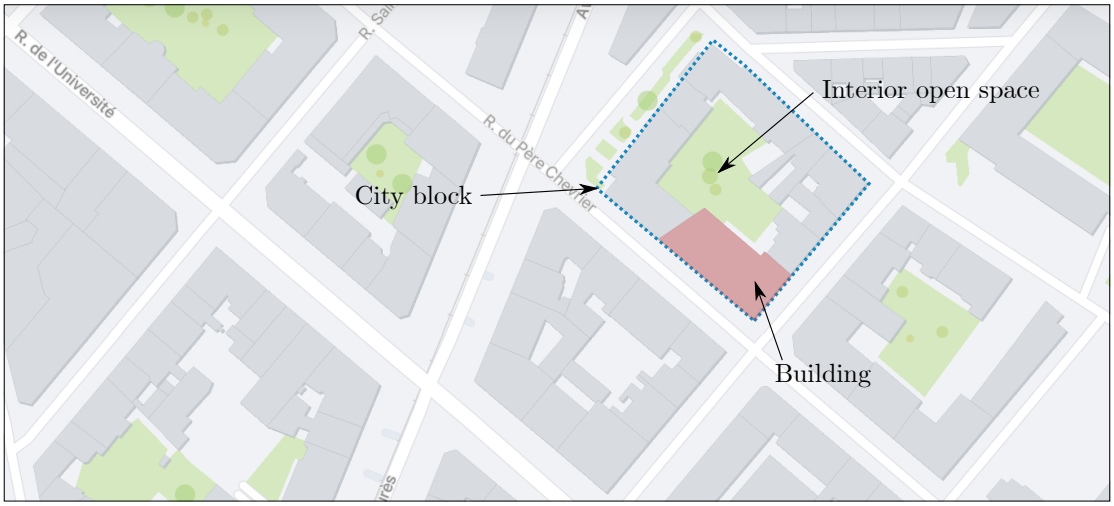

FIGURE 1.4. Plan view of a common urban area, where buildings are clustered in city blocks. Within these there are different facilities such as gardens, parking lots, courtyards, etc.

used method, especially those solving the two-dimensional (2-D) depth-averaged shallow water equations (e.g. Mignot et al., 2006; Soares-Frazão et al., 2008; Guinot, 2012; Bazin et al., 2017), since: (*i*) flows within urban areas are too complex for one-dimensional (1-D) models; (*ii*) the involved horizontal geometrical length-scales (typically street lengths and width) are often large compared to flow depths; and (*iii*) studies using 3-D modelling demand a high computational cost (Paquier et al., 2019). In these 2-D models, different approaches have been developed to incorporate buildings and take into account their effects. We can regroup these approaches into those that consider buildings (or city blocks) as non-porous elements (the most common) and those that consider them as porous elements.

Within the first group most of them completely exclude buildings from the computational mesh, i.e. the city is seen as a street network, as the grid is generated with holes, which are aligned with the building footprint (e.g. Aronica and Lanza, 2005; Schubert et al., 2008). The second approach integrates the buildings into the computational mesh, assigning to the mesh cells, corresponding to the building footprints, their respective buildings roof top elevation, then, water can flow through these cells if the flow depth is greater than the buildings' height (e.g. Hunter et al., 2008). In the second group, which considers buildings as porous elements, three main approaches can be listed. The first one consists of assigning buildings a threshold elevation (elevation of the building's entrance), removing all building walls and once the flow depth exceeds this threshold, water can flow through the mesh cells of the buildings footprint (e.g. Shen et al., 2018). The second approach consists of removing the

buildings and assigning a larger resistance parameter to the cells of the buildings footprint or developed parcels (e.g. Liang et al., 2007; Gallegos et al., 2009). Finally, the third approach also removes all buildings and introduces porosity coefficients, accounting for the reduction in water *storage* volume and reduction in the available surface for water *conveyance*, due to the presence of buildings. This latter approach has been quite developed in the last decades, being applied in various manners, e.g. at the scale of the computational cells (e.g. Sanders et al., 2008), at large-scale as statistical descriptors (e.g. Soares-Frazão et al., 2008), dependent (e.g. Özgen et al., 2016) or not (e.g. Guinot et al., 2017) on the flow depth, etc. An extended recent review of the different options in porosity models is provided by Dewals et al. (2021). A first conclusion raised by this short literature review is that 2D models do not reproduce the complexity of buildings or city blocks geometries (e.g., occupation density, number of openings, internal walls), but only their external footprints.

Although numerical models have been developed extensively and are widely used, the scarcity of detailed and reliable data on real-world urban flood events represents a drawback to their calibration and validation (Macchione et al., 2019). Future 2D numerical models aiming to better reproduce the interior of flooded buildings will face a significant lack of information, such as in-situ validation data. In this context, laboratory physical models are a convenient alternative, especially useful, for investigating flow patterns in complex geometries under controlled conditions (Finaud-Guyot et al., 2018). These can provide reliable information and detailed flow measurements at local scale under controlled conditions, which makes them particularly useful benchmark tool for the calibration of numerical models. Nevertheless, in the literature most experimental urban flood studies consider buildings or city blocks as non-porous structures through which the flow cannot enter (e.g. Ishigaki, 2003; Araud et al., 2014; Finaud-Guyot et al., 2018). Consequently, validation data in physical models reproducing the flow intrusion within buildings or city blocks is still lacking, even if recent improvements have been done.

In this context, the present PhD thesis (which is included in the Detailing Urban Flood Impact project, DEUFI) aims to investigate the lateral flow exchanges between buildings and streets in a small urban area during an urban flood, relying on laboratory experiments. The latter were conducted on a tilting physical model termed MURI (Maquette Urbaine pour l'étude du Risque d'Inondation, i.e. urban model for the study of flood risk), at the

Hydraulics and Hydro-morphology Laboratory of INRAE centre Lyon-Villeurbanne, France (https://riverhydraulics.inrae.fr). We have restrained the study to the flow exchanges between a single city block and its adjacent streets, considering the mechanisms that affect the capacity of the city block to convey and store flood flows.

1.2 DEUFI project

The DEUFI project aims to study the urban flood processes at local scale, focusing on the lateral flow exchanges between streets and buildings, which can impact flow depth and velocity, and subsequently, flood hazard both in buildings and in the street network. The project is funded by the French National Research Agency, ANR (Agence Nationale de la Recherche) and involves various research institutions in France and abroad:

- RiverLy, INRAE (https://riverly.inrae.fr/)
- LMFA, INSA de Lyon (http://lmfa.ec-lyon.fr/)
- ICube, Université de Strasbourg (https://icube.unistra.fr/)
- GRED (https://gred.ird.fr/)
- Cerema - EMF (https://www.cerema.fr/fr/cerema/directions/cerema-risques-eau-mer)
- Artelia (https://www.arteliagroup.com/fr)
- G-EAU (http://www.g-eau.fr/index.php/fr/)
- HECE, Université de Liège (http://www.hece.ulg.ac.be/cms/)
- Department of Hydro Science and Engineering Research, KICT (https://www.kict.re.kr/).

To meet the objectives, the project comprises 3 main tasks:

1. **Laboratory experiments**. The aim is to investigate the hydrodynamic processes related with lateral flow exchanges between buildings and streets, using various laboratory scale models. This part comprises 3 levels of research:
    - *Facade level*. The experiments focus on the flow exchange through a single opening located within a building facade during a flood. The study focuses on the factors

that affect the discharge from the street towards the building through the different types of facade openings (windows, gates, doors). The physical scale model for this research is located in the Laboratory of Fluid Mechanics and Acoustics (LMFA) at INSA Lyon in France. For more information on this study, please refer to Mignot et al. (2020).

- *City block level.* The experiments focus on a city block and its surrounding streets, studying the effect on flood flows in the streets and within the block. For this level of study, three physical models are used: the first one is located at INRAE in France (model used in the present PhD thesis); the second one is located at the Engineering Hydraulics Laboratory at University of Liege, in Belgium (for more information about the study conducted on this model, refer to Li et al., 2021); and the third one is located at the Korea Institute of Civil Engineering and Building Technology (KICT).
- *Urban district level.* This experimental work considers a larger spatial scale, covering several city blocks and streets. The physical scale model for this research is located in the Laboratory of Engineering, Computer Science and Imagery, ICube, at the University of Strasbourg. The results and findings should be used for the elaboration of flood management strategies (for more information about the studies conducted on this model, refer to Finaud-Guyot et al., 2019).

2. **Field cases**. This task aims at developing field-scale tools and their application in order to assess the relevance of the results for local stakeholders. Two study cases have been considered for which a large set of data is available:

   - *Nîmes field case.* The city is located in the Occitanie region of Southern France. In Nîmes, the main flood risk arises from runoff on the hills (for details on the work carried out on this task, please refer to Monteil et al., 2022).
   - *Oullins field case.* Oullins belongs to the metropolitan area of Lyon in the Auvergne-Rhône-Alpes region of France. In Ollins, the main flood risk comes from the overflow of a small river, Yzeron river (for details on the work carried out on this task, please refers to https://arcg.is/qyG0O0).

3. **Hydrodynamic models**. The third task aims at adapting/improving hydrodynamic

models (1D, 2D and 3D), to account for the flow exchanges between streets and buildings. This task benefits from the measurements detailed above for the validation of these models against experimental and field data. These models will be useful to investigate more complex geometries than those considered in tasks 1 and 2, and additional flow types. (for details on the work carried out on this task, please refer to Choley et al., 2021).

For more information on the DEUFI project, refer to the websites of the ANR and the River Hydraulics team of INRAE Lyon at the following links:

- https://anr.fr/Projet-ANR-18-CE01-0020
- https://riverhydraulics.inrae.fr/en/projects/ongoing-project/anr-project-deufi-detailing-urban-flood-impact/

1.3 Objectives of the PhD thesis

The objective of this research is to obtain quantitative data on the influence that flood flow exchanges between a porous city block and streets have on the flood hazard for inhabitants in a city block and in the adjacent streets. Among the different parameters used to denote flood hazard, the most widely used are flow depth and velocity. Therefore this research is focus on quantifying the impact of flow exchanges on these parameters, together with the discharge distribution in the study area.

To improve the knowledge on such processes, two main questions are raised:

- Q1: What is the influence of a porous city block (compared to a non-porous city block) on flood hazard in a long-duration flood event (i.e., under steady flow conditions).
- Q2: What is the influence of a porous city block on flood hazard in a flash flood event (i.e., under unsteady flow conditions).

Under steady flow conditions, the main effect of the porous city block on floodwaters is its property to convey the flow between different streets through itself. The parameter able to quantify the flow conveyance through the block walls is referred to as *conveyance porosity*, it is denoted as ψ and is defined as follows:

$$\psi = \frac{\text{opening length along the city block wall}}{\text{total length of the city block wall}} \tag{1.1}$$

Figure 1.5.A provides a schematic view of a city block showing the opening along one of the block walls. Flow exchanges between the city block and streets take place through this open area.

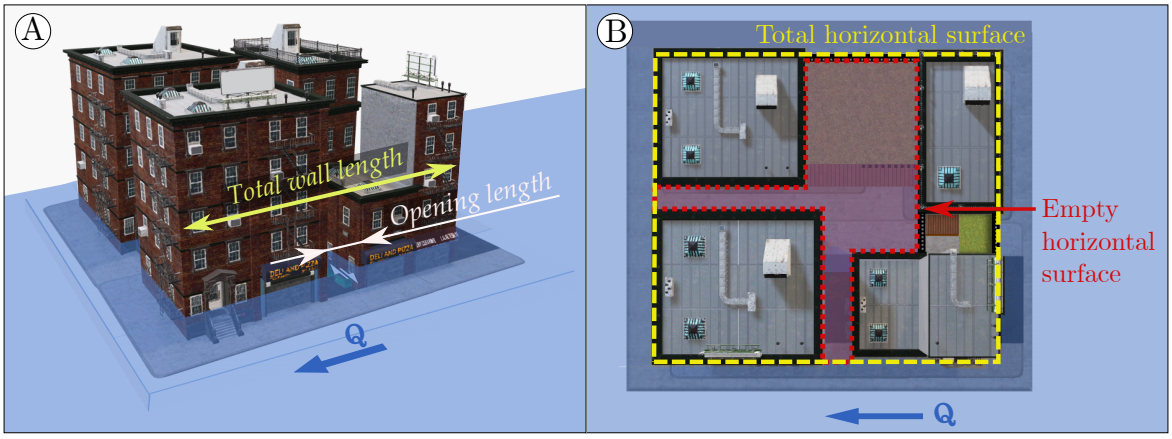

FIGURE 1.5. A) Isometric view of a city block, composed of four buildings. One opening is displayed in one side of the block. B) Plan view of a city block, showing the empty interior space in red color.

Under unsteady flow conditions, in addition to the property of the block to convey flow, it also has the capacity to store part of the floodwater volume in its available empty space. The parameter to quantify the capacity of the city block to store this volume is referred to as *storage capacity*, it is denoted as ϕ and is defined as follows:

$$\phi = \frac{\text{empty horizontal surface within the city block}}{\text{total horizontal surface within the city block}} \tag{1.2}$$

Figure 1.5.B shows a schematic plan view of a city block, the red shaded area displays the empty horizontal surface available for floodwater volume storage within the block.

To answer the two main questions of this PhD work, three key issues have been addressed:

- *Key issue 1.* What is the influence of varying the magnitude of the city block conveyance porosity, ψ, on flow depths, velocities and discharges in the streets and within the block under steady flow conditions?

- *Key issue 2.* What is the influence of varying the distribution of the city block conveyance porosity, ψ, on flow depths, velocities and discharges in the streets and within the block under steady flow conditions?

- *Key issue 3.* What is the influence of varying the city block storage capacity, ϕ, on flow depths, velocities and discharges in the streets and within the block under unsteady flow conditions?

1.4 Manuscript outline

The manuscript is divided into 6 chapters. After the present chapter 1, chapter 2 contains a literature review on urban flood research works that have contributed to the understanding of the different processes involved in urban flooding. Followed by a review on flood hazard assessment and the different criteria found in the literature.

Chapter 3 describes the methodology followed in this research work, which contains: (*i*) the description of the equipment and instruments employed; (*ii*) the measurement techniques applied; and (*iii*) the data processing for both steady and unsteady flows. The last section exposes an updated criterion for pedestrian flood hazard, which takes into account recent results and findings on pedestrian instability in flood flows.

Chapter 4 presents the experiments carried out to study the influence of conveyance porosity of the city block on flood hazard (Q1). Firstly, experiments carried out to answer the key issue 1 are shown, detailed the flow features and its influence on the flood hazard assessment. Then, experiments dedicated to the key issue 2 and the results obtained on the measured flow features and flood hazard are displayed. Conclusions on the results of these tests are given at the end of this chapter.

Chapter 5 exposes the experiments carried out to investigate the effects of storage capacity of the city block on flood hazard (Q2). The different flow cases tested under steady and unsteady flow conditions are described, along with resulting flow features. A specific attention is paid for comparing different unsteady and steady flows. For both types of flow, the flood hazard to pedestrians is shown. This chapter ends by presenting the conclusions on the results found. Finally, Chapter 6 draws the general conclusions of this thesis work and perspectives on possible future research and improvements for the study of urban flooding.

CHAPTER 2

STATE OF THE ART

This section aims to detail the available information on the flow processes that take place during an urban flood in the different areas of a flooded city and their consequences in terms of the level of hazard for inhabitants.

2.1 Flood flow mechanisms in urban areas

2.1.1 Characteristics of an urban area

The label of urban area is commonly dependent on population density and total population. However, there is no standard definition of an urban area, there are different criteria depending on the country: In England an urban area is a location with a population of over 10,000 inhabitants, while in Australia with a population above 1000 inhabitants and a density above 200 inhabitants/km^2. In France an urban area is a continuous area providing at least 10 000 jobs (source: Institut National de la Statistique et des Etudes Economiques). According to the OECD (Dijkstra et al., 2019), an urban area is a cluster of contiguous grid cells of 1 km^2 with a density of at least 1500 inhabitants and a population of at least 50,000 inhabitants overall. Thus, having looked at all these different criteria, the common feature is that it refers to a densely populated area, which comprises a huge number of facilities necessary for the daily life of its inhabitants, such as residential and commercial buildings, roads, bridges,

sewage network, urban transport systems etc.

All the facilities necessary to supply the needs of a densely populated area strongly alter the landscape. Modifications in slope, elevation, soils and vegetation cover influence how rainfall is captured, stored and released in hydrological systems (McGrane, 2016). In a temperate area, approximately 10% of the rainfall becomes runoff, the rest infiltrates into the ground or evaporates. Whereas in a dense urban area, runoff can be as much as 85% of rainfall (Tjallingii, 2012). Therefore, urban flooding occurs due to a complex interaction of natural and anthropogenic processes, some of which operate at very local scales (Dawson et al., 2008), see Figure 2.1.

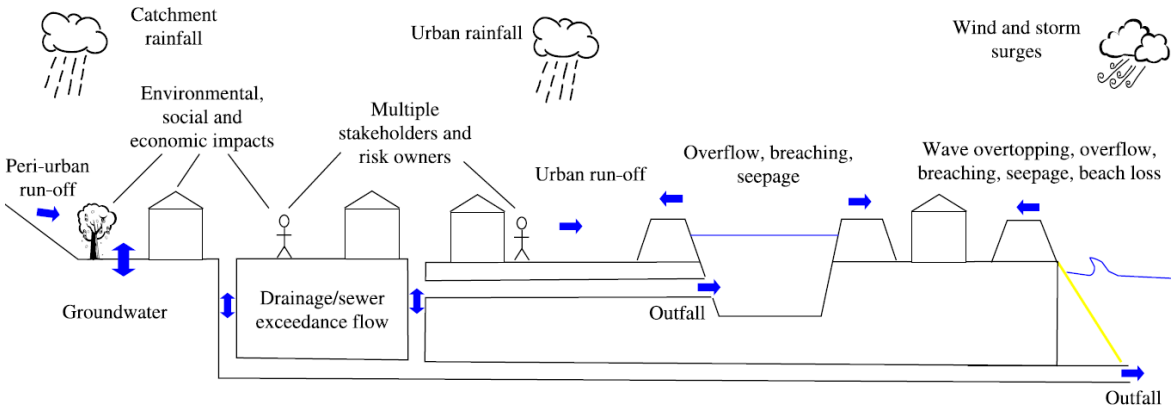

FIGURE 2.1. Integrated urban drainage, from Dawson et al. (2008).

The main characteristic of an urban area is the density of built-up areas. *Buildings* are usually clustered in *city blocks*, which are surrounded by communication routes such as *roads for vehicles* , *rail* or *tramway tracks*, etc. Because a large portion of permeable soil is replaced by impermeable surfaces, the presence of engineered water systems are necessary. These include dense network of *ditches*, *culverts* and subsurface *sewerage networks* that reduce the distance that water must travel overland to reach streams and rivers (Konrad, 2003), which resulted in a totally altered water cycle.

2.1.2 Flood sources in an urban area

The sources of flooding in an urban area include *pluvial flooding*, caused by intense rainfall producing surface runoff and quite possibly sewer overflows, *fluvial flooding* caused by overflowing rivers carrying very high flows, *coastal flooding* produced by storm surges that

penetrate inland, and also *groundwater flooding* (Dawson et al., 2008). In the case of river and coastal floods, these can be exacerbated due to levee failures, and the consequences are usually catastrophic. However rain-generated flooding is becoming increasingly common in urban areas (Fritsch et al., 2016; Rosenzweig et al., 2018), related to the increase in rainfall intensity and frequency. According to Oke (1982), due to heat-absorbing materials and heat-generating processes coupled with the lack of cooling vegetation contribute to increased temperatures in urban areas, which impact the proliferation of rainfall in downwind areas. Thus, the above-mentioned factors, together with reduced infiltration and evapotranspiration and increased surface runoff make the urban area particularly susceptible to flooding.

2.1.3 Surface runoff dynamics

In order to prevent the stagnation of surface runoff in the impervious surfaces of an urban area, the hydraulic infrastructure is designed to capture and direct this runoff into the subsurface sewerage network. This infrastructure is designed for a certain amount of runoff, resulting from the evaluation of different design rainfall events. However, in extreme weather-related events, this infrastructure may not adequately meet the requirements to prevent inhabitants from being affected. Streets then become the main pathways for conveying runoff. However, in this street network various facilities and elements modify the flood flow features, such as crossroads, underground spaces (e.g., public transport facilities, pedestrians and vehicle passages), as well as street furniture and vehicles (privet and public service); the latter two may even be swept along with the flow (Figure 2.2.A).

Buildings and infrastructure dedicated to the protection of people from inclement weather (e.g., wind, rain, heat, snowfall), being located on the side of these streets, with their ground level often at the same level as streets level for access purposes, may be at risk under a flood scenario. Flood flows enter gardens, courtyards, parking lots through the access areas of the buildings, enter homes through damage doors and windows (Figure 2.2.B) or even through the walls themselves (according to testimonies on the 2021 flood in Liège).

2.2 Experimental modelling of urban flooding

The study of floods began in earnest in the second half of the last century (e.g. White, 1961; Kates, 1962; Ward, 1978; Paul, 1984), and in the last two decades it has increased, mainly

FIGURE 2.2. A) Flood in Belgium during the summer of 2021. Source: Sky News (https://news.sky.com/). B) Floods of 2015 in Graiguenamanagh, Ireland. Source: Independent.ie (www.independent.ie).

for urban areas, incorporating more and more complex flows (Mignot et al., 2019). Given the variability and complexity of urban flood flow processes, and the limited availability of field data, the experimental research approach has been the primary means to gain insight into these flow patterns. These investigations have been carried out to study one or more of the processes that take place in urban areas during a flood event, and could be classified as follows:

- Flood flows in street intersections
- Vertical flow exchanges between streets and the underground sewerage system
- Flood flows around idealised built-up areas[1]
- Horizontal flood flow exchanges between streets and built-up areas

The following sections provide an overview of experimental studies that have contributed to a better understanding of the complex processes that occur during urban flooding within the categories listed above.

2.2.1 Flood flow at crossroads

There are numerous studies on branch crossing flow, which, although many were not conducted to investigate street crossings, but rather natural or man-made water channels (e.g.,

[1]A built-up area can be an individual building or a group of buildings clustered together to form a city block.

riverine, sewer and irrigation networks), are relevant and the flow characteristics can be considered to be similar.

2.2.1.1 3-branch intersection

In a 3-branch intersections, the flow can come from one branch (main branch) and after the intersection continue within two branches, i.e., 3-branch bifurcation (upstream and downstream main branches and lateral branch) or it can come from two upstream branches and merge into one, i.e., 3-branch junction. For a 3-branch bifurcation, the flow characteristics are shown in Figure 2.3. According to Neary et al. (1999) and Ramamurthy et al. (2007), different zones and hydraulic structures can be identified under subcritical flow regime: (*i*) a dividing surface which starts when the flow accelerates laterally due to the suction pressure by the lateral branch, it divides the flows entering the main and side branches, (*ii*) a separation zone together with a contraction zone in the lateral branch, (*iii*) a separation zone in the main branch, (*iv*) a stagnation zone in the downstream corner of the intersection and (*v*) secondary currents in both downstream branches.

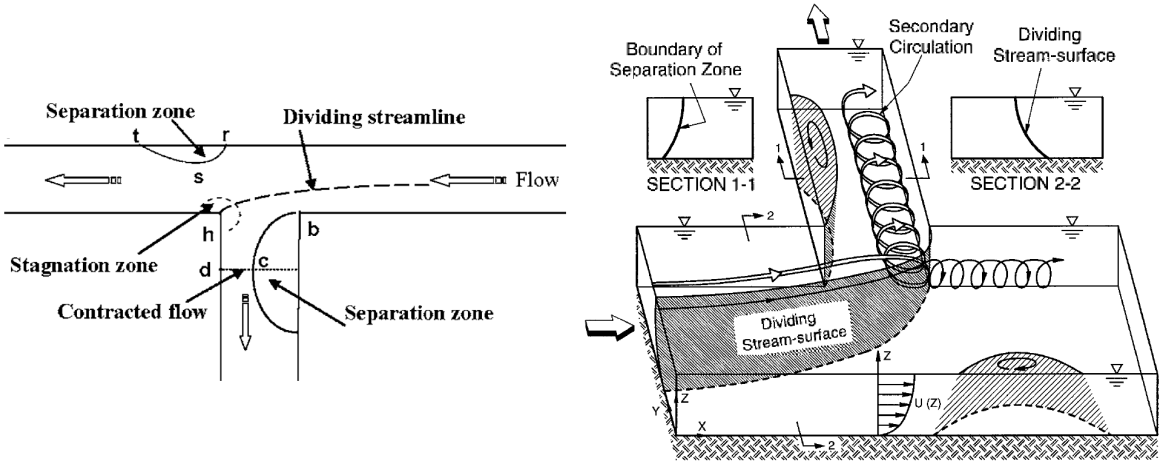

FIGURE 2.3. Flow characteristics in open-channel bifurcation. Scheme on the left taken from Ramamurthy et al. (2007), and on the right taken from Neary et al. (1999).

For a 3-branch junction, several authors (e.g. Gurram et al., 1997; Hsu et al., 1998b; Weber et al., 2001; Tang et al., 2018) have identified different structures, characteristic in this particular area, shown in Figure 2.4: (*i*) a separation zone in the downstream branch where the flow velocity decreases within a recirculation cell, (*ii*) a contraction zone in the downstream branch, adjacent to the separation zone, where the flow accelerates, (*iii*) a shear

plane at the boundary between the two streams coming from the upstream branches and (*iv*) secondary currents downstream of the separation zone.

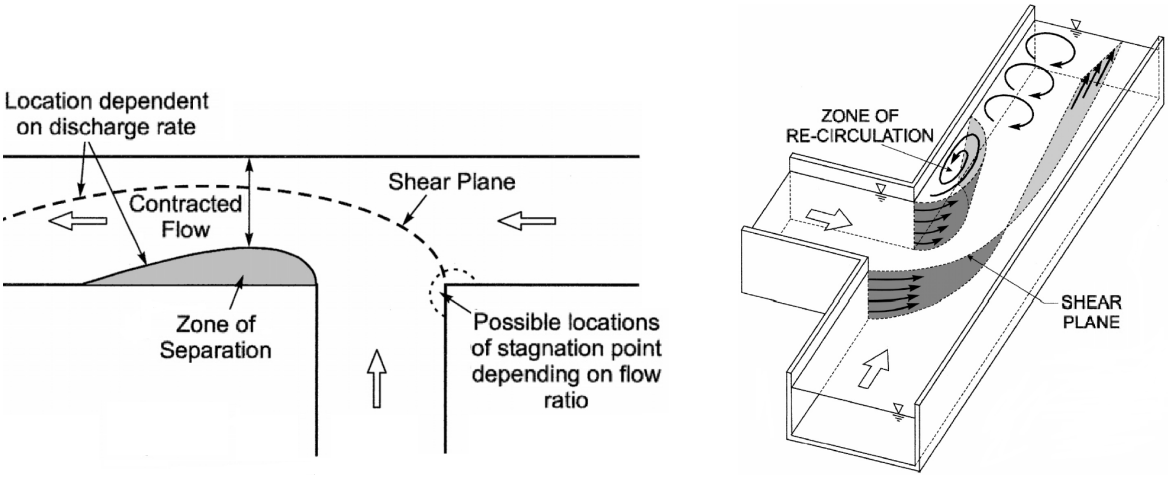

FIGURE 2.4. Flow characteristics in open-channel junction, from Weber et al. (2001).

Both, bifurcations and junctions, have been extensively studied since the last century, under different conditions. Table 2.1 lists some of the studies conducted over the years using experimental laboratory models. Among these research works, the one carried out by Mignot et al. (2013) differs from all the others, as it incorporated in a 3-branch bifurcation configuration square obstacles at the crossing zone, to simulate certain topographical details typical of an urban area (street furniture and parking vehicles). The authors reported that discharge to downstream branches is strongly impacted by the number of obstacles and their position, while for flow depths the effect is very limited.

Similarly, El Kadi et al. (2007) and Paquier (2009) studied on a 3-branch bifurcation, the vehicular blockage due to flooding (Figure 2.5). Unlike all other studies, this one was conducted under unsteady flow conditions, simulating a flood wave. Small-scale vehicles (1:44) were placed on the upstream branch of the bifurcation, aligned, oblique and parallel to the flow direction. The authors reported a 68% increase in flow depth due to the blockage of displaced vehicles.

2.2.1.2 4-branch intersection

4-branch intersections have been less studied than 3-branch intersections, and unlike the latter, they have been carried out in the context of urban flooding (4 branch intersections are not common features of sewer, riverine and irrigation networks), to study the flow distribution

TABLE 2.1. Experimental studies on 3-branch intersection.

Reference	Intersection angle (°)	Flow regime	Characteristics	Type of data
		3-branch bifurcation		
Lakshmana-Rao et al. (1968)	90	Subcritical	Narrower lateral branch	Discharge distribution and flow depth
Ramamurthy and Satish (1988)	90	Subcritical	Same-width branches	Discharge distribution and flow depth
Neary and Odgaard (1993)	90	Subcritical	Narrower lateral branch	3D Velocity field
Barkdoll et al. (1998)	90	Subcritical	Same-width branches	3D Velocity field and flow depth
Hsu et al. (2002)	90	Subcritical	Same-width branches	Discharge distribution and flow depth
Mignot et al. (2013)	90	Subcritical	Same-width branches, obstacles to represent urban furniture	2D Velocity and flow depth
El Kadi Abderrezzak et al. (2011)	90	Critical Supercritical	Same-width branches	Discharge distribution and flow depth
		3-branch junction		
Taylor (1944)	45	Subcritical		Flow depth
Best and Reid (1984)	15, 45, 70 and 90	Subcritical	Same-width branches	Flow depth and separation zone
Gurram et al. (1997)	30,60 and 90	Subcritical Transcritical	Same-width branches and narrower lateral branch	Flow depth
Hager (1989b)	22.5, 45 and 90	Transitional	Same-width branches	2D Velocity
Hager (1989a)	22.5, 45	Supercritical	Same-width branches	2D Velocity
Hsu et al. (1998b)	30, 45, 60	Subcritical	Same-width branches	Flow depth
Hsu et al. (1998a)	90	Subcritical	Same-width branches	Flow depth
Weber et al. (2001)	90	Subcritical	Same-width branches	3D Velocity field
Mignot et al. (2012)	90	Subcritical	Same-width branches	3D Velocity field
Schindfessel et al. (2015)	90	Subcritical	Same-width branches. Rectangular cross-section with chamfers	3D Velocity field

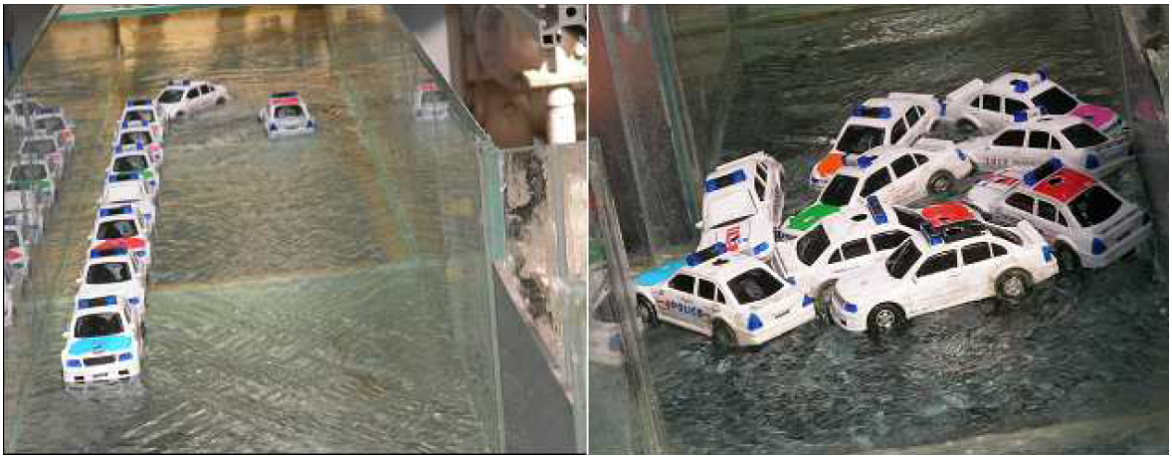

FIGURE 2.5. Leftt: Vehicles aligned with the direction of flow in the upstream branch. Right: Blockage of vehicles after being impacted by the flood wave., from Paquier (2009).

to the downstream branches. All experimental studies on 4-branch intersection, to the best of my knowledge, have been carried out for a configuration with 2 inflow and 2 outflow branches, in subcritical flow (e.g., Rivière et al., 2006; Nania et al., 2011; Rivière et al., 2011), supercritical flow (e.g., Nanía et al., 2004; Mignot et al., 2008; Nanía et al., 2014) and transcritical flow (e.g., Rivière et al., 2014).

According to Nania et al. (2011), under subcritical flow conditions, a recirculation zone (separation zone) appears in each of the downstream branches (similar to the 3-branch bifurcation), see Figure 2.6.A. In this zone of the downstream branch, the section contracts and as the flow accelerates, there may be a regime change to supercritical flow, as reported by (Rivière et al., 2014), see Figure 2.6.B. In the case where the flow in the upstream branches is in supercritical regime, the recirculation zones in the downstream branches are still formed, but in addition, when entering the junction, a hydraulic jump is formed in each upstream branch. This hydraulic jump can be displaced within the intersection itself at an oblique angle, depending on the inflow distribution and Froude number in the two upstream branches (Nanía et al., 2004; Mignot et al., 2008).

2.2.2 Flow exchange between street and sewerage network

A sewerage network is designed to convey rainwater and/or sewage. Due to the large impervious surface in an urban area, there are manholes in public areas (usually on the street sides) to drain rainwater into the sewerage network. Therefore, the flow interplay between

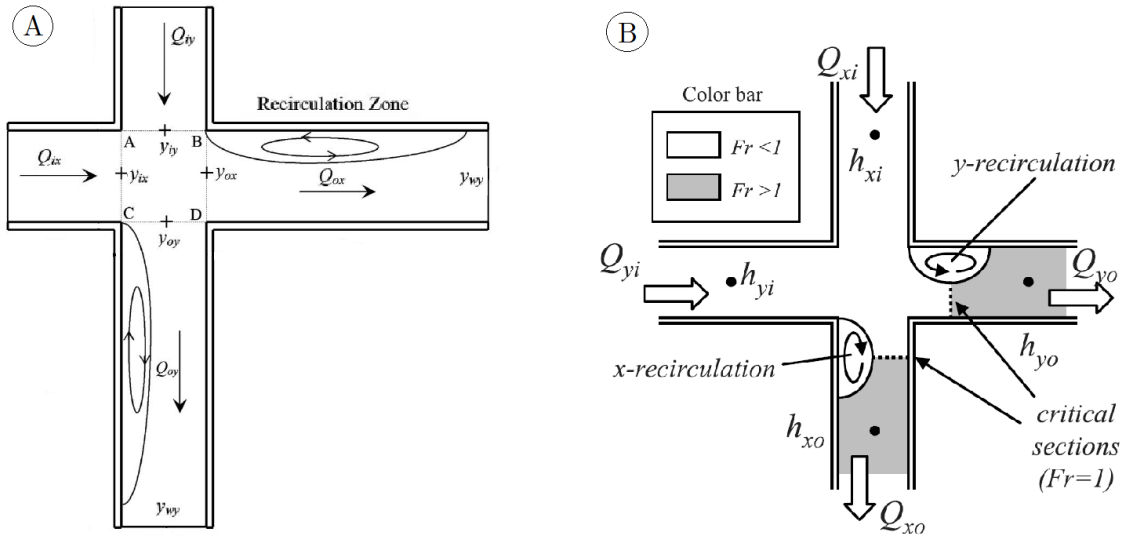

FIGURE 2.6. A)Recirculation zones in a 4-branch junction, from Nania et al. (2011). B) Change of flow regime in the downstream branches in a 4-branch junction, from Rivière et al. (2014).

streets and sewerage systems has been a subject of study, especially with the increase in rainfall generated flooding in recent years. According to various research works (e.g., Djordjevic et al., 2005; Kemper and Schlenkhoff, 2019), three conditions can occur that determine the flow exchange process:

- Free drainage. The hydraulic head within the sewerage system is below ground level, thus the flow discharge from the street to the sewerage network is free (e.g., Lee et al., 2012, 2013; Djordjevic et al., 2013; Lee et al., 2013; Sabtu et al., 2016; Kemper and Schlenkhoff, 2019), see Figure 2.7.a.

- Submerged drainage. The hydraulic head within the sewerage system is at ground level and there is still flow discharge from the street to the sewerage network (e.g., Lee et al., 2012, 2013; Bazin et al., 2014; Martins et al., 2014; Sabtu et al., 2016; Beg et al., 2018; Chibane et al., 2021), see Figure 2.7.b.

- Overflowed drainage. The capacity of the sewerage system is exceeded, the hydraulic head is above ground level and the flow discharge is from the sewerage network to the street (e.g., Leandro et al., 2010; Lee et al., 2013; Leandro et al., 2014; Djordjevic et al., 2013; Romagnoli et al., 2013; Bazin et al., 2014; Sabtu et al., 2016; Martins et al., 2017; Beg et al., 2018; Gómez et al., 2019; Chibane et al., 2021), see Figure 2.7.c.

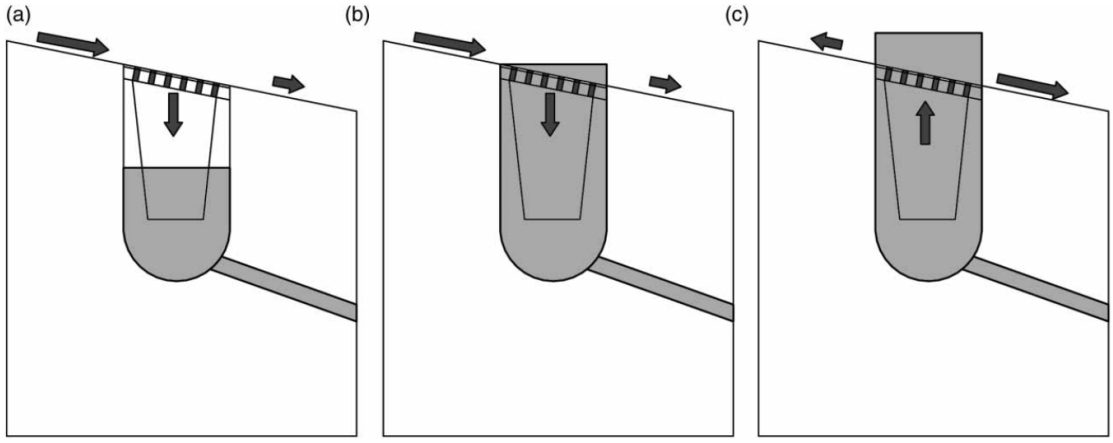

FIGURE 2.7. Flow exchange scenarios between street and sewerage network: (a) Free drainage; (b) Submerged drainage; (c) Overflowed drainage. Diagram taken from Kemper and Schlenkhoff (2019).

The studies on vertical flow exchanges have been carried out for multiple purposes: to estimate the discharge coefficients for the different conditions mentioned above (e.g., Lee et al., 2012; Martins et al., 2014; Gómez et al., 2019), to estimate drainage efficiency of different types of grating (e.g., Gómez and Russo, 2011; Russo et al., 2013b; Sabtu et al., 2016; Kemper and Schlenkhoff, 2019), for measuring flow characteristics in the street next to a manhole (e.g., Leandro et al., 2014; Bazin et al., 2014; Beg et al., 2018; Chibane et al., 2021), etc. Most of these studies were investigated locally, at the level of a single exchange structure (e.g., Djordjevic et al., 2013; Leandro et al., 2014; Martins et al., 2014; Sabtu et al., 2016; Martins et al., 2017; Kemper and Schlenkhoff, 2019; Gómez et al., 2019), see Figures 2.8.C and 2.8.D, and at single street level with two or more manholes (e.g., Leandro et al., 2010; Lee et al., 2012, 2013; Bazin et al., 2014; Noh et al., 2016; Chibane et al., 2021; Dong et al., 2021), see Figures 2.8.A and 2.8.B. Therefore, as Mignot and Dewals (2022) had pointed out, research considering an entire urban area is still required.

2.2.3 Flood flows around idealised built-up areas

In urban flooding, the study of the interaction of flood flows with built-up areas is a highly prevalent issue. One of the most recurrent approaches is to consider these built-up areas (buildings or city blocks) as non-porous areas, thus there is only flood flow in the streets. The most simple consideration is to represent the built-up areas as square obstacles, stag-

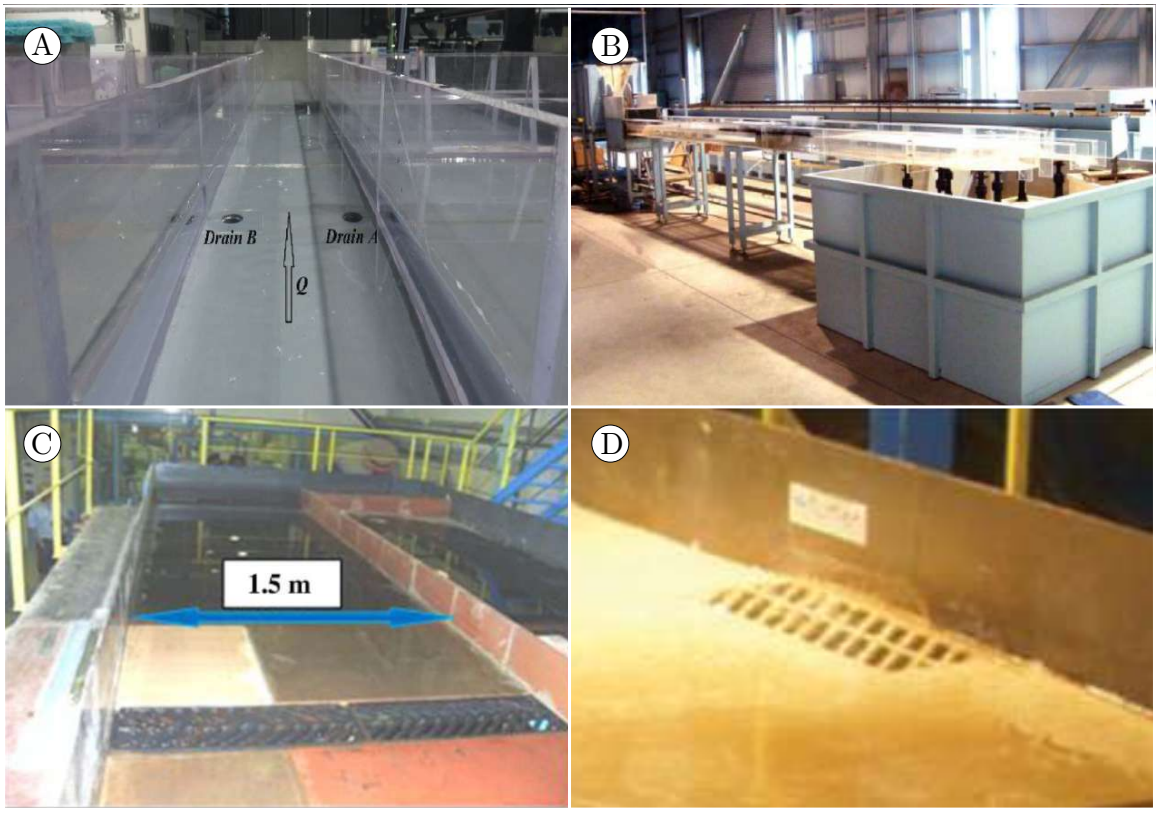

FIGURE 2.8. A) Straight channel with 2 lateral manholes, from Chibane et al. (2021). B) Straight channel with various central manholes, from Lee et al. (2012). C) Transverse grates, from Russo et al. (2013b). D) Rectangular grate, from Gómez et al. (2019).

gered and aligned on a plain (Figure 2.9). Many of these studies focused on the impact of built-up areas on flow features, such as flow depth and/or velocity, under steady flow conditions (e.g. Karvonen et al., 2000; Huang et al., 2014b; Velickovic et al., 2017; Beretta et al., 2018) and unsteady flow conditions, by simulating a dam-break (e.g. Testa et al., 2007; Soares-Frazão and Zech, 2008; Kim et al., 2015) or a tsunami (e.g. Tomiczek et al., 2016). All have reported an increase in flow depth immediately upstream of the urban area (aligned or staggered built-up areas), within the urban area (due to reduced section) the flow velocity increased and the flow depth decreased. Moreover Testa et al. (2007) reported an increase in flow depth in the urban area when built-up areas are staggered compared to aligned.

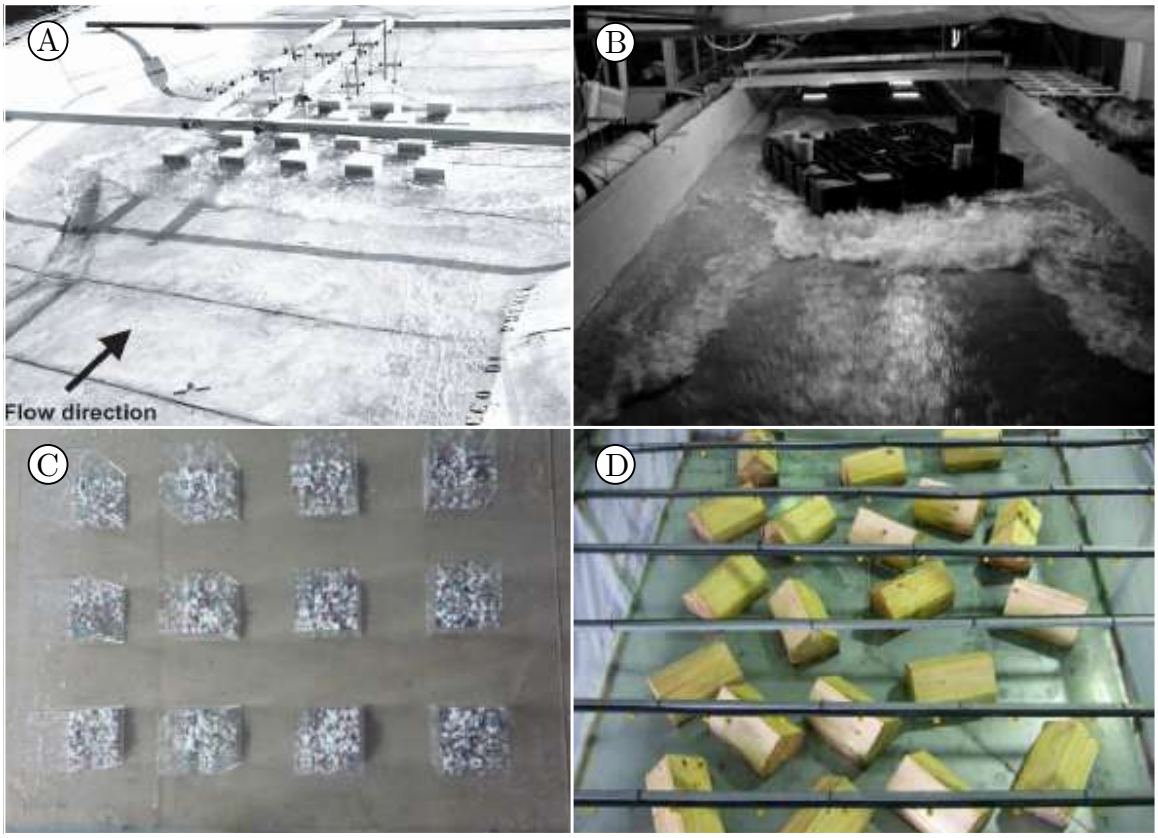

FIGURE 2.9. (A) Impervious concrete blocks, staggered for a flash-flood simulation, from Testa et al. (2007). (B) Impervious wooden blocks, staggered and aligned for dam-break-generated flood simulation, from Soares-Frazão and Zech (2008). (C) Impervious plastic blocks, for a fluvial flood experiment, from Huang et al. (2014b).(D) Impervious wooden blocks for a rainfall-generated flood experiment, from Cea et al. (2010).

Other research works have also considered aligned and staggered built-up areas to study a rainfall-generated flood (e.g., Cea et al., 2010; Isidoro et al., 2013), reported that increasing

rooftop connectivity leads to a peak discharge reduction.

FIGURE 2.10. (A) Impervious plastic-coated wooden blocks, realistically aligned, for a fluvial flood experiment, from Sattar et al. (2008). (B) Realistic urban layout with impervious buildings, for dam-break-generated flood experiment, from Güney et al. (2014). (C) Realistic urban layout with impervious real-shaped buildings, for a coastal flood experiment, from Yasuda et al. (2004).(D) Realistic urban layout with impervious real-shaped buildings, for dam-break-generated flood experiment, from Smith et al. (2016).

Experimental studies also considered more realistic urban layouts. Most of these replicated real urban areas, for instance, Sattar et al. (2008) replicated a neighbourhood layout of the City of New Orleans, USA in a 1:50 scale model ((Figure 2.10.A) to study the 2005 urban flood event induced by a levee breach during hurricane Katrina. The model was designed to investigate various possible methods for breach closure (e.g., toe dumping, transverse dumping, single- and multibarrier embankments). Güney et al. (2014) considered a distorted scale model in an available space of 300 m^2 (Figure 2.10.B) to reproduce the urban layout of the coastal city of Ürkmez in Turkey. This research was conducted under unsteady flow conditions, measuring flood flow propagation, flow depths and velocities. They reported that the

velocity variations showed markedly different behaviour during the rising and falling stages. The increase in velocity in sparse residential areas was normally constant during the rising stage and fluctuated during the falling stage.

Similar to the work research mentioned above, the research of Cox et al. (2009) and Park et al. (2013) on a scale model replicating the city of Seaside, Oregon, USA, and that of Smith et al. (2016) on a scale model replicating a neighbourhood in Newcastle, Australia (Figure 2.10.D), were carried out to quantify the effects of built-up areas on flood flow features (flow depths, velocities, flood extension). A special feature is the research work carried out by Yasuda et al. (2004), they replicated in a scale model an area of Fukuoka, Japan, carefully considering the geometry and roughness of the building facades, and also underground spaces that simulate shopping centres and parking lots. To simulate a tsunami, this research was conducted under unsteady flow conditions, measuring the flow features and estimating the flood risk. They found that volume in the underground space is about 10% of total volume regardless of the tsunami condition. Furthermore, they conclude that the flood risk to people in compound urban areas (ground and underground levels) exceeds the acceptable limit.

A last approach used for urban flooding research, less common than the others, considers the urban area as a street network, streets are then bounded by city blocks. Typically these physical models have represented high-density urban areas. Among them, Ishigaki (2003) used a scale model 1:100 representing a district area of Kyoto, Japan (Figure 2.11.A. Similar to the study carried out by Yasuda et al. (2004), this research took into account underground spaces accounting for multi-level shopping centres and parking lots. A fluvial flood was simulated to measure flow depths, velocities and quantify the runoff volume in the underground area. They concluded that 50% of the runoff flows into the underground space, and the flow depth rises very rapidly. Therefore, the flood hazard must be assessed very carefully in an urban area with underground spaces.

Araud et al. (2014), Arrault et al. (2016) and Finaud-Guyot et al. (2018) conducted research on a scale model consisting of a street network with a synthetic urban layout (Figure 2.11.B). By implementing steady flow conditions, the authors measured the spatial distribution of flow depths and the discharge distribution in the street network. They concluded that at district level, the outflow discharge distribution is independent of the total inflow

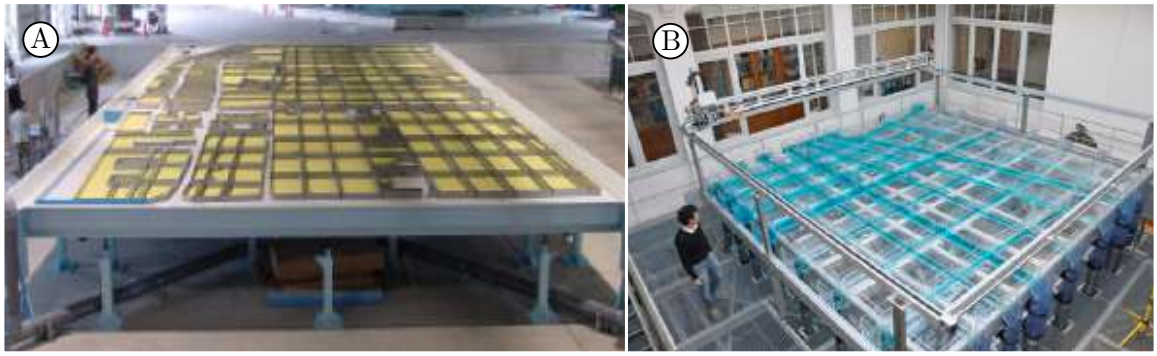

FIGURE 2.11. (A) Street network bounded by a real urban layout of impervious city blocks, for a fluvial flood simulation, from Ishigaki (2003). (B) Street network bounded by impervious city blocks in a synthetic urban area, for a fluvial flood simulation, from Finaud-Guyot et al. (2018).

discharge. Finally, Seong et al. (2020) by using a scale model 1:200, investigated a rainfall-generated urban flood in the Sadan area in South Korea. They quantified flow depths and velocities by changing the rainfall intensity. This scale model also incorporated underground spaces, corresponding to the urban transport system. They conclude that for intensities greater than 160 mm/h, flow velocities and depths in some areas of the city exceed the instability limits for people. In addition, at such intensities, the flow discharge into underground spaces may be hazardous.

Thus, as has been noted, in all these studies, buildings and city blocks were considered to be *non-porous elements*.

2.2.4 Intrusion of flood flows into built-up areas

Much scarcer than all the flow processes described above are the investigations that consider built-up areas as porous areas where the flow can penetrate. According to Chock et al. (2013), field studies on the damage of near-shore buildings impacted by flood flows during the 2011 tsunami in Japan, showed that openings in the walls (increased window area) were beneficial in mitigating the damage. Therefore, most of the research that can be found in the literature considering openings in buildings has been conducted on the forces exerted by flood flows on detached buildings. Table 2.2 lists some of these research works, together with some characteristics of the physical models and the data collected. In this table, the research work by Sturm et al. (2018) has been added, which, unlike the others, studied a river flood with sediment deposition.

TABLE 2.2. Research work on the forces exerted on porous buildings by flooding.

Experimental set-up	Set-up	Building characteristics	Scale	Flow state	Data collected
Thusyanthan and Gopal Madabhushi (2008) 	Wave-generating tank, 4.5 m long and 1 m wide	Typical coastal Sri Lankan house with open door and windows, made of wood and masonry	1:25	Unsteady (tsunami surge)	Induced force on the house walls and surge speed
van de Lindt et al. (2009) 	Wave-generating basin, 43.7 long and 13.3 m wide	Typical Gulf Coast two-storey residential building with open windows, made of wood	1:6	Unsteady (tsunami surge)	Induced force on the house walls

TABLE 2.2 (continued)

Experimental set-up	Set-up	Building characteristics	Scale	Flow state	Data collected
Triatmadja and Nurhasanah (2012) 	Flume with sluice gate, 24 m long and 1.45 m wide	Parallelepiped-shaped building with a central opening in its front and rear faces. The size of the opening was varied.	1:15	Unsteady (tsunami surge)	Flow depths, surge speed and induced force on the building
Liu et al. (2018)  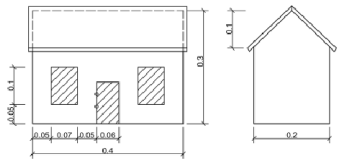	Flume with sluice gate, 40 m long and 3.5 m wide	Real-shaped one-storey house with open doors and windows, made of PVC plates	1:20	Unsteady (dam-break)	Flow depths and induced force on the house

TABLE 2.2 (continued)

Experimental set-up	Set-up	Building characteristics	Scale	Flow state	Data collected
Wüthrich et al. (2018) 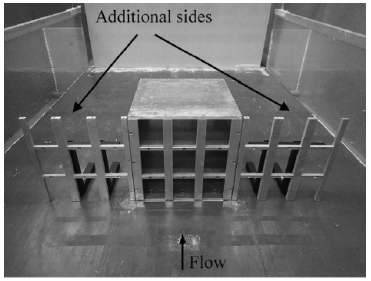	Wave-generating flume with vertical release, 15.5 m long and 1.4 m wide	Parallelepiped-shaped building with square openings. The size of the openings, and the faces with openings were varied	1:30	Unsteady (tsunami surge)	Flow depths and induced force on the building
Sturm et al. (2018)  	Basin, 9 m long and 6 m wide	Real-shaped buildings with open doors and windows. Three buildings were considered with porosity (red), while the others were non-porous (white) in a real urban layout	1:30	Steady	Flow velocity and induced force on building walls

There are also other research works that focused mainly on the characteristics of flood flows. Among them, Zhou et al. (2016) studied the effect of parallelepiped-shaped buildings on flow depths and velocities in a series of various urban layouts, from 3 to 15 aligned buildings. They reported an important difference in the wake zone downstream the buildings when comparing with non-porous buildings. Mignot et al. (2020) studied the flow intrusion through various types of openings (door, window, window with gratings) from a flooded street into an adjacent building facade (i.e., without modelling explicitly the building, only the one side facade), see Figure 2.12.A. The authors found that the flow through the opening was strongly influenced by large objects (such as parked vehicles) located in the vicinity of the opening, and thus these objects should be taken into account for an accurate flood hazard prediction.

Finally, the research work performed by Li et al. (2021) could be considered in this category. It considers a synthetic urban layout of non-porous buildings within a city block surrounded by a street network (Figure 2.12.B). Therefore, on that basis, it would be argued that there is a flow exchange between the streets and the city block. The size of the non-porous buildings was varied to change the magnitude of the conveyance porosity within the block. Their results highlighted that the conveyance porosity in the dominant flow direction has a strong influence on velocities, flow depths and downstream discharge distribution.

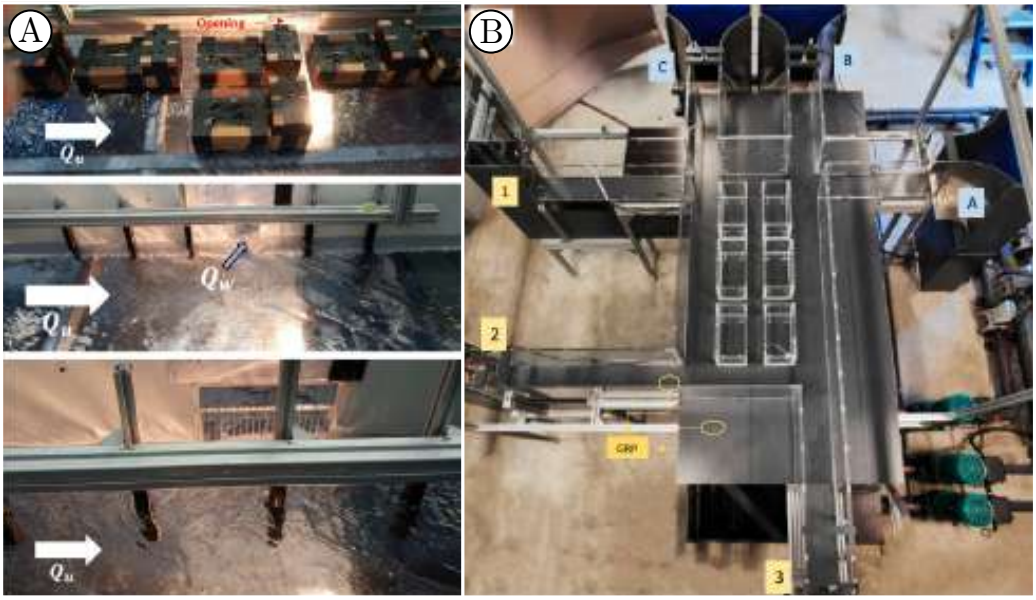

FIGURE 2.12. (A) Experimental set-up for a flow intrusion from a flooded street into a building under different conditions, from Mignot et al. (2020). (B) Experimental set-up with a synthetic building layout within a city block, from Li et al. (2021).

2.2.5 Conclusions on experimental modelling of urban flooding

Several advances have been made over the last 20 years in urban flood research. In the current global context, it is imperative to continue this research in order to improve flood hazard assessment and the applicability of operational numerical models, for the benefit of the population.

As already discussed in Chapter 1, buildings, usually clustered in city blocks in urban areas, are the primary elements of an urban area. Thus, during a flood event, the flow processes that take place between the streets and these elements should be a major subject of research. Nevertheless, there is currently almost no research work on this topic. As shown in this section, most of the research work on the intrusion of flood flows into built-up areas have only considered detached buildings. Therefore, research work focusing on flow intrusion towards buildings, and adapted to the conditions of an urban environment, is still lacking.

In this context, this research work aims to contribute to filling this gap by adapting an experimental set-up representing of an urban area, with a city block that allows the interaction of flood flows with the surrounding streets, as occurs in a real flood event.

2.3 Flood hazard assessment

According to UNISDR (2009), natural hazard is defined as a natural process or phenomenon that may cause loss of life, injury or other health impacts, property damage, loss of livelihoods and services, social and economic disruption, or environmental damage. Among all the natural events that can lead to a hazard, floods are the most frequent and widely geographically distributed natural hazard worldwide (Rudari, 2017). Smith et al. (2014) have pointed out that people tend to be at risk during a flood in one of three main categories: on foot, in vehicles or in buildings. Therefore, developing methodologies to assess the urban flood hazard and the associated risk with higher precision is particularly relevant (Cea and Costabile, 2022).

Flood hazard is usually described by flow depth, flood extent, flow velocity, flood wave propagation, flood duration and the water's rising rate (de Moel et al., 2009). Among these, the most common parameters are the local velocity and flow depth, used for the prediction of building damage, for instability of parked and transit vehicles, and for people's instability.

2.3.1 Hazard to buildings

Buildings are liable to structural failure if subjected to the combined effects of great flood depths and velocities (Smith, 1994). According to Bignami et al. (2019a), a building stressed by flood flow is affected by three main actions: (*i*) buoyancy; (*ii*) hydrostatic loads; and (*iii*) hydrodynamic forces.

Several studies on the stability of buildings during flooding can be found in the literature. The most well-known is possibly the research carried out by Black (1975). It was one of the first studies that presented threshold curves for building stability during a flood, as a function of flow depth and velocity (Figure 2.13). This study was developed for residential timber buildings in rural floodplains, taking into account the buoyancy effect and hydrodynamic forces. Clausen and Clark (1990) developed an empirical criterion to estimate potential damage to brick and masonry buildings during a dam failure. They proposed different types of damage bounded by curves of constant velocity (U) times flow depth (d): *Low damage* for Ud values below 3 $\mathrm{m^2\,s^{-1}}$; *Partial damage* between 3 $\mathrm{m^2\,s^{-1}}$ and 7 $\mathrm{m^2\,s^{-1}}$; and *Total damage* above 7 $\mathrm{m^2\,s^{-1}}$. Similar studies can be found in the literature, for different types of buildings and under different criteria, which propose stability thresholds curves as a function

of velocity and flow depth.

A comparison of the various criteria developed over the years was carried out by Smith et al. (2014), see Figure 2.14. The various threshold curves are plotted together, a wide range of values is observed, mainly because these were designed for different types of buildings and under different types of analysis (e.g., based on structural analysis, field observations, numerical modelling, considering debris flow). After analysing all the criteria, the authors proposed two threshold curves to define the flood hazard for buildings: $Ud = 1\ \mathrm{m^2\,s^{-1}}$, indicates the lower threshold for residential houses (green curve), while $Ud = 4\ \mathrm{m^2\,s^{-1}}$, indicates the higher threshold for all buildings (red curve), after this limit a building is considered to be prone to collapse.

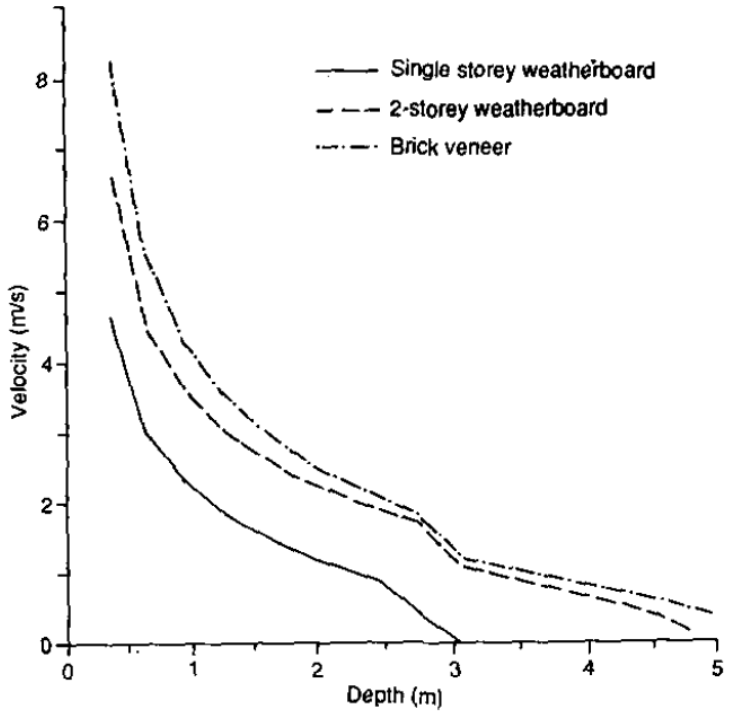

FIGURE 2.13. Critical flow depth and velocity for building failure for different residential building types (Black, 1975). Taken from Smith (1994).

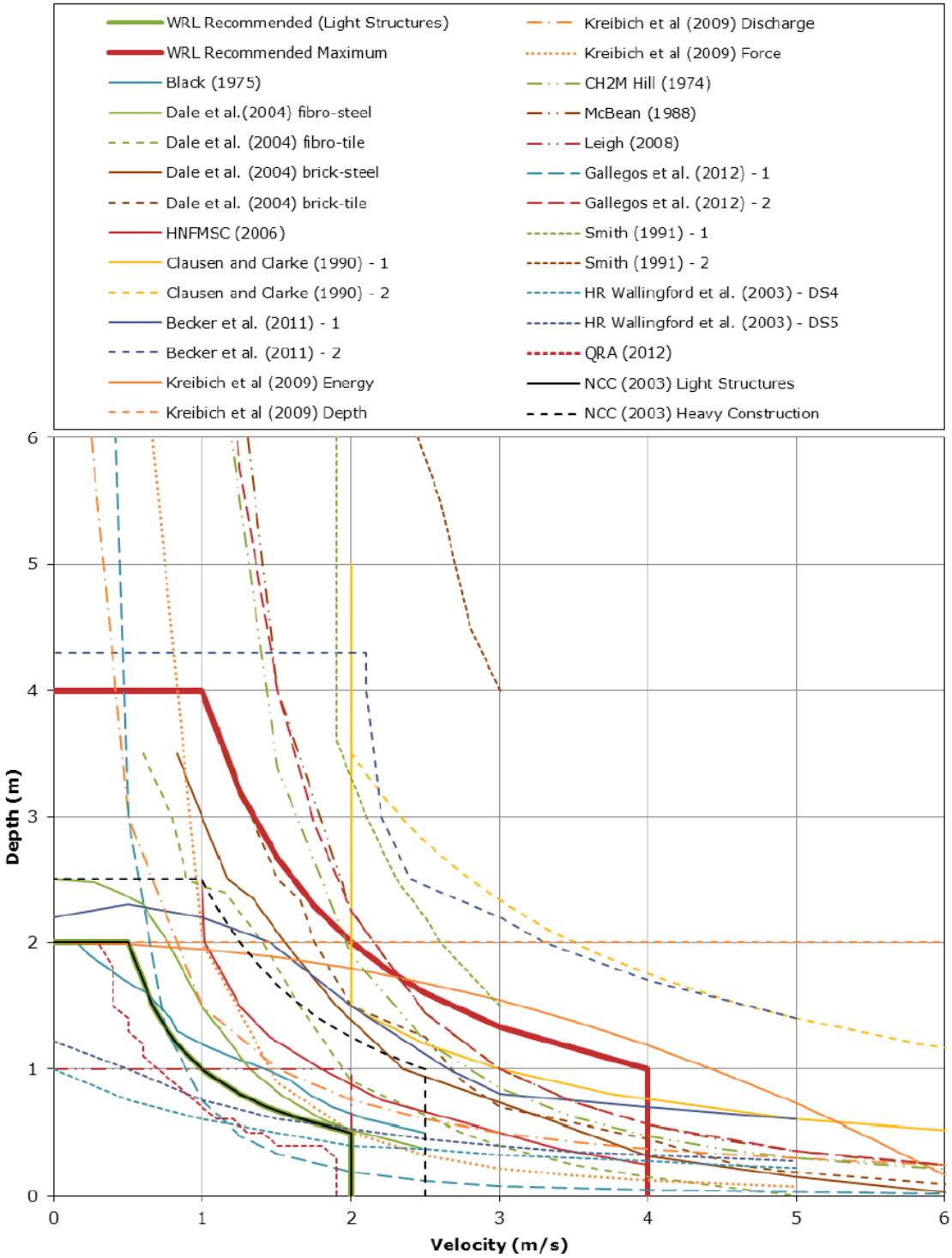

FIGURE 2.14. Comparison of building stability curves found in the literature. Taken from Smith et al. (2014).

2.3.2 Hazard to vehicles

A common hazard that causes a risk of death or serious injury to people is the instability of vehicles in flood flows (Ramsbottom et al., 2006). According to Shand et al. (2011), two hydrodynamic mechanisms cause instability in a vehicle: buoyancy and slipping. Buoyancy instability occurs when the upward force exerted by the flood flows exceeds the downward force exerted by the mass of the vehicle. Sliding instability occurs when the horizontal force exerted on the vehicle is greater than the vertical restoring force, which depends mainly in the friction between the car tyres and the road surface. The first one is dominant in low velocity and deep flows, while the second one is dominant in high velocity flows.

Several studies have therefore focused on finding the critical flow depth and critical velocity at which a vehicle remains stable in flood flows. The earliest study on this subject was carried out by Bonham and Hattersley (1967), exposing a 1:25 scale vehicle sideways to the flood flow. The tests were performed for flow depth and velocity ranges from 0.11 to 0.57 m and from 0.48 to 3.09 $\mathrm{m\,s^{-1}}$, respectively (values at prototype scale). The loss of stability due to buoyancy, was found to occur at a flow depth of 0.57 m. Once the horizontal and vertical forces were determined, a friction coefficient, μ, that would lead to the loss of stability due slipping was defined. A friction coefficient equal to 0.3 was proposed as the minimum threshold.

Similar tests were carried out by Gordon and Stone (1973), on a 1:16 scale vehicle, but exposed frontal and rear to the flood flow. A review of these and other stability criteria was carried out by Martínez-Gomariz et al. (2018), who displayed in the same plot the results of the available theoretical and experimental studies (Figure 2.15). The results are shown for specific vehicles, as instability depends on physical characteristics, such as vehicle weight, height and length, ground clearance and tyre spacing.

Arrighi et al. (2016) used the experimental results from Shu et al. (2011), Xia et al. (2011) and Xia et al. (2014b) to propose a new parameter (mobility parameter, θ_v) to define the instability of any vehicle in flood flows (Figure 2.16). This parameter considers the physical characteristics of the car, its orientation with respect to the direction of flow and the flood depth (see Figure 2.16.A). The values of the computed mobility parameter are plotted against the Froude number to identify a unique threshold of incipient motion. This threshold separates safe conditions (above the curve) and dangerous conditions (below the curve), see

Figure 2.16.C

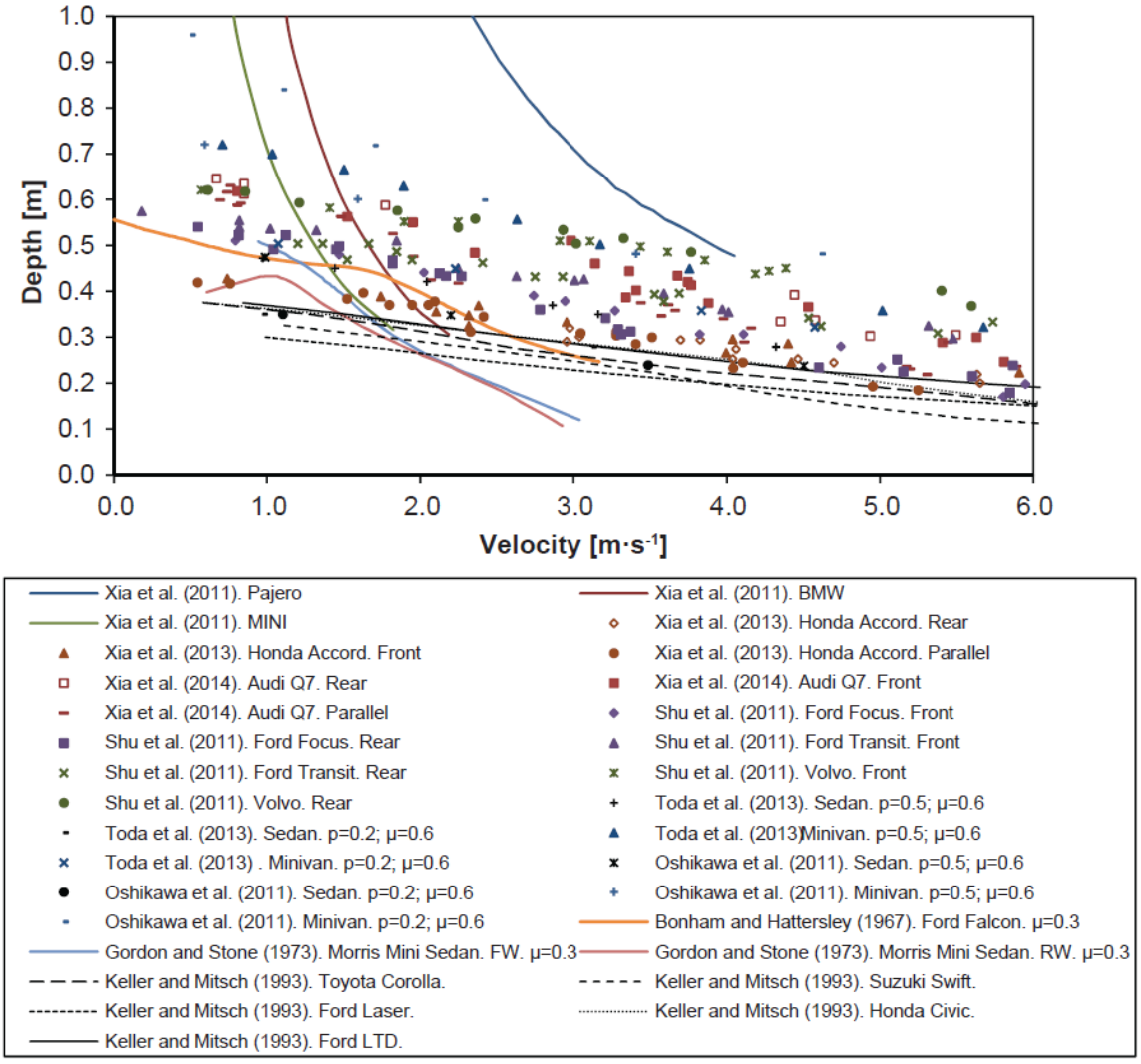

FIGURE 2.15. Comparison of vehicle instability curves and instability points, found in the literature, obtained experimentally and theoretically. Taken from Martínez-Gomariz et al. (2018).

More recent studies have also incorporated terrain factors. Milanesi and Member (2019), in addition to taking into account the characteristics of the vehicle and its orientation with respect to flood flows, considered the ground slope, as it reduces the stability by acting on the weight components and on the buoyancy. The authors used experimental data from Shu et al. (2011), Xia et al. (2014b) and Kramer et al. (2016) to calibrate their model, resulting in the following expressions:

$$U \leq \left[\frac{(604 - 685\tan\vartheta - 1218d)\cos\vartheta}{38d + 1}\right]^{\frac{1}{2}} \quad \text{(frontal impact)} \tag{2.1}$$

$$U \leq \left[\frac{(390 - 443\tan\vartheta - 788d)\cos\vartheta}{68d + 1}\right]^{\frac{1}{2}} \quad \text{(lateral impact)} \tag{2.2}$$

where ϑ is the ground slope. Eqs. 2.1 and 2.2 account for vehicles impacted frontally and laterally, respectively. Similar to Arrighi et al. (2016), these expressions apply to any vehicle.

2.3.3 Hazard to pedestrians

According to Ramsbottom et al. (2006), flood hazard describes the flow conditions in which people are likely to be swept over or drown in a flood. Bignami et al. (2019b) pointed out that flood hazard for people depends on three factors: flow depth, stream velocity and the ground surface characteristics. Therefore, many studies have been devoted to investigating the response of people in flood flows within the context of flood hazard assessment, to determine the critical flow depth and velocity that caused instability. This relation

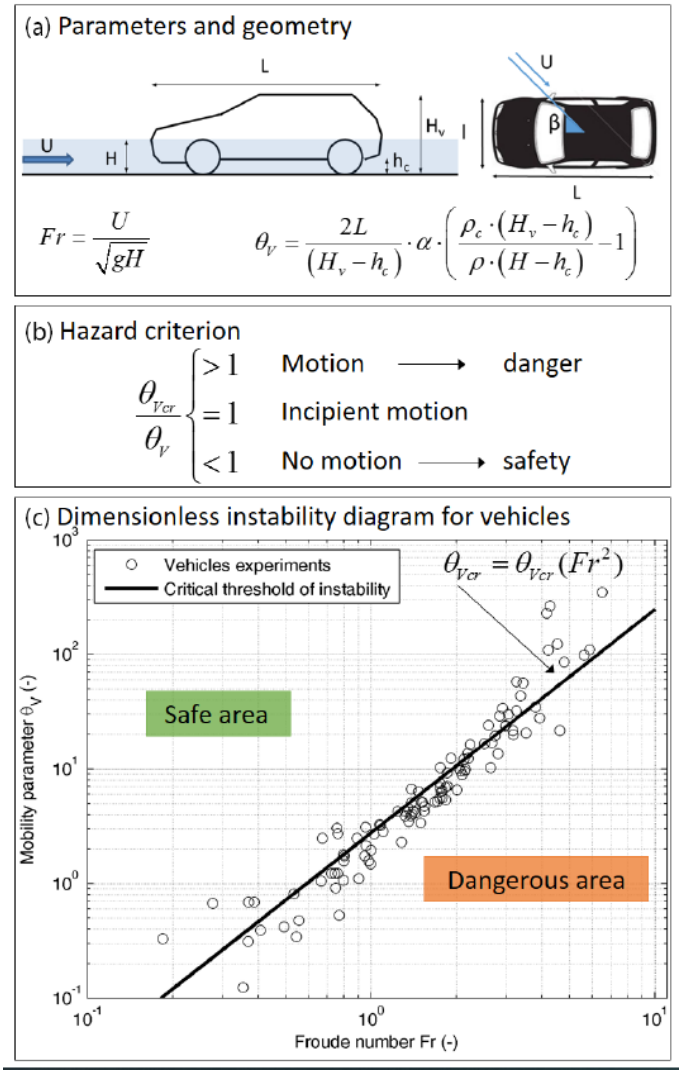

FIGURE 2.16. Sketch of the car geometry and definition of the mobility parameter. (a) definition of hazard criterion, (b) hazard criterion and (c) dimensionless instability diagram for flooded vehicles with identification of the critical threshold. Taken from Arrighi et al. (2016).

defines the so-called *Product Number* (Abt et al., 1989), PN, which is the product of the velocity and flow depth at which the human instability begins:

$$PN = Ud \tag{2.3}$$

where U is the depth-average velocity and d the flow depth. One of the pioneering studies on this subject was carried out by Abt et al. (1989). They performed tests on human subjects and on a human-size concrete monolith (an extremely conservative consideration that stands for the lower limit of human instability) to determine the critical velocity and flow depth for human instability. An empirical expression was derived from the results:

$$PN = Ud = 0.0929 \left(\mathrm{e}^{0.0011906 h_s m_s + 1.09}\right)^2 \tag{2.4}$$

where h_s and m_s are the subject's height (m) and mass (kg), respectively. Further studies were carried out under different conditions, applying diverse criteria and methodologies. Table 2.3 lists these studies, with the characteristics of the set-up, the surface and slope on which the subjects were tested, the general characteristics of the subjects, the failure mechanism considered and the range of measured flow velocities and flow depths. Similar to Abt et al. (1989), most of these studies have led to the development of expressions to define human instability based on physical characteristics (e.g., Karvonen et al., 2000; Jonkman and Penning-Rowsell, 2008; Russo et al., 2013a; Xia et al., 2014a; Martínez-Gomariz et al., 2016).

In addition to these studies, different authors have used these datasets to derive empirical expressions for the threshold of human instability in flood flows (e.g., Milanesi et al., 2015; Arrighi et al., 2017) and to define flood hazard levels. Ramsbottom et al. (2006), based on the experimental results from Abt et al. (1989) and Karvonen et al. (2000), proposed an expression to define the flood hazard to pedestrians, which related flow depth and velocity together with the amount of debris in the flow:

$$\text{Flood hazard} = d\,(U + 0.5) + DF \tag{2.5}$$

where DF is the debris factor, being in urban areas equal to 0 for flow depths below 0.25 m, otherwise $DF = 1$. The flood hazard was categorized in four levels as shown in Table 2.4.

TABLE 2.3. Research work on human instability on flood flows.

Reference	Set-up	Surface	Slope	Subject characteristics	Failure mechanism	U ($\mathrm{m\,s^{-1}}$)	d (m)
Abt et al. (1989) 	Wide flume	artificial grass, smooth concrete, steel and gravel-sand	0.005 and 0.015	(1) Adults with safety equipment, standing and walking. (2) Human-sized monolith concrete concrete monolith.	Losing footing	0.43 - 1.20	0.36 - 3.05
Takahashi et al. (1992)	Funnelled basin	Metal load cell	0.0	Adults standing	Losing footing	0.58 - 2.00	0.44 - 0.93
Karvonen et al. (2000) 	Moving platform through a basin	Metal grating	0.0	Civilian adults and rescue workers, all with safety equipment, standing and walking	Losing footing	0.60 - 2.60	0.40 - 1.10

TABLE 2.3 (continued)

Reference	Set-up	Surface	Slope	Subject characteristics	Failure mechanism	U ($\mathrm{m\,s^{-1}}$)	d (m)
Jonkman and Penning-Rowsell (2008) 	Flood relief channel with sluice gates	Concrete	0.01	Professional stuntman, standing and walking	Losing footing	1.8 - 3.1	0.23 - 0.35
Russo et al. (2013a) 	Tilting platform simulating a street	Concrete	0.02, 0.04, 0.06, 0.08 and 0.10	Adults with safety equipment, standing and walking	Feeling unsafe or losing footing	1.82 - 3.17	0.11 - 0.17

TABLE 2.3 (continued)

Reference	Set-up	Surface	Slope	Subject characteristics	Failure mechanism	U ($\mathrm{m\,s^{-1}}$)	d (m)
Xia et al. (2014a) 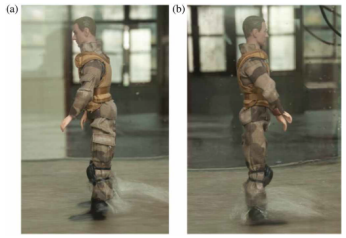	Flume	Concrete	0.0	Small scale model of a real-shape human body, facing backwards and forwards.	Losing footing	0.53 - 3.96	0.13 - 0.74
Martínez-Gomariz et al. (2016) 	Tilting platform simulating a street	Concrete	0.04, 0.06, 0.08 and 0.10	Adults with safety equipment, walking in different directions	Losing footing	2.13 - 3.70	0.07 - 0.16

TABLE 2.3 (continued)

Reference	Set-up	Surface	Slope	Subject characteristics	Failure mechanism	U ($\mathrm{m\,s^{-1}}$)	d (m)
Milanesi et al. (2016) 	Videos on real flood events	-	Unknown	Adults	Losing footing	0.97 - 4.61	0.08 - 1.09
Postacchini et al. (2021) 	Moving trolley along a flume	Metal plate	0.0	Reduced scale model of a human body, made of plastic. Scale model standing, facing backwards and forwards.	Losing footing	0.40 - 3.00	0.16 - 1.20

TABLE 2.4. Levels of flood hazard to pedestrians as a function of velocity and flow depth, for Eq. 2.5, from Ramsbottom et al. (2006).

$d\,(U + 0.5)$ ($m^2\,s^{-1}$)	Flood hazard level	Description
< 0.75	Low	Caution. Shallow flowing water or deep standing water
0.75 - 1.25	Moderate	Dangerous for some. Deep or fast flowing water
1.25 - 2.5	Significant	Dangerous for most people. Deep fast flowing water
> 2.5	Extreme	Dangerous for all. Deep fast flowing water

Cox et al. (2010) proposed a new criterion for assessing the flood hazard to pedestrians, based on human instability data sets from Abt et al. (1989); Takahashi et al. (1992); Karvonen et al. (2000) and Jonkman and Penning-Rowsell (2008), and the criterion proposed by Ramsbottom et al. (2006), see Figure 2.17. In this criterion, four hazard levels are proposed for adults: above $Ud = 1.2\ m^2\,s^{-1}$ is the extreme hazard zone; between $Ud = 0.8\ m^2\,s^{-1}$ and $Ud = 1.2\ m^2\,s^{-1}$ is the significant hazard zone; between $Ud = 0.6\ m^2\,s^{-1}$ and $Ud = 0.8\ m^2\,s^{-1}$ is the moderate hazard zone; and below $Ud = 0.6\ m^2\,s^{-1}$, the low hazard zone. A curve$Ud = 0.4\ m^2\,s^{-1}$ was also proposed, which indicates the instability threshold for children. The proposed maximum values of flow velocity and flow depth for good conditions are $U = 3\ m\,s^{-1}$ and d =1.2 m. This is possibly the most widely known criterion, which has also served as a reference for later criteria on flood hazard to pedestrians.

Russo et al. (2013a) and Martínez-Gomariz et al. (2016), who mainly explored conditions of instability in shallow flows with high velocities (see Table 2.3), integrated their instability data series into this criterion proposed by Cox et al. (2010), see Figure 2.18. These authors explored velocities up to 3.7 $m\,s^{-1}$ (higher than previous studies), and found that human instability in flood flows begins at shallower depths than reported by previous studies. Therefore they proposed a new minimum threshold curve to define the onset of flood hazard for pedestrians, $Ud = 0.22\ m^2\,s^{-1}$.

Similarly, Chanson et al. (2014) plotted people instability points found in field observations, together with instability data sets from previous studies, suggesting that instability for pedestrians in the face of flooding begins earlier than reported in those studies. According to the authors, this is due to the complex topography of an urban area (sidewalks, vehicles and street furniture) and debris, commonly in real-world flooding events, which was not taken

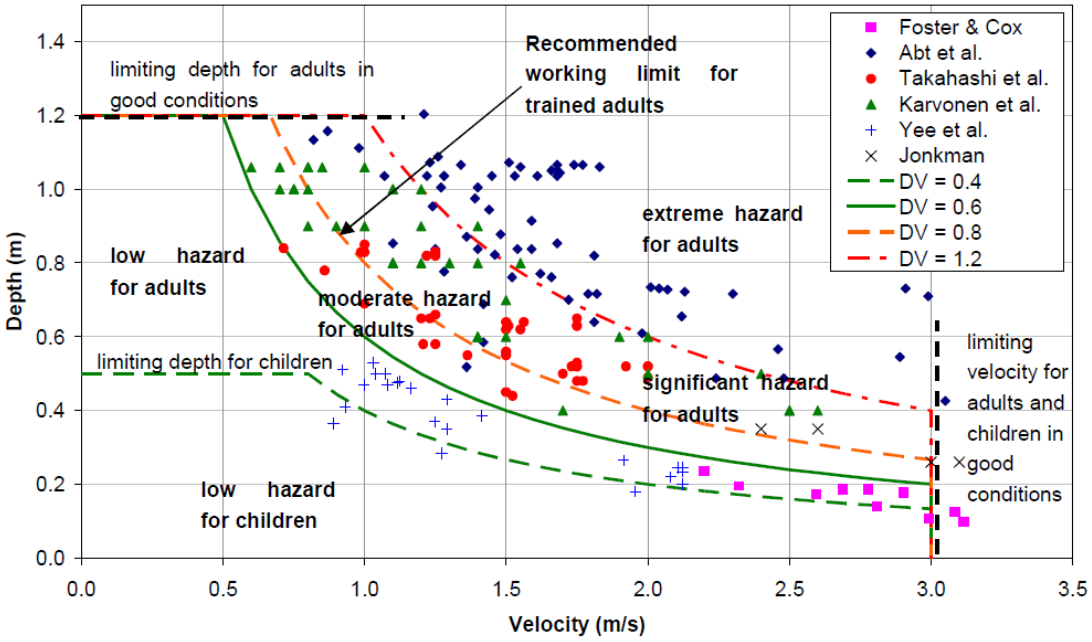

FIGURE 2.17. Flood hazard criterion for pedestrians proposed by Cox et al. (2010), with four levels of hazard. DV in the legend corresponds to Ud with present nomenclature.

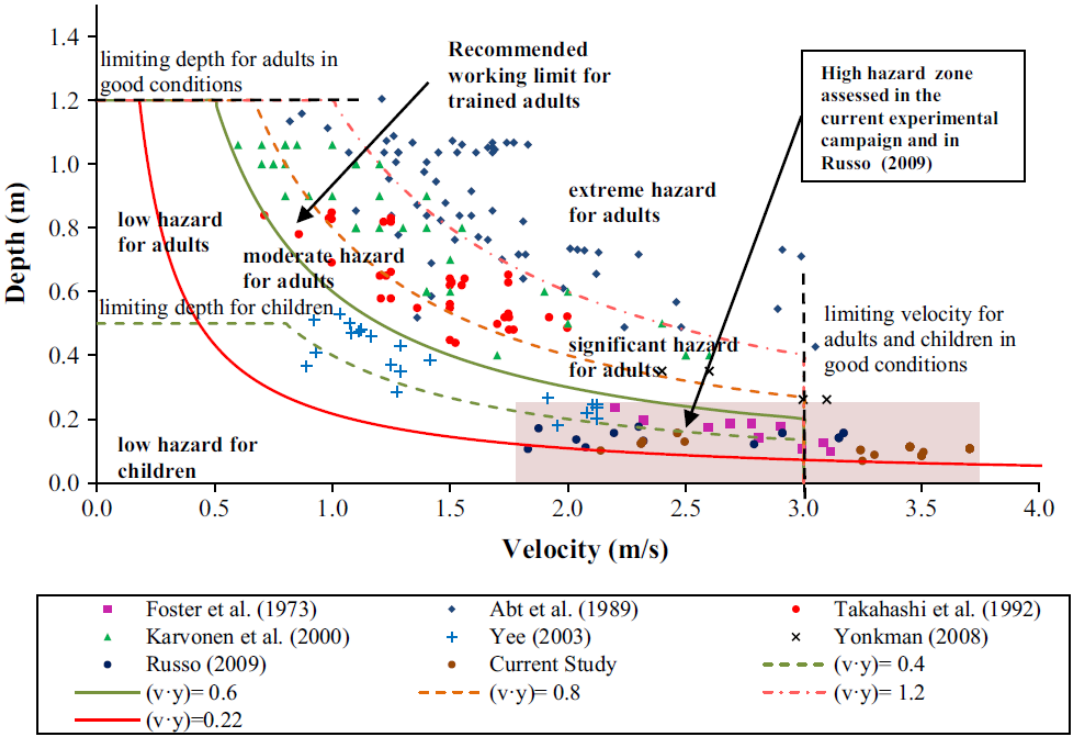

FIGURE 2.18. Human instability points and and threshold curve $Ud = 0.22$ m^2 s^{-1} from Russo et al. (2013a) and Martínez-Gomariz et al. (2016), integrated into the flood hazard criterion for pedestrians proposed by Cox et al. (2010). Taken from Martínez-Gomariz et al. (2016), where (v·y) in the legend corresponds to Ud in present nomenclature.

into account in these studies, but plays a very important role and constitute a major hazard.

Other research that has contributed to the knowledge on flood hazard to people is that carried out in Japan on the evacuation from underground spaces during a flood (e.g., Ishigaki et al., 2009, 2010; Baba et al., 2017). Ishigaki et al. (2009) proposed a criterion for evacuation from underground spaces in a flood situation, based on the force per unit width of the flood flow, M_0:

$$M_0 = \frac{U^2 d}{g} + \frac{d^2}{2} \tag{2.6}$$

where g is the gravity force. According to Ishigaki et al. (2009), $M_0 = 0.125$ m^2 and $M_0 = 0.25$ m^2 are the values for safe evacuation and critical self-evacuation without any help, respectively. Therefore, according to these expressions, when the flood flow velocity is $U = 0$, $d = 0.5$ m and 0.7 m for safe evacuation and self-evacuation without any help, respectively.

Finally, among all the criteria for flood hazard assessment found in the literature, there is a general criterion proposed by Smith et al. (2014), where buildings, vehicles and pedestrians are considered. This criterion is the combination of individual flood hazard criteria, i.e. criteria for buildings, for vehicles and for pedestrians, previously proposed by the same authors.

Figure 2.19 shows this general flood hazard criterion. It is interesting to see how the lowest instability thresholds (Ud) correspond to vehicles, mainly because the instability of vehicles occurs from low flow depths. For pedestrians, the range of flow depths where instability occurs is much greater than for vehicles. Furthermore, in this criterion, the velocity threshold that causes instability in pedestrians and vehicles is the same, however, several studies have shown a higher velocity threshold for vehicles, as shown in Figure 2.15. For buildings, the instability thresholds, of course, are higher than those of vehicles and pedestrians.

2.3.4 Economic flood damage

Flood damage includes *direct* and *indirect* damage. According to Merz et al. (2010), direct damages are those that occur due the physical contact between flood flows and people, infrastructure and assets, while the indirect are induced by the indirect impacts and occur in space or time outside the flood event area. They are normally classified into tangible and intangible, see Table 2.5.

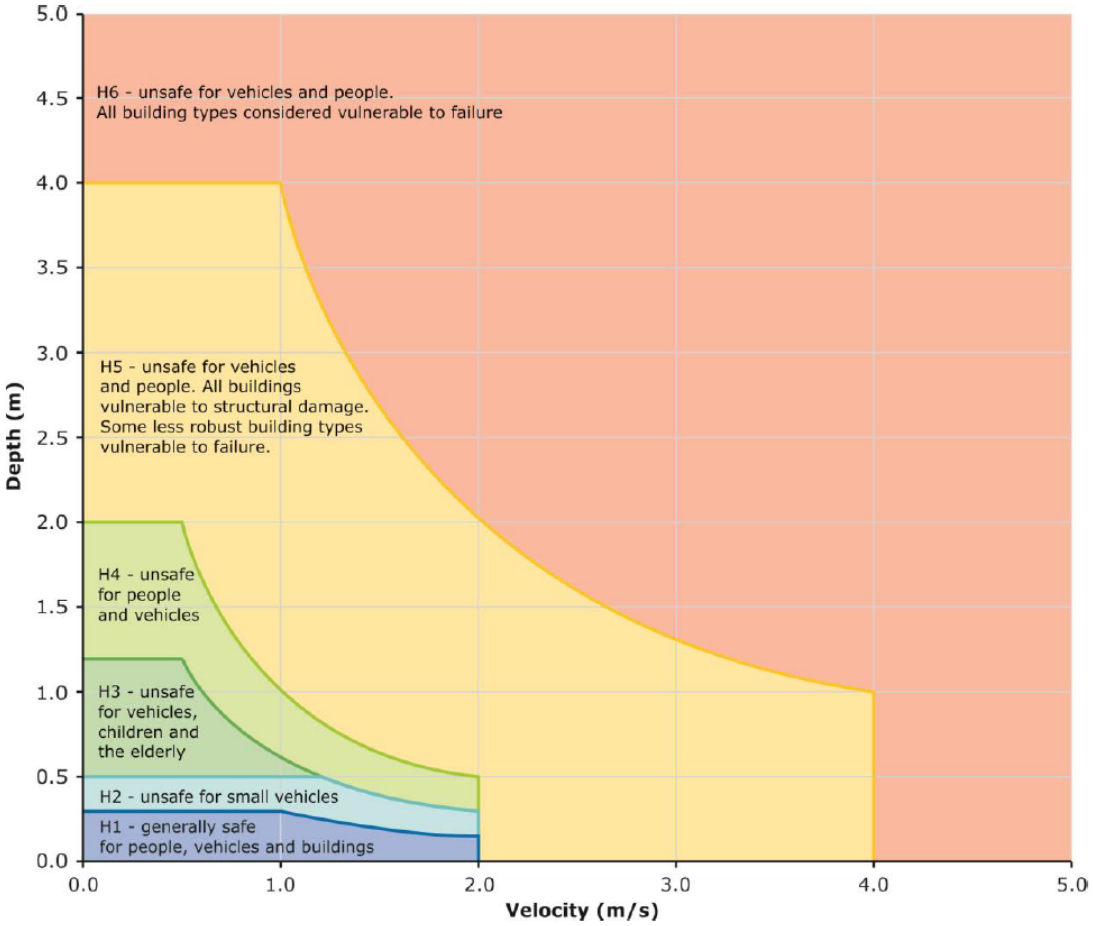

FIGURE 2.19. General flood hazard criterion on a floodplain, from Smith et al. (2014).

TABLE 2.5. Economic flood damage typology and examples. Taken from Nicholls et al. (2015).

	Tangible	Intangible
Direct	• Damage to private buildings and assets • Destruction of infrastructure • Evacuation and rescue measures • Business interruption inside the flooded area • Clean up costs.	• Injuries and loss of life • Psychological distress • Damage to cultural heritage • Negative effects on ecosystems
Indirect	• Disruption of public services outside the flooded area • Induced production losses to companies outside the flooded area • Cost of traffic disruption; loss of tax revenue • Loss of tax revenue due to mitigation of companies in the aftermath of floods	• Trauma • Loss of trust in authorities

For direct damage estimation, there are damage functions or loss functions, which relate damage for a specific element to the flood features, e.g., flooding extent and duration, flow depth, velocity, contamination of floodwaters, etc. One of the most common are the stage-damage curves, which relate the flood damage to different objects with respect to the flow depth. For instance, Figure 2.20 shows stage-damage curves for residential houses reported by Jonkman et al. (2008). The authors considered that total damage to a building is reached at about $d = 4.7$ m, and this comprises structural damage plus damage to the contents within the building (70% corresponds to structural damage, while 30% corresponds to the contents in the building). Lo et al. (2012) conducted a study for the city of Taiwan on the impact of debris flows, concluded that the total damage is reached when the flow depth is equal to 3.5 m. Therefore, the characteristics of these damage-curves or damage-functions normally correspond to specific regions, since accurate flood damage assessment requires accounting for all factors endemic to the region under study.

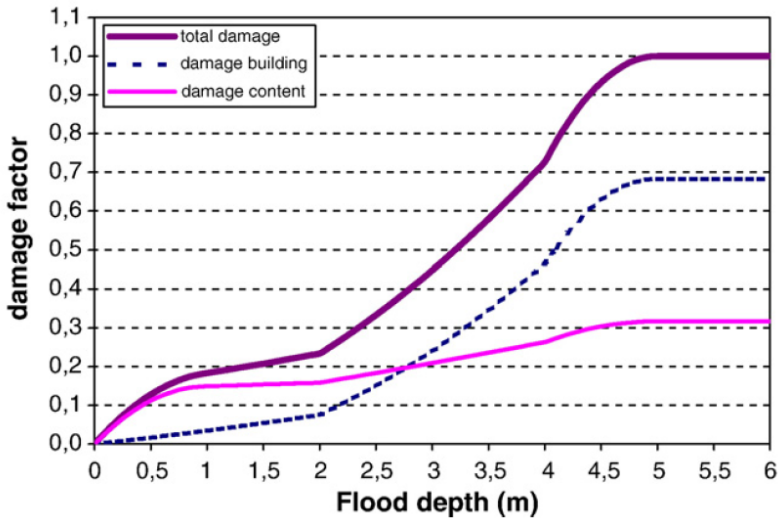

FIGURE 2.20. Stage-damage curves for residential houses, from Jonkman et al. (2008).

Indirect damage result from losses caused by the interruption of physical and economical connections in the economy, incorporating elements of spatial and temporal propagation (Cançado et al., 2010). Therefore, for indirect damage assessment it is necessary to choose the temporal and spatial boundaries (Merz et al., 2010).

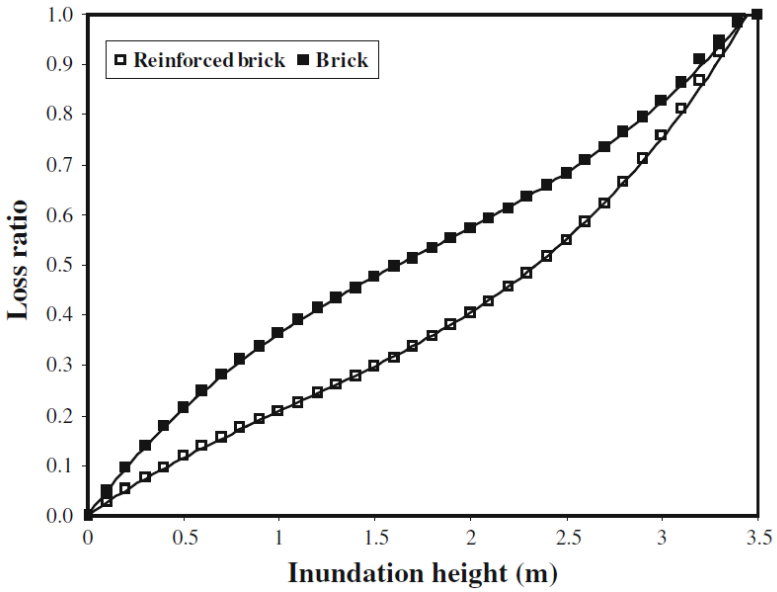

FIGURE 2.21. Loss ratio of reinforced brick and brick structures along with its contents at different flow depth for debris flows, from Lo et al. (2012).

2.3.5 Conclusions on Flood Hazard Assessment

As has been seen in this section, velocity and flow depth are the main characteristics that denote the flood hazard to different targets (buildings, cars, people). These are therefore the main parameters to be quantified in urban flood studies.

Flood hazard is very much based on instability studies, which aim to define the factors that determine instability for different targets, due to floodwaters. One of the most studied is the hazard to people, based on studies on the human instability. However, as Chanson et al. (2014) points out, most of these studies did not take into account the characteristics that exist in an urban area, which can enhance the flood severity. It would therefore appear that the thresholds defining the hazard levels proposed by Cox et al. (2010), one of the most frequently mentioned criterion in the literature, are overly optimistic. This is why authors such as Martínez-Gomariz et al. (2016) and Chanson et al. (2014) have proposed lower thresholds.

This present research work then aims at providing, in Chapter 3, an update of the flood hazard criterion for people proposed by Cox et al. (2010), taking into consideration the findings and recommendations reported in recent research on human instability. The new criterion will then be used, together with the flow depths and velocities measured in this research work, to produce maps of flood hazard to people.

CHAPTER 3

METHODOLOGY

To meet the objectives detailed in the previous chapters, three experimental campaigns are conducted, one for each addressed key issue. For the study of the first two key issues (what is the influence of a variation in the conveyance porosity magnitude of the city block and the variation in the conveyance porosity distribution on flood flow features) experiments are carried out under *steady flow conditions*. For the third key issue (what is the influence of a variation in the city block storage capacity on flood flow features), experiments are carried out under *steady* and *unsteady flow conditions*. For these campaigns, the experimental methodology is mostly similar, with certain variations adapted to the needs of each part. The following sections explain this methodology, including the characteristics of the physical model used, its adaptation for the study of the three key issues, the characteristics of the measurement instruments and the techniques developed.

3.1 The physical model MURI

The physical model MURI, is a 5.4 m long and 3.8 m wide rectangular tilting platform, which represents an urban district (Figure 3.1, pictures A and B). Its slope can be modified from 0 to 5% in both, longitudinal (aligned with the $x-$axis) and transverse (aligned with the $y-$axis) directions. It comprises three longitudinal streets, crossing three transverse streets,

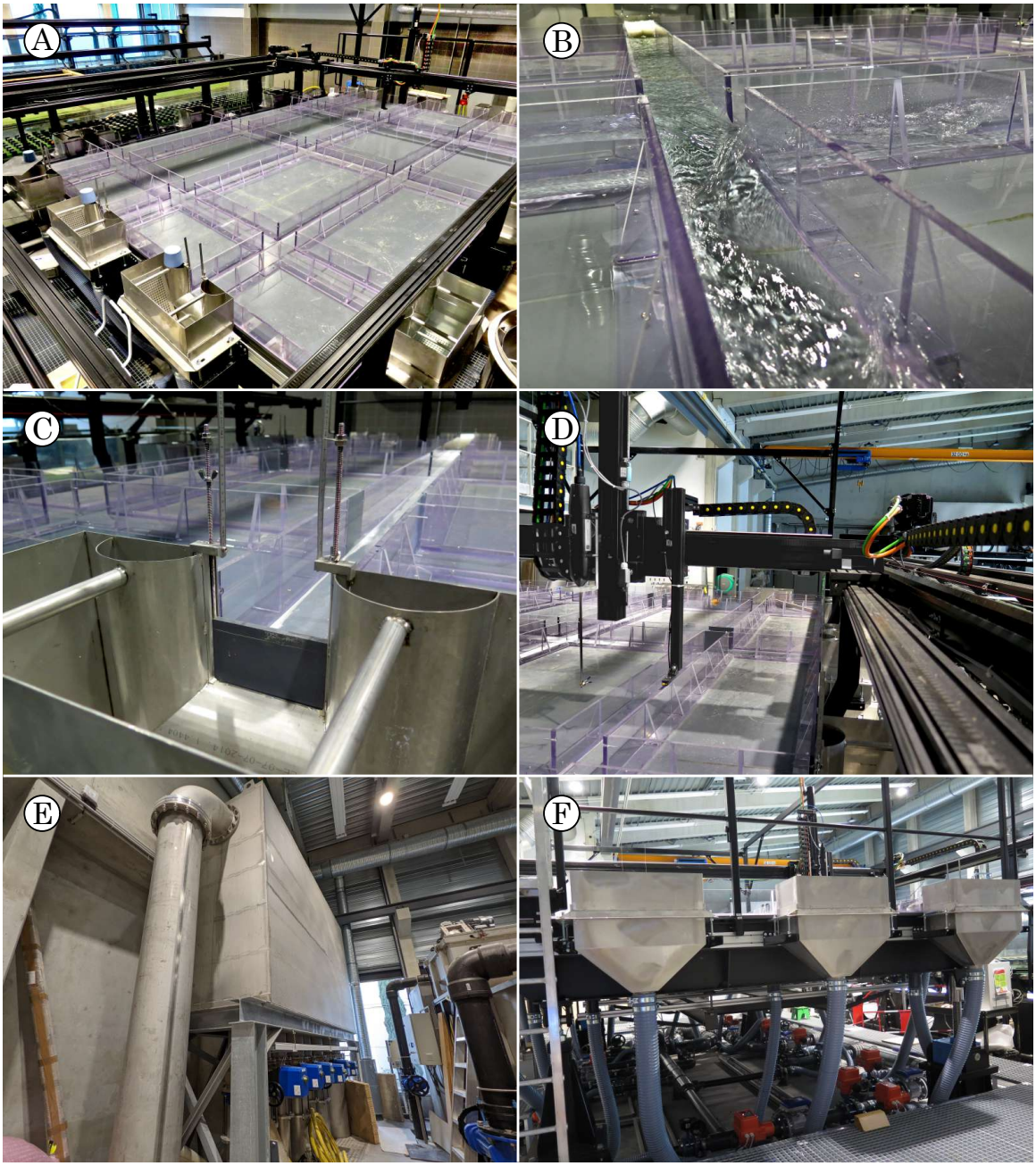

FIGURE 3.1. A) General overview of the urban model for the study of flood risk, MURI. B) View of water flowing in the streets. C) Movable vertical weir located at the downstream end of a longitudinal street. D) Mechanical gantry system for automated displacement of measuring instruments. E) Tower with a constant water level reservoir for water supply to physical models, including MURI. F) Inlet tanks of the three longitudinal streets.

all 0.15 m wide, and sixteen rectangular city blocks of different sizes, see Figure 3.2. The city block side walls are made of smooth transparent plastic (PETG), they are 0.15 m high, and can be removed if required. The platform bed is made of smooth grey PVC plates. A movable vertical tail weir is located at the upstream and downstream ends of each street

(Figure 3.1, picture C).

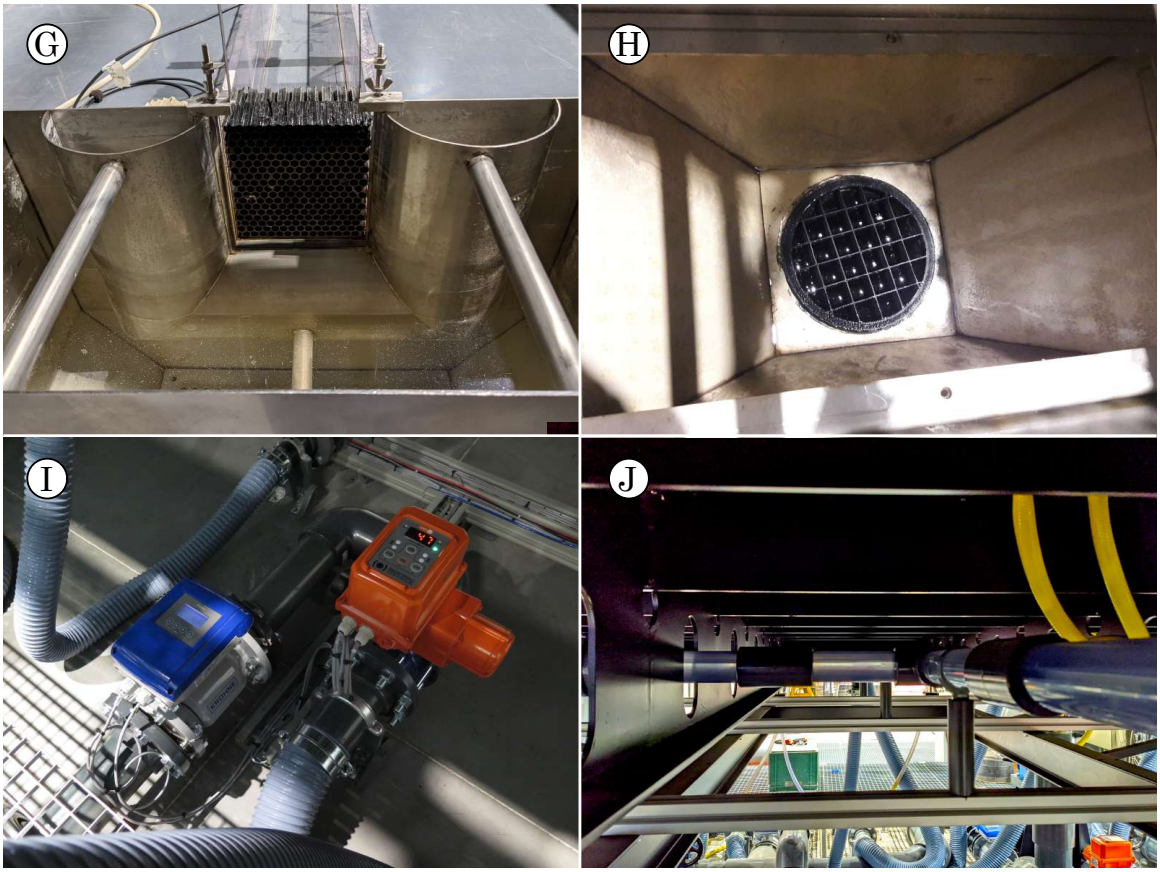

FIGURE 3.1. (Continued) G) Inlet tank, with a plastic honeycomb grid. H) Plastic grid in the connection between the inlet duct and inlet tank. I) Electromagnetic flowmeter (left) and an electrovalve (right), controlling the inflow discharge at each street. J) Pipes underneath the streets platform, which represents a sewer network.

The model is equipped with a mechanical gantry system for an automated displacement of the different measuring instruments along both, longitudinal and transverse directions, see picture D in Figure 3.1. The water supply in the model is gravity-fed, with an elevated water reservoir of constant water level (Figure 3.1, picture E), water first arrives at an inlet tank (Figure 3.1, picture F) and then flows into the streets. At the connection between the inlet conduit and the inlet tank, a plastic grid, manufactured with 3D printing, is installed (Figure 3.1, picture H). The inlet tanks comprise a vertical and transverse 3D converging device, ended by plastic grids, type honeycomb (Figure 3.1, picture G), which, together with the conduit-tank connection plastic grid, ensure a homogeneous flow distribution, free of turbulent structures coming from the pumping loop and the directional changes of the inlet

conduit. The inflow discharge is controlled by a flow-measuring control system upstream each inlet tank, consisting of an electromagnetic flowmeter and an electro-valve (Figure 3.1, picture I).

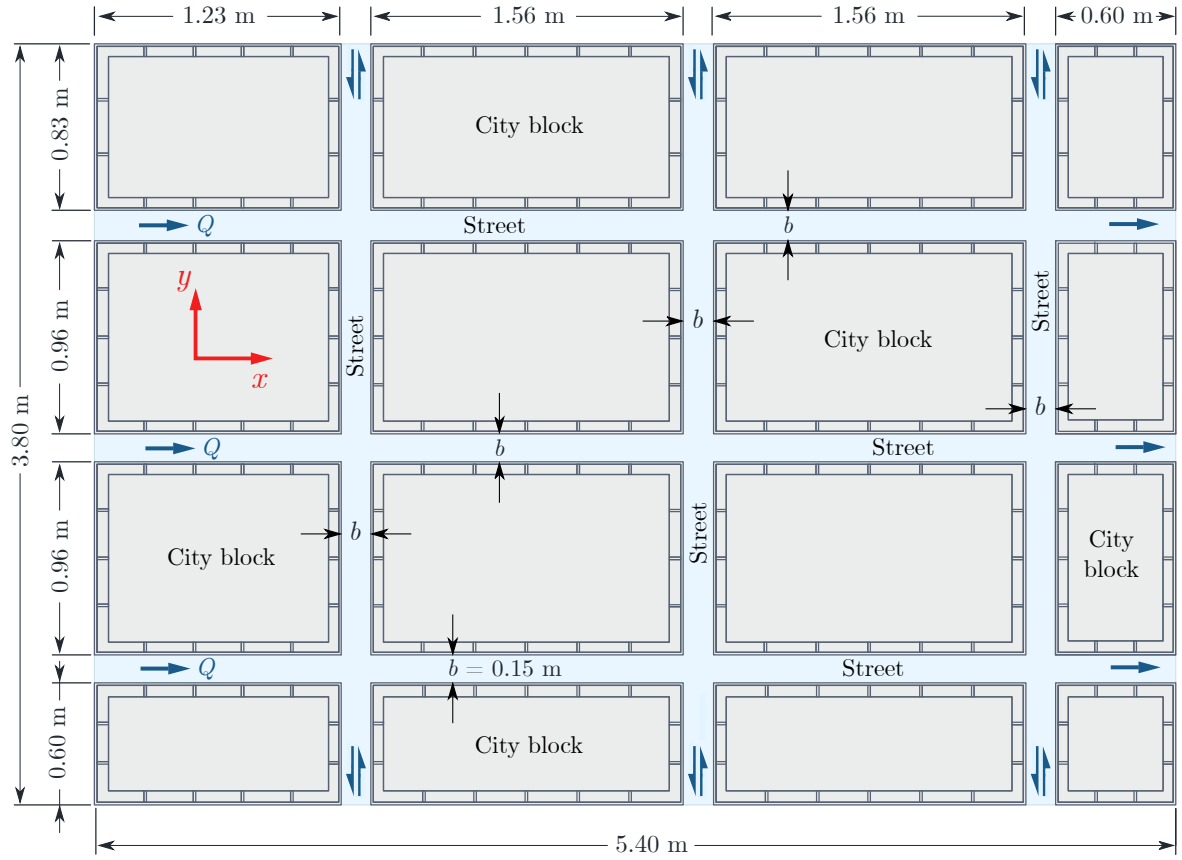

FIGURE 3.2. Schematic plan view of the experimental model MURI. It comprises 16 non-porous city blocks, three longitudinal streets (along the x-axis) and three transversal streets (along the y-axis). Arrows at the upstream and downstream ends of the streets depict the possible flow direction.

The model has also a circular-section pipe network made of smooth transparent plastic, located underneath the streets and blocks platform, which represents a sewer network (Figure 3.1, picture J). The slope of this pipe network can be modified independently of the platform slope. By perforating the platform bed, it is possible to connect the pipes with the streets (the yellow hoses shown in the picture J in Figure 3.1 are connections between the pipe network and the streets), see also Chibane et al. (2021). In addition to this, MURI is also prepared for the installation of a rain simulation system (not yet available), which would be located above the platform. For this study, only the main platform with streets and city blocks is used.

3.2 Experimental set-up

For the present PhD work, the physical model MURI is adapted by reducing the study area to 5.4 m (along x-axis) $\times$ 3.2 m (along y-axis), i.e., focusing on a single rectangular-shaped city block and the four surrounding streets, respectively labelled, *upstream*, *downstream*, *right* and *left*, see Figure 3.4. The remaining streets are simply isolated by smooth plastic plates. The city block under study, which was originally non-porous (Figure 3.2), is replaced by a porous city block of the same size, with three available openings along each wall, for a total of twelve openings, see Figure 3.3. The openings in the walls are 0.06 m wide, and these represent open gates (the flow remains with free-surface through these openings). The porous city block dimensions are $L_{B,x} = 1.56$ m by $L_{B,y} = 0.96$ m, made of smooth plastic vertical walls 0.02 m thick and 0.15 m high. The model bed slope in the longitudinal direction (aligned with the $x-$axis), $S_{0,x}$, is set at 0.12%, and the slope in the transverse direction (aligned with the $y-$axis), $S_{0,y}$, equals zero.

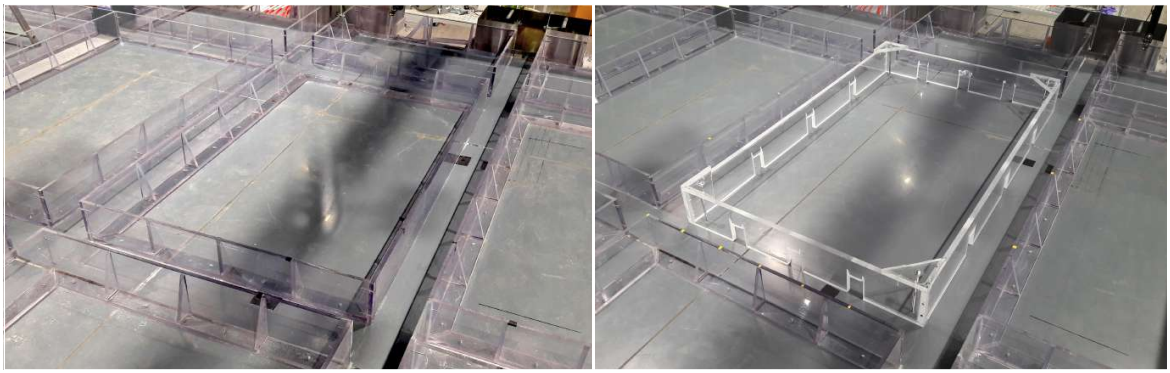

FIGURE 3.3. Left: Original non-porous city block. Right: Porous city block used in this PhD.

Two different experimental set-ups are used for this research, and are referred to as *variant 1* and *variant 2*. They differs by the number of discharge inlets and the incorporation or not of weirs at the outlets. These differences are outlined in the following sections.

3.2.1 Variant 1

The experimental set-up *variant 1* is used for the study of the *conveyance porosity* of the city block, i.e., for the first two key issues described in the objectives:

- *Key issue 1.* What is the influence of varying the magnitude of the city block conveyance porosity, ψ, on floodwater features under steady flow conditions?

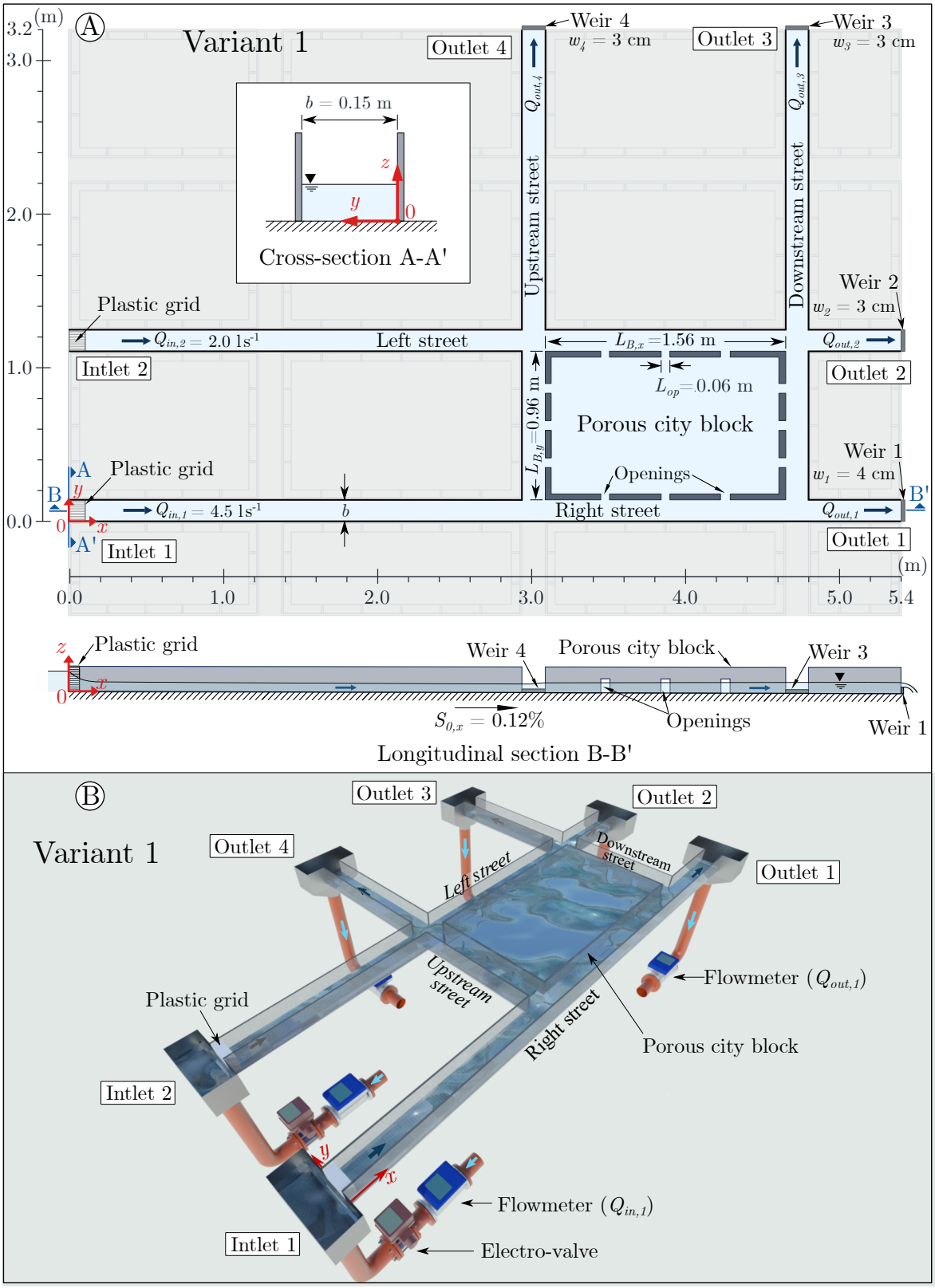

FIGURE 3.4. A) Schematic plan view of the experimental set-up *variant 1*. A cross-section and a longitudinal section of the right street are provided. In these schematic views, the global coordinates, x, y, z, are displayed. B) Isometric view of the experimental set-up *variant 1*, inlet and outlet tanks are shown and instruments for measuring and regulating discharges.

- *Key issue 2.* What is the influence of varying the distribution of the city block conveyance porosity, ψ, on floodwater features under steady flow conditions?

The set-up includes two discharge inlets, denoted as inlet 1 and inlet 2, on the right and left streets, respectively. The total inflow discharge, $Q_{in,T} = 6.5$ ls^{-1}, is partitioned as $Q_{in,1} = 4.5$ ls^{-1} ($\approx 70\%$ of $Q_{in,T}$), and $Q_{in,2} = 2.0$ ls^{-1} ($\approx 30\%$ of $Q_{in,T}$), as showing in Figure 3.4.A. Water leaves the experiment device through four outlets, one at each street (Outlets 1, 2, 3 and 4, in the right, left, downstream and upstream streets, respectively). A vertical tail weir is placed at the downstream end of each street to control the flow depth and ensure a subcritical regime flow throughout the study area. The weir heights, w, are set to ensure a higher flow depth in the right street than in the left street, favouring a transverse flow through the porous city block, along y-axis ($w_1 = 4$ cm at outlet 1, while $w_2 = w_3 = w_4 = 3$ cm at outlets 2, 3 and 4). At the outlet of each street, water falls into an outlet tank, then in the outlet pipe the discharge is monitored with an electromagnetic flowmeter, (Figure 3.4.B.)

3.2.2 Variant 2

The second experimental set-up, entitled *variant 2* is used for the study of *key issue 3*: What is the influence of varying the city block storage capacity, ϕ, on floodwater features?. The experiments are carried out under both steady and unsteady flow conditions. For a better control of the inflow discharge during unsteady flow tests, as well as to decrease the measuring instruments uncertainty, a single inlet discharge is considered here. Water enters through the right street inlet and is evacuated through the four outlet streets (right, left, upstream and downstream). To avoid any backwater effect in the unsteady flows, no weirs have been set at the street outlets (Figure 3.5.A), resulting in free outflow conditions.

In this variant, only one opening is included in each side wall of the porous city block. In addition, to change the occupied space within the block, a non-porous building of decreasing area is installed here (Figure 3.5). The building is installed in the central part of the porous city block, the distance between the block walls and the building walls, denoted l, is the same on all 4 sides.

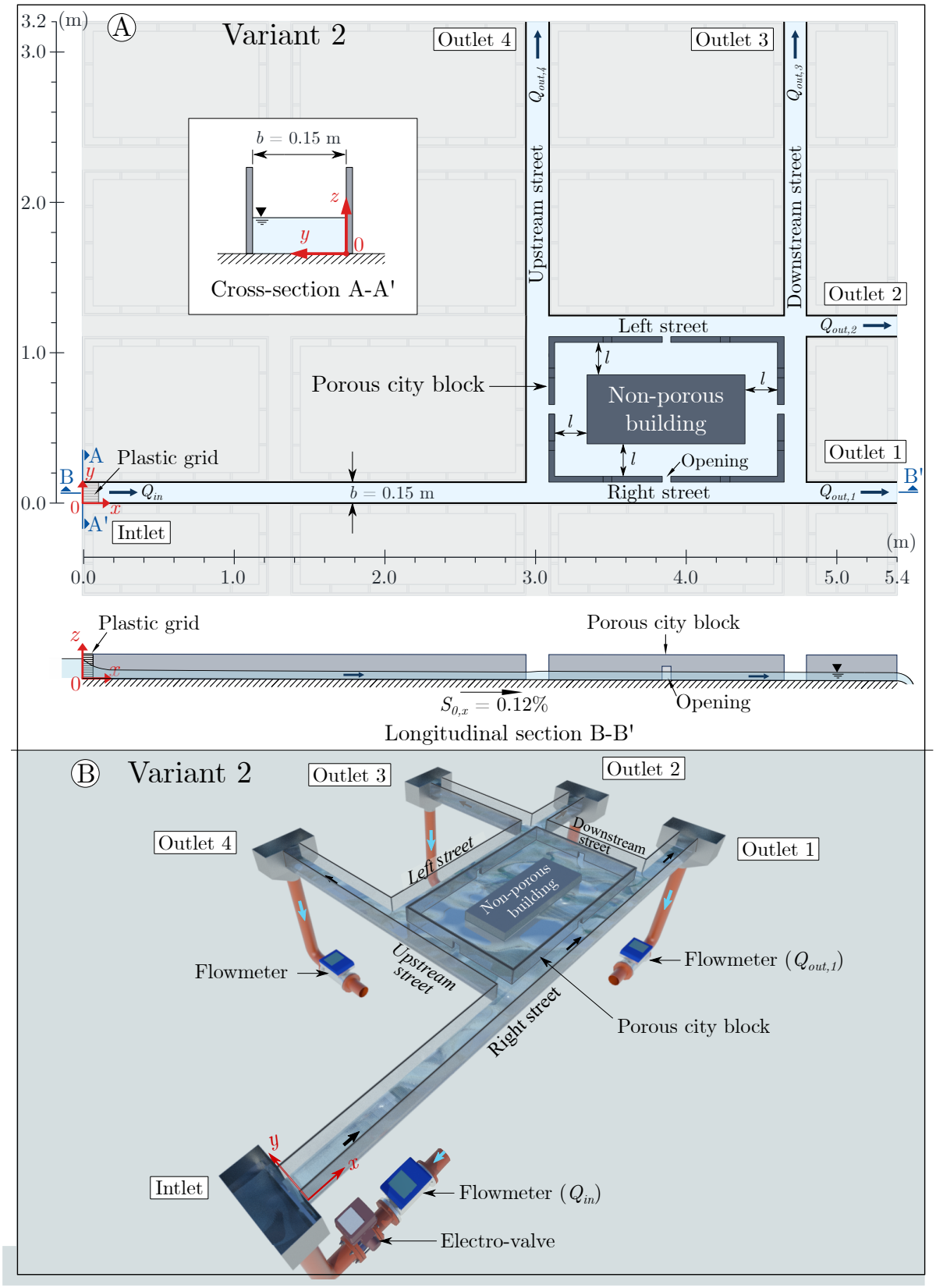

FIGURE 3.5. A) Schematic plan view of the experimental set-up *variant 2*. B) Isometric view.

3.3 Measuring techniques and data processing

To characterize the flood flow within the urban area, the measurements combine inflow and outflow discharges (section 3.3.1), flow depth (3.3.2) and velocity (3.3.3) in the streets and within the city block. However, the way in which these parameters are collected and processed differs for steady and unsteady flows. In steady flows, for a given inflow discharge, reliable results are obtained by monitoring each parameter over a certain period of time, hence all the values presented are *time-averaged* values. For unsteady flows, an inflow hydrograph is injected and replicated a certain number of times, monitoring each parameter for the entire duration of all hydrograph replicates, hence the presented values are *ensemble-averaged* values (indicated with notation $\langle\ \rangle$). The following sections explain the procedure followed to obtain each flow parameter.

3.3.1 Discharge

3.3.1.1 Time-averaged discharges (steady flow)

Inflow and outflow discharges are measured with dedicated electromagnetic flowmeters (OPTIFLUX 2000 by KROHNE), with an accuracy of 0.3% (according to manufacturer), and capable of measuring a minimum discharge value of 0.13 $\mathrm{l\,s^{-1}}$ (according to preliminary tests carried out). Each inflow discharge is adjusted independently with an automatic valve-flowmeter system, with a maximum observed standard deviation of 3% of the discharge. To determine the appropriate acquisition duration for time-averaged discharges, the time convergence of the flowmeters data is tested by performing independent tests with discharges ranging from 0.2 to 5 $\mathrm{l\,s^{-1}}$. For each flowmeter (two at the inlets and four at the outlets), eight independent measurements are carried out at a sampling rate of 50 Hz during 600 s. For each measurement, the time-averaged discharge over each partial acquisition duration is computed and compared to the time-averaged discharge over the total acquisition duration (600 s), as:

$$\Delta Q(n_{(t)}) = \frac{\frac{1}{n_{(t)}}\sum_{i=1}^{n_{(t)}} Q_i - \frac{1}{n_{(t=600)}}\sum_{i=1}^{n_{(t=600)}} Q_i}{\frac{1}{n_{(t=600)}}\sum_{i=1}^{n_{(t=600)}} Q_i} \times 100 \tag{3.1}$$

where Q_i is the instantaneous discharge and $n_{(t)}$ is the number of samples recorded at time t. The appropriate acquisition duration was defined as the time, t, for which ΔQ is lower

than 0.3[1] % (manufacturer's specified accuracy). Figure 3.6 shows the convergence curves corresponding to each flowmeter used in this study (six flowmeters in total, two inlets and four outlets). Then, the minimum necessary acquisition duration is set at 400 s, which covers the acquisition duration necessary to achieve convergence in all flowmeters.

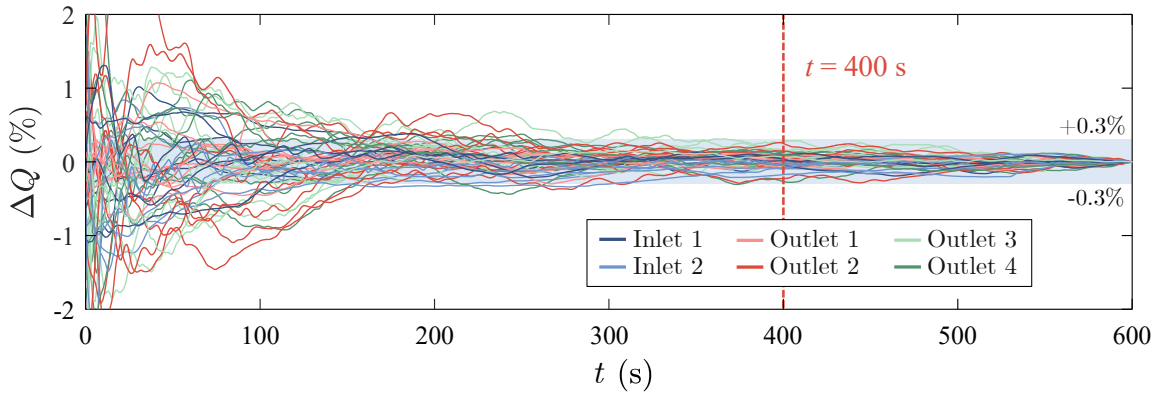

FIGURE 3.6. Time convergence of the time-averaged discharge for flowmeters located in the inlet and outlet conduits. Convergence is reached when $\Delta Q \leq \pm 0.3$ % (Eq. 3.1). The shaded area indicates the convergence range (± 0.3 %).

3.3.1.2 Ensemble-averaged discharges (unsteady flow)

Under unsteady flow conditions, an inflow hydrograph, controlled by the automatic electrovalve-flowmeter system, is injected. To determine the appropriate number of replicates and thus obtain the convergence of the ensemble-averaged inflow hydrograph, the inflow hydrograph is replicated 200[2] times. The hydrograph replicates are injected one after the other, with a time delay, Δt, equal to 60 s between the end of one hydrograph and the beginning of the next one, see Figure 3.7.A.

Instantaneous discharges, Q, are measured at a sampling rate of 50 Hz. The ensemble-averaged discharge,$\langle Q(t) \rangle$, at each time, t, of the inflow hydrograph is obtained by averaging the first j replicates, using as pivot the starting point of the hydrograph rising limb (Figure 3.7.B), until the total number of replicates is reached (i.e. 200 inflow hydrograph replicates):

[1]Although a maximum standard deviation of 3% was observed in the inflow discharges, which directly affects the outflows, by averaging these discharges over time it is observed that their variability is much lower. Thus the manufacturer's reported accuracy is defined as the convergence criterion, which resulted in a feasible acquisition duration.

[2]When the first hydrograph is injected, the experimental set-up is completely dry, but for the following hydrographs there is always a residual water volume in the experimental set-up from the previous replicate. To ensure similar conditions for all hydrograph replicates, the first hydrograph of all series is always put aside. Therefore in this case the hydrograph is replicated 201 times, removing the first one.

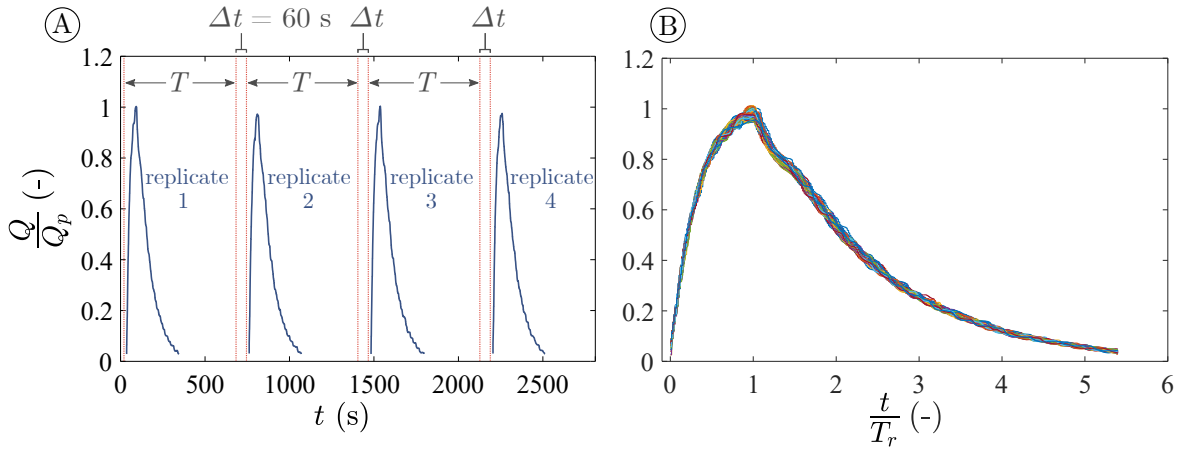

FIGURE 3.7. A) Inflow hydrograph replicates (only 4 of the 200 replicates are shown). The hydrographs do not cover fully the total duration, T, because the minimum discharge that the flowmeter is able to measure is 0.13 ls^{-1}. B) Overlapped inflow hydrograph replicates, using the starting point of the rising limb as a pivot point. In both plots, the discharges were normalized by the peak discharge, Q_p. The time t in plot B was normalised by the hydrograph rising time, T_r.

$$\langle Q(t)\rangle_j = \frac{1}{j}\sum_{i=1}^{j} Q(t)_i \quad (j = 1, 2, \ ..., 200) \tag{3.2}$$

The minimum number of replicates required for the convergence of the averaged hydrograph is obtained by plotting in Figure 3.8 the ensemble-averaged standard deviation, $\langle\sigma(Q(t))\rangle_k$, computed at each instant t, for the first k ensembled-averaged discharges until the total number of values is reached (i.e. 200 ensemble-averaged discharges):

$$\langle\sigma(Q(t))\rangle_k = \left(\frac{1}{k}\sum_{j=1}^{k}\left(\langle Q(t)\rangle_j - \overline{\langle Q(t)\rangle_j}\right)^2\right)^{\frac{1}{2}} \quad (k = 1, 2, \ ..., 200) \tag{3.3}$$

The convergence criterion is defined as a standard deviation lower than 1% of the peak flow, i.e., when $\langle\sigma(Q(t))\rangle_k \leq 0.05$ ls^{-1}. The number of replicates set for the ensemble-averaged inflow hydrograph equals 50.

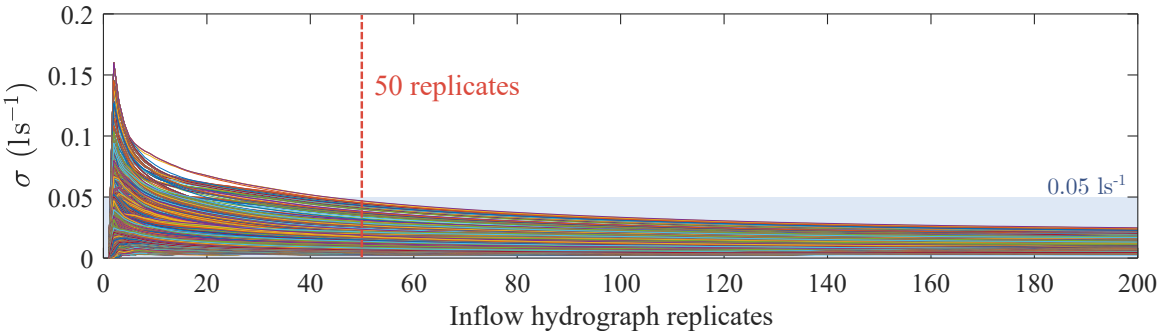

FIGURE 3.8. Ensemble-averaged standard deviation of the ensemble-averaged discharges as a function of the number of inflow hydrograph replicates for each time t. Convergence is reached when $\langle \sigma(Q(t)) \rangle_k \leq 0.05$ ls^{-1} (Eq. 3.3). This convergence limit is indicated by the shaded area. Each of the curves stands for a time t of the ensemble-averaged hydrograph.

3.3.2 Flow depth

3.3.2.1 Time-averaged flow depths (steady flow)

The 2-D field of flow depth, d, is obtained using an Ultrasonic distance-measuring Sensor (US), manufactured by BAUMER (BAUMER UNDK 20I6914/S35A), see Figure 3.9). It consists of a transducer that emits sonic waves that are reflected by an object and received back. The time elapsed between emitting and receiving is proportional to the distance of the object from the sensor. To obtain flow depths, the distances from the sensor to the bed and from the sensor to the water free-surface are measured for each location, the difference between these distances is equal to the flow depth. According to the manufacturer, the US has an accuracy better than 0.3 mm and reproducibility better than 0.5 mm. To define the appropriate acquisition duration of each local flow depth measurement, the time convergence of the US signal is assessed by performing thirteen independent flow depth measurements at various locations (in the streets, within the block and in specific areas with significant fluctuations in flow depth, such as crossroads). Each measurement is carried out for 400 s at a sampling rate of 50 Hz. For each measurement, the time-averaged flow depth over each partial acquisition duration is computed and compared

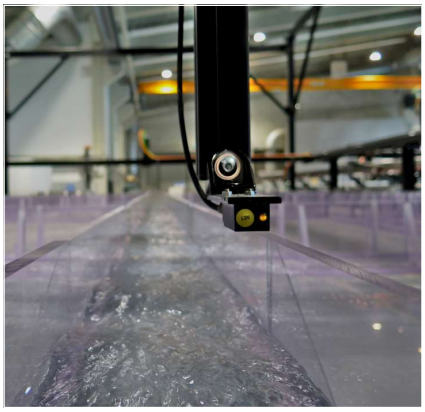

FIGURE 3.9. Ultrasonic distance-measuring Sensor (US), fixed on the MURI mechanical gantry system.

to the time-averaged flow depth over the total acquisition duration (400 s), as:

$$\Delta d(n_{(t)}) = \frac{1}{n_{(t)}} \sum_{i=1}^{n_{(t)}} d_i - \frac{1}{n_{(t=400)}} \sum_{i=1}^{n_{(t=400)}} d_i \tag{3.4}$$

where d_i is the instantaneous flow depth and $n_{(t)}$ is the number of samples at time t. Then, the appropriate acquisition duration is defined as the time, t, for which $\Delta d(n_{(t)})$ is lower than 0.3 mm (US accuracy specified by the manufacturer). Figure 3.10 demonstrates that the duration equals 50 s.

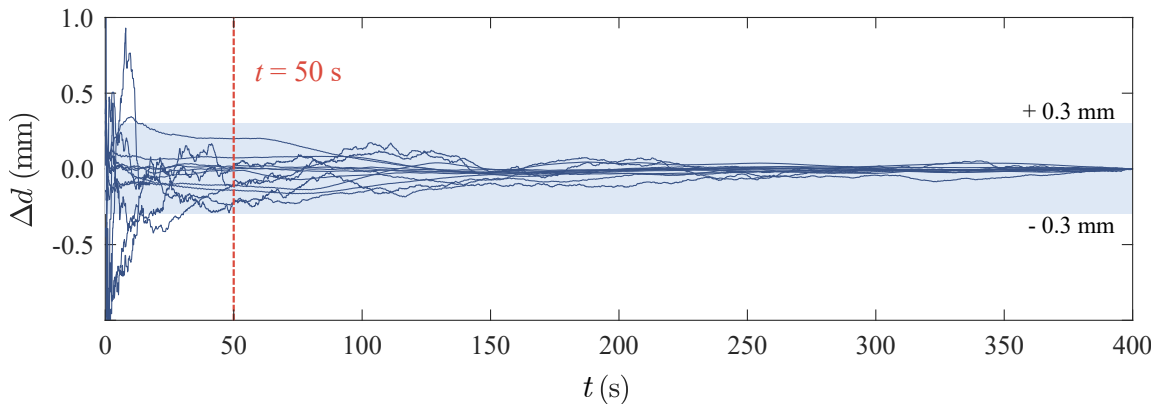

FIGURE 3.10. Convergence plot of the time-averaged flow depth at 13 various locations. Convergence is reached when Δ (Eq. 3.4) is lower than the probe accuracy ($\pm$0.3 mm), showed by the shaded area.

The spatial interval between two measurements in the streets is equal to 5.0 cm and 6.5 cm in the streamwise and spanwise directions, respectively (3 measurements in the street cross-section, one on the centreline and one near each side wall). Within the city block the spatial interval between two measurements is equal to 12.0 cm along both directions (a greater spatial interval than in streets because here the flow depth spatial gradients are lower). The study area where flow depth measurements are performed for the steady flows in key issues 1 and 2 is shown in Figure 3.11.

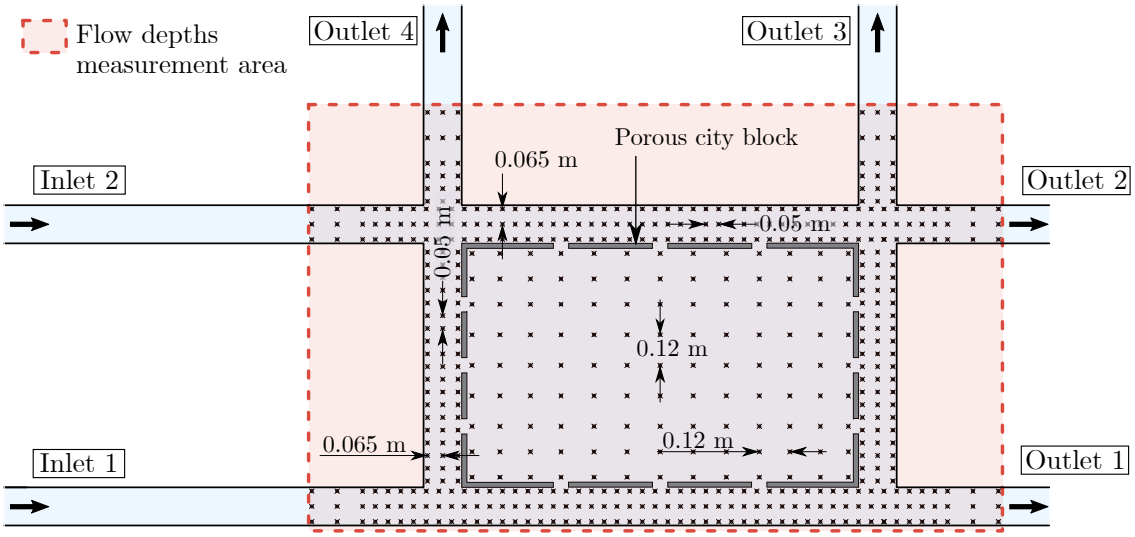

FIGURE 3.11. Study area in the experimental set-up *variant 1*, where flow depths are measured with the US probe for the steady flows in key issues 1 and 2.

3.3.2.2 Ensemble-averaged flow depths (unsteady flow)

For unsteady flows, the flow depth is measured at various locations in the experimental set-up variant 2 (Figure 3.5), for which several US probes (BAUMER UNDK 20I6914/S35A) are installed: one at each street surrounding the block (P_{RS}, P_{LS}, P_{US} and P_{DS}), one 15 cm upstream of each outlet (P_{out1}, P_{out2}, P_{out3} and P_{out4}), one more in the inlet street (P_{in}), and two more located above the city block (P_{BU} and P_{BD}), see Figure 3.12.

To estimate the minimum number of replicates required for the convergence of the ensemble-averaged flow depths, the same procedure is followed as for the ensemble-averaged inflow hydrograph, described in section 3.3.1.2. Instantaneous flow depths, d, are measured in the inlet street (at P_{in}) at a sampling rate of 50 Hz. The ensemble-averaged flow depth, $\langle d(t) \rangle$, at each time, t, of the stage hydrograph is computed by averaging the first j stage hydrograph replicates, using as pivot the starting point of the stage hydrograph rising limb, until the total number of replicates is reached (i.e. 200 stage hydrograph replicates).

$$\langle d(t) \rangle_j = \frac{1}{j} \sum_{i=1}^{j} d(t)_i \quad (j = 1, 2, \ ..., 200) \tag{3.5}$$

The minimum number of replicates required for the convergence of the ensemble-averaged flow depths is computed based on Figure 3.13, the ensemble-averaged standard deviation,

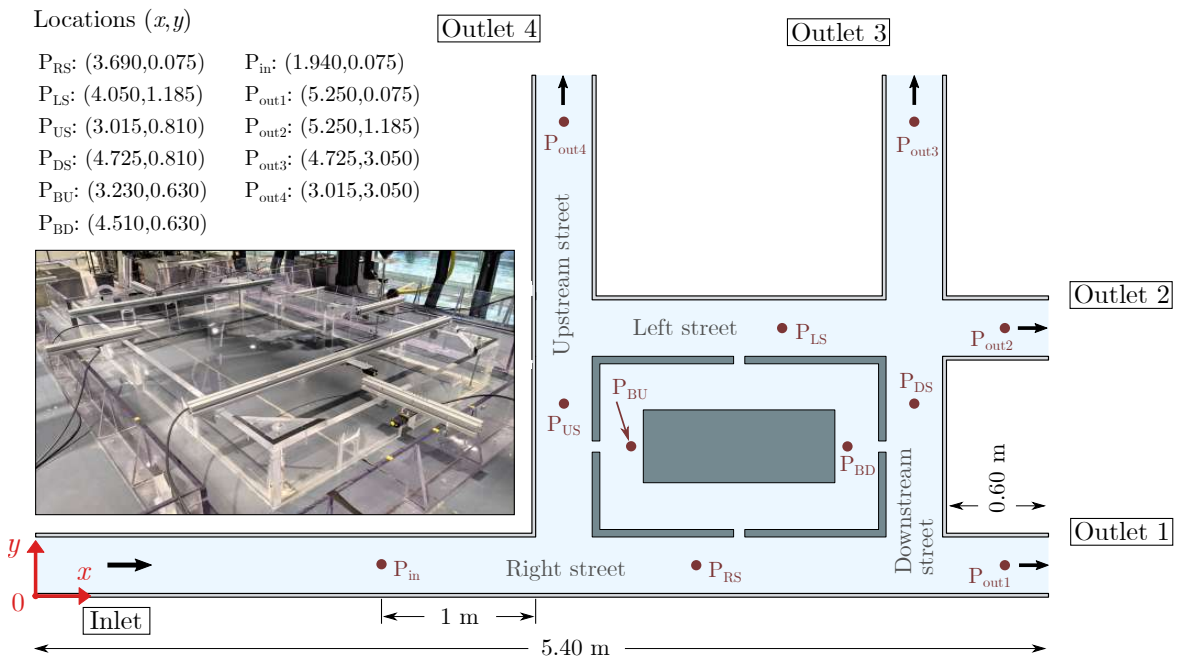

FIGURE 3.12. Schematics plan view of the experimental set-up *variant 2*, with the various locations of the measuring points of the flow depth, when addressing key issue 3. The schematic is not a scale, and the width of the streets has been distorted (enlarged) to fit all the required information.

$\langle\sigma(d(t))\rangle_k$, computed at each instant t, for the first k partial averaged flow depths until the total number of values is reached (i.e. 200 partial averaged flow depths):

$$\langle\sigma(d(t))\rangle_k = \left(\frac{1}{k}\sum_{i=1}^{k}\left(\langle d(t)\rangle_j - \overline{\langle d(t)\rangle_j}\right)^2\right)^{\frac{1}{2}} \quad (k = 1, 2, \ ..., 200) \tag{3.6}$$

The convergence of the ensemble-averaged standard deviation is achieved when $\langle\sigma(d(t))\rangle_k$ is lower than 1 mm. Figure 3.13 shows that the number of replicates set for the ensemble-averaged stage hydrograph equals 50 (same number of replicates as for the ensemble-averaged inflow hydrograph).

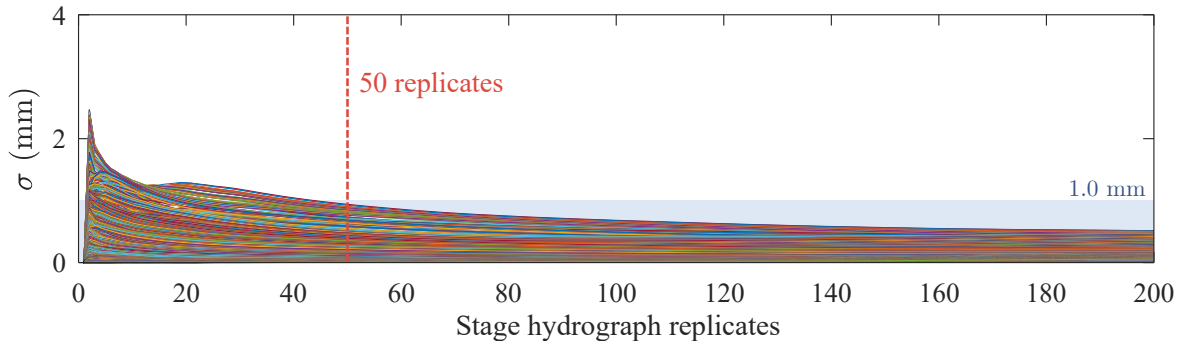

FIGURE 3.13. Ensemble-averaged standard deviation of the ensemble-averaged flow depths constituting the stage hydrograph at measuring point P_{in}. Convergence is reached when $\langle\sigma\rangle_j(t) \leq 1$ mm (Eq. 3.6). This limit is indicated by the shaded area.

3.3.3 Velocity

3.3.3.1 Time-averaged velocities within the water column (steady flows)

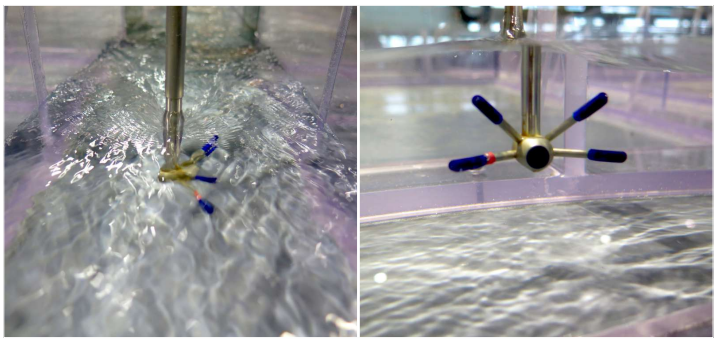

FIGURE 3.14. Acoustic Doppler Velocimeter (ADV) whit a side-looking probe, fixed on the MURI mechanical gantry system.

The flow velocity in the water column is measured using an Acoustic Doppler Velocimeter (ADV) with a side-looking probe (NORTEK Vectrino +, see Figure 3.14). The center circular transmitter probe emits ultrasound beams of periodic signal with a given frequency f_0 that travel in flow. This signal is backscattered by particulate matter located in the flow (e.g. suspended sediments, small organisms, artificial particles, etc.), with a frequency f_1 and received by four receiving probes with a frequency f_2. The frequency difference $f_2 - f_0$, named Doppler shift effect, can be related to flow velocity along the bisector of the emitted/received signal axes angle. A geometrical reconstruction finally permits to assess the three instantaneous velocity components (u_x,u_y,u_z) at a distance of 5 cm away from the transmitter probe (for non-intrusive flow measurements). The ADV accuracy is 0.5% of the measured value, according to the manufacturer. Water is seeded with polyamide particles (VESTOSINT®), with an average particle diameter of 55 µm to increase the signal-to-noise ratio. The WinADV software is used to process the ADV raw data, including a filtering step

based on the despiking technique proposed by Goring and Nikora (2002).

TABLE 3.1. Location of the ADV measurements in experimental set-up variant 1, for time convergence tests. z^* is a local coordinate in the vertical direction for each test location, with $z^* = 0$ at the bottom.

Test	x (m)	y (m)	z^*/d	U (cm s^{-1})	Description
1	3.40	0.075	0.15	35.93	Single straight street, close to the bed
2	3.40	0.075	0.70	44.64	Single straight street, close to the surface
3	3.40	0.145	0.50	37.09	Single straight street, close to the left wall
4	2.14	0.075	0.55	59.06	Right street, in configuration without block
5	4.85	0.075	0.45	20.72	(town square configuration)
6	3.69	0.075	0.47	52.14	Right street, in configuration with porous
7	3.69	0.145	0.47	49.07	block with one opening in right and left walls
8	3.69	1.255	0.48	18.80	Left street, in configuration with porous block with one opening in right and left walls
				Within the city block	
9	3.47	0.990	0.50	5.07	Block with one opening in right and left walls
10	3.87	0.630	0.50	7.07	
11	4.53	0.630	0.50	5.17	
12	4.270	0.270	0.50	4.99	
13	3.870	0.400	0.51	1.45	Block with one opening in upstream and downstream walls
14	3.870	0.630	0.51	7.56	Block with one opening in each wall

Although the ADV is capable of measuring the three velocity components, for the present study, only the horizontal component aligned with the streamwise direction is of interest (u_x or u_y, as applicable). Moreover, although it is recommended to make an angular correction due to a misorientation of the ADV probe (Peltier et al., 2013), here it has been observed that this correction has a negligible impact on the streamwise velocities (similar results according to Peltier, 2011). Therefore, no angular correction is applied to the measured velocities, however, every time the ADV probe is moved, it is aligned with special attention, in order to avoid any excessive misorientation.

To define the appropriate acquisition duration, the time convergence of the ADV velocity data is tested by measuring the flow velocity at fourteen locations around the study area (eight in the streets and six within the city block, see Table 3.1), during 600 s at a sampling rate of 100 Hz (i.e. 60000 samples per sampling location). Is considered a time convergence criterion 3% of the time-averaged value, equal to the value of the standard error observed of the inlet discharges. The percentage error of the time-averaged velocity for each partial acquisition duration is obtained with the following expression:

$$\%\,\mathrm{Error}(n_{(t)}) = \frac{\frac{1}{n_{(t)}}\sum_{i=1}^{n_{(t)}} u_i - \frac{1}{n_{(t=600)}}\sum_{i=1}^{n_{(t=600)}} u_i}{\frac{1}{n_{(t=600)}}\sum_{i=1}^{n_{(t=600)}} u_i} \times 100 \tag{3.7}$$

where u_i is the instantaneous velocity component. In general, the convergence is obtained earlier in the streets than within the block (Figure 3.15), therefore two appropriate acquisition durations are proposed for the time-averaged velocities computation (U_x,U_y), 100 s in the streets and 200 s within the city block.

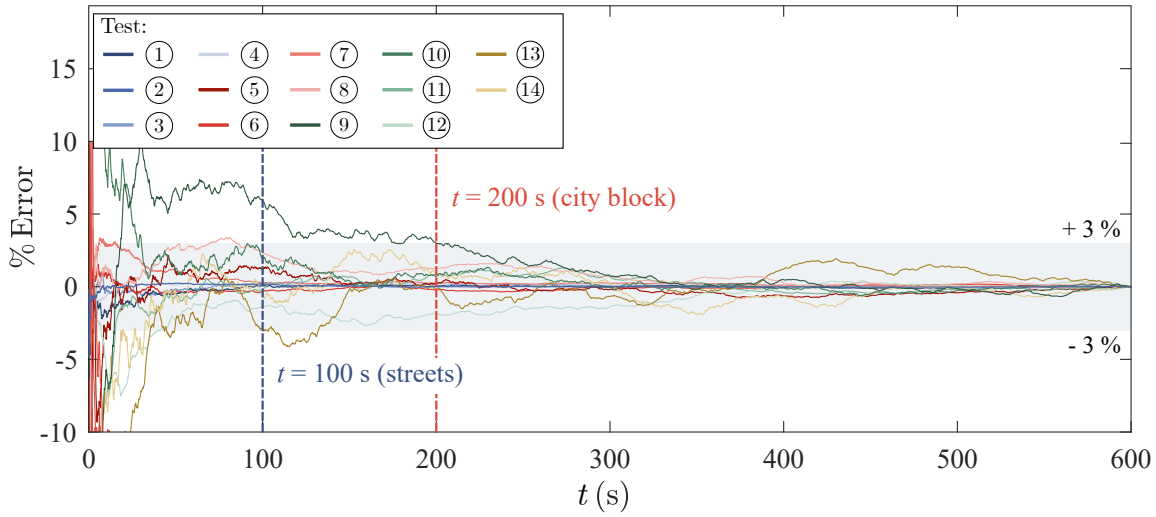

FIGURE 3.15. Time convergence of the time-averaged streamwise velocity (ADV) at 14 various locations. Convergence is reached when %Error $\leq \pm$ 3% (Eq. 3.7). The shaded area indicates the range $\pm$ 3%.

3.3.3.2 Time-averaged surface velocity (steady flow)

The surface velocity, U_s in the streets and within the block is measured using the Large Scale Particle Image Velocimetry technique (LSPIV), which is derived from the Particle Image Velocimetry technique (PIV). This is a non-intrusive measurement technique, initially developed for the estimation of velocities in large sectors on the surface of natural streams, which has been extended to laboratory applications for several years now. In previous studies, this technique proved to be reliable for a laboratory use (e.g. Muste et al., 2000; Kantoush et al., 2011), being able to accurately measure small velocities in shallow-depth flows (Meselhe et al., 2004), and to properly distinguish large-scale and small-scale flow structures (Fujita et al., 1998).

According to Muste et al. (2000), this technique comprises 4 components: illumination, tracer seeding, recording, and image processing. The technique consists of seeding the flow with tracers at the water surface (floating material that follows the current), while recording its movement with a video camera. The tracers' movement is detected by auto-correlating the patterns enclosed in a small area, called the interrogation area (IA), from one image to the following. This IA is searched within the searching area (SA), to finally estimate its potential displacement, see Figure 3.16. With this displacement and the time difference, it is possible to compute the velocity.

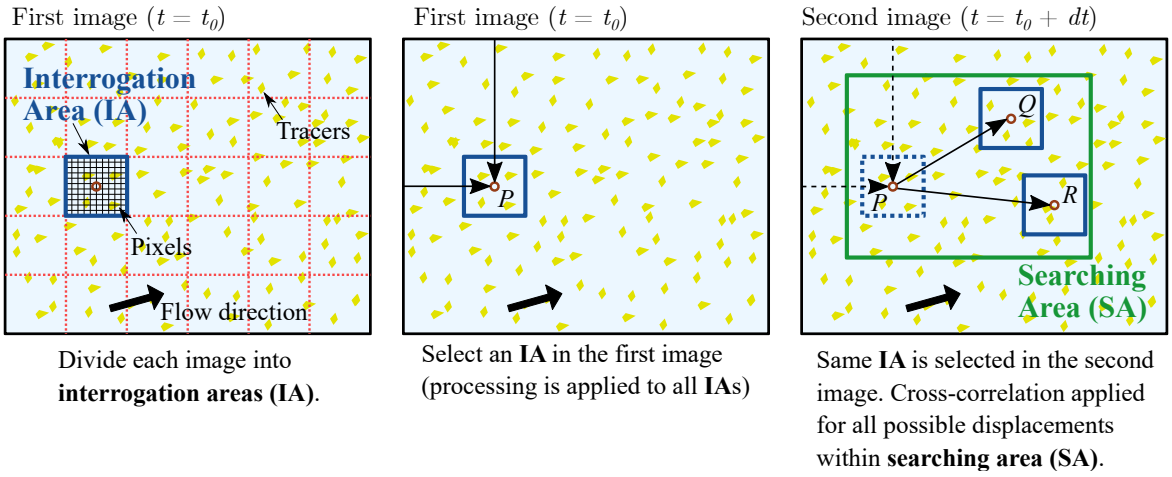

FIGURE 3.16. Conceptualization of the LSPIV image processing algorithm. Diagram replicated from Muste et al. (2008).

For this study, wood shavings with diameters ranging from 1 to 4 mm are used as free-surface tracers. This light and pale material sharply contrasts with the dark grey colour of the model bed. A video camera (Panasonic, HC-V770) was placed 2.8 m above the experimental set-up, with the optical axis perpendicular to the model bed (see Figure 3.17). The spatial resolution of the camera is 1920 px $\times$ 1080 px, with a recording rate of 25 frames per second. In addition to natural light, four led lamps with an adjustable light intensity are used along with light diffusion screens to light up the set-up. The free Fudaa-LSPIV software co-developed by EDF/INRAE (Le Coz et al., 2014) is used to process the videos and compute the time-averaged surface velocities. Due to the complexity of the flow in the study area (wide velocity range and several recirculation areas), extensive processing and post-processing work is carried out (different IA, SA and criteria for filtering out outliers, implemented according to the velocity and flow direction).

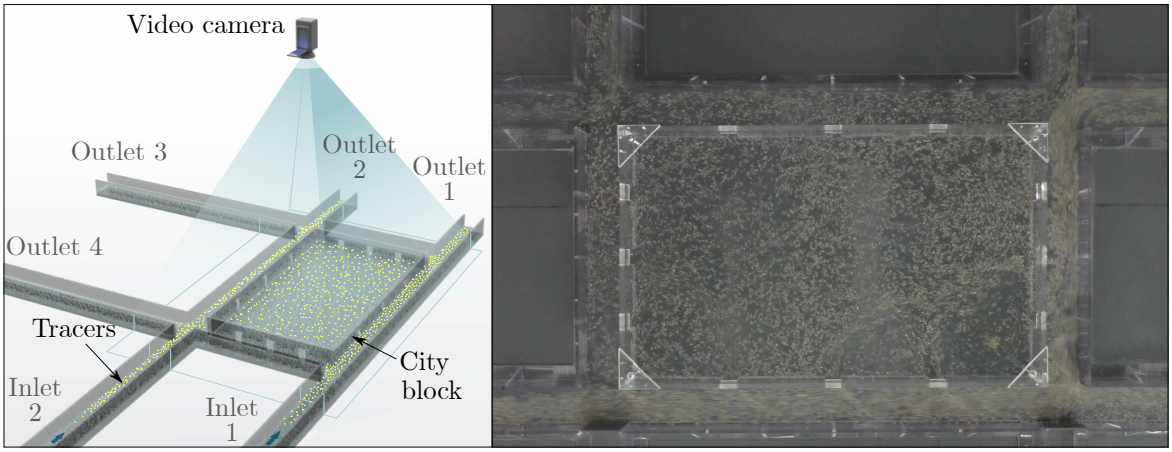

FIGURE 3.17. Left: Schematic of the set-up for the Large Scale Particle Image Velocimetry technique (LSPIV). Right: Plan view of the study area, showing the tracers on the flow surface during the implementation of the LSPIV technique.

To evaluate the appropriate video recording duration for the LSPIV technique, convergence tests are established by recording at a rate of 25 frames per second the surface velocity field during 180 s, averaging over time and for different durations (from 10 s to 180 s), the surface velocity over the entire area. Two different configurations are used for these tests, one with the porous city block with all its possible openings (three in each sidewall) and the second one without the city block, i.e. as a town square, see schematics of these configurations at the top of Figure 3.18. The first configuration is used to estimate the velocities only within the city block, the second configuration is used to estimate the velocities in the whole area (streets and the city block area). The convergence criterion is the duration for which the velocity difference for each point of the velocity field with respect to the averaged velocity of the total recording time (t = 180 s) is equal or less than 1 cm s^{-1}, for at least 80% of the total number of points in the measuring grid. The time-averaged velocity difference for each point in the velocity field is computed as follows:

$$\left|\Delta U_s(n_{(t)})\right| = \left| \frac{1}{n_{(t)}} \sum_{i=1}^{n_{(t)}} u_i - \frac{1}{n_{(t=180)}} \sum_{i=1}^{n_{(t=180)}} u_i \right| \tag{3.8}$$

The convergence is obtained earlier within the block, after 10 s (as indicated on the upper plot in Figure 3.18) than in the streets, after 60 s (lower plot in Figure 3.18). Consequently, 60 s was defined as the appropriate recording duration for time-averaged velocities estimation with the LSPIV technique. Additionally, Section A.1 of Appendix A shows time-averaged

surface velocity maps for different averaging durations, to expose a visual comparison of the velocity field over the entire domain.

During this tests, seeding the flow with tracers at single location to estimate velocities over the entire study area is found to be inappropriate. In this case, a large seeding generates clogging in small velocity areas and along the main streets, while a limited seeding does not deliver sufficient tracers in the upstream (transverse) street and within the city block. The best procedure arising is to perform various videos with different seeding locations and seeding concentrations for a given flow case (a procedure only possible under steady flow conditions). It consisted in: first, seeding the flow at the entrance of the right and left streets while recording the tracer movements in the right, left and downstream streets. Second, seeding at the entrance of the upstream street, while recording the tracers in this street. Last, seeding the flow near the block openings (on the street side), a third video is taken to record the tracer movements within the city block. Application of the LSPIV technique is then performed in each of these three areas independently, and the resulting surface velocities are finally plotted together. The agreement in velocity magnitude and velocity direction at the intersections of the three zones gives confidence in the quality of the surface velocity measurement.

Finally, to validate the surface velocity results, velocities measured by LSPIV and ADV are compared. Two types of ADV velocity data are considered here: near-surface velocities[3] and depth-averaged velocities. Within the block, the fair agreement of the LSPIV velocities with these two types of ADV velocity data proves that flow is mainly two-dimensional (see figure 3.19), which is characteristic of very shallow flows. In the streets, although velocity magnitude and recirculating flow areas are adequately captured by LSPIV, the results in some areas near the crossroads appear to be less accurate, mainly due to the presence of strong flow depth variations. In addition, the slight decrease in velocity when approaching the walls in some areas is not observed either (see figure 3.19). Thus, overall, it is noted that both flow patterns and velocity magnitudes are adequately estimated in the study area using the LSPIV technique, with excellent results being obtained within the city block. For more details on the comparison of the LSPIV and ADV measured velocities, refer to Section A.2 of Appendix A.

[3]Velocities obtained close to the free-surface, ensuring that the ADV probes which measure streamwise velocity are always within the flow.

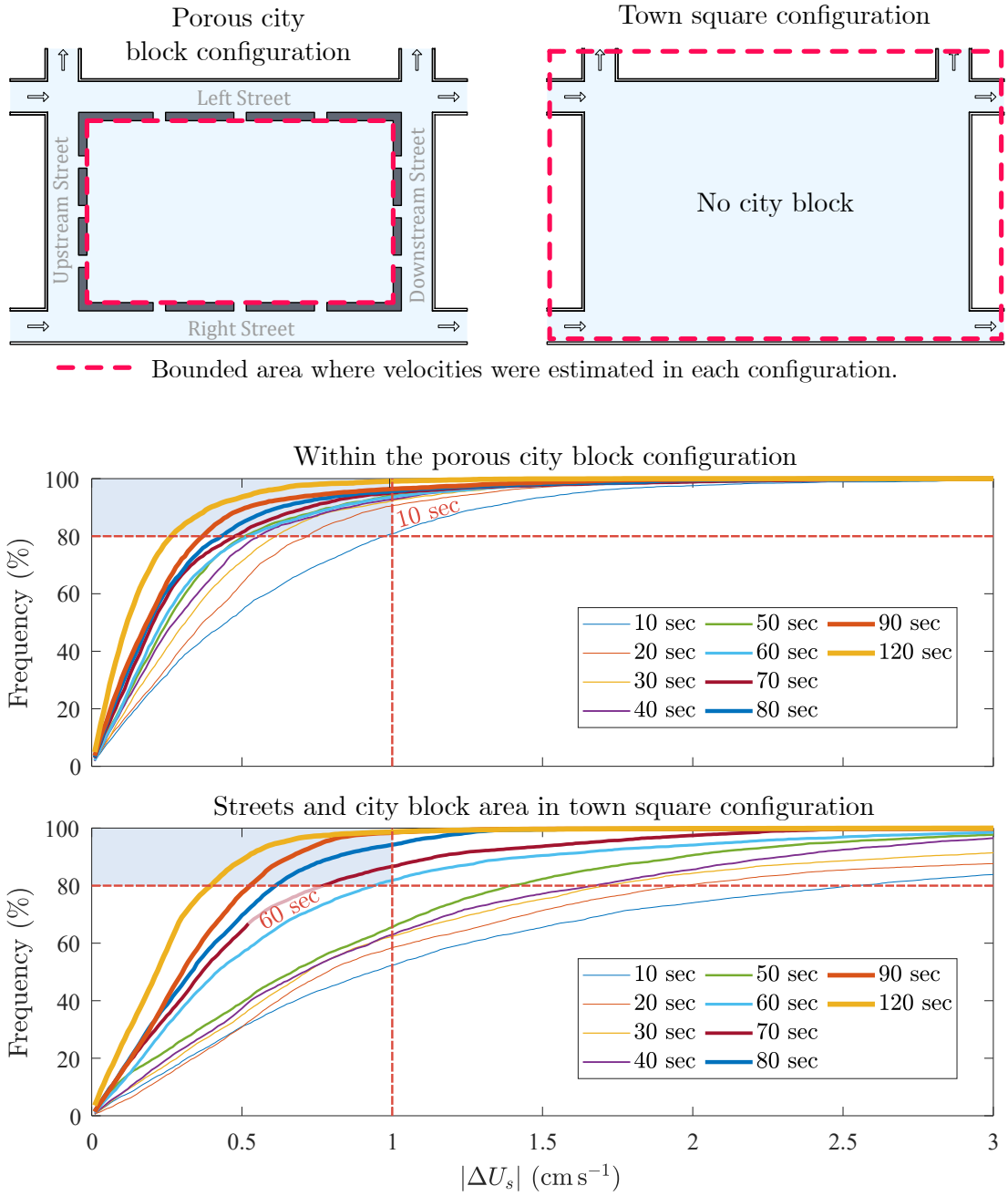

FIGURE 3.18. Time convergence of the time-averaged surface velocity difference, ΔU_s (Eq. 3.8), for various recording durations, from 10 s to 120 s. Two configurations were used: a configuration with the porous city block and all its possible openings (3 on each wall), as shown in the upper left schematic; and a second one without the city block, i.e. as a town square, as shown in the upper right schematic. Convergence is reached when $|\Delta U_s| \leq 1$ cm s^{-1} and frequency $\geq 80\%$.

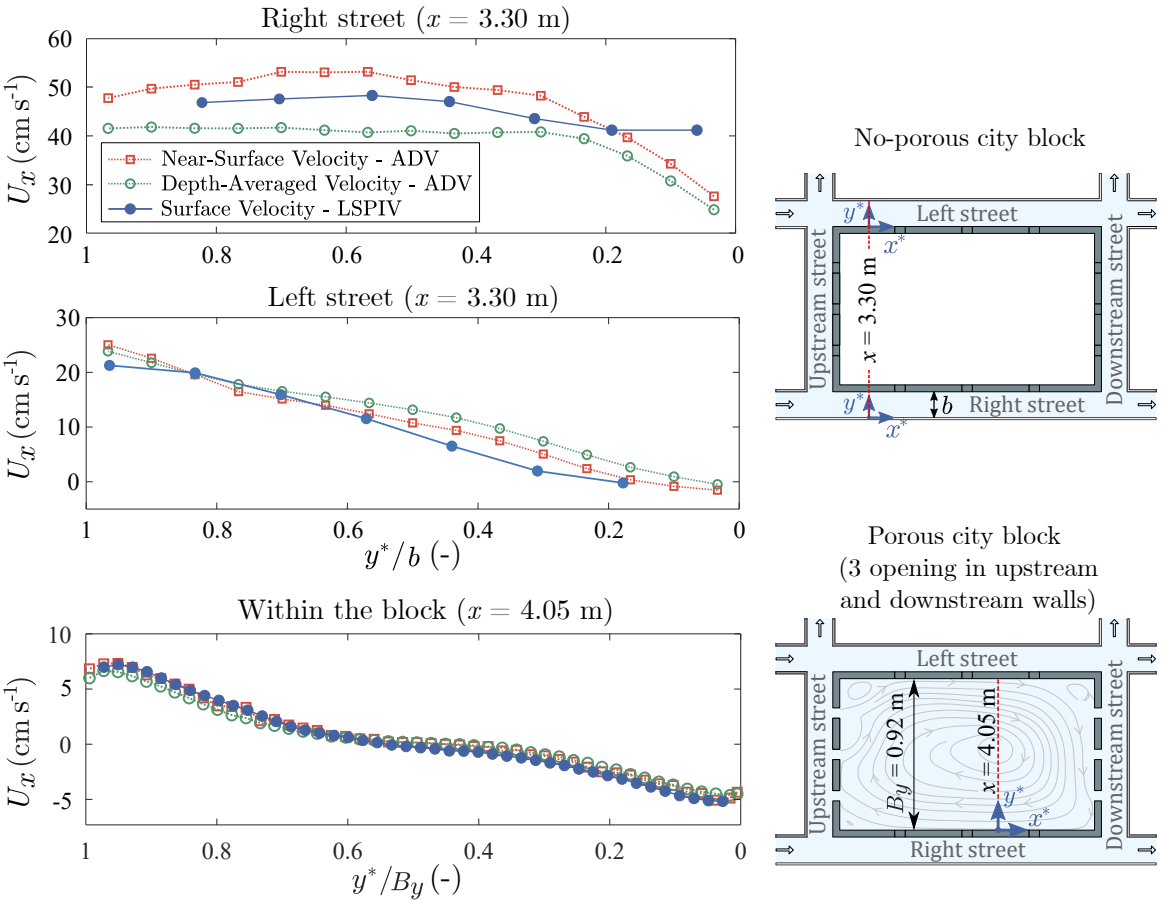

FIGURE 3.19. Comparison of horizontal profiles of time-averaged streamwise velocity measured by LSPIV and ADV, in the right and left streets for a configuration with a non-porous city block (the two upper plots) and within the city block (velocity along x-axis) for a configuration with a porous city block (plot at the bottom). For the latter configuration, the schematic of the set-up also shows the streamlines within the block, found during the tests. For each plot two ADV velocities are displayed: in green the depth-averaged velocity and in red the velocity measured close to the free-surface. Local coordinates are denoted as x^* and y^* for each cross-section as shown in each set-up schematic.

3.3.3.3 Average time-varying surface velocity (unsteady flow)

Due to the complexity encountered in setting up and running the LSPIV technique in unsteady flow in an urban model (e.g. spatial and temporal regime shifts, backwater effect due to cross roads) and the vast amount of processing and post-processing work required, 50 replicates of the event are not feasible (as done for discharges and flow depths). Therefore, to verify if a single hydrograph replicate could be representative of the velocity field, reproducibility tests are performed by replicating an inflow hydrograph 3 times and video recording each one, for its entire duration. For these tests, the experimental set-up variant 2 is used, i.e. with a single inlet and four outlets, with no weir at the outlets, see Figure

3.5. The procedure for recording the tracers on the flow surface is the same as described in the previous section. The videos are recorded with a commercial camera (Sony ZV-1[4]) at a rate of 25 frames per second. The instantaneous surface velocity is estimated for each video, at five different instants of the event. However, the instantaneous measured velocity field may contain areas with no data or incorrect data (due to clogged or missing tracers). To filter these outliers, but also to preserve the instantaneousness of the velocity data for the unsteady flows, quasi-instantaneous surface velocities are computed by averaging over 2 s the instantaneous velocities (50 consecutive instantaneous velocities), which seems a good compromise between a high enough sampling frequency and a converged estimate of average time-varying surface velocity.

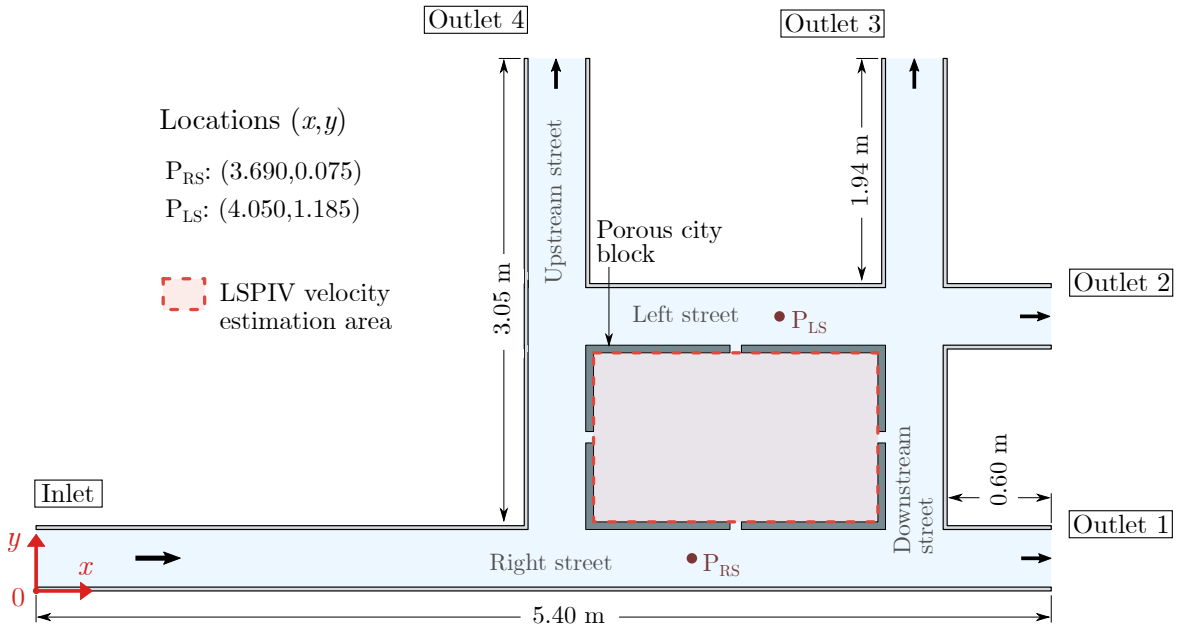

FIGURE 3.20. Location of the punctual areas in the streets and zone within the city block where the surface velocity was estimated by means of the LSPIV technique, for unsteady flow tests. The width of the streets is distorted (enlarged) in this schematic, to fit all the necessary information.

[4]The video camera differs from the one used in the steady flow tests, only because the previous one is not available for these tests. The resolution is the same and they have similar characteristics.

During preliminary tests, it was found that estimating surface velocities over the whole study area during the entire duration of a hydrograph, mainly in streets, is practically impossible. Therefore, for unsteady flows, the surface velocity is estimated only in the entire area within the block and in a punctual location on right and left streets[5], see Figure 3.20. For these reproducibility tests, in Figure 3.21, only the velocities within the block are considered: The first column shows the velocities obtained in replicate 1, the second column in replicate 2 and the third column in the replicate 3. Each line corresponds to the same instant during the course of the hydrograph: The first line of velocity maps corresponds to the instant during the hydrograph rising stage when the flow depth within the block is 50% of the maximum recorded flow depth ($0.5d_{max}$); the second line corresponds to the instant when the flow depth is the maximum (d_{max}) within the block; and the third line corresponds to the instant when the flow depth is also 50% of d_{max} within the block, but during the hydrograph falling stage. At the top of the same Figure 3.21, the inflow hydrograph is shown, as well as the stage hydrograph measured within the block, and the instant corresponding to each velocity map is indicated. In general, it can be observed that from one replicate to the other the flow patterns are very similar, as well as the magnitude of the velocities.

Although the results among the three replicates for the different instants are not perfectly identical, many similarities are observed, such as the directions of the flow through the openings, the number and size of the recirculation cells and the velocity magnitude in different areas. Therefore, surface velocities in unsteady flows are estimated based on a single inflow hydrograph replicate.

[5]The presence of an oblique hydraulic jump, which moved along the street while the discharge is changing, made the use of the LSPIV technique for velocity estimation in the upstream and downstream streets unfeasible.

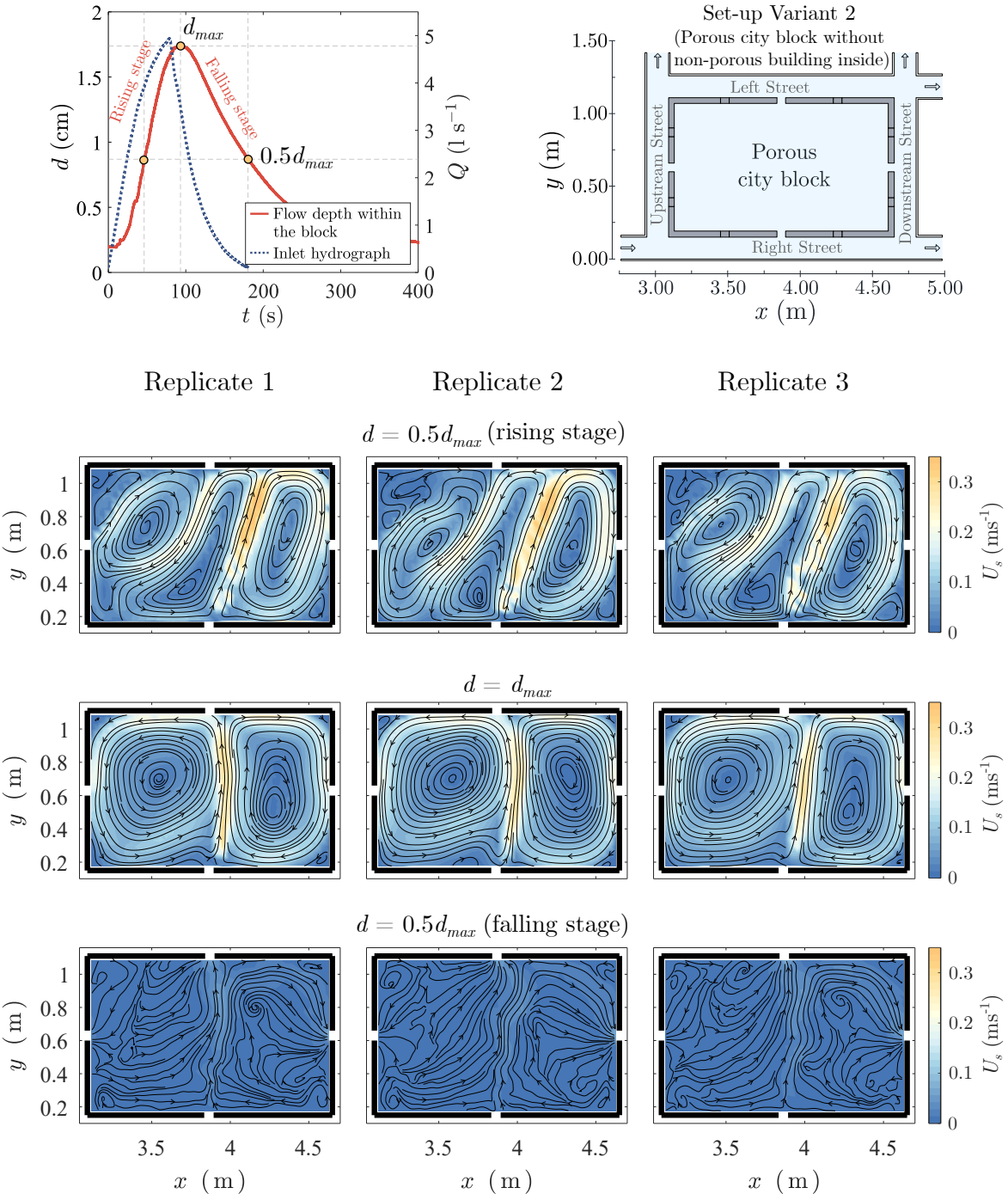

FIGURE 3.21. Average time-varying surface velocity, within the city block, for 3 replicates of the inflow hydrograph. The velocities are shown for the rising and falling stage, as well as at dmax. At the top, the inflow hydrograph is shown (blue dashed line), as well as the stage hydrograph measured within the block (red line), and the instant corresponding to each velocity map is indicated (yellow markers).

3.3.4 Velocity-Area Method for discharge estimation across a street

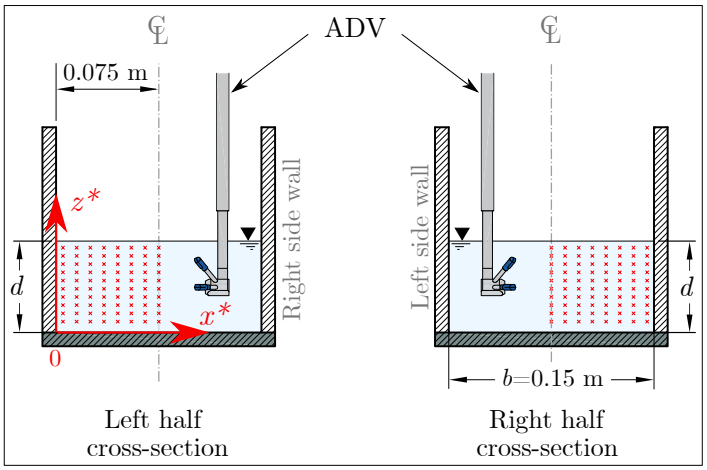

FIGURE 3.22. ADV velocity measurement grid in the street cross-section (red dots). x^* and z^* are local coordinates, which follow the direction of the global coordinates (x, y, z) and only change the position of the origin, in this case (street oriented along the y-axis) to the lower left corner of the street cross section.

While the inflow and outflow discharges are measured by the electromagnetic flowmeters, the discharges in the streets within the urban area need to be computed by integrating spatially the time-averaged streamwise velocity distribution in the street cross-section. To do so, for steady flows, the velocity is measured within the water column at 9 to 10 depths (depending on flow depth) and at 15 transverse positions across the wetted area in a street. Due to the size of the ADV probe in relation to the street width, velocity measurements are carried out in two stages, first measuring one half of the cross section and then measuring the other half, see Figure 3.22. The only common punctual velocity measurements between the two measurement stages are the vertical dots on the street's centre line, which serves as a cross-check between the results of both stages.

The discharge in a street reach is then computed by integrating the ADV velocity data across the street as follows:

$$Q_{st} = \int_0^b \int_0^d U_x \, \mathrm{d}z^* \, \mathrm{d}y^*, \quad \text{for } x\text{-axis-oriented streets} \tag{3.9}$$

and

$$Q_{st} = \int_0^b \int_0^d U_y \, \mathrm{d}z^* \, \mathrm{d}x^*, \quad \text{for } y\text{-axis-oriented streets} \tag{3.10}$$

where Q_{st} is the discharge in the street reach, U_x and U_y are the local time-averaged velocity components along the local x^*-axis and y^*-axis, respectively.

While the velocity field is measured as close as possible from the bed, side walls and

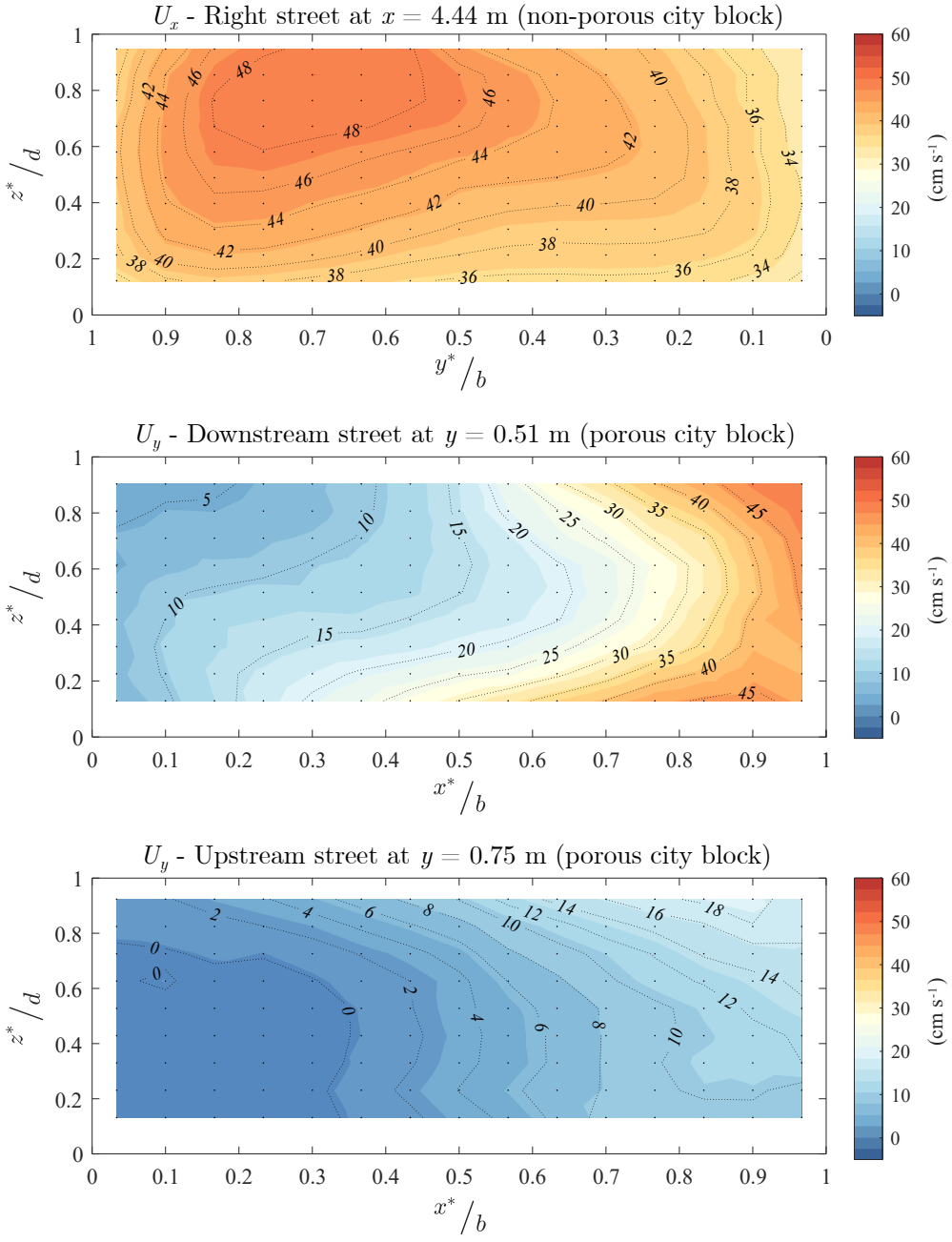

FIGURE 3.23. Cross-sectional distribution of the time-averaged streamwise velocity, in different streets and different city block configurations. In areas close to the boundaries there is no velocity data measured with the ADV. The z*-axis (vertical) and x*-axis and y*-axis (transverse), have been normalised by the local flow depth, d, and the street width, b, respectively.

free-surface, areas along all four boundaries of a street cross-section remain blind with no available velocity measurement, see Figure 3.23. To estimate the discharge using Eqs. 3.9 and 3.10, an extrapolation of the measured velocity field is thus required in these areas. Due to the complex and varied flow patterns measured in the streets, distinct assumptions are evaluated for this extrapolation. Three conditions are proposed: (*i*) the *no-slip boundary condition* assumes that the velocity of the fluid layer in direct contact with the boundary is equal to the boundary velocity (Rapp, 2017), in this case $U = 0$ (see left plot in Figure 3.24); (*ii*) the *slip boundary condition* assumes a relative movement between the fluid layer and the boundary, in this case it is assumed that the velocity at the boundary is equal to the nearest velocity fluid (see right plot in Figure 3.24); and (*iii*) and *average condition* (50% - 50%) between the no-slip and slip boundary conditions.

Using these three conditions at the bed and walls, and the slip boundary condition at the free-surface, tests are conducted (on a single straight street, on streets surrounding a non-porous city block and on streets surrounding a porous city block), to compare the discharges[6] estimated by Eqs. 3.9 and 3.10 with the discharges measured by the electromagnetic flowmeters, located upstream of the inlet tanks and downstream of the outlet tanks. It is found that for all of these discharges, applying the average of the no-slip and slip boundary conditions on the bed and walls yields the smallest error, 1.5% on average (for more details see Appendix B). Hence, the *slip condition* at the free-surface and the *average* between the slip and non-slip conditions for the other boundaries are applied to all cross-sectional velocity distributions to compute the discharges.

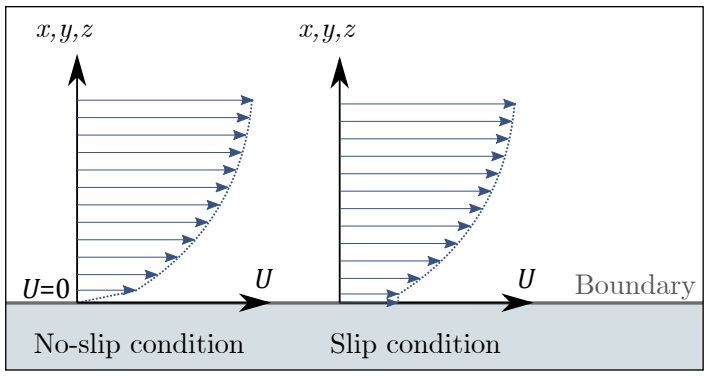

FIGURE 3.24. No-slip and slip boundary conditions. In no-slip noundary conditions, the flow velocity at the bundary is zero, whereas in slip boundary conditions there is relative movement between the boundary and the flow.

Finally, it should be reminded that the estimate of the discharge at a given cross-section in a street network remains a challenging task, even though innovative techniques tend to arise

[6]Discharges through street cross-sections at different locations. For these tests, conditions similar to those of the definitive tests are established to obtain similar cross-sectional velocity distributions.

(Finaud-Guyot et al., 2019). Therefore, although the method requires assumptions to cover the blind zones near the boundaries (bed, walls and free surface), as well as the inconvenience of using an intrusive instrument (ADV) in a narrow cross-section (see Appendix C for more on the effect of ADV intrusion on the velocity distribution), the results seem to be fairly reliable.

3.4 Distorted-scale model

For this study, it is considered the use of a distorted scale model, i.e. with the horizontal scale ratio, λ_{xy}, differing from the vertical scale ratio, λ_z.

$$\lambda_{xy} = \frac{L_{xy_P}}{L_{xy_M}} \tag{3.11}$$

$$\lambda_z = \frac{L_{z_P}}{L_{z_M}} \tag{3.12}$$

where L_{xy} corresponds to the dimensions in the horizontal plane (xy) and L_z to the dimensions in the vertical direction (z). Subscripts M and P denote the scale model and the real-world prototype, respectively. Chanson (2004) listed the advantages of a distorted model in shallow flows: i) greater flow depths, allowing greater measurements accuracy, and ii) larger Reynolds number, improving dynamic similarity with the prototype. Still some disadvantages remain due to the distorting effects, related to three-dimensional flow processes associated with the aspect ratio (d/b), or the impact of the roughness coefficient (Li et al., 2019).

Since the effects of the gravity force are predominant in free surface flows, the Froude similitude is used to up-scale the values from the experimental model to the real-world prototype, $Fr_M = Fr_P$. It implies the following ratios for flow depth, velocity, discharge and time:

$$\frac{d_P}{d_M} = \lambda_z \tag{3.13}$$

$$\frac{U_P}{U_M} = \lambda_z^{\frac{1}{2}} \tag{3.14}$$

$$\frac{Q_P}{Q_M} = \lambda_z^{\frac{3}{2}} \lambda_{xy} \tag{3.15}$$

$$\frac{t_P}{t_M} = \lambda_z^{\frac{-1}{2}} \lambda_{xy} \tag{3.16}$$

3.5 Flood hazard criterion for pedestrians

The different results obtained with the various steady and unsteady flow tests for the three key issues are used to estimate the flood hazard to pedestrians. For each flow case, the local measured flow depth and depth-averaged velocity together with instability threshold curves for people enable to assess the hazard level.

As shown in Section 2.3.3, over the past 40 years, several studies have been conducted to estimate the human instability threshold in flood flows, and thus define flood hazard criteria. The best known criterion, proposed by Cox et al. (2010), defines four levels of hazard, based on the experimental results on human instability available at that time. However, additional studies on human instability carried out in the last years (e.g. Russo et al., 2013a; Xia et al., 2014a; Martínez-Gomariz et al., 2016), and experiences acquired and observations made on a real urban flood event by Chanson et al. (2014), suggested that for urban areas this instability begins at lower flow depths and velocities than those reported in previous studies.

Therefore, following a procedure similar to that performed by Cox et al. (2010), an update criterion of hazard to pedestrian during flooding in urban areas is proposed herein. The experimental data sets on human instability in flood flows considered are from Abt et al. (1989), Takahashi et al. (1992), Karvonen et al. (2000), Jonkman and Penning-Rowsell (2008), Russo et al. (2013a), Xia et al. (2014a), Martínez-Gomariz et al. (2016) and Milanesi et al. (2016). The characteristics of the tests and the methodology used in each of these studies where described in Chapter 2 (Table 2.3). The urban flood instability data reported by Chanson et al. (2014) are also considered. The instability results obtained for the human-sized concrete monolith (from Abt et al., 1989) and for the small scale model of a real-shape human body (from Xia et al., 2014a), which are a conservative approaches, are considered the threshold limit for people with reduced mobility (e.g., elderly or disabled people). In contrast, the instability results obtained for rescue workers (from Karvonen et al., 2000) and professional stuntman (from Jonkman and Penning-Rowsell, 2008) are considered to account for sporty people with strong physical skills. Recommendations of these same studies and

guidelines from the study on safety evacuation from underground spaces in a flooding situation, performed by Ishigaki et al. (2009) are considered as well, see safety evacuation curves in Figure 3.25.

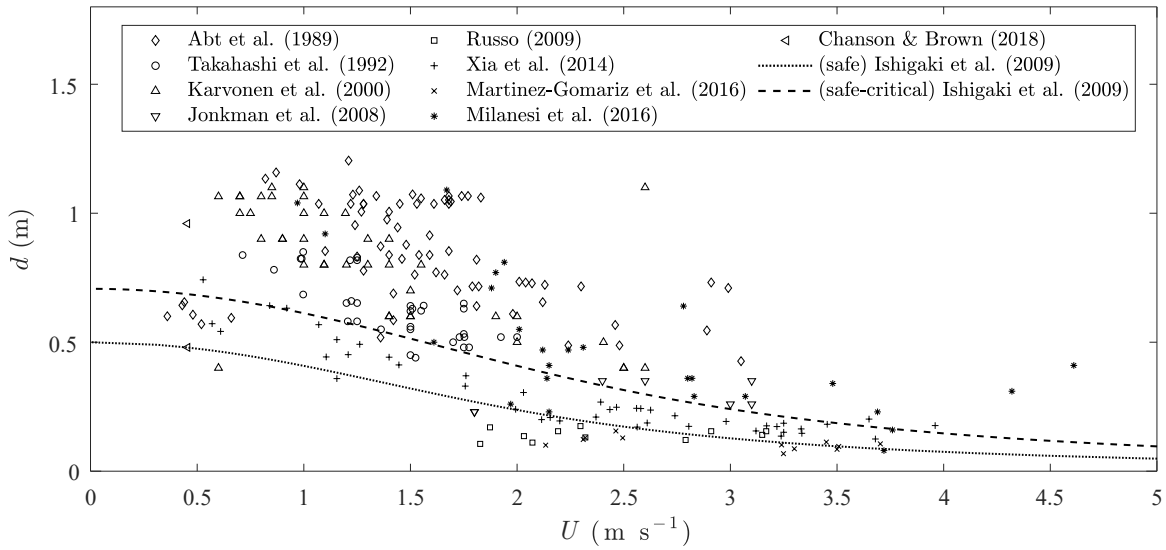

FIGURE 3.25. Human instability events in flood flows from different research works, and curves for safety evacuation during a flooding situation proposed by Ishigaki et al. (2009).

When plotting all the instability points (from the above mentioned studies) on a single graph, a significant scatter is observed (Figure 3.25). However, this could be considered normal, as the instability threshold can be influenced by many parameters defining human beings (e.g. the weight, height, age, strength, skills, psychological characteristics), as well as the test conditions (e.g. experimental set-up, protective equipment, clothing of subjects) and methodology (e.g. subject standing or walking, criteria for instability). Therefore, this may well represent the range of possibilities that exist when a human being is exposed to a flood event. All these points are used to propose new thresholds defining the different hazard levels. These thresholds rely on the product number approach, PN (Eq. 2.3). Three product number thresholds are proposed:

- $PN = 0.3\ \mathrm{m^2\,s^{-1}}$. Defines the lower limit of people's stability according to Xia et al. (2014a) and Abt et al. (1989) (results obtained using the concrete monolith), up to $d = 0.7$ m, based on the curve for critical self-evacuation proposed by Ishigaki et al. (2009) and up to $U = 2.0\ \mathrm{m\,s^{-1}}$, based on the limit of people's stability in small flow depths found by Russo et al. (2013a) and Martínez-Gomariz et al. (2016).

- $PN = 0.7$ m^2 s^{-1}. It is the upper limit of Xia et al. (2014a) results and lower limit of those obtained by Abt et al. (1989), Takahashi et al. (1992) and Karvonen et al. (2000), up to $d = 0.95$ m and up to $U = 2.70$ m s^{-1}, which represents approximately the mid-point in the range of velocities measured for people' instability in small flow depths by Russo et al. (2013a) and Martínez-Gomariz et al. (2016).

- $PN = 1.0$ m^2 s^{-1}. Corresponds to approximately the 50% limit of instability cases of the total data set used herein, and up to $d = 1.2$ m, proposed by Cox et al. (2010), being the largest flow depth tested in the available data series, and up to $U = 3.5$ m s^{-1}, which is approximately the upper limit of people's stability in shallow flows according to Russo et al. (2013a) and Martínez-Gomariz et al. (2016), i.e. above this limit almost all pedestrians exhibit instability.

All these threshold curves are shown in the flood hazard diagram for pedestrians in Figure 3.26, and they define four flood hazard levels, which are as follows:

- *Low*, very few pedestrians exhibit instability (up to 2% of the total data set).

- *Moderate*, some pedestrians exhibit instability (up to 20% of the total data set).

- *Significant*, many pedestrians exhibit instability (up to 50% of the total data set).

- *High*, most pedestrians exhibit instability (above 50% of total data set).

The information from the different data series on human instability during a flood is also shown in the diagram.

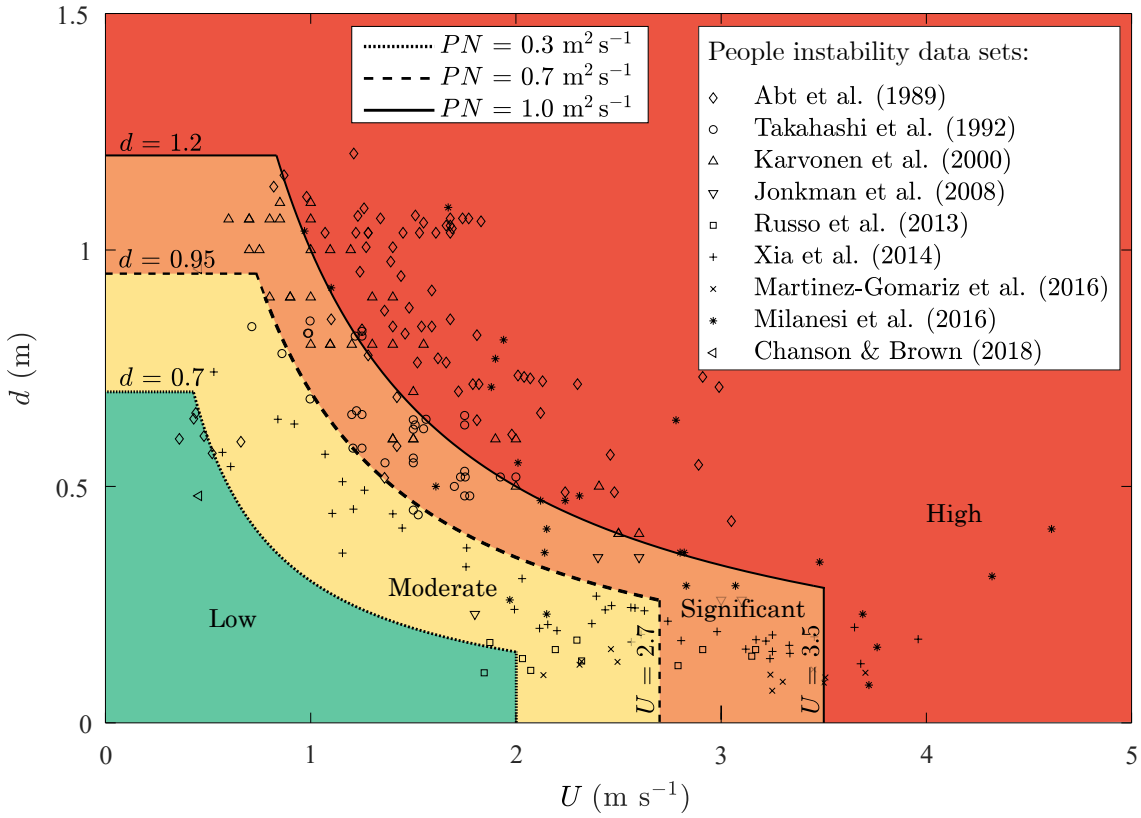

FIGURE 3.26. Proposed diagram for flood hazard to pedestrians, defining four levels of hazard. Based on available experimental data and field observations on people instability, and recommended guidelines for the safety of people during floods. Published in Mejía-Morales et al. (2021).

3.6 Conclusions

Different methodologies were developed in this thesis work in order to make accurate measurements and thus obtain reliable data.

For the three main parameters measured in this thesis work, flow depth, velocity and discharge, various methodologies were developed in order to obtain reliable results. In addition, because the tests are performed under steady and unsteady flow conditions, it was necessary to develop different methodologies for the same parameter. Different tests were also carried out on each measuring instrument and the following results were found:

- Electromagnetic flowmeters in the experimental set-up perform fairly reliable discharge measurements, even with small discharge values. However, a drawback of this instrument is that the minimum value it is able to measure is 0.13 l s^{-1}, which could represent a very large value considering that relatively low discharges are used in this set-up.

- The ultrasonic sensor (US), used to compute the flow depths, is suitable for the tests

carried out in this research work. Although there are fluctuations of the flow depth in some areas, mainly near the crossroads, it was observed that with sufficient acquisition duration and by filtering out outliers, reliable results can be obtained in these areas.

- The ADV proved to be useful for the purposes of this research. Despite the narrow street size and the effects that this intrusive instrument has on the flow under these conditions, reliable results were obtained for the estimation of street discharge. A drawback in its application in this set-up is that to measure velocities along a complete street cross-section, it needs to be rotated. In addition, its orientation must be different when measuring velocities in right and left streets than in upstream and downstream streets. Therefore, a lot of work is required to adjust its alignment with respect to the flow during the measurement process.

- The LSPIV technique has been successfully tested under different flow conditions. Within the city block, remarkable results were obtained, and in the streets, although some differences were observed compared to ADV velocity measurements, they seem to be fairly reliable. A drawback of this technique, mainly due to the characteristics of the experimental set-up (e.g., various flow directions, fluctuations in the water free-surface, a wide range of velocity magnitudes, etc.), is that a lot of processing and post-processing work is required to obtain velocities over the whole study area.

The use of a distorted scale model was proposed, which has helped to have sufficiently large flow depths in the set-up to carry out the different measurements required. The upscaled results are used to obtain the flood hazard for pedestrians, and for this a new criterion of flood hazard for pedestrians has been proposed. New findings on human instability during flooding and recommendations on safe evacuations during urban flooding have been used in the development of this new criterion.

CHAPTER 4

CITY BLOCK CONVEYANCE POROSITY

Vehicle and pedestrian access facilities that are systematically located in city block walls are considered potential access zones for flood flows. This property to convey the flow through the block walls is here referred to as *conveyance porosity*, denoted as ψ. In the experiments dedicated to studying the conveyance porosity of the city block, these access zones are represented by rectangular openings along a city block walls. Two characteristics of ψ are then studied, its magnitude (key issue 1) and its distribution (key issue 2) along the city block.

The following sections describe, for both key issues, the flow conditions for the experiments and the boundary conditions, the experimental cases and the results obtained for flow depths, velocities, discharge in street and outflow discharges, as well as on the flood hazard to pedestrians.

4.1 Flow conditions

The experiments dedicated to study the influence of the conveyance porosity of the city block, ψ, are conducted in the experimental set-up *variant 1* (Figure 3.4), under steady flow conditions and subcritical regime. The bed slopes and the hydraulic boundary conditions (i.e., inflow discharges and weir height at each outlet) for this experiments are shown in Table

4.1.

As pointed out in Section 3.4, the scale ratio between the scale model (experimental set-up) and the real-world prototype in the horizontal plane, λ_{xy}, differs from the vertical scale ratio, λ_z. In these experiments, λ_{xy} is equal to 50 and λ_z is equal to 10. The scale model then represents, in the real-world, a 78.0 m $\times$ 48.0 m city block with 3 m wide open gates and 7.5 m wide streets. This difference in scale ratios leads to a distorted-scale model with a distortion ratio $\lambda_{xy}/\lambda_z = 5$.

TABLE 4.1. Hydraulic boundary conditions for the study of the conveyance porosity, ψ.

Inlet discharge ($\mathrm{l\,s^{-1}}$)		Weir height (cm)				Bed slope (%)	
$Q_{in,1}$	$Q_{in,2}$	w_1	w_2	w_3	w_4	$S_{0,x}$	$S_{0,y}$
4.5	2.0	4.0	3.0	3.0	3.0	0.12	0.0

4.2 Conveyance porosity magnitude (key issue 1)

4.2.1 Introduction

As shown in Chapter 2, most studies on urban flooding consider, for the sake of simplicity, that city blocks are non-porous elements. It is assumed that the discharge in the streets is much greater than the discharge that could be conveyed into the city blocks and the latter is then neglected. Therefore, some questions are addressed here:

1. Is it justified to neglect the flow exchanges between streets and city blocks when simulating an urban flood?
2. How ψ modifies the flood flow features in the street?
3. How ψ modifies the flood flow features within the city block?
4. If ψ increases, do the effects on the flow flood features also increase?

The study of the conveyance porosity magnitude in the city block then requires that the openings along the block walls be modified as required. A porous block with three openings in each wall (i.e. twelve in total) is available for this study (Figure 3.3). To modify the magnitude of the conveyance porosity, the openings along the block walls can be closed with

transparent plastic plates (same material as the porous block) and removed as necessary, according to the required ψ value for each case.

4.2.2 Experimental cases

As described in expression 1.1, the conveyance porosity, ψ, is a characteristic defined for each wall. The city block (with four walls) thus comprises four ψ values. The conveyance porosity for each city block wall is defined as follows:

$$\psi = \frac{N \cdot L_{op}}{L_{B,i}}; \quad i = \{x, y\} \tag{4.1}$$

where N is the number of openings along the block wall, L_{op} is the length of the opening and $L_{B,i}$ is the total length of the wall, oriented in direction i (see Figure 3.4.A). The rectangular openings are sufficiently high to ensure free-surface flow, i.e., they are never submerged and thus ψ is not depth-dependent.

Eight cases with different conveyance porosities are considered, all of them with a symmetrical conveyance porosity in facing walls, i.e., the same value along the upstream and downstream walls, and the same along the right and left walls. Each case (C) is labelled as follows:

Conveyance porosity (in %) for upstream and downstream walls

$$\overbrace{\text{C}}\text{XX-}\underbrace{\text{XX}}$$

Conveyance porosity (in %) for right and left walls

TABLE 4.2. Values of conveyance porosity, ψ, (Eq. 4.1) and number of openings, N, along each wall, for the eight flow cases corresponding to *key issue 1.*

Case	Upstream & Downstream walls		Right & Left walls	
	N	ψ (%)	N	ψ (%)
C00-00	0	0	0	0
C100-100	-	100	-	100
C00-04	0	0	1	4
C00-12	0	0	3	12
C06-00	1	6	0	0
C19-00	3	19	0	0
C06-04	1	6	1	4
C19-12	3	19	3	12

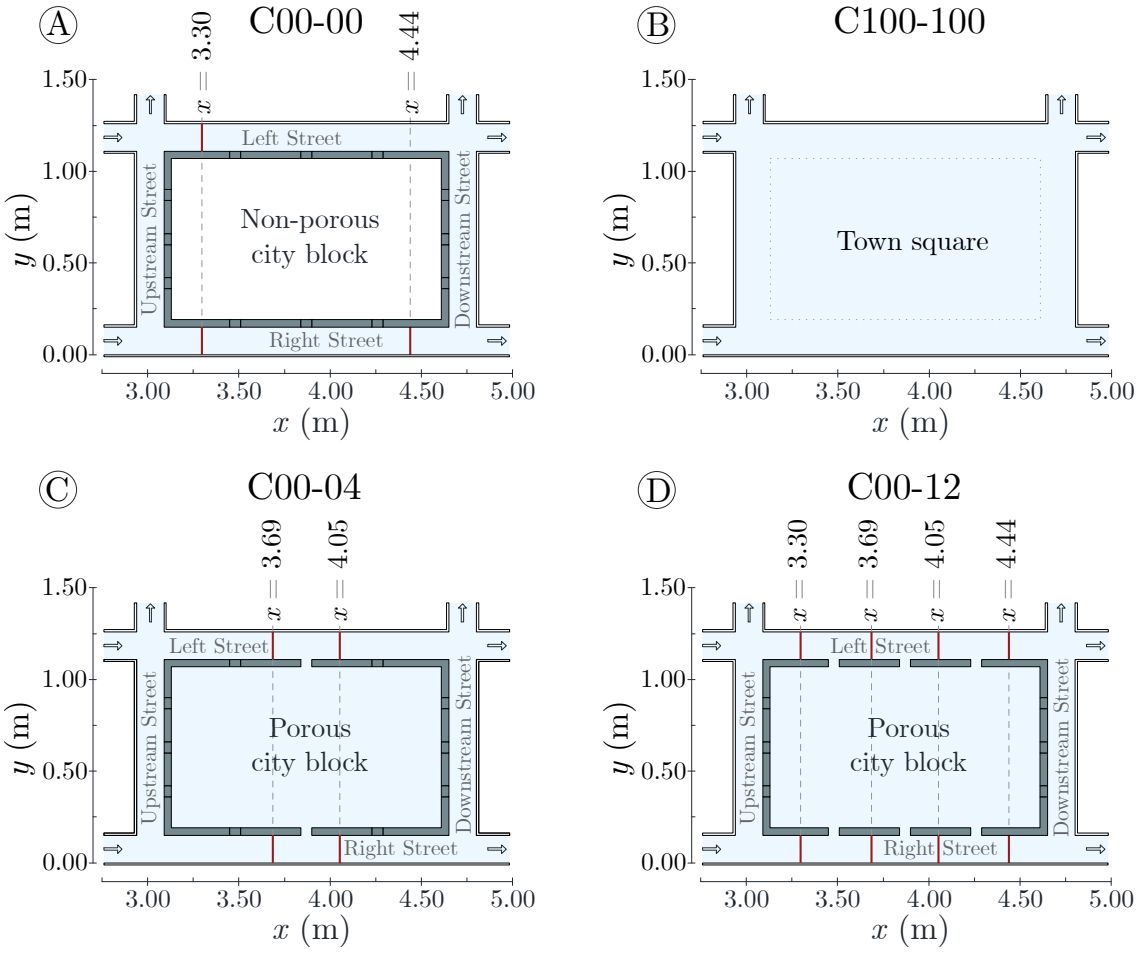

FIGURE 4.1. Top view schematics of the experimental cases corresponding to *key issue 1*. Red lines across the streets show the cross-section locations where discharges are estimated by the Velocity-Area method

.

The different experimental cases corresponding to key issue 1 and their conveyance porosity values are detailed in table 4.2. A reference flow case is considered, C00-00, which comprises a non-porous city block, i.e., $\psi = 0$ in all walls (Figure 4.1, A), as mostly considered by previous works in the literature. An extreme opposite case is considered, C100-100, where ψ is equal to 100% in all block walls, hence, without the city block, which represents an urban configuration of a town square (Figure 4.1, B). In between these two cases, a small ψ (a single opening along a block wall) and a large ψ (three openings along a block wall) are both studied with six cases featuring the same conveyance porosity along face-to-face block walls. Along the block walls oriented in the x-direction, C00-04 and 00-12 (Figure 4.1, sketches C and D), oriented in the y-direction, C06-00 and C19-00 (Figure 4.1, sketches E and F), and

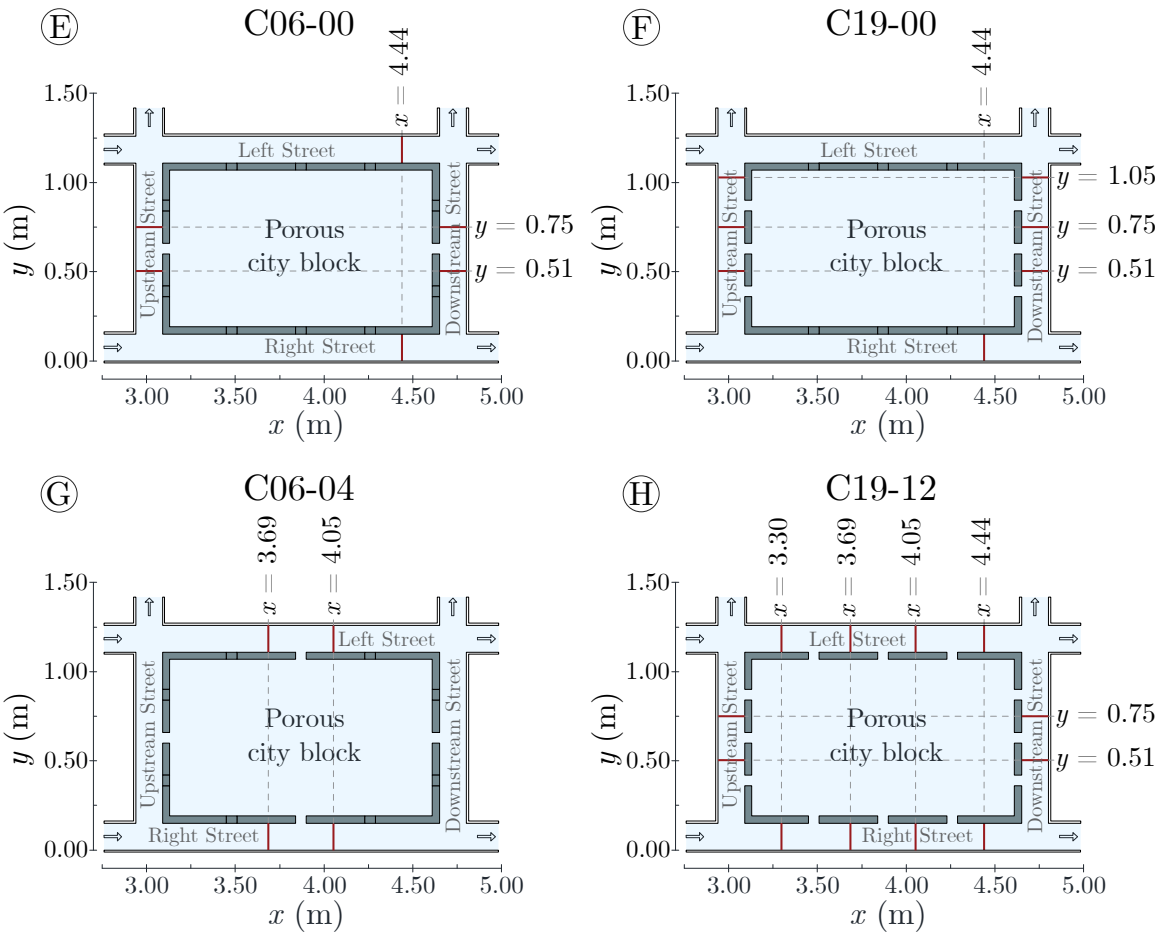

FIGURE 4.1. (Continued).

finally along both directions, C06-04 and C19-12 (Figure 4.1, sketches G and H). Therefore, the conveyance porosity considered in the city block for this six cases is anisotropic, since ψ is different in the x-axis and the y-axis directions.

4.2.3 Measured flow features

4.2.3.1 Flow depths

The spatial distribution of flow depth, d, in the streets and city block for all cases is shown in Figure 4.2. Putting aside the case C100-100, flow depths range from 5 cm to 7.5 cm (0.50 m - 0.75 m at the prototype scale) for all flow cases. The largest flow depths are observed in the right street (Fr $\approx$ 0.55 and Re $\approx$ 60000), due to both the high inflow discharge in this street and the backwater effect due to the 4 cm weir crest height located at the outlet of this street. Inside the city block, as the free-surface is almost horizontal, the flow depth slightly increases along the x-axis due to the set longitudinal bed slope (Figures 4.2 and 4.3) .

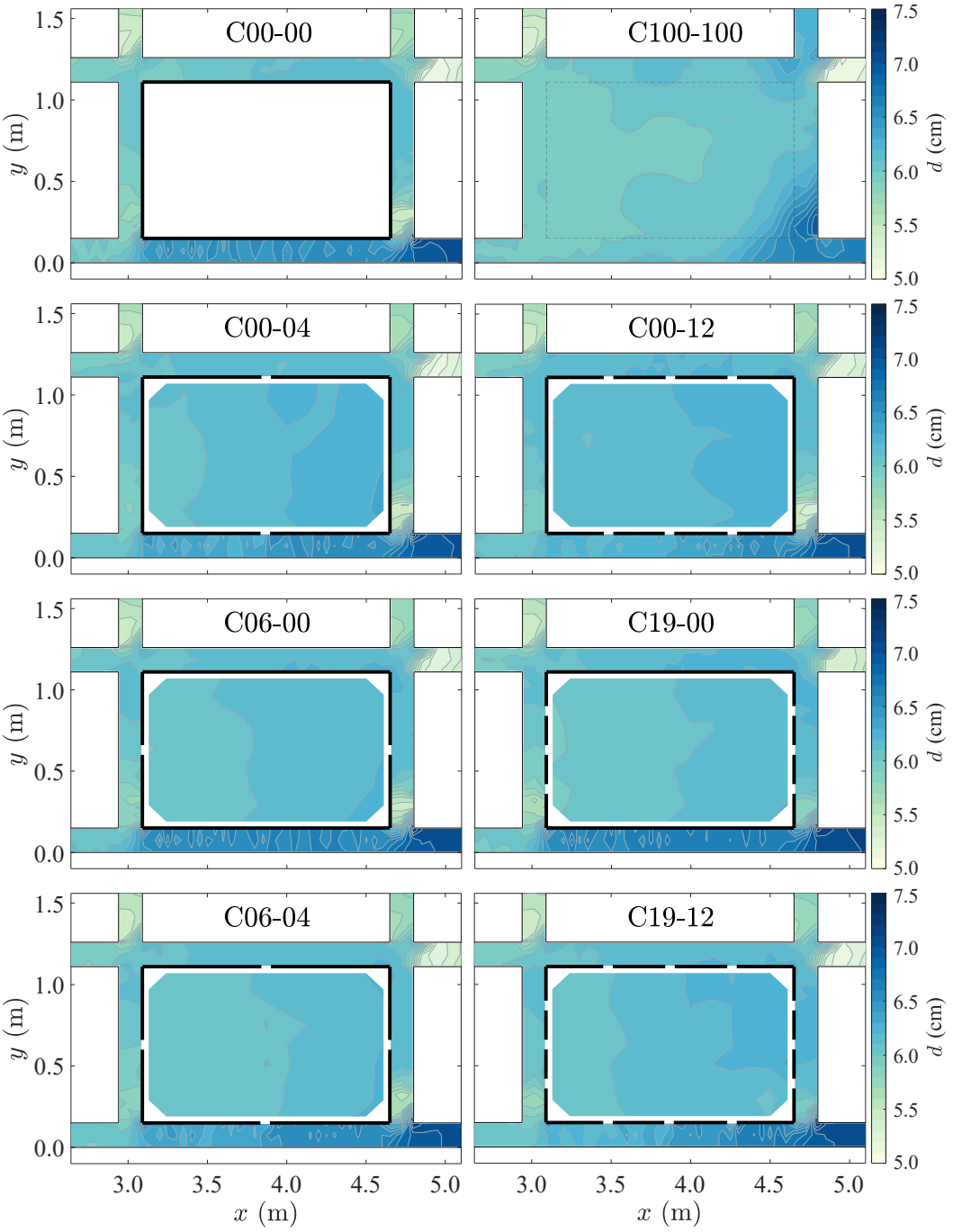

FIGURE 4.2. Flow depth, d (scale model), measured in the streets and within the city block for all flow cases corresponding to *key issue 1*. Deep blue indicates the greater flow depths and light colour indicates the shallower flow depths.

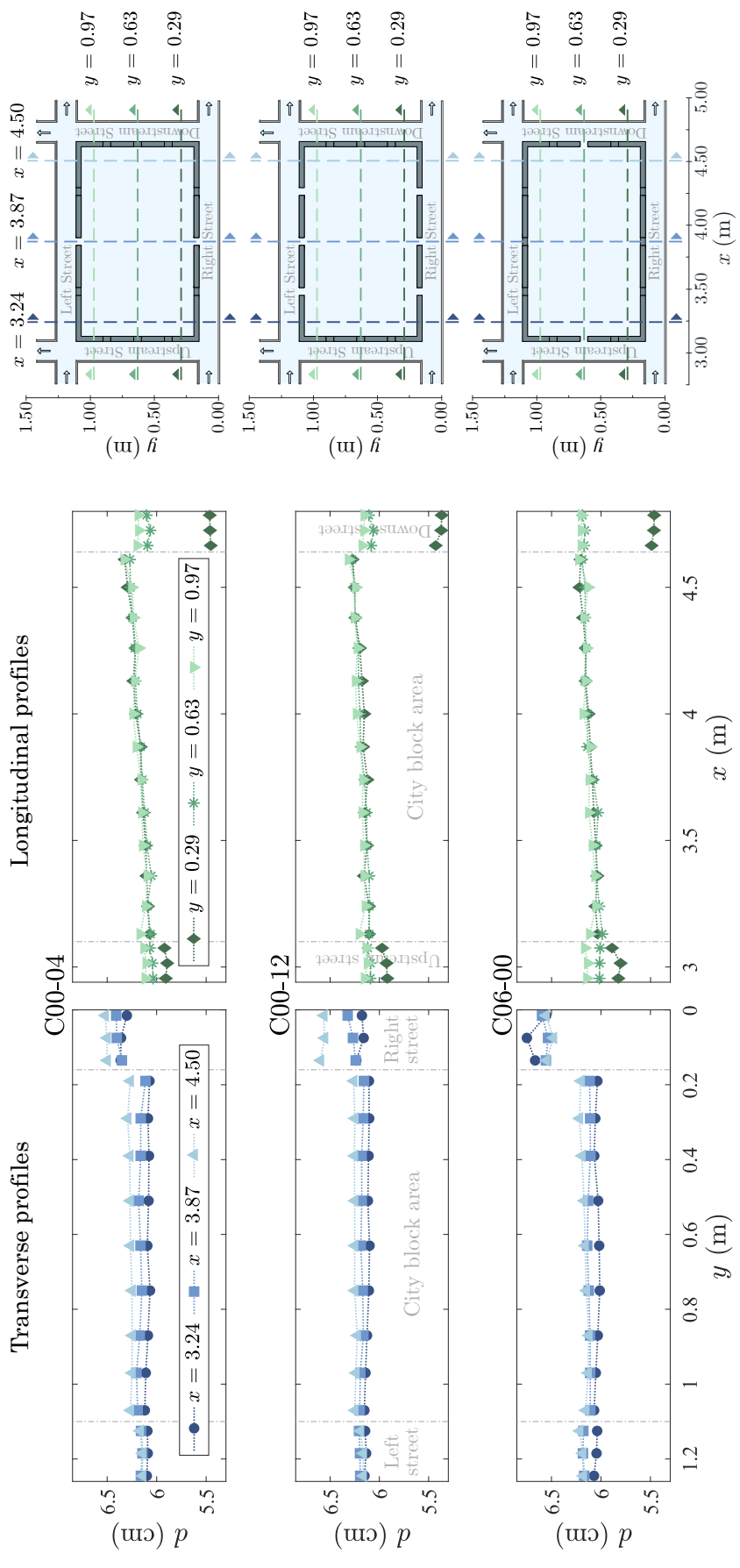

FIGURE 4.3. Transverse (blue tones) and longitudinal (green tones) measured flow depth profiles in the streets and within the city block, for cases corresponding to *key issue 1*.

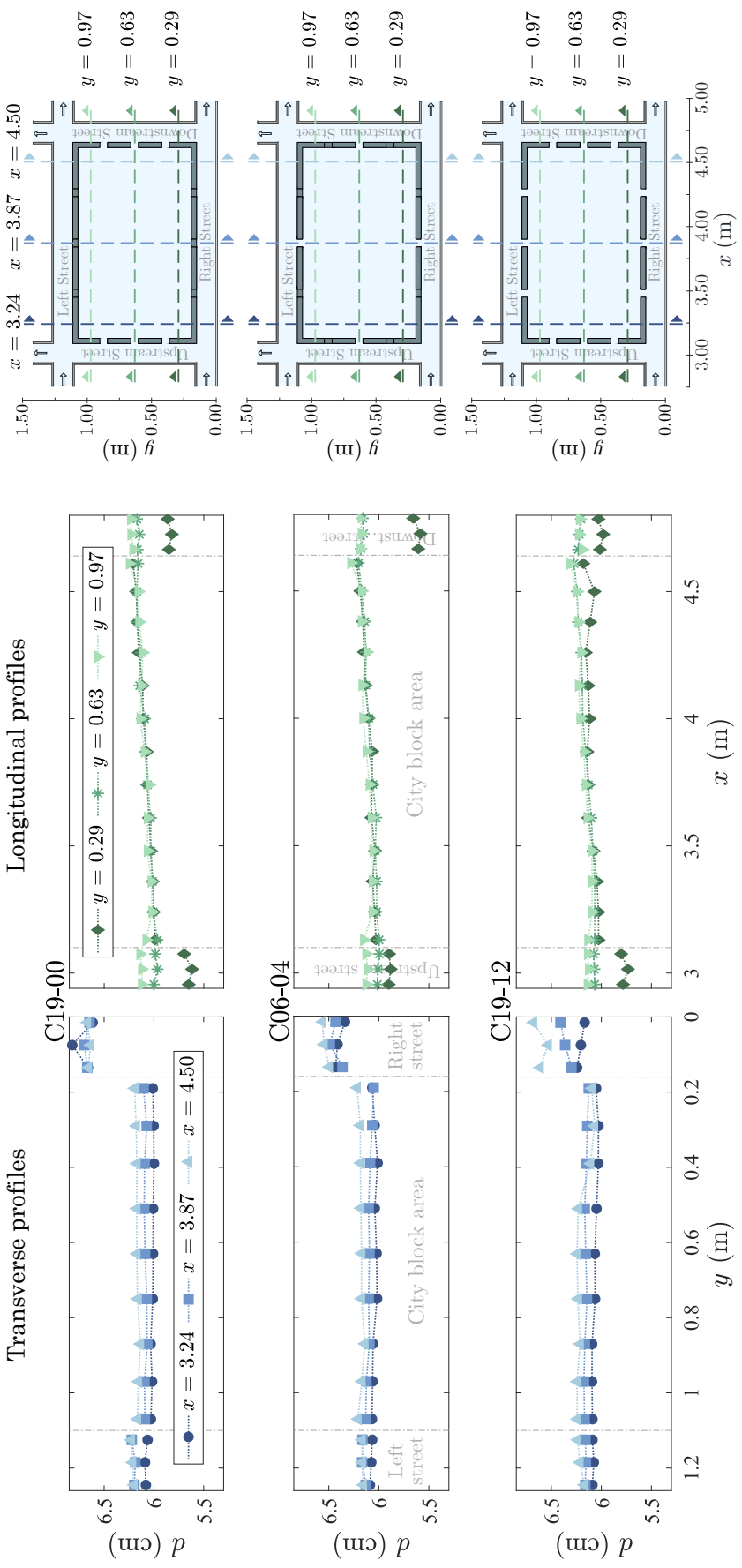

FIGURE 4.3. (Continued).

Interestingly, flow depths within the city block can differ from the flow depths in the adjacent streets. In the right street, the flow depth is higher than in the block, by up to 10% at $x = 3.24$ m for cases with a conveyance porosity along the upstream and downstream block walls only, i.e. cases C06-00 and C19-00 (Figure 4.3). In contrast, the flow depth can be smaller in the downstream street than in the block, e.g. by 14% at $y = 0.29$ m for cases with a conveyance porosity along the right and left block walls only (C00-04 and C00-12).

Figure 4.4 shows the spatial distribution of the relative difference in flow depth, Δd, for each case with respect to the reference case (C00-00), defined as:

$$\Delta d = \frac{d - d_{ref}}{d_{ref}} \times 100 \tag{4.2}$$

where d_{ref} refers to the flow depth of the reference case, C00-00. In the streets surrounding the city block, the relative difference in flow depth, Δd, can reach up to -7% in the right street and 12.5% in the downstream street for case C19-12 (case with the largest conveyance porosity). In contrast, when moving away from the block, flow depths in the street reaches not adjacent to the block (for $x < 2.94$ m, $x > 4.80$ m and $y > 1.26$ m) do not show significant variations with respect to the reference case, with a maximum of 3.5 % (case C19-00).

4.2.3.2 Discharges and bulk-velocity in the streets

Discharges in streets and through every opening in the city block are computed with the Velocity-Area method (Section 3.3.4) and the principle of mass conservation at each cross-road by considering the inflow and outflow discharges measurements, performed by the electromagnetic flowmeters. Figure 4.5 shows an overview of the discharges in the streets and the city block for all cases. All the discharge values are shown as a percentage of the total inlet discharge ($Q_{in,T} = 6.5\,\mathrm{l\,s^{-1}}$). The inlet and outlet discharges (monitored by electromagnetic flowmeters) are indicated by shaded boxes (statistical data on inflow and outflow discharges of all cases are shown in Appendix D); the discharges computed with the Velocity-Area method (Eqs. 3.9 and 3.10) are highlighted in purple (all cross-sectional distributions of the streamwise velocity, used to compute the discharges for all cases, are shown in Appendix E); and the discharges computed from the mass conservation equation are highlighted in orange colour. Additionally, in the middle of the city block, the intrusion discharge is high-

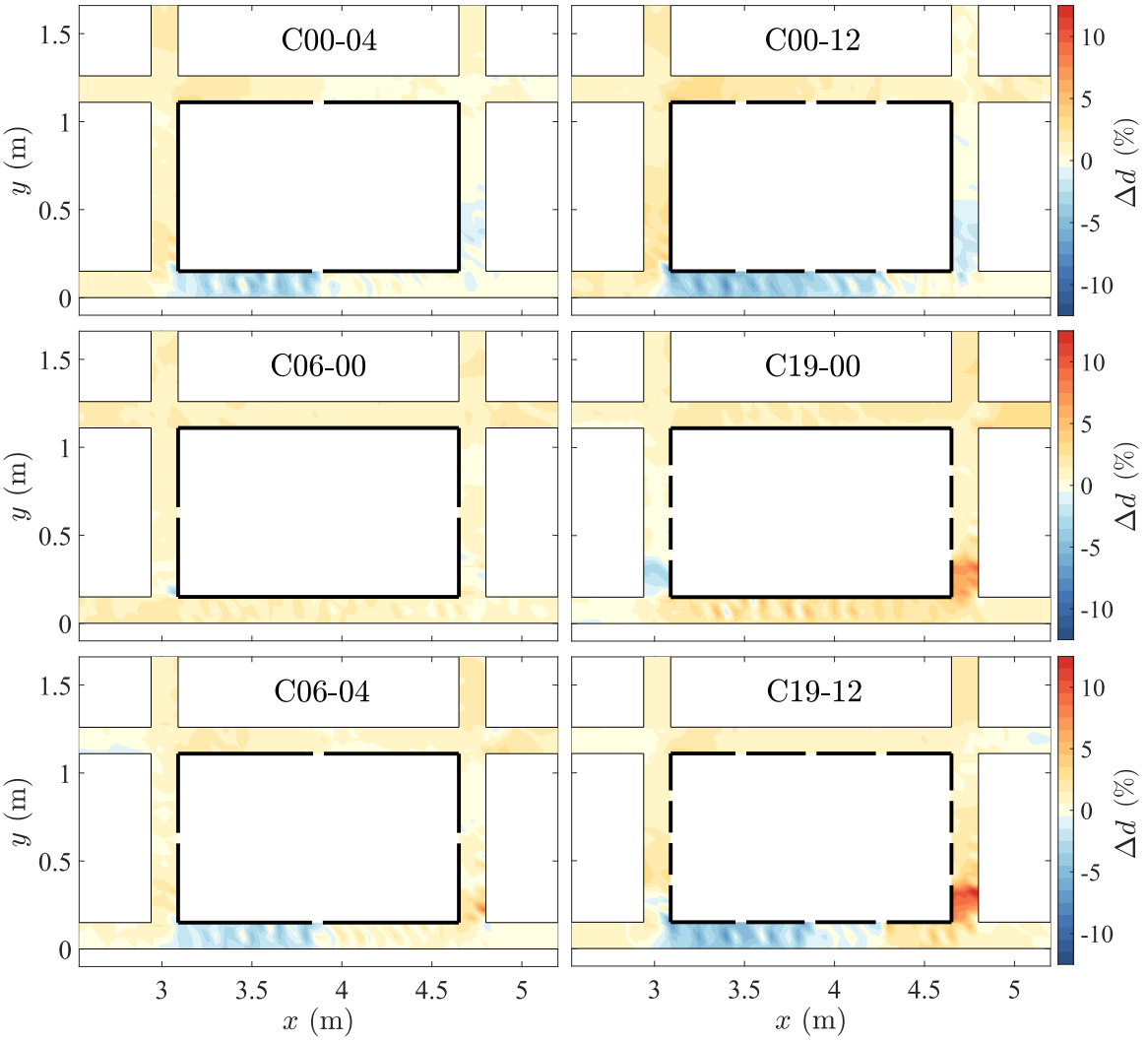

FIGURE 4.4. Relative difference in flow depth, Δd (Eq. 4.2), in the streets, with respect to the reference case C00-00, for cases corresponding to *key issue 1*. Warm colors indicate areas where flow depths are greater than in the reference case, while cool colours indicate areas where flow depths are smaller.

lighted in pink, obtained as the average between the sum of discharges entering (green filled arrows) and leaving (red filled arrows) the block along with the corresponding uncertainty. This uncertainty includes the errors coming from the measuring instruments (electromagnetic flowmeter and ADV) and from the discharge computation method. Due to additional discharges computed with the Velocity-Area method in some streets for a cross-check only, several error values can be obtained; in all cases the maximum value obtained is about 1% of the total inlet discharge, and this is the one displayed in all the cases in Figure 4.5. In the streets, the direction of the flow is the same for all cases, i.e. from upstream to downstream in the two longitudinal streets (along x-axis), and from right to left in the two transverse streets (along y-axis). In contrast, the direction of the exchange flow through the openings may vary from one case to another. These flow directions were derived from the difference between the street discharges, upstream and downstream of each opening. For C19-12 there is a discrepancy in the flow direction through the first openings in the upstream wall with respect to the flow direction reported by the LSPIV measurements. Therefore, for this case, a red blank arrow is also displayed, corresponding to the flow direction through the openings observed in the LSPIV tests.

Regarding the discharge magnitude, when using case C00-00 as a reference flow situation, Figure 4.5 shows that the conveyance porosity: (i) significantly affects the discharges in the streets surrounding the urban block; (ii) significantly affects the discharge entering the block, which logically increases with an increasing conveyance porosity; and (iii) hardly alters the outflow discharges, putting aside the extreme case without city block (C100-100).

Street discharges. The relative differences in discharge in the streets, with respect to the reference flow case, ΔQ_{st}, are computed as:

$$\Delta Q_{st} = \frac{Q_{st} - Q_{st,ref}}{Q_{st,ref}} \times 100 \tag{4.3}$$

where $Q_{st,ref}$ refers to the street discharges in the reference case, i.e., for C00-00 (Table 4.3). $Q_{st,ref}$ are computed at the upstream end of the four streets surrounding the block, i.e., for right and left streets, at $x = 3.09$ m, and for upstream and downstream streets, at $y = 0.15$ m (Figure 4.6). This relative difference ΔQ_{st} increases with increasing conveyance

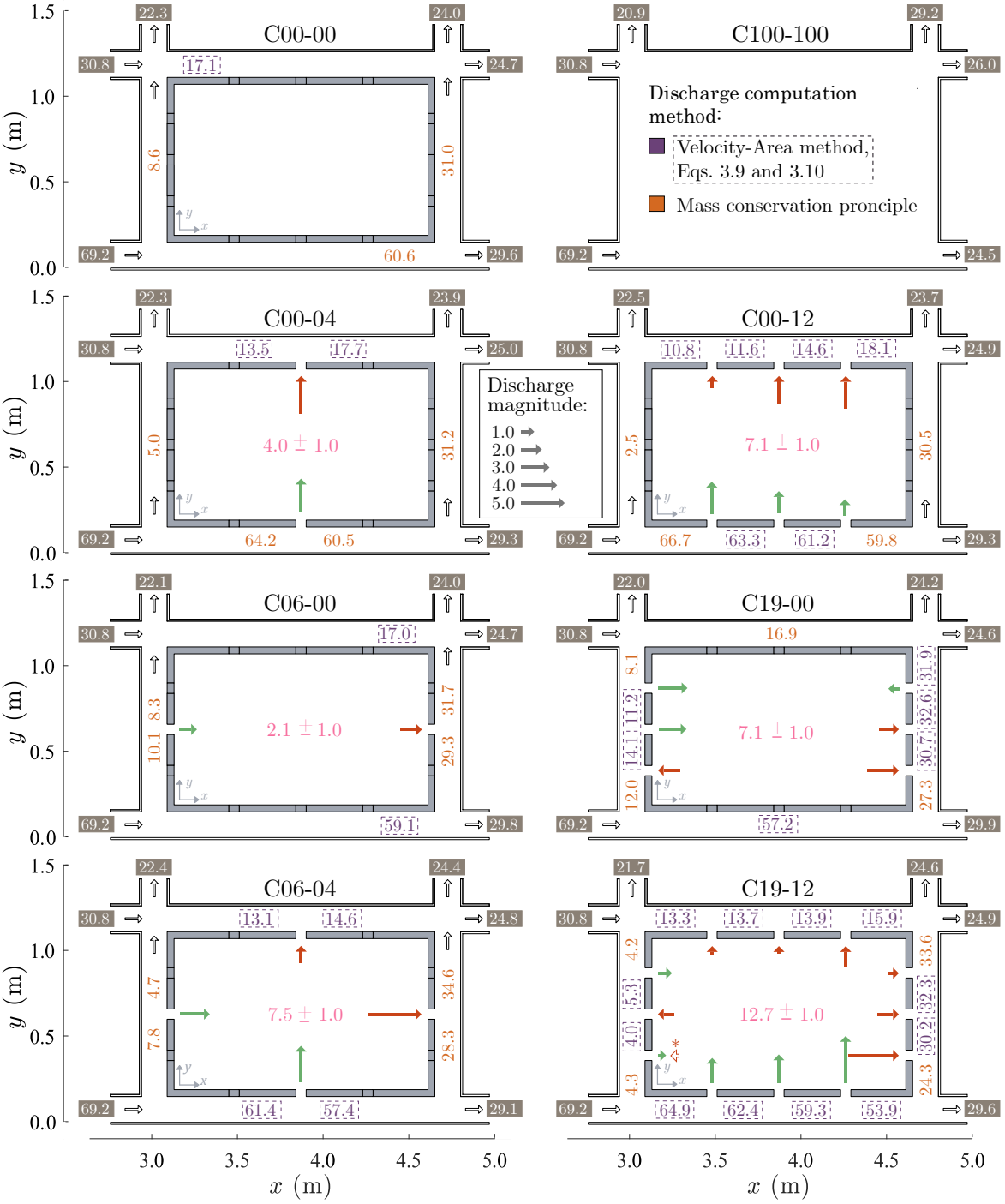

FIGURE 4.5. Discharges in the streets, city block, and inlet and outlet discharges for all flow cases. All the discharge values are presented as a percentage of the total inlet discharge, $Q_{in,T} = 6.5\ \mathrm{l\,s^{-1}}$. The inlet and outlet discharges are indicated by shaded boxes. Discharges computed from Eqs. 3.9 and 3.10 are indicated by purple boxes. Discharges deduced from mass conservation are highlighted in orange colour. The intrusion discharge in the block and the associated uncertainty are highlighted in pink colour. Green and red filled arrows show the flow direction through the block openings, obtained from the discharge estimation. *The red blank arrow show the flow direction observed in the videos recorded for the LSPIV technique.

porosity, for instance, for cases C00-04 and C00-12, ΔQ_{st} = -40% and -70% in the upstream street, ΔQ_{st} = -21% and -36% in the left street, and ΔQ_{st} = 6% to 10% in the right street, respectively. The same tendency is observed when comparing cases C06-00 and C19-00, or cases C06-04 and C19-12.

TABLE 4.3. Discharge at the upstream end of the surrounding streets for the reference case, C00-00.

Configuration	Q_{st} ($l\,s^{-1}$)			
	Right	Left	Upstream	Downstream
C00-00	3.94	1.11	0.56	2.02

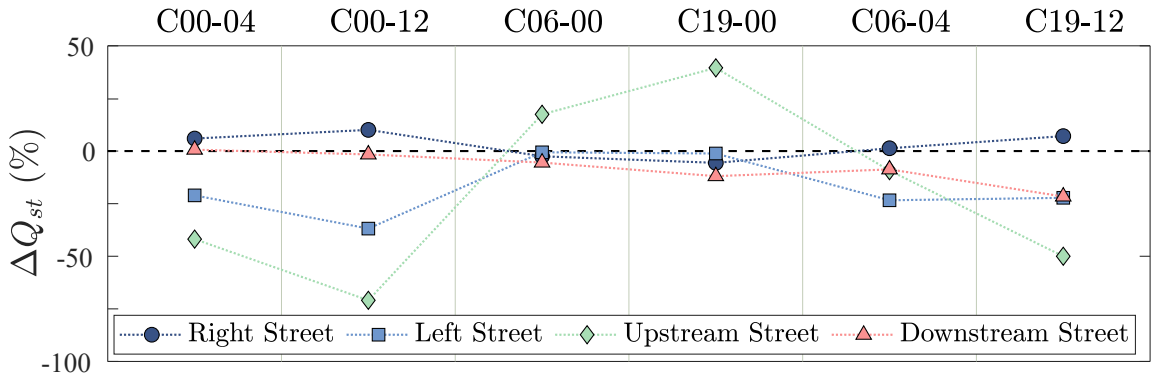

FIGURE 4.6. Relative difference in discharge with respect to the reference case, ΔQ_{st}, at the upstream end of each street surrounding the urban block (i.e. at x = 3.09 m for the right and left streets and at y = 0.15 m for the upstream and downstream streets).

Discharge through the city block. The exchange discharges through the city block openings also increase with increasing conveyance porosity (Figure 4.7). However, no tendency arises for the total intrusion discharge as a function of the conveyance porosity. For instance, if we compare three pairs of cases where ψ is increased by 200%, the increase in discharge is 78% from C00-04 to C00-12, 240% from C06-00 to C19-00 and 70% from C06-04 to C19-12. It is also interesting to investigate the influence of the porosity distribution for a fixed total number of openings along the block walls. For two openings (cases C00-04 and C06-00), Figure 4.7 indicates that the discharge through the city block is greater, by approximately 90%, when openings are located in the right and left walls (C00-04) than in the upstream and downstream walls (C06-00). However, for six openings, when comparing

cases C00-12 and C19-00, the discharge through the city block is practically the same. Hence, the exchange discharge between streets and block does not depend only on the conveyance porosity magnitude. This is a more complex process, depending on the location of the openings, the flow orientation through these openings and the flow patterns within the block.

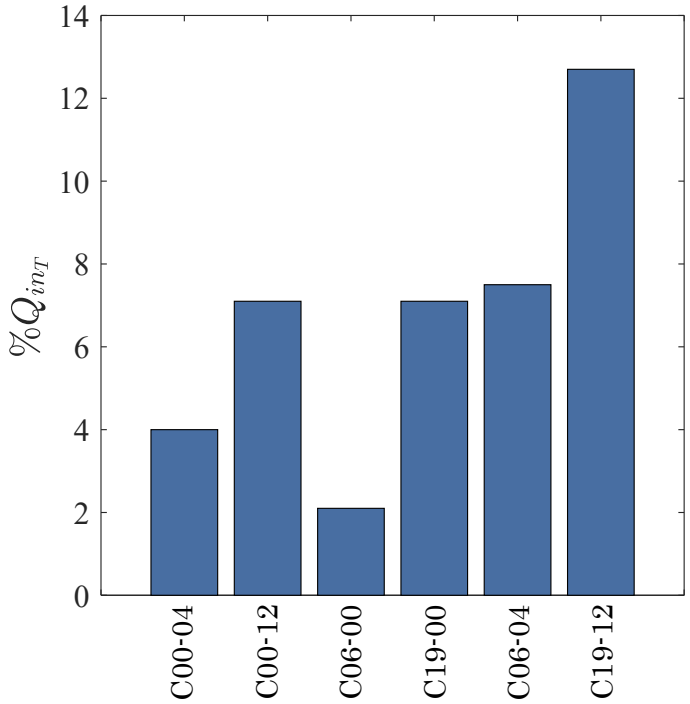

FIGURE 4.7. Exchange discharge through the city block for six flow cases corresponding to *key issue 1*, as a percentage of the total inflow discharge, $Q_{in,T} = 6.5\ \mathrm{l\,s^{-1}}$.

Outflow discharge distribution. When moving away from the city block, the outflow discharges are hardly affected by a change in conveyance porosity, the discharge distribution among the four outlets is rather constant from one case to another, when putting aside the extreme case without block, i.e., C100-100 (Figure 4.8). The maximum variation with respect to the reference case remains limited to around 1%. Hence, to verify whether this is due to the imposed weir heights and inflow distribution, additional experiments are conducted to study the impact of the conveyance porosity on the outflow discharge distribution under different hydraulic and geometric conditions, i.e., different inflow distribution, longitudinal and transversal bed slopes and height of weirs at the outlets. The inlet discharge distribution ($Q_{in,1} - Q_{in,2}$) varies between 70%-30% and 90%-10%, the longitudinal bed slope varies between mild and steep slope, and the height of the weirs was set to 0 or to the heights already defined ($w_1 = 4$ cm , $w_2 = w_3 = w_4 = 3$ cm). Table 4.4 shows the different series

of experiments, with their corresponding boundary conditions. For each set of experiments, four cases with different conveyance porosity values are used: C00-04, C00-12, C19-12, and the reference case C00-00. The set of experiments M7030W corresponds to the original experiments already carried out (i.e., with a mild longitudinal slope, an inflow distribution 70-30 of the total inlet discharge ($Q_{in,1} - Q_{in,2}$) and a weir in each outlet).

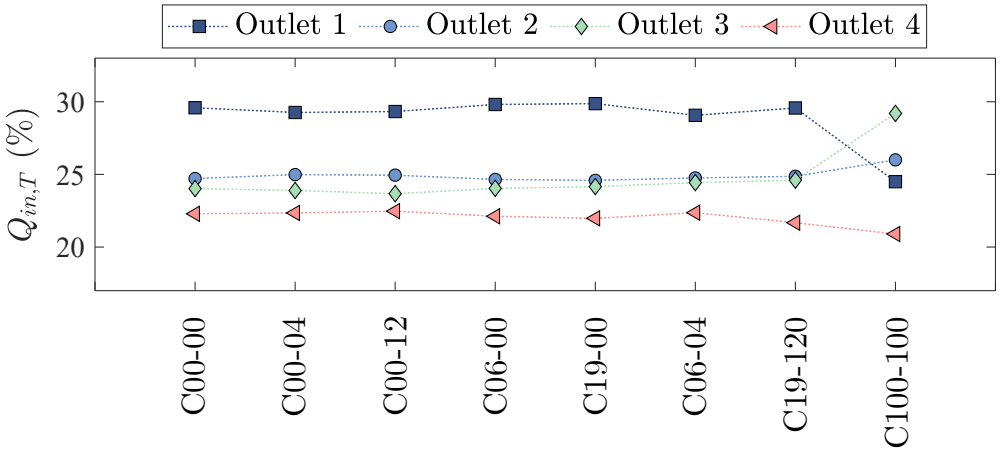

FIGURE 4.8. Outflow distribution as a percentage of the total inlet discharge ($Q_{in,T} = 6.5\ \mathrm{l\,s^{-1}}$) for all eight cases corresponding to key issue 1.

TABLE 4.4. Characteristics of the additional sets of experiments. M7030W corresponds to the original set of experiments, with a mild longitudinal slope, an inflow distribution 70-30 of the total inlet discharge ($Q_{in,1} - Q_{in,2}$) and a weir in each outlet.

Set of experiments	Height of the weir (cm) w_1	w_2	w_3	w_4	Inflow (%) $Q_{in,1}$ - $Q_{in,2}$	S_{0_x} (%)	S_{0_y} (%)
M7030W	4.0	3.0	3.0	3.0	70 - 30	0.12	0.00
M7030	0.0	0.0	0.0	0.0			
M9010	0.0	0.0	0.0	0.0	90 - 10		
S7030W	4.0	3.0	3.0	3.0	70 - 30	1.02	0.20
S7030	0.0	0.0	0.0	0.0			
S9010W	4.0	3.0	3.0	3.0	90 - 10		
S9010	0.0	0.0	0.0	0.0			

Figure 4.9 shows the outflow discharge distribution as a percentage of the total inflow discharge (keeping $Q_{in,T} = 6.5\ \mathrm{l\,s^{-1}}$ constant) for all set of experiments. The bars indicate the average between the largest and smallest outflow discharge values found among the 4

cases with different ψ and the error bar indicates the variability among these cases. We can notice that the variability in the outflow discharge distribution increases for the set of experiments with steeper bed slopes, however, these variations remain low, the largest variation is $\pm$ 1.79% at outlet 1 in the set of experiments S9010W.

The results obtained are similar as in the main experiment: the city block conveyance porosity does not significantly change the discharge distribution among the four outlets. The latter is mainly driven by the presence of the city block, irrespective of the conveyance porosity value of its walls.

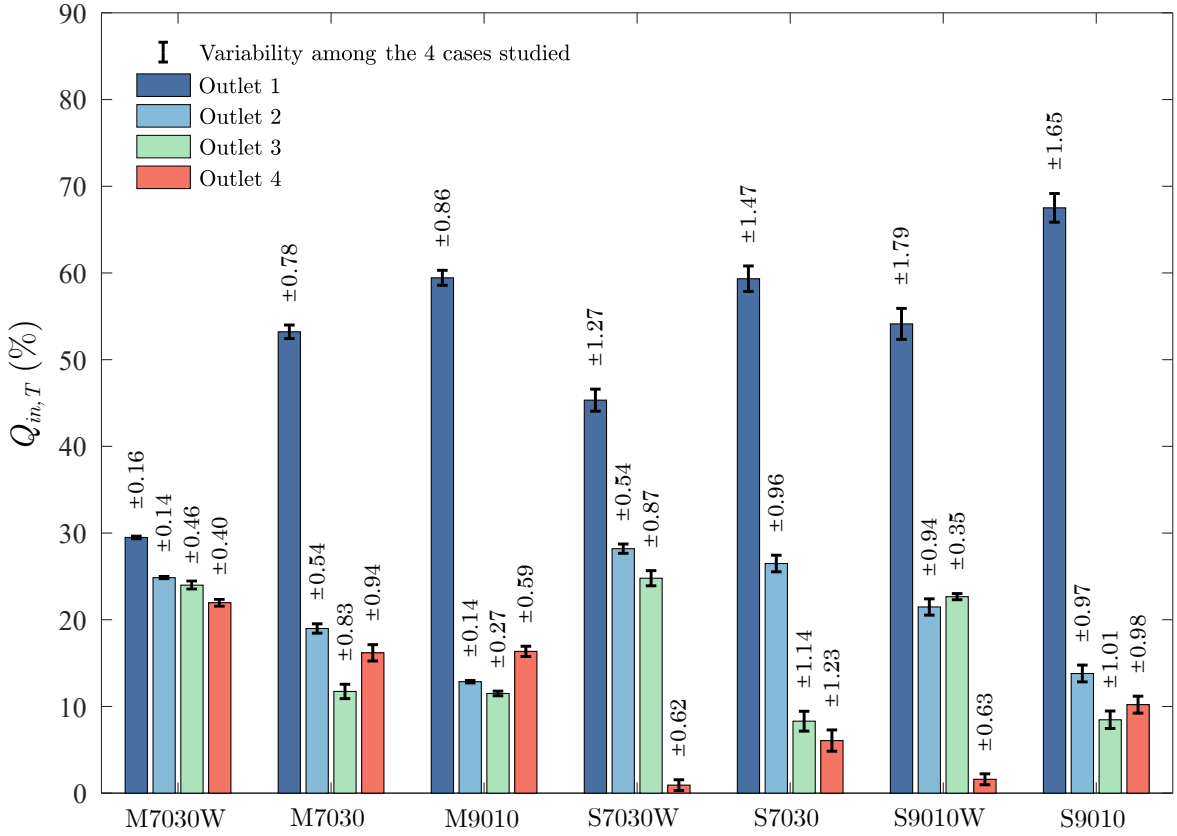

FIGURE 4.9. Discharge distribution at the different outlets for each set of experiments, values shown as a percentage of the total inlet discharge ($Q_{in,T}$ = 6.5 $\mathrm{l s^{-1}}$). The set of experiments M7030W corresponds to the original experiments.

Bulk velocity in the streets. The bulk velocities in the streets for the six cases with a porous city block are now compared with those of the reference case, computing the relative difference in streamwise bulk velocity as:

$$\Delta U_{b,i} = \frac{U_{b,i} - U_{b,i,ref}}{U_{b,i,ref}} \times 100; \quad i = \{x, y\} \tag{4.4}$$

where $U_{b,i,ref}$ refers to the bulk velocity in the streets oriented in i-direction for the reference case (i.e., for C00-00). Figure 4.10 shows the relative difference in streamwise bulk velocity ($\Delta U_{b,x}$ and $\Delta U_{b,y}$, as appropriate) for all the streets. In the streets surrounding the block, the bulk velocities considerably vary with respect to the reference case, and this variation increases with an increasing conveyance porosity. Among the six cases presented in the figure, for all the streets, the larger velocity difference compared to the reference case corresponds to cases with greater conveyance porosity, i.e. cases C00-12, C19-00 and C19-12. The major differences are observed in the upstream street, with maximum differences between 55% and 70%. As the variation in flow depth in the streets with respect to the reference case is limited (Section 4.2.3.1), the significant variation in velocity observed here is mainly due to the variation in discharge in the streets.

4.2.3.3 Surface velocity and recirculation flow patterns

Figure 4.12 shows the spatial distribution of the time-averaged surface velocity magnitude, U_s, along with the time-averaged streamlines, in all accessible areas. For all cases, the surface velocity magnitude ranges from 0 to 60 $\mathrm{cm\,s^{-1}}$ (0.0 - 1.9 $\mathrm{m\,s^{-1}}$ at the prototype scale). The highest velocity magnitude is observed in the right street due to the high inflow discharge at the entrance of this street. The velocity in the left street is three to four times lower. The upstream street exhibits one or two recirculating flow areas (depending on the flow case) induced by the shearing with the flow in the right street, and on average, the flow along this street is the slowest among all the streets. The downstream street is characterized by a wide range of velocity magnitude (from 0 to 50 $\mathrm{cm\,s^{-1}}$), with the highest velocities mainly located along the right wall, opposite to the block under study. Besides, the velocity magnitude within the city block is significantly smaller than in the streets, with a maximum value of 20 $\mathrm{cm\,s^{-1}}$ (0.63 $\mathrm{m\,s^{-1}}$ at the real-world prototype scale), a third of the maximum velocity in

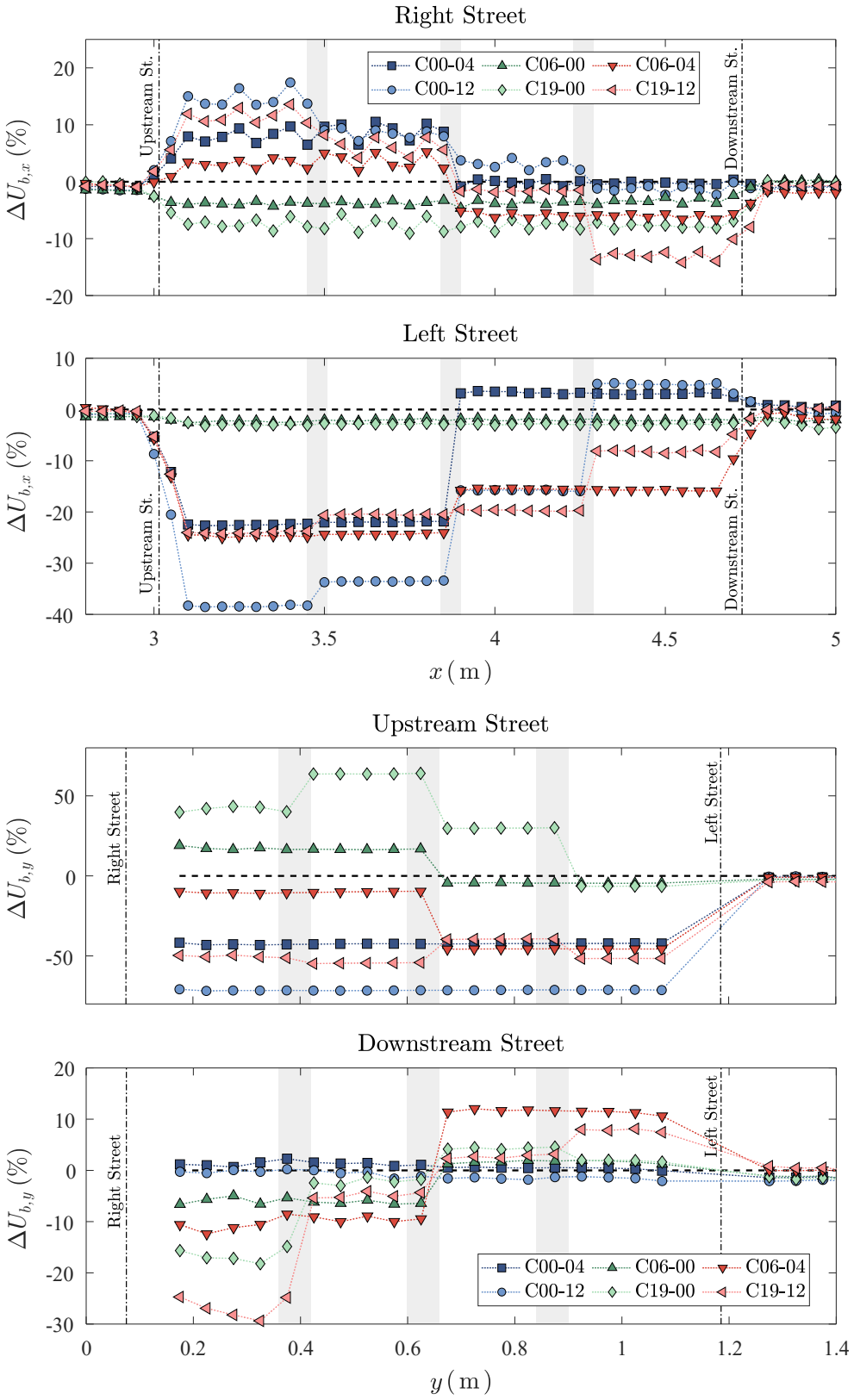

FIGURE 4.10. Relative difference in bulk velocity with respect to the reference case, $\Delta U_{b,x}$ and $\Delta U_{b,y}$, in the longitudinal direction (x-axis) and transverse direction(y-axis), respectively. Vertical shaded bands indicate the location of the openings along the city block walls.

the streets.

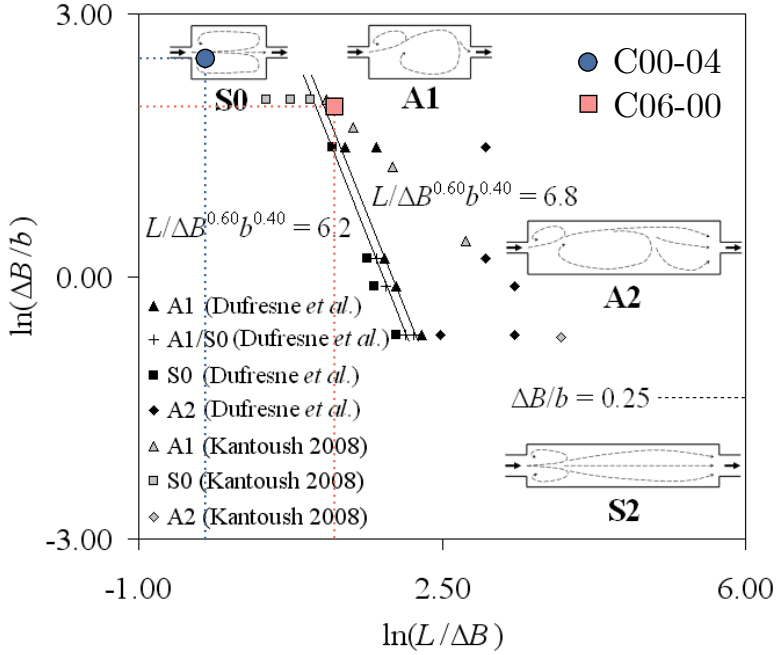

FIGURE 4.11. Classification diagram for flow patterns as a function of rectangular shallow reservoir geometry, from Dufresne et al. (2010). The points corresponding to the cases C00-004 (with an opening in the right and left walls of the block) and C06-00 (with an opening in the downstream and upstream walls) are indicated in the diagram.

Within the city block, from two to five large scale recirculating cells can be observed. The spatial distribution and the size of the recirculating cells are mainly driven by the direction of the jets through the openings. For instance, case C00-04 shows two cells, nearly symmetrical, on each side of the entering jet. In contrast, case C06-00 (with the same number of openings but aligned with the longitudinal direction) shows a main recirculating cell and a smaller secondary one on the right side upstream. These results are in agreement with those presented in several studies on shallow reservoirs (e.g. Dewals et al., 2008; Dufresne et al., 2010; Goltsman and Saushin, 2019) see Figure 4.11. The difference in the flow pattern between C00-04 and C06-00 is partly due to the length-width ratio of the block, which is higher for C06-00, and to the exchange flow rate magnitude (three times higher for C00-04). A similar trend is observed for cases C00-12 and C19-00, with the same number of openings, but along opposite axes: case C00-12 exhibits two main recirculation cells (one larger than the other), plus three small recirculation cells driven by the jets through the right wall; however, C19-00, exhibits a single recirculation cell and three much smaller ones, two upstream and one downstream. Finally, case C06-04 comprises two main recirculation

cells and a small one upstream, while case C19-12 comprises two main recirculation cells and three small ones next to the right wall. As expected the higher number of openings can increase the number of recirculation cells. To conclude, the flow pattern within the city block depends on its length-width ratio (length = main jet direction), the magnitude of the jets, the number of openings (porosity magnitude) and their locations (porosity distribution).

In absence of city block (case C100-100), two recirculating flow cells of similar size are generated. Contrary to what is observed for the other cases within the block, in this case the flow velocity in the recirculation cells does not decrease drastically compared to the streets velocity, mainly in the downstream cell.

4.2.4 Flood hazard to pedestrians

Assuming that the surface velocity (calculated with LSPIV) is equal to the depth-averaged velocity (valid assumption according to figures shown in the Section 3.3.3.1), using the spatial distribution of local flow depth and applying the Froude similarity detailed in Eqs. (3.13) and (3.14), a 2-D map of flood hazard level for pedestrians is built for each flow case (Figure 4.13). This enables to assess the impact of conveyance porosity of the city block on the hazard level in the urban area. The latter is defined by the criterion proposed in Figure 3.26.

For each flow case, the flood hazard ranges from *low* to *high*, the highest hazard being located in the right street due to the high velocity and flow depth along this street. The hazard level is also important in the downstream street near the right sidewall, with strong flow velocities (even in absence of block, as it is the main path of the high-speed stream as previously mentioned). In contrast, the level of hazard inside the block is small due to the very low velocity in this open area.

Figure 4.13 also shows that the conveyance porosity can enhance the level of flood hazard at one specific location while reducing it at another. For instance, when passing from C00-00 to C00-12, the level of hazard decreases in the upstream street but increases in the right street. This same tendency is observed in these two streets, to a greater or lesser extent, for the other cases, except for case C19-00, where a local increase in the level of hazard is computed in the vicinity of the openings in the upstream street. For the other streets, only limited and local differences in the level of hazard are predicted, mainly in the vicinity of the

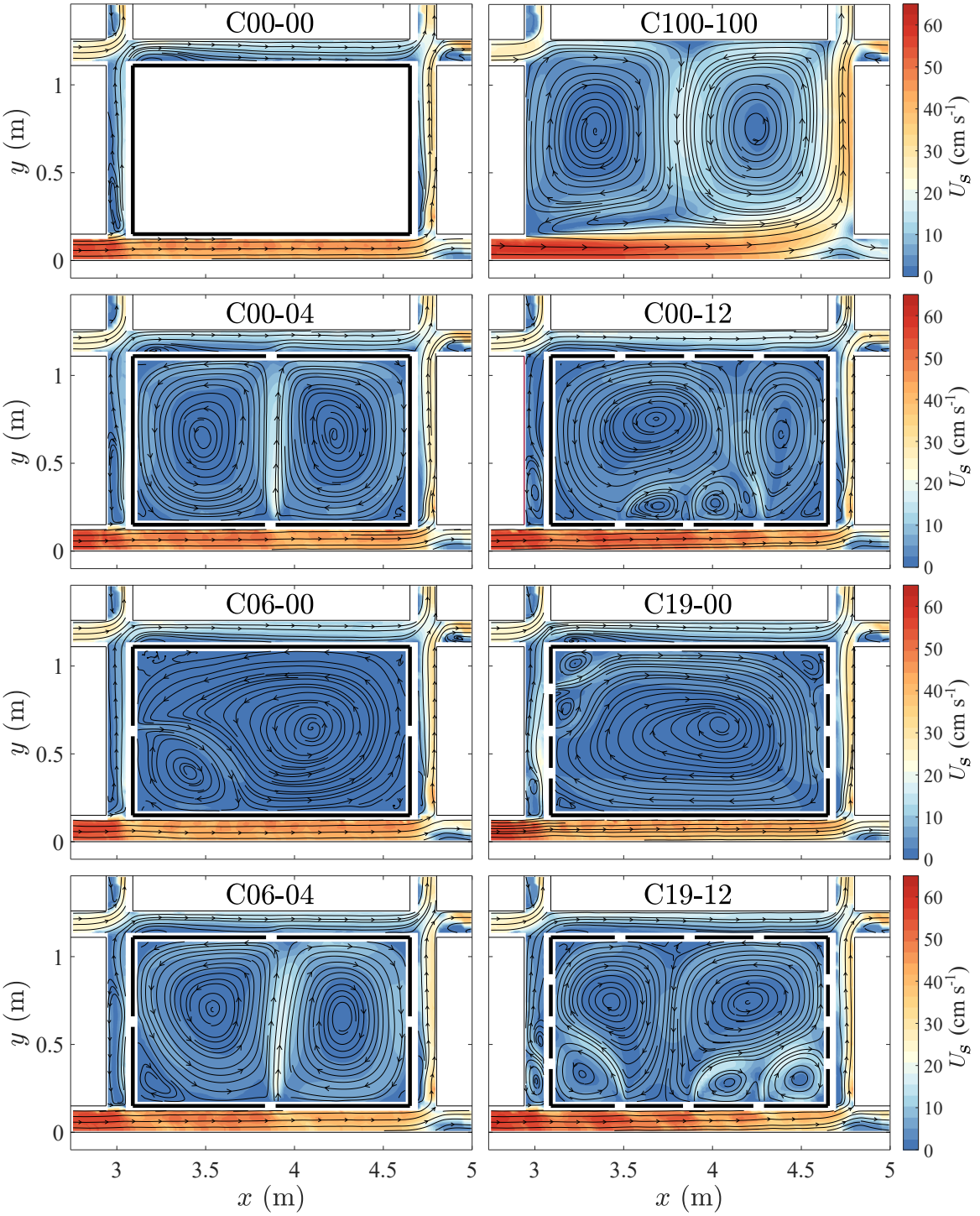

FIGURE 4.12. 2D maps of time-averaged surface velocity magnitude (model scale), U_s, and streamlines in the streets and within the city block (derived from LSPIV data), for all cases corresponding to *key issue 1*.

openings, as for instance, in the downstream street for case C19-12, with a higher level of hazard. Within the urban block, the modifications of the level of hazard are mainly due to changes in velocity magnitude, since flow depths are almost the same throughout the area for all cases. The areas of greatest hazard occur near the openings along the incoming flow jets. Therefore, the impact on the flood hazard increases when conveyance porosity increases, but this is spatially limited to the areas in the vicinity of the openings.

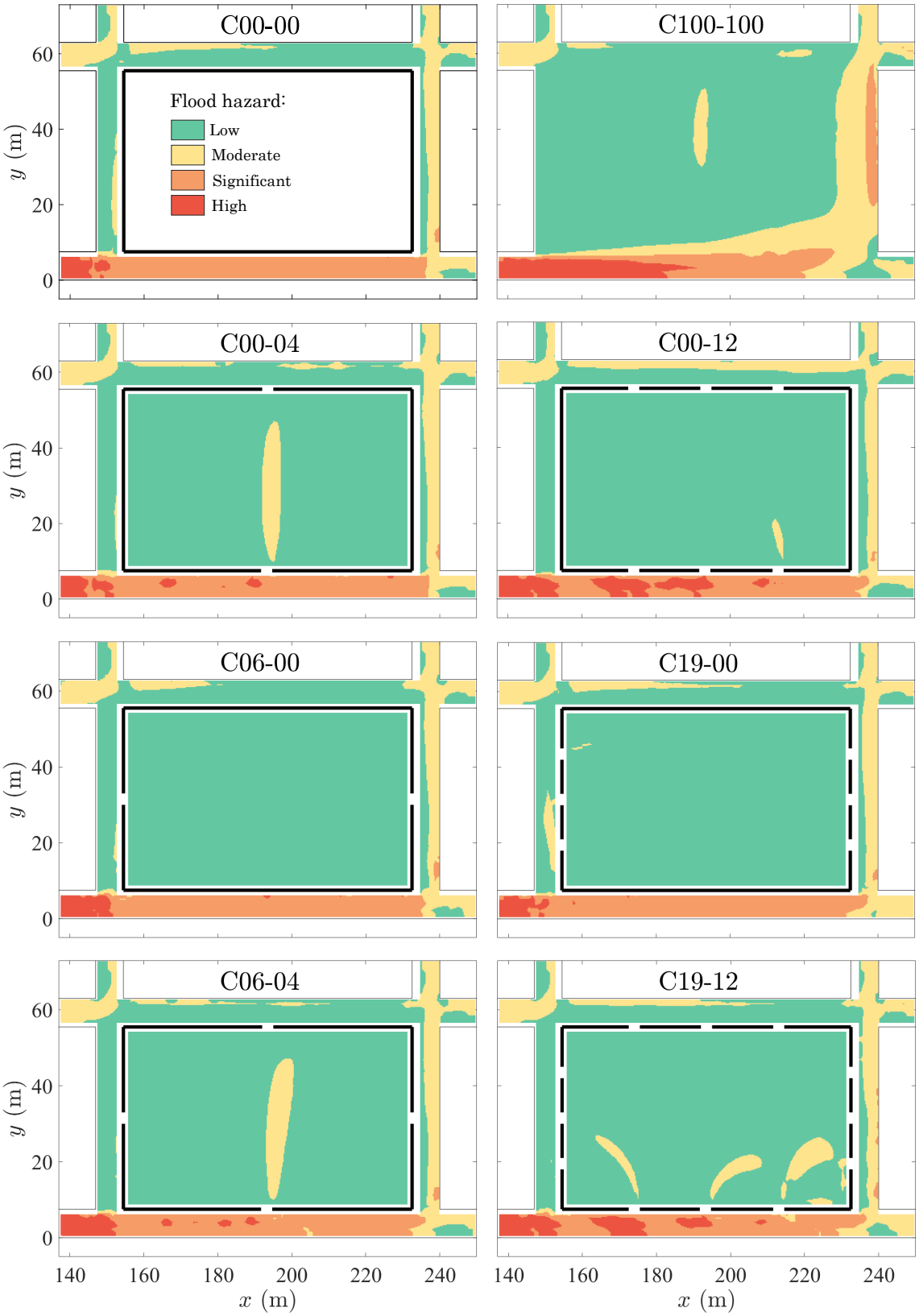

FIGURE 4.13. Flood hazard maps for pedestrians, for each flow case corresponding to *key issue 1*, obtained by scaling flow depths and velocities at the real-world prototype scale using Froude similitude (Eqs. 3.13 and 3.14).

4.3 Conveyance porosity distribution (key issue 2)

4.3.1 Introduction

In the tests corresponding to key issue 1, described above, the flow enters the city block mainly through the wall openings in the right and upstream streets, while it is evacuated mainly through the walls openings connected to the downstream and left streets. Therefore, when considering the distribution of conveyance porosity, ψ, along the city block, some questions arise:

1. For the same ψ magnitude in the whole city block, does the flow through the block increase when the openings are distributed over all four walls rather than just in a few?
2. What is the effect on flow features when having an asymmetric ψ magnitude on facing walls compared to having it symmetrical?
3. What is the effect on flow features when having ψ on facing block walls compared to having it on adjacent walls?
4. What is the effect on flow features when ψ is concentrated in one area of the city block?

The study of the conveyance porosity distribution detailed below focuses on these questions.

4.3.2 Experimental cases

Six cases are studied, with the same conveyance porosity magnitude along the city block perimeter, but with a different distribution. A porous city block with four rectangular openings of 6 cm long each is considered. Therefore, the total conveyance porosity at the block scale is defined as:

$$\psi_B = \frac{N_T \cdot L_{op}}{2L_{B,x} + 2L_{B,y}} \tag{4.5}$$

where $N_T = 4$ is the total number of openings along the four city block walls, L_{op} is the length of each opening ($L_{op} = 6$ cm and $L_{B,x}$ and $L_{B,y}$ are the total length of the city block walls, oriented in direction x and y, respectively (see Figure 3.4.A). The conveyance porosity

value, ψ in each wall (Eq. 4.1) and the total conveyance porosity ψ_B for the different cases considered are detailed in Table 4.5. Case C06-04 is a experimental case already studied in key issue 1, which meets the characteristics required for the study of key issue 2, therefore it is considered here as well.

TABLE 4.5. Conveyance porosity values, ψ, in each wall (Eq. 4.1) and total, ψ_B (Eq. 4.5) for the six flow cases corresponding to *key issue 2*.

Case	City block wall								Total	
	Upstream		Downstream		Right		Left			
	N	ψ (%)	N	ψ (%)	N	ψ (%)	N	ψ (%)	N_T	ψ_B (%)
C06-04	1	6	1	6	1	4	1	4	4	5
RL08	0	0	0	0	2	8	2	8	4	5
R04L12	0	0	0	0	1	4	3	12	4	5
D13R08	0	0	2	13	2	8	0	0	4	5
U06R12	1	6	0	0	3	12	0	0	4	5
D06L12	0	0	1	6	0	4	3	12	4	5

Cases RL08 and R04L12 include a conveyance porosity along face-to-face block walls, in the right and left walls. However, for RL08, the conveyance porosity magnitude is symmetrical, i.e., same value of ψ on both facing walls (two openings in each wall, Figure 4.14.A), while in R04L12 it is asymmetric, ψ is three times higher in the left wall than in the right wall (one opening in the right wall and three openings in the left, Figure 4.14.B). For case D13R08, there is conveyance porosity in adjacent block walls, in the right and downstream (two openings both walls, see Figure 4.14.C). In the last two cases, U06R12 and D06L12, ψ is concentrated in a specific region of the block, in the upstream/right walls area for U06R12 (Figure 4.14.D)and in the downstream/left walls area for D06L12 (Figure 4.14.E).

These six cases have been proposed to answer the questions addressed in Section 4.3.1. The case C06-04 allows to answer question 1 by comparing the results with all other cases. Cases RL08 and R04L12 help in the research to answer question 2. Cases RL08 and D13R08 permits to answer question 3 and cases U06R12 and D06L12 to answer question 4.

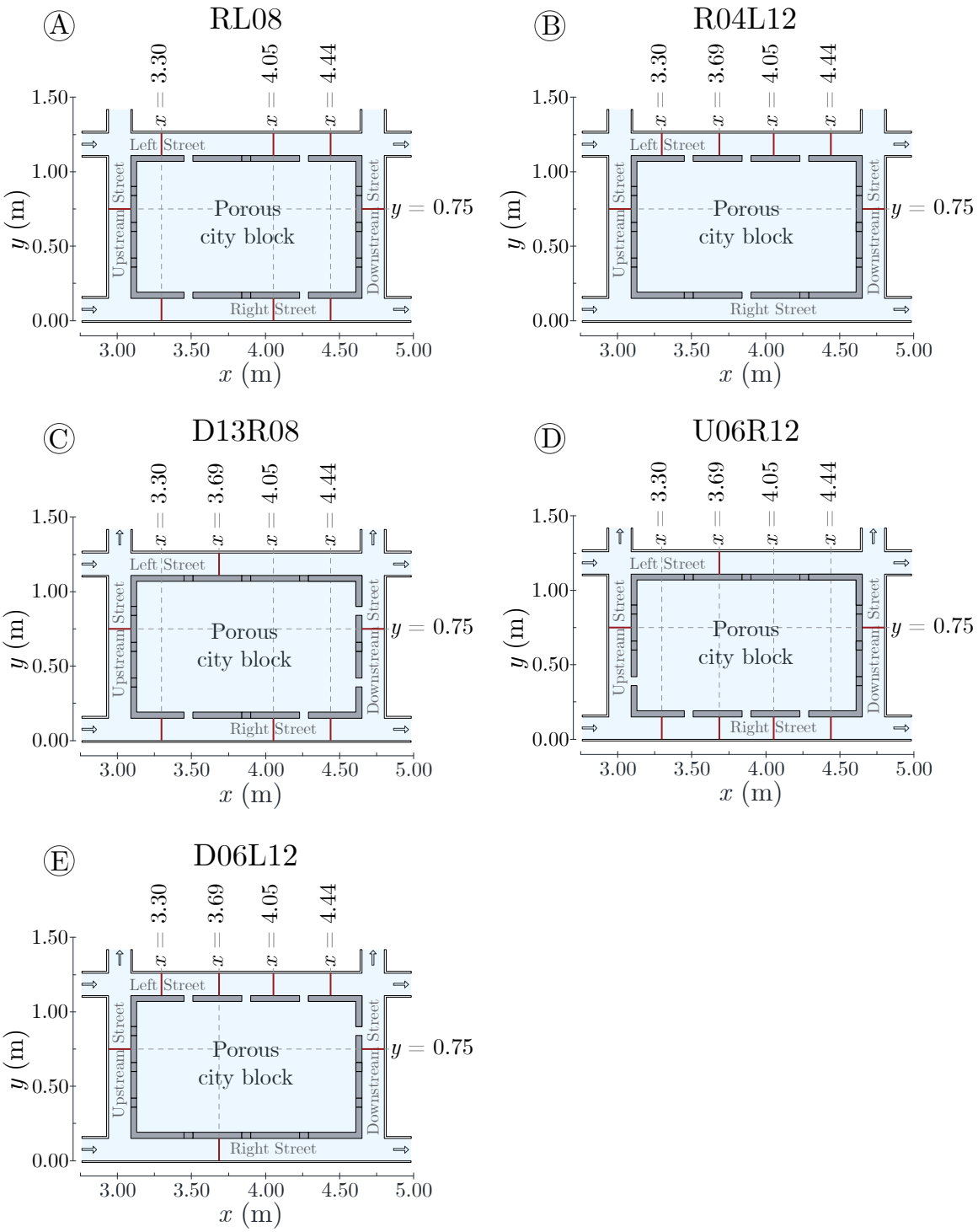

FIGURE 4.14. Top view sketches of the experimental cases corresponding to *key issue 2*, considered to study the conveyance porosity distribution. Red lines across the streets show the sections where ADV velocities are measured to compute the discharges by the Velocity-Area method.

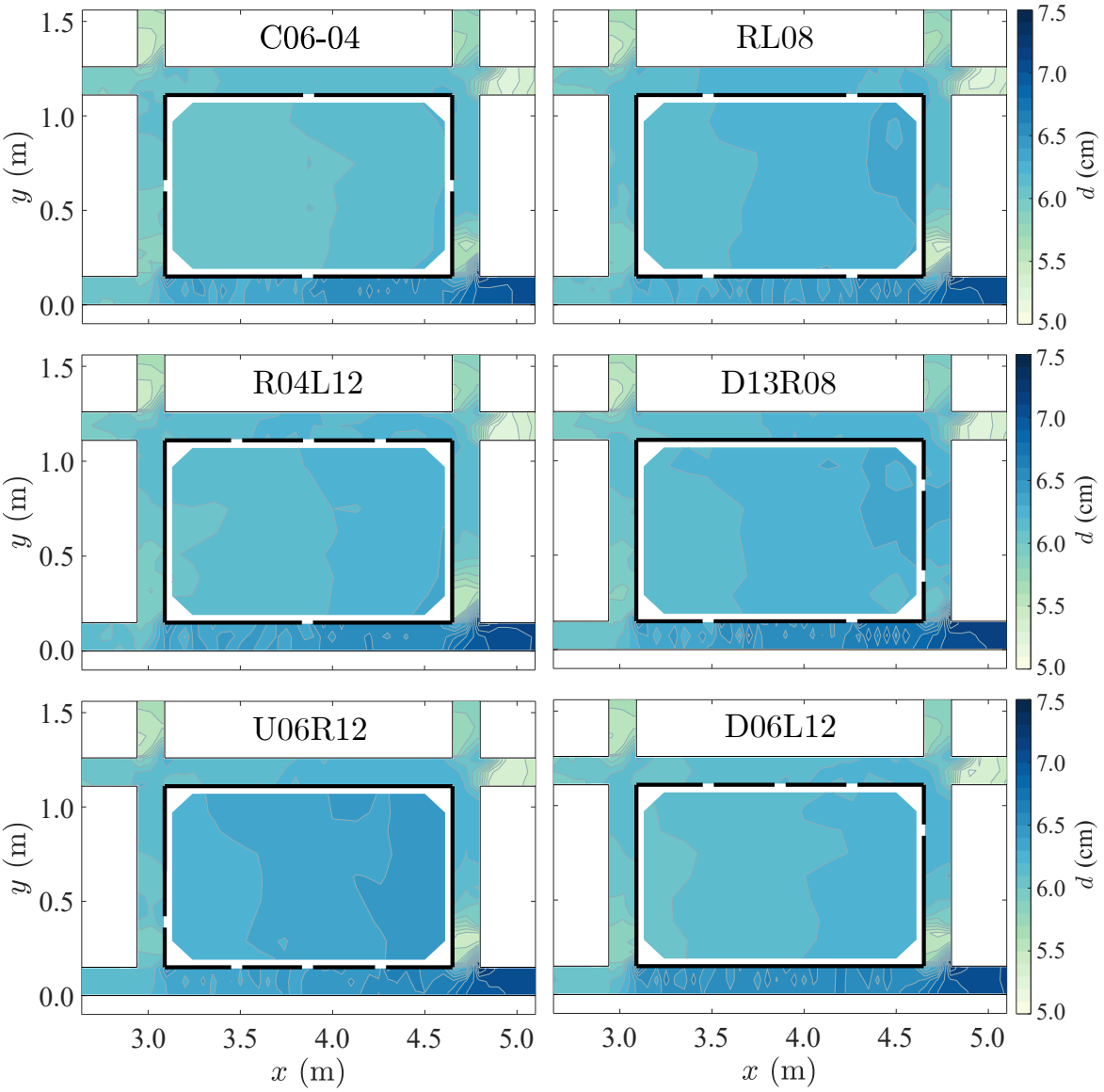

FIGURE 4.15. Flow depth (model scale), d, in the streets and within the city block for all flow cases corresponding to *key issue 2*. Deep blue colour indicates the greater flow depths and light colour indicates the shallower flow depths.

4.3.3 Measured flow features

4.3.3.1 Flow depths

Similar to the tests for key issue 1, the flow depths do not vary greatly between the different cases (Figure 4.15). The flow depths for all cases range between 5.0 and 7.5 cm, being always greater in the right street, due to the height of the weir at the outlet of this street ($w_1 = 4$ cm). Within the block the flow depths are also very similar, slightly higher in the downstream zone compared to the upstream zone, mainly due to the longitudinal bed slope, $S_{0,x}$. Among all cases, U06R12 shows a slight increase in flow depth compared to the other cases, by around 3%, mainly due to the absence of conveyance porosity in the walls through which the flow is usually evacuated (i.e., downstream and left walls), and thus there is a slight backwater effect.

To have a proper comparison between the six cases, the relative difference with respect to the reference case of key issue 1 (i.e. case C00-00, with non porous city block, see Figure 4.1, sketch A) is computed and plotted in Figure 4.16, by applying Eq. 4.2. For all cases except D06L12 (case without openings in the right street) flow depths decrease in the upstream area of the right street, mostly in the cases with higher conveyance porosity along the block wall in this street (up to 6%). In case D13R08 a strong increase in flow depth is observed at the beginning of the downstream street (up to 14%) due to the backwater effect created by the flow leaving the block through the first opening in this wall (this was also seen for the cases in key issue 1, when the flow is evacuated through the downstream street, e.g., C19-12). This effect extends to the downstream area of the right street, where an increase in flow depth is also observed (see right downstream area of case D13R08 in Figure 4.16). Among all the cases, the flow depth varies the least for D06L12, by just 1.1% on average, in the streets surrounding the city block.

Therefore, although it is observed that flow depths are not strongly impacted globally, there are local changes due to the location of the openings along the block walls (i.e., due to the conveyance porosity distribution), which can be significant.

4.3.3.2 Discharges

The inflow and outflow discharges, indicated by shaded boxes (statistical data on inflow and outflow discharges of all cases are shown in Appendix D), as well as those computed in

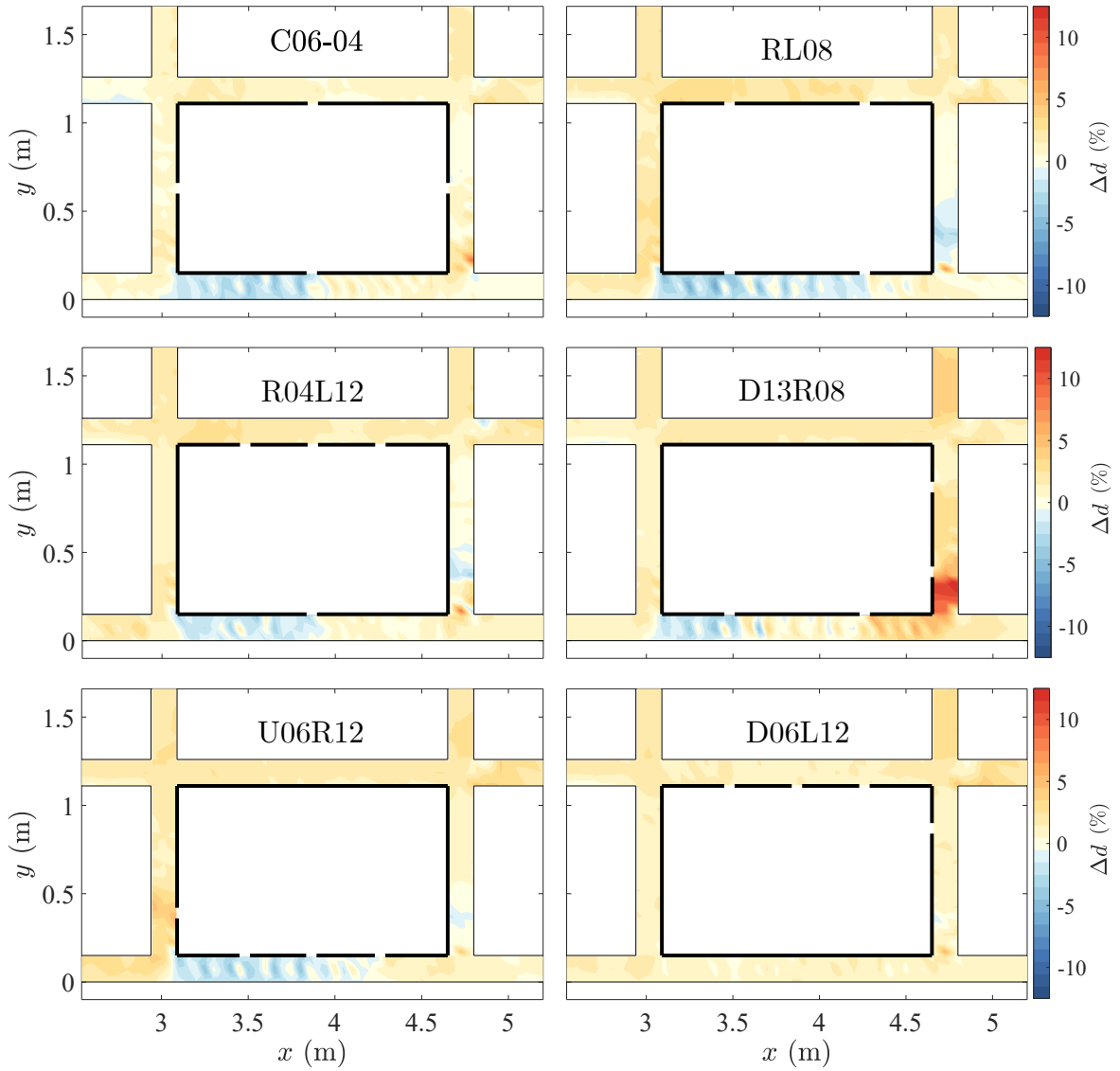

FIGURE 4.16. Relative difference in flow depth, Δd (Eq. 4.2), in the streets, with respect to the reference case C00-00 (from key issue 1), for cases corresponding to *key issue 2*. Warm colors indicate areas where flow depths are greater than in the reference case, while cool colours indicate areas where flow depths are smaller.

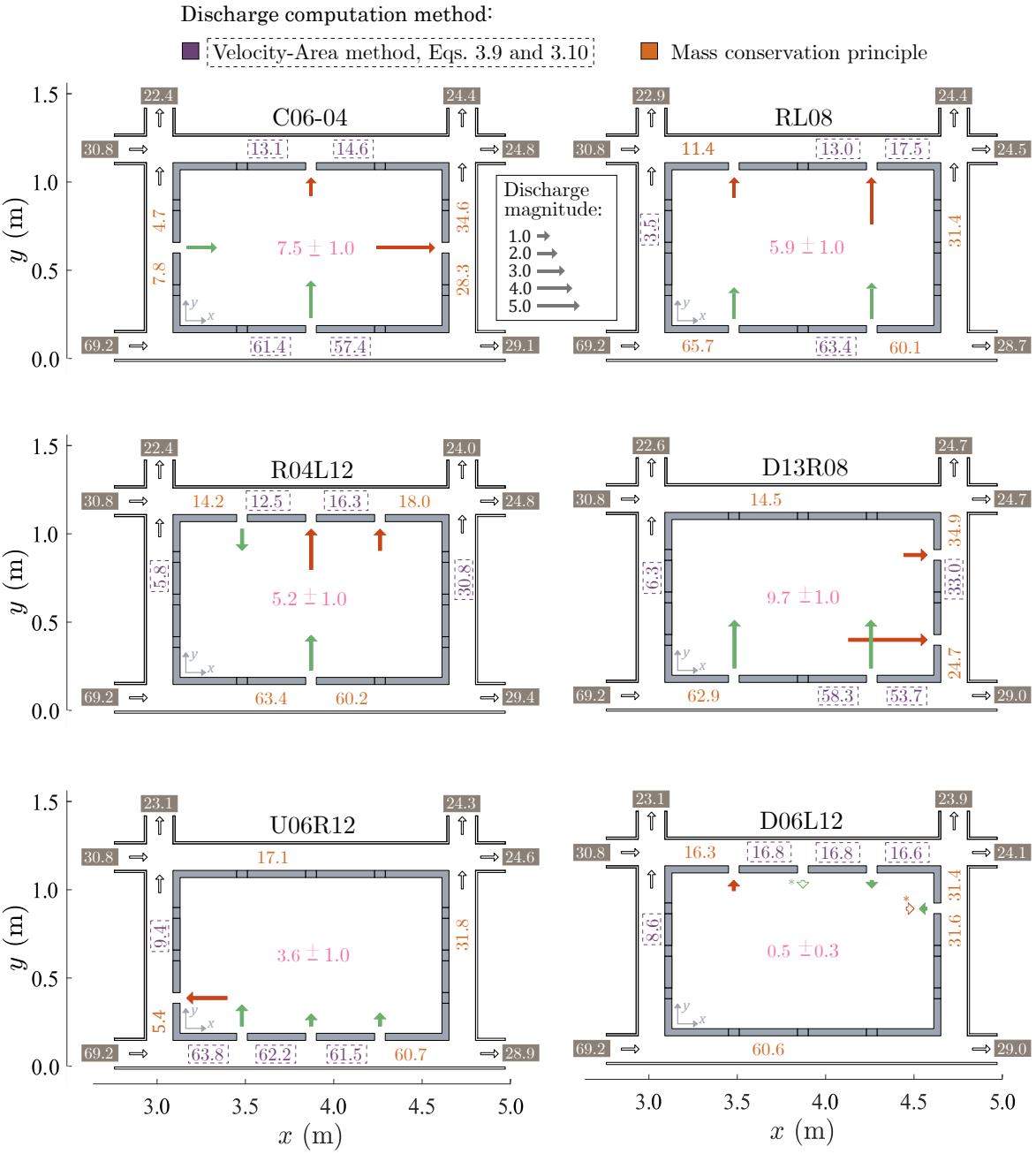

FIGURE 4.17. Discharges in the streets, city block, and inlet and outlet discharges for all flow cases corresponding to *key issue 2*. All the discharge values are presented as a percentage of the total inlet discharge, $Q_{in,T} = 6.5\ l s^{-1}$. The inlet and outlet discharges are indicated by shaded boxes. Discharges computed via Velocity-Area method (Eqs. 3.9 and 3.10) are indicated by purple boxes. Discharges deduced from mass conservation are highlighted in orange colour. The intrusion discharge in the block and the associated uncertainty are highlighted in pink colour. Green and red filled arrows show the flow direction through the block openings, obtained from the discharge estimation. *Green and red blank arrows show the flow direction observed in the videos recorded for the LSPIV technique.

all street reaches (highlighted in purple within a dashed lines box for those computed with the Velocity-Area method and in orange colour for those obtained by the principle of mass conservation) and through each opening in the block walls are shown in Figure 4.17 (all cross-sectional distributions of the streamwise velocity, used to compute the discharges for all cases, are shown in Appendix E). In the centre of each city block, the discharge through the block is indicated in pink colour along with the corresponding uncertainty (obtained by the same procedure as in key issue 1, already explained in Section 4.2.3.2). Red and green filled arrows show the flow direction through the block openings (green arrows when the flow is directed from the streets to the block and vice versa for the red ones), obtained with the estimation of the street discharges. However, for case D06L12 there is a discrepancy in the flow direction through some openings with respect to the flow direction reported by the LSPIV measurements. Therefore, for this case, green and red empty arrows are also displayed, corresponding to the flow direction through the openings observed in the LSPIV tests.

All the discharge values are shown as a percentage of the total inlet discharge ($Q_{in,T} = 6.5\ \mathrm{l\,s^{-1}}$). The inlet and outlet discharges (monitored by electromagnetic flowmeters) are indicated by shaded boxes (statistical data on inflow and outflow discharges of all cases are shown in Appendix D); the discharges computed with the Velocity-Area method (Eqs. 3.9 and 3.10) are highlighted in purple (all cross-sectional distributions of the streamwise velocity, used to compute the discharges for all cases, are shown in Appendix E);

For cases C06-04, RL08 and D13R08 the flow direction through the openings in the walls remains similar to those observed in the experimental cases of key issue 1, i.e. through the right and upstream walls the flow enters the block while through the left and downstream walls it leaves the block. In case R04L12 (with an asymmetric conveyance porosity between the two facing walls), the flow direction changes in one of the left wall openings. Having then two openings through which the flow enters the block (green arrows) and two through which it is evacuated (red arrows), similar to the other three cases already mentioned. For case U06R12, the flow direction through the openings along the right wall remains oriented from the street towards the block and the flow is evacuated only through the single opening in the upstream wall. In case D06L12, the flow discharge through the openings is very small, for most of them it is smaller than the uncertainty value. For this reason, in this case, there

is a discrepancy between the flow direction reported by LSPIV measurements and the flow direction obtained from the discharge computation in the streets.

Regarding the discharges through the city block, the highest discharge corresponds to D13R08, followed by C06-04 (Figure 4.18), therefore, having the openings distributed in all the block walls does not increase the discharge through the block. Furthermore, this discharge is also much higher than that reported for RL08, the difference between the two is the location of the openings through which the flow is evacuated: through the left wall for RL08 and through the adjacent downstream wall for D13R08. The significant discharge through the block for case D13R08 is mainly enhanced by the openings located near the right downstream corner. In this area, the flow passes almost directly from the right street to the downstream street through these two openings (this effect is also observed for C19-12 in key issue 1). Finally, the smallest discharges through the block are obtained for cases where the openings are concentrated in only one zone of the city block. In case U06R12 the discharge is evacuated through only one opening, in the upstream wall. For case D06L12 almost no flow enters the city block, because the openings are in the walls through which the flow is usually evacuated. This very small discharge through the block also explains the small variation in flow depths reported for this case, compared to the reference case (C00-00).

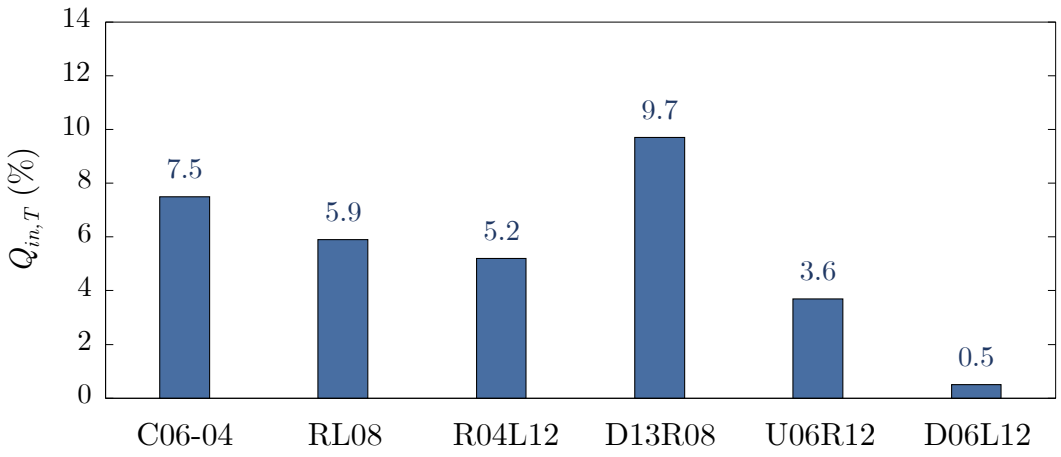

FIGURE 4.18. Discharge through the city block as a percentage of the total inflow discharge, $Q_{in,T} = 6.5\,\mathrm{l\,s^{-1}}$, for the six flow cases corresponding to *key issue 2*.

4.3.3.3 Surface velocity and recirculation flow patterns

The surface velocity magnitude in the streets and within the city block is very similar for these cases of key issue 2 to that obtained in key issue 1, ranging from 0 to 60 $\mathrm{cm\,s^{-1}}$ in the streets and from 0 to 20 $\mathrm{cm\,s^{-1}}$ within the block (Figure 4.19). In the streets, the velocity increases as the conveyance porosity increases, e.g., among all cases, the lowest velocity in the right street is reported in case D06L12, whit no openings along the right block wall. Within the city block, the maximum surface velocity varies strongly among the different cases, with the largest found for case C06-04 ($\sim 21\ \mathrm{cm\,s^{-1}}$) and the lowest in case D06L12 ($4\ \mathrm{cm\,s^{-1}}$). Although the largest discharge through the city block is reported for case D13R08, due to significant flow exchange in the downstream right corner, as explained above, no large velocities are measured in this area. The water jet through the downstream opening in the right wall was quite unstable, changing direction (this can be seen in the streamlines of this recirculation cell, see right downstream corner within the block for case D13R08 in Figure 4.19) and producing some fluctuations in the free surface. This instability has hindered the uniform distribution of the tracers, affecting the estimation of the velocity, therefore it is possible that the surface velocity in this area is underestimated.

Several recirculation cells are identified in the different cases. C06-04 and R04L12 exhibit two recirculation cells, nearly symmetrical, one on each side of the dominant inlet water jet (through the right street). In cases RL08 and D13R08, although both have two inlet jets through the right wall, the flow patterns are very different because the outflow openings are in a different walls: three main recirculation cells are observed for case RL08 and four for case D13R08, two large and two small cells next to the right wall. In contrast, flow patterns in case U06R12 are very similar to those observed in case C00-12 (corresponding to the key issue 1 experiments), even though the magnitude and distribution of the conveyance porosity of the city block differs. The flow in these two cases enters the city block through the same three openings in the right wall, but it is evacuated through different walls and different number of openings. In case D06L12, three main recirculation cells are observed, one large expanding over the whole block area and two small ones near the left wall.

Finally, the experimental cases of both key issue 1 and key issue 2, reveal that the openings through the block wall in the right street, the street with the predominant flow

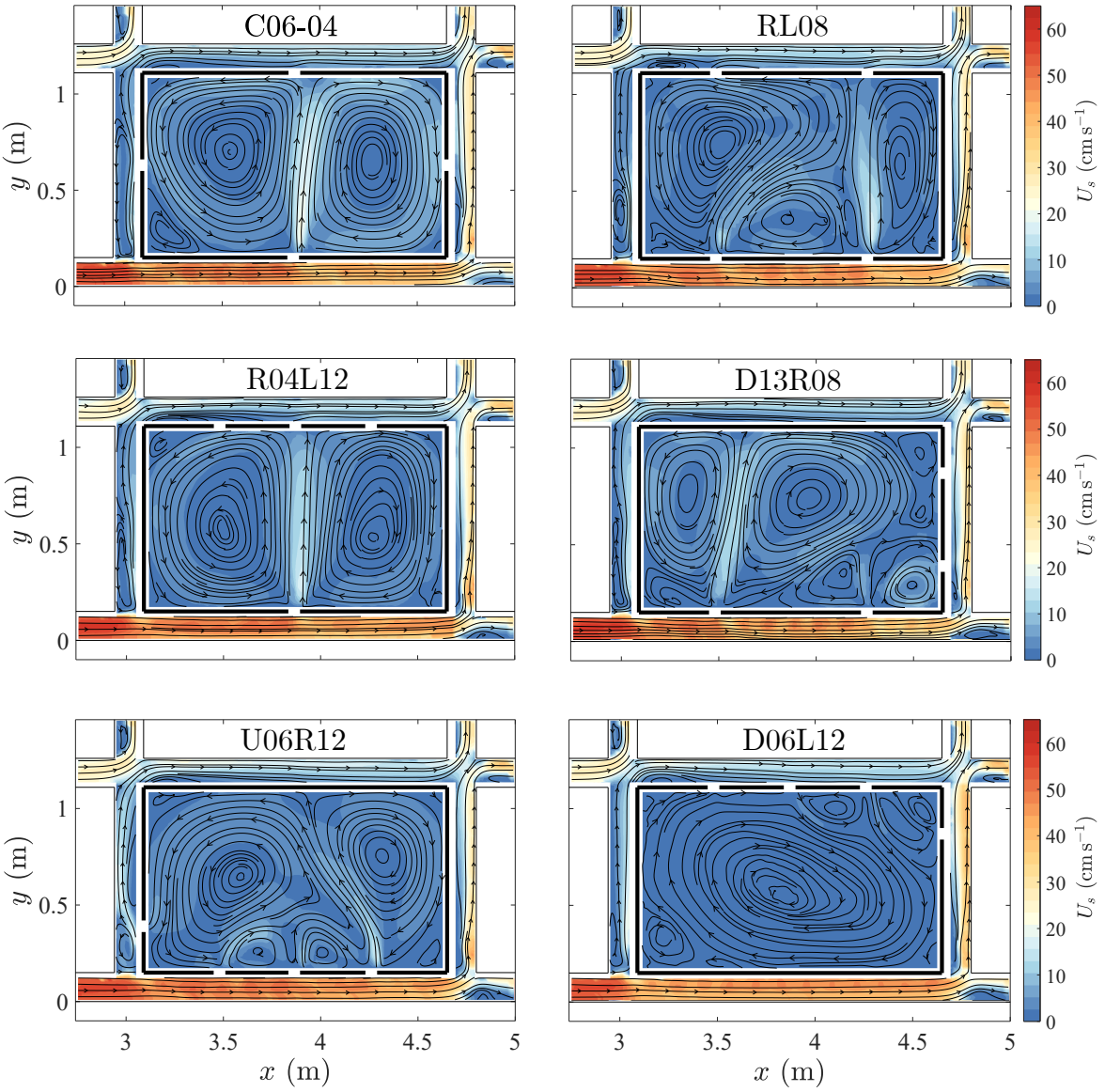

FIGURE 4.19. 2D maps of the time-averaged surface velocity magnitude (model scale), U_s, and streamlines in the streets and within the city block for cases corresponding to *key issue 2*.

discharge, have the greatest impact on the discharge through the block and on the flow patterns within the block. Through this wall, the direction of flow never changes, in all cases the flow was enters the block. Next, in order of significance, are the block wall openings in the downstream street, where the flow is predominantly evacuated. These openings can increase the discharge through the block and modify the flow patterns as well (as observed when comparing cases RL08 and D13R08). The upstream and downstream wall openings have the least impact, these streets are also the ones with the lowest flow discharge among the four streets. The flow direction through the openings in these walls changes from case to case (e.g., as observed in the left street between cases RL08 and R04L12).

4.3.4 Flood hazard to pedestrians

Following the same procedure as described in Section 4.2.4, a 2-D map of flood hazard level for pedestrians is built for all six flow cases of key issue 2 (Figure 4.20). For each flow case, the flood hazard ranges in the streets from *low* to *high*, always having the greatest level of hazard in the right street. In general, the level of hazard in the right street increases locally near the block wall openings. Nevertheless, in case D13R08, a decrease in the level of hazard is observed at the downstream of the right street, mainly because the discharge in this street decreases considerably downstream of the second opening and also the flow depth increases (as explained in Section 4.3.3.1). For the rest of the streets the level of hazard is mainly low to moderate, with local increases in areas near the openings.

Within the block, velocities are much lower than in most streets and therefore the level of hazard is low in most of the area. The moderate hazard areas coincide fairly with the inflow water jets, hence the location of moderate hazard areas change among the different cases, depending on the location of the openings (i.e., depending on the conveyance porosity distribution).

4.4 Conclusions

Steady urban flood flows were experimentally investigated on a 5.4 m long and 3.2 m wide physical model, representing a rectangular urban block and four adjacent streets. The focus of the study was on assessing the effects of the porosity of the urban block walls (openings such as gates, windows and doors) on the spatial distribution of flow depth and velocity in a

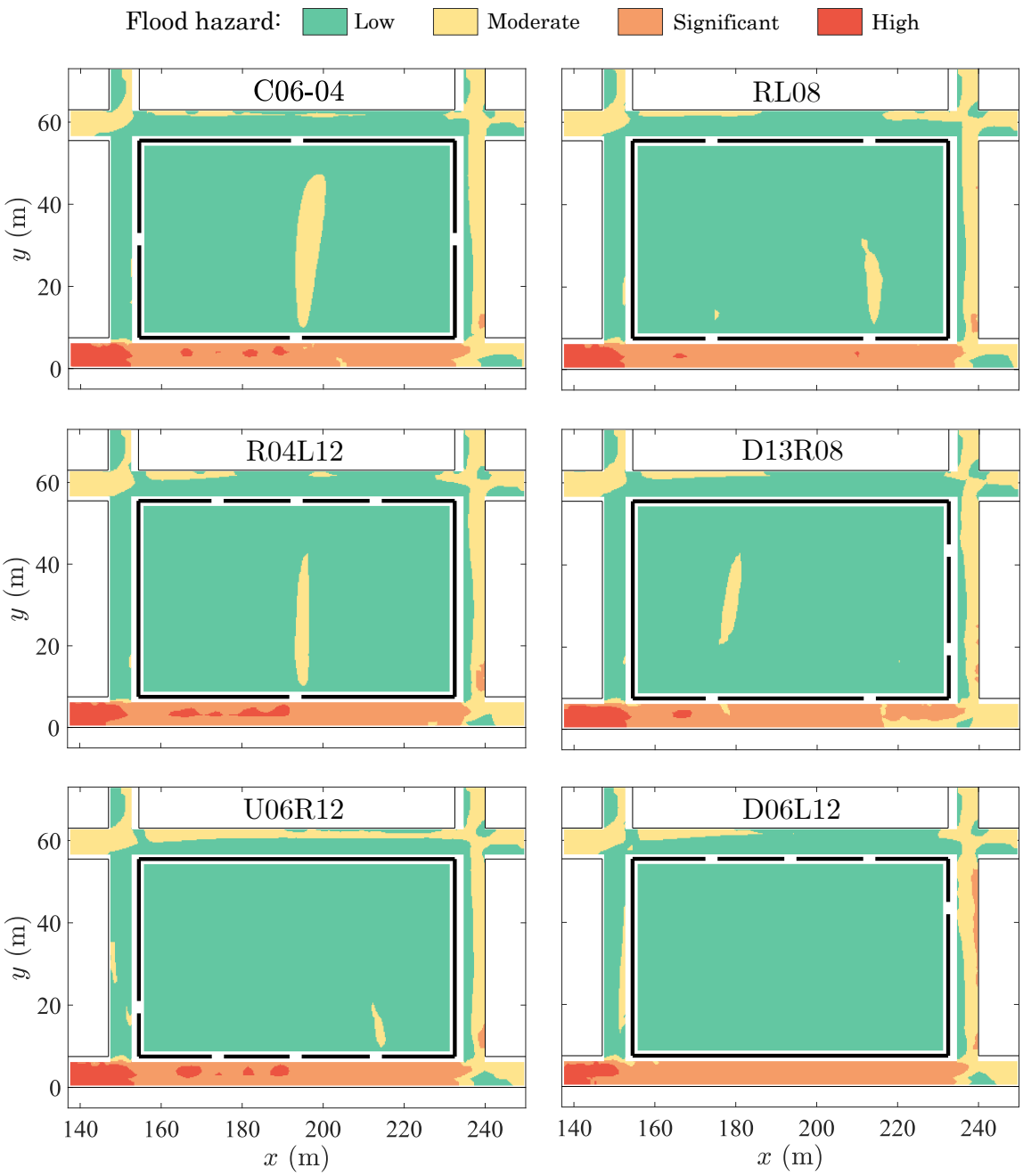

FIGURE 4.20. Flood hazard maps for pedestrians, for each flow case in *key issue 2*, obtained by upscaling flow depths and velocities at the real-world prototype scale.

street network of limited spatial extent. The effect of the block porosity on the flood hazard to pedestrians was also estimated.

Eight flow cases have been studied for key issue 1: a reference case with a non-porous city block; six cases varying the porosity magnitude of the conveyance porosity along the block walls; and an extreme case without the city block. For key issue 2, six cases have been studied, with the same conveyance porosity but varying the spatial distribution. For all these cases, the flow depth and surface velocity were measured in the streets and within the city block. The discharge in each street reach and the exchange discharges between block and streets were also computed.

Conveyance porosity magnitude was found to have a small influence on the spatial distribution of flow depths. In the streets surrounding the block, the average difference in flow depth (compared to the reference case) is approximately of 1.5%, and the maximum difference of 12%. However, as these variations in flow depth occur locally, in the vicinity of the openings, it was found that the conveyance porosity distribution significantly affects the location of these variations. Being always larger in the street through which the flow from the block is evacuated (i.e., downstream street).

When moving away from the city block (i.e., in the street reaches not adjacent to the block), the influence of both, conveyance porosity magnitude and distribution is much lower, with a maximum measured difference about 3% (compared to the reference case). It should be noted that flow depth can strongly vary from either side of a block wall, i.e. between the block and the street: from -14% (smaller flow depth in the street) to +10% (higher flow depth in the street). This result questions the common practices to consider the flow level in the building equal to that in the adjacent street to estimate the potential damages of a flooding scenario.

The impact of the conveyance porosity is far more significant on the local bulk velocity and discharges in the streets surrounding the block (changes in flow discharge up to 70% compared with the reference case). Inside the block, the value and distribution of the porosity have a significant influence on the flow pattern. The number and size of the recirculating flow cells are mainly driven by the magnitude and locations of the exchange inflows and outflows between street and block. However, when moving further away from the block, the influence of the porosity is limited, similar to that observed for flow depths, and could therefore be

neglected.

Within the city block the variation in flow depth among the different cases is minimal when the magnitude and distribution of porosity changes (variations in the range of 3% were found). Oppositely, velocities are largely affected, mainly because they are exarcerbated by the water jets entering the block. The flow velocities then increase when the conveyance porosity is located on the block walls adjacent to the predominant flow street (i.e. the street with the largest discharge). Hence, the magnitude of the conveyance porosity and its distribution have a major impact on flow velocities and flow patterns within the block.

Last, variations in conveyance porosity magnitude and distribution modify the flood hazard to pedestrians only locally, near the openings, both in the streets and within the city block. As a result, it is recommended to take them into account when performing flood hazard maps if a detailed local assessment is required.

CHAPTER 5

CITY BLOCK STORAGE CAPACITY

5.1 Introduction

City blocks can contain indoor open spaces such as parking lots, gardens and courtyards, as well as multiple vehicular and pedestrian access facilities (e.g., doors, gates and passages). Therefore, city blocks can store part of the floodwater volume, which could then modify the flow features in the area. This property to store part of the floodwater volume is here referred to as *storage capacity*, denoted as ϕ.

In Chapter 2 it was shown that there is no research on experimental modelling of urban flooding that takes into account the potential capacity of buildings and city blocks to store floodwater volume. However, a few research work dealt with this topic using 2D numerical modelling. Some of these research works have suggested to use spaces underneath buildings and city blocks as a flood mitigation measure. Among these, Avila et al. (2016), based on 1D-2D numerical modelling, proposed the use of existing tanks underneath houses and buildings for the storage of floodwater volume, reporting that by storing 3 - 17% of this volume, the peak discharge can be reduced by 25 to 75% in the watershed under study.

During a flood event, the combined effects of non-porous buildings and porous buildings were investigated by Abdullah et al. (2011). The authors implemented an algorithm to filter LiDAR data, generating a Digital Terrain Model (DTM) that detected and classified

buildings as: (*i*) impervious; (*ii*) with basements; and (*iii*) with internal ground spaces. By applying this DEM in 1D/2D numerical modelling, they reported on average a 40% reduction in flow depths within the study area when incorporating this storage spaces in buildings, as well as better agreement with recorded data from real-world flood events. Huang et al. (2014a) also incorporated runoff storage in ground spaces within buildings in a 2D numerical model once the flood flow exceeded a defined threshold elevation. They concluded that the runoff volume storage in buildings reduced the flow depth within the urban area, but that flash flooding could still cause major impacts due to the rapidly increasing flow depth and quick flood propagation. Finally, Paquier et al. (2019) studied the sensitivity of input parameters in 2D numerical modelling of urban flooding, including building treatment. The authors found that by allowing floodwaters to be stored in the building-free areas within the city blocks (e.g., gardens, courtyards, etc.) the maximum flow depth in the study area was hardly reduced ($< 1\%$) and the maximum velocity was reduced by only 5%, compared to a simulation where the city blocks were treated as non-porous elements.

With the limited existing results detailed above, no definitive conclusion can be drawn on the effect of internal storage areas on flood flow features. A number of questions therefore arise:

1. Can the floodwater volume stored within the city block mitigate the peak discharge in the street network?

2. How ϕ modifies the flood flow features in the street and within the city block?

3. How the unsteadiness degree of the inflow discharge can modifies the flood flow features in the street and within the city block?

The study of the effect of the storage capacity detailed below focuses on these questions.

5.2 Inflow conditions

The experiments dedicated to study the influence of the storage capacity of the city block, ϕ, are conducted in the experimental set-up *variant 2* (Figure 3.5), under steady and unsteady flow conditions. Three different inflow hydrographs are considered (Figure 5.1.A). They have the same peak discharge ($Q_{pk} \approx 5$ ls^{-1}) but different features, i.e. the rising time,

T_r, the falling time, T_f, and the total floodwater volume dispatched, V (Figure 5.1.B). For each feature the magnitude is either *Small* (denoted as S) or *Large* (denoted as L). These characteristics are shown on each inflow hydrograph label, the first, second and third letters after H corresponds to the magnitude of T_r, T_f and V. H.LSS thus refers to an inflow hydrograph with large T_r, small T_f and small V, and for the other two inflow hydrographs, the label also shows the magnitude of each characteristic. All characteristics of the three inflow hydrographs are listed in Table 5.1. The values are averaged over the 50 inflow hydrograph replicates (as explained in Section 3.3.1.1), and are thus indicated with notation $\langle\rangle$.

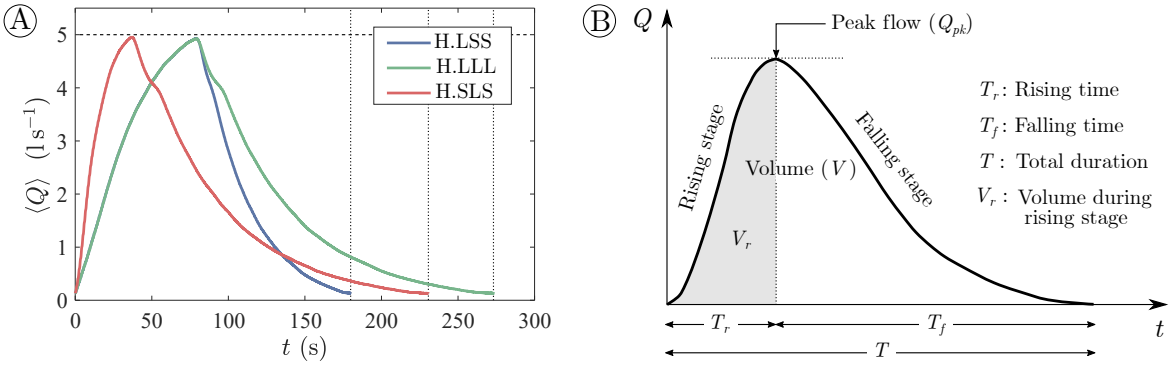

FIGURE 5.1. (A) Inflow hydrographs considered, listed in Table 5.1. The minimum recorded discharge is 0.13 l s^{-1}, as explained in the Section 3.3.1.1. (B) Sketch of the inflow hydrograph characteristics listed in Table 5.1.

The unsteadiness degree of each of the three inflow hydrographs is quantified using the parameter α proposed by Nezu and Nakagawa (1993), which involves the rising speed of the free-surface, S, and the convection velocity of turbulent eddies, U_c, defined as:

$$S = \frac{d_{pk} - d_{bs}}{T_r} \tag{5.1}$$

$$U_c = \frac{U_{bs} + U_{pk}}{2} \tag{5.2}$$

$$\alpha = \frac{S}{U_c} = \frac{2(d_{pk} - d_{bs})}{T_r(U_{bs} + U_{pk})} \tag{5.3}$$

where subscripts bs and pk refer to the base flow and peak flow, respectively (e.g., d_{bs} is the base flow depth and d_{pk} is the peak flow depth).

In the present work, no base flow is considered, thus the city block has no stored water

TABLE 5.1. Characteristics of the inflow hydrographs, where Q_{pk} is the peak discharge, T_r is the rising time, T_f is the falling time, T is the total duration, V_r is the volume dispatched from $t = 0$ to $t = T_r$ (Figure 5.1), V is the total volume dispatched by the inflow hydrograph and α is the unsteadiness parameter (Eq. 5.3) for the rising (r) and falling (f) stages of the inflow hydrograph.

Inflow Hydrograph	$\langle Q_{pk} \rangle$ (l s^{-1})	$\langle T_r \rangle$ (s)	$\langle T_f \rangle$ (s)	$\langle T \rangle$ (s)	$\langle V_r \rangle$ (l)	$\langle V \rangle$ (l)	α_r $\times 10^{-3}$	α_f $\times 10^{-3}$
H.LSS	4.94	79.40	100.50	179.90	251.34	408.12	2.22	1.54
H.LLL	4.93	79.38	193.88	273.26	250.33	525.46	2.20	0.79
H.SLS	4.95	37.16	193.54	230.70	124.67	400.29	4.49	0.77

before the begining of the inflow hydrograph. However, as an inflow hydrograph starts just at the end of the previous hydrograph, a residual volume remains in the experimental set-up between two inflow hydrograph replicates. For this reason, d_{bs} is very small but not zero. Conversely, as the velocity of this residual volume is almost nil, it is considered that $U_{bs} = 0$. For each inflow hydrograph, two values of the unsteadiness parameter are computed and reported in Table 5.1, one corresponding to the rising stage, α_r (computed with Eq. 5.3), and the other to the falling stage, α_f (replacing T_r by T_f in Eq. 5.3). These values are estimated at the measurement point P_{in} along the inlet street (Figure 3.12). For H.LSS and H.LLL, with the same T_r, α_r is quite similar ($\sim 2.2 \times 10^{-3}$), while for H.SLS, with a smaller T_r, α_r is higher and equal to 4.5×10^{-3}. The same analysis hold for α_f, which increases as T_f decreases.

In addition to unsteady flows, steady flows are also investigated with five inflow discharges, Q_{in}= 1, 2, 3, 4 and 5 l s^{-1}, for comparison with the unsteady flow tests.

For these experiments, the horizontal scale ratio, λ_{xy}, is equal to 50 (equal to that considered for the experiments in the previous chapter) and the vertical scale ratio, λ_z, is equal to 30. Therefore, the street and city block dimensions at the prototype scale are the same as in the previous chapter: the city block is 78 m long by 48 m wide, with a 3 m wide opening through each of the four sidewalls and the streets are 7.5 m wide. The characteristics of the different inflow hydrographs at the prototype scale are reported in Table 5.2.

TABLE 5.2. Characteristics of the inflow hydrographs at the *prototype scale*.

Inflow Hydrograph	$Q_{pk,P}$ (m^3 s^{-1})	$T_{r,P}$ (min)	$T_{f,P}$ (min)	T_P (min)	V_P (m^3)
H.LSS	40.50	12.08	15.29	27.37	30609
H.LLL	40.50	12.08	29.50	41.58	39426
H.SLS	40.67	5.65	29.45	35.10	30035

5.3 Variable storage capacity within the city block

Within the city block, non-porous rectangular buildings (with smooth plastic side walls) of decreasing size are successively placed at the center of the city block (Figure 3.5) to increase the block storage capacity, ϕ, defined as:

$$\phi = \frac{A_B - A_b}{A_B} \tag{5.4}$$

where A_B is the total horizontal surface within the city block and A_b is the horizontal surface covered by the non-porous building.

Five different cases are considered, as depicted in Figure 5.2. First, a reference scenario, for which the city block is completely closed ($A_B = A_b$), i.e., storage capacity $\phi = 0$ (Figure 5.2.A). Then, three non-porous rectangular buildings of different size are placed within the block, to vary the storage capacity. Their dimensions are 1.19 m $\times$ 0.59 m for $\phi = 0.5$ (Figure 5.2.B), 0.96 m $\times$ 0.36 m for $\phi = 0.75$ (Figure 5.2.C), and 0.78 m $\times$ 0.18 m for $\phi = 0.90$ (Figure 5.2.D). Last, the maximum possible storage capacity, i.e., $\phi = 1$, is obtained by keeping the city block empty (Figure 5.2.E).

5.4 Measured flow features

5.4.1 General flow patterns

For all unsteady flow tests, the flow in the right street on the side of the city block, is supercritical (Fr $\approx$ 1.6, Re $\approx$ 80000), and the surface velocity is maximum, with $U_s \approx 90$ cm s^{-1} and flow depth $d \approx 3.0$ cm . In the upstream and downstream streets, a hydraulic jump

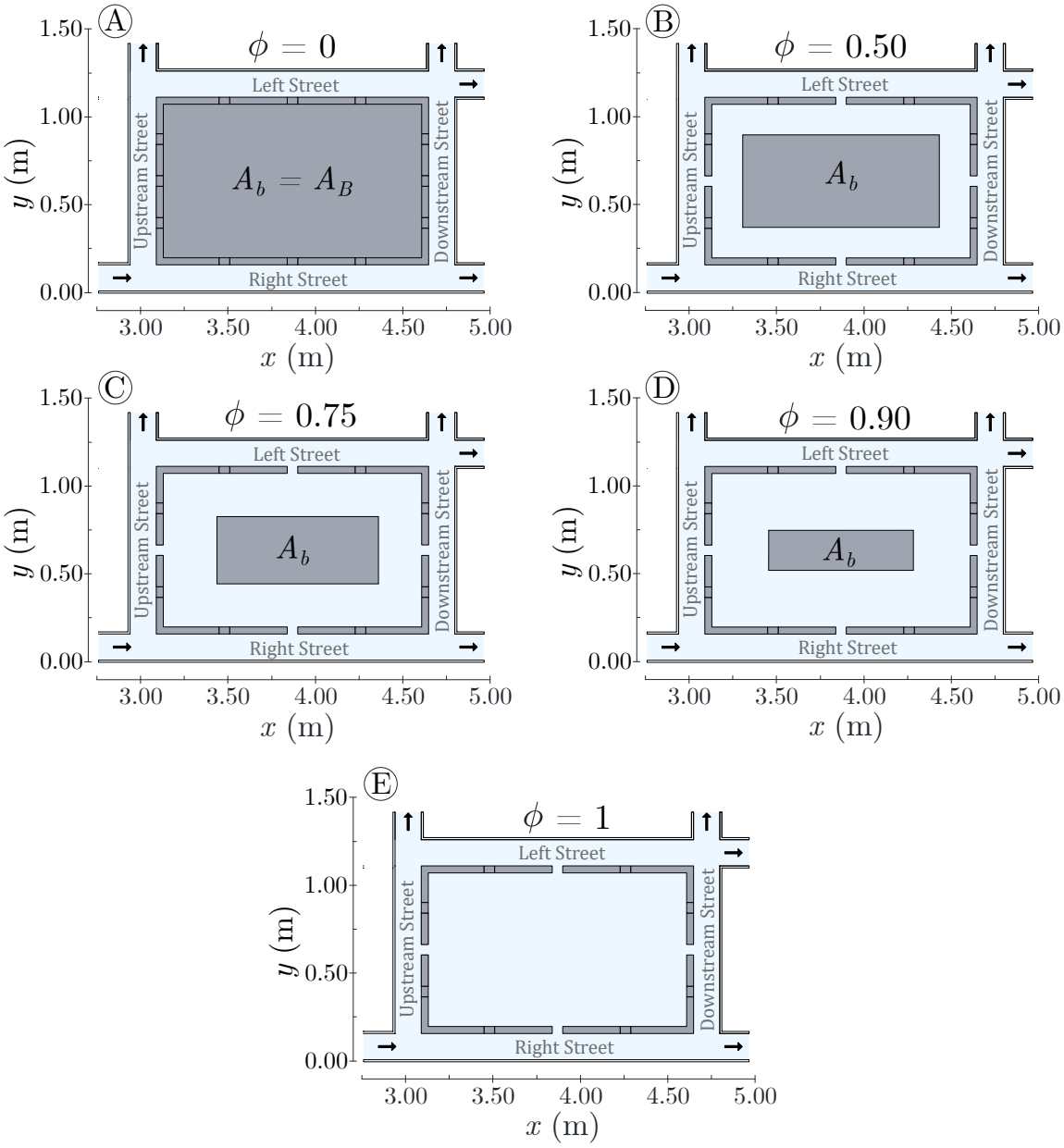

FIGURE 5.2. Variable block storage capacity, ϕ (Eq. 5.4) within the city block. The case with $\phi = 0$ serves as the reference flow condition.

makes the flow pass to subcritical regime (Figure 5.3), with a maximum value of $d \approx 2.0$ cm. In the left street, the flow remains subcritical (Fr ≈ 0.5, Re ≈ 13000), the maximum flow depth is also 2.0 cm and the maximum velocity is about 21 cm s^{-1}.

Within the city block, water enters mainly through the opening connected to the right street with a maximum value of $U_s \approx 33$ cm s^{-1}. The flow then goes around the non-porous building, with several recirculation cells taking place in the area between the building and the city block. The flow finally leaves the block mainly through the openings connected to the left and downstream streets. The free surface is more or less horizontal most of the time, with the flow depth always being slightly lower in the upstream zone (at P_{BU}) than in the downstream zone (at P_{BD}) due to the longitudinal slope, S_{0_x}. The maximum flow depths range from 1.6 to 2.0 cm, depending on the block storage capacity value and the inflow hydrograph. Finally, the outflow discharges at the 4 outlets is quite different, being much greater at outlet 1 (right street), in the range of 61-66% of the total outflow discharge. The discharges through outlets 2 and 3 (left and downstream streets) are similar, about 10%, and the discharge at outlet 4 (upstream street) ranges from 15 to 18% of the total outflow discharge. Figure 5.4 displays all the inflow and outflow hydrographs for the reference flows, i.e., with $\phi = 0$.

The features of the steady flows are similar for some parameters to those described for the unsteady flows, with some noticeable differences for others that will be discussed in the following sections.

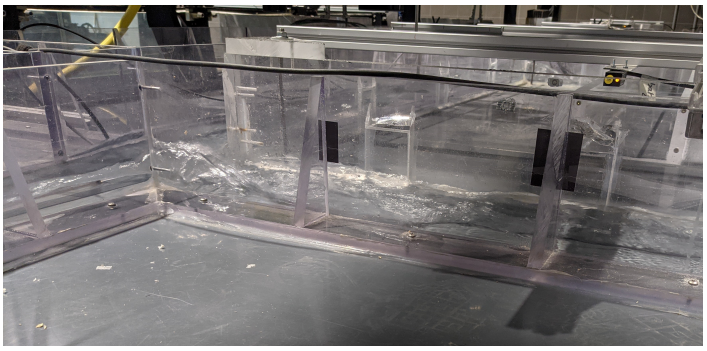

FIGURE 5.3. Hydraulic jump in the downstream street, found for all flows corresponding to *key issue 3*.

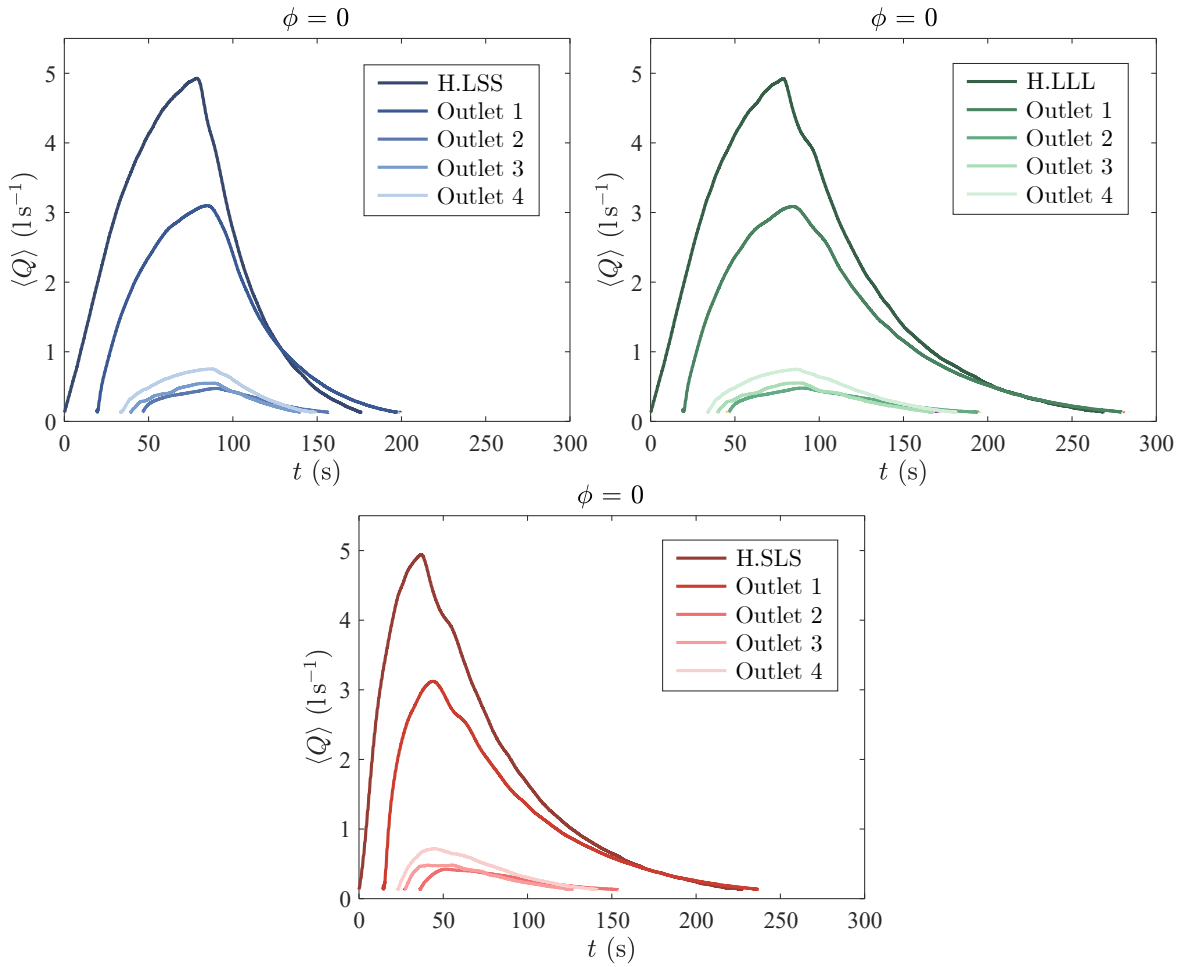

FIGURE 5.4. Inflow hydrographs (H.LSS, H.LLL and H.SLS) and outflow hydrographs (at outlets 1,2,3 and 4) for the reference flows, i.e., $\phi = 0$.

5.4.2 Outflow discharges

Since the city block stores part of the floodwater volume (when $\phi \neq 0$), an attenuation of the peak discharge, Q_{pk}, in the outflow hydrographs is expected, with respect to the reference scenario (with no storage capacity, i.e., $\phi = 0$). This is observed for the outflow hydrograph 1 (outlet 1) for all storage capacity values (Figure 5.5), and also most of the storage capacity values for the outflow hydrograph 3 (outlet 3). However, flow exchanges between the city block and streets can increase the discharge in streets reaches where the exchange flow is directed from the block to the street, as shown in previous Chapter. This is the case for outflow hydrograph 4 (outlet 4), for which an increased peak discharge is observed (Figure 5.5), except for the cases of H.SLS (whit the largest α_r). Consequently, the variations in the peak discharge are not only related to the block storage capacity, ϕ and the conveyance porosity of its walls, ψ, but also to the different flow pathways resulting from the modification of the arrangement within the block. This is supported by the results for the steady flow case ($Q_{in} = 5\ \mathrm{l\,s^{-1}}$), for which there is no floodwater volume storage variation within the block (same discharge enters and leaves the block), but still some influence is observed when the space within the block is modified, as shown by the circular markers in Figure 5.5.

The bottom plot in Figure 5.5 depicts the relative change in peak discharge for the global outflow hydrograph, for which the four outflow hydrographs are combined. It confirms that overall, increasing the storage capacity of the city block attenuates the peak discharge for all unsteady flows. The largest relative change occurs for the inflow hydrograph H.SLS, with a 10% reduced peak discharge when $\phi = 1$. For H.LSS and H.LLL (inflow hydrographs with similar α_r), the peak discharge attenuation is very similar, 5.9% and 5.2%, respectively. Thus, the unsteadiness of the inflow hydrograph strongly impacts the peak discharge of the outflow hydrographs. Furthermore, the larger α_r is, the greater the peak discharge attenuation of the global outflow hydrograph.

In addition, Figure 5.6 shows for the different storage capacity values the relative change respect to the reference case in time lag, denoted as t_L and defined as the time difference between the peak discharges of the inflow and global outflow hydrographs. From $\phi = 0$ to $\phi = 0.5$ the time lag increases by about 10% in all three inflow hydrographs, but it does not increases notably for larger storage capacity values. Therefore, the relative increase in time lag seems to be mostly related to the conveyance porosity of the block, ψ (openings in the

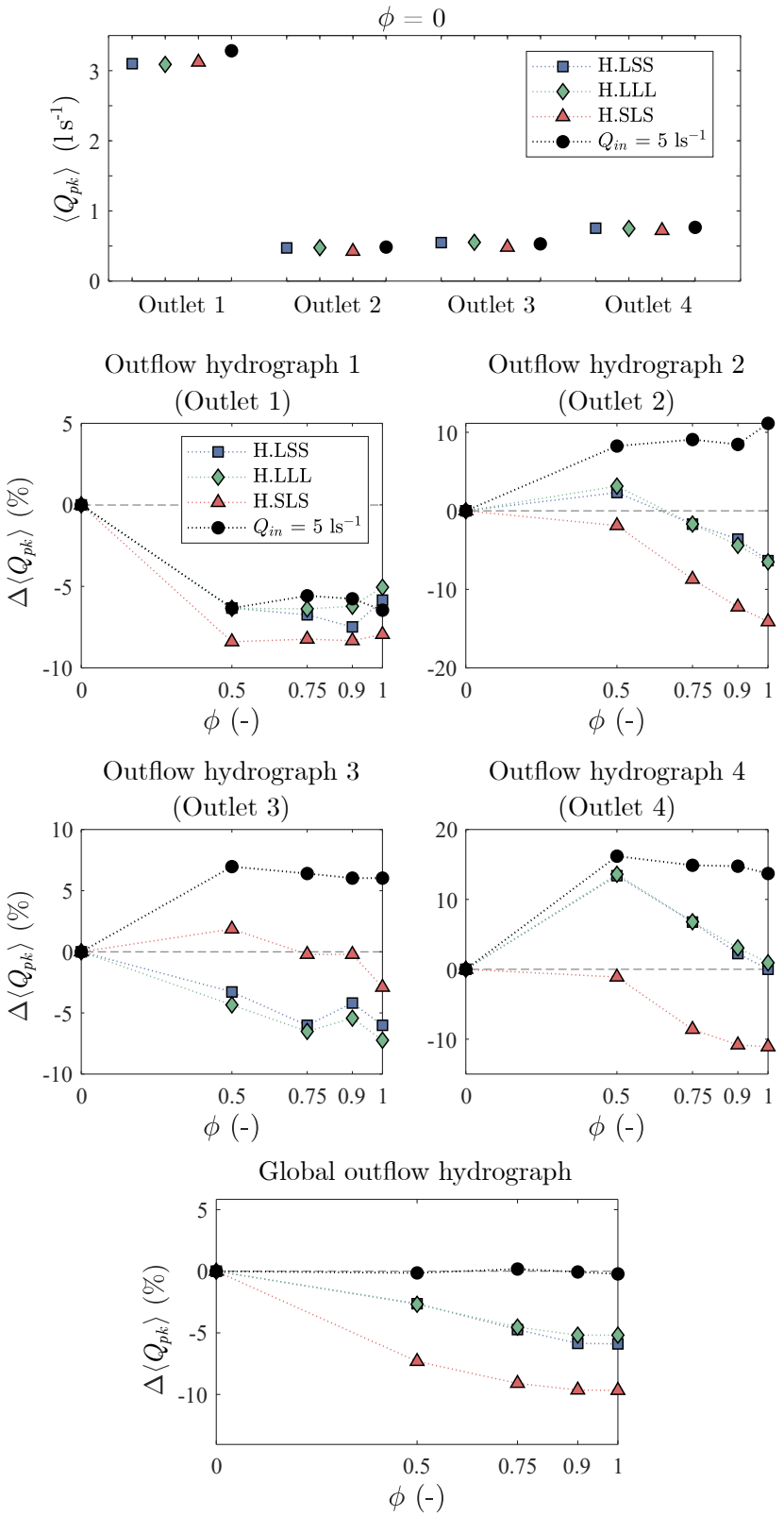

FIGURE 5.5. Peak discharge, $\langle Q_{pk} \rangle$, of each outflow hydrograph for the reference case (i.e., for $\phi = 0$) at the top. Relative change in peak discharge, $\Delta\langle Q_{pk} \rangle$, for each outflow hydrograph (centre) and for the global outflow hydrograph (bottom) with respect to the reference case, as a function of the block storage capacity, ϕ. Results are shown for the three inflow hydrographs (H.LSS, H.LLL and H.SLS) and for the steady flow case with $Q_{in} = 5\,\mathrm{l\,s^{-1}}$.

walls), rather than the storage capacity, ϕ.

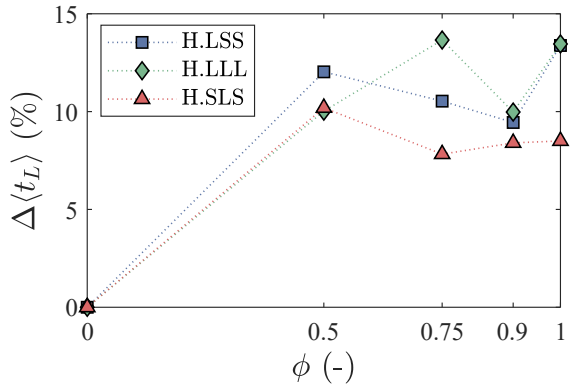

FIGURE 5.6. Relative change in time lag, $\Delta\langle t_L\rangle$, between the peak discharges of the inflow and global outflow hydrographs, with respect to the reference case ($\phi = 0$) as a function of the storage capacity of the city block.

5.4.3 Flow depth

TABLE 5.3. Maximum flow depths, $\langle d_{max}\rangle$, for the unsteady flows (H.LSS, H.LLL and H.SLS) and time-averaged flow depths, d, for the steady flow ($Q_{in} = 5$ l s^{-1}), corresponding to the reference case (i.e., $\phi = 0$), measured along the urban area at locations: P_{in}, P_{RS}, P_{LS}, P_{US}, P_{DS}, P_{out1}, P_{out2}, P_{out3} and P_{out4} (see Figure 3.12).

$\phi = 0$	$\langle d_{max}\rangle$ (mm)								
Inflow hydrograph	P_{in}	P_{RS}	P_{LS}	P_{US}	P_{DS}	P_{out1}	P_{out2}	P_{out3}	P_{out4}
H.LSS	53.98	32.67	18.76	16.68	17.30	29.26	8.88	13.04	15.98
H.LLL	54.61	32.73	18.86	17.05	17.46	29.32	9.29	13.03	15.84
H.SLS	53.58	32.64	18.39	17.11	17.86	28.96	9.14	12.29	15.64
$Q_{in} = 5$ l s^{-1}	57.73	31.59	18.96	17.34	16.90	29.79	7.29	12.65	15.97

The storage capacity of the city block strongly affects flow depths in the surrounding streets, as previously reported by Huang et al. (2014a), but some particularities are found herein. In the right street (street with the dominant discharge) the maximum flow depth, d_{max}, barely changes for all flows (steady and unsteady), limited to 4%, compared to the reference case (Figure 5.7). Conversely, for the rest of the streets (left, upstream and downstream), this change is much more noticeable and it differs according to the inflow hydrograph unsteadiness, α_r. For H.SLS, d_{max} always decreases, up to -13% in the right and downstream streets when $\phi = 1$. For H.LSS and H.LLL, there is always an initial increase in d_{max} (i.e., from $\phi = 0$ to $\phi = 0.5$), then with the increase of ϕ, d_{max} decreases. Therefore for these two inflow hydrographs, the initial increase is related to the block conveyance porosity, ψ, (same

as for the steady flow $Q_{in} = 5\,\mathrm{l\,s^{-1}}$) and contrary to H.SLS, for most cases, d_{max} is always higher than in the reference case, up to 11% in the upstream street.

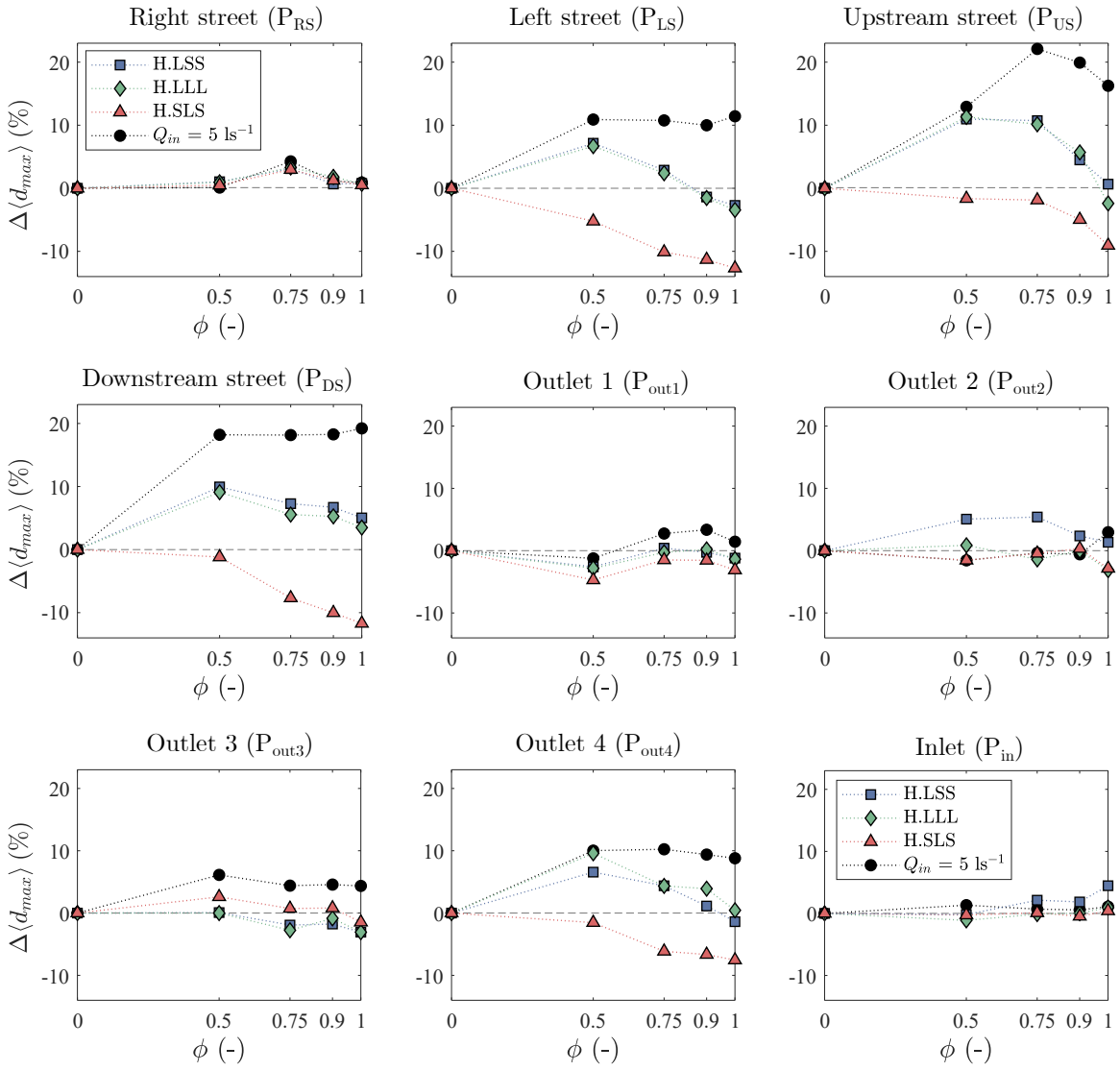

FIGURE 5.7. Relative change in maximum flow depth, $\Delta\langle d_{max}\rangle$, with respect to the reference scenario (d_{max} for $\phi = 0$) as a function of the storage porosity, for the three inflow hydrographs and the steady flow with $Q_{in} = 5\,\mathrm{l\,s^{-1}}$. The plots are shown for the street reaches surrounding the city block (locations $\mathrm{P_{RS}}$, $\mathrm{P_{LS}}$, $\mathrm{P_{US}}$ and $\mathrm{P_{DS}}$) and for the street reaches not adjacent to the block (locations $\mathrm{P_{in}}$, $\mathrm{P_{out1}}$, $\mathrm{P_{out2}}$, $\mathrm{P_{out3}}$ and $\mathrm{P_{out4}}$), see Figure 3.12

For the street reaches not adjacent to the block (inlet street and street reaches next to the outlets) the effect of storage capacity, ϕ, is reduced in most cases. The smallest effect is mainly found in the inlet street (location $\mathrm{P_{in}}$, see Figure 3.12), where a maximum relative change of about 4%, respect to the reference case is observed. For the reaches next to the outlets, the influence of ϕ is slightly higher, mainly in the reach next to the outlet 4, with a

maximum relative change of 10% compared to the reference case.

Within the city block, the flow depth was averaged between locations P_{BU} and P_{BD} (Figure 3.12). The flow depth decreases when the storage capacity increases (Figure 5.8.A). Moreover, for the steady flow case, $Q_{in} = 5\ \mathrm{l s^{-1}}$, and for all storage porosity values, the flow depths are greater than those observed in unsteady flows, up to 30%, for the case with the maximum storage capacity, $\phi = 1$. Here, the evolution of the flow depth is again very similar for the inflow hydrographs H.LSS and H.LLL. This proves the significant incidence that the rising stage unsteadiness, α_r, has on the flow depth within the block, and thus on the stored floodwater volume.

The maximum flow depths (Figure 5.8.A) permit to compute, the maximum floodwater volumes stored within the block, $V_{B,max}$, for the three inflow hydrographs and all storage capacity values. These volumes are normalised by the volume dispatched by each inflow hydrograph during the rising stage, V_r[1] (Figure 5.8.B). H.LSS and H.LLL, inflow hydrographs with same T_r and V_r, exhibit similar $V_{B,max}/V_r$ ratios for all ϕ values. For H.SLS, the stored volume related to V_r is much greater than for the other two, by about 100%, which explains the higher peak discharge attenuation, and also the greatest influence on maximum flow depths, d_{max}, observed for this inflow hydrograph. This is attributed to the influence of a high α_r value.

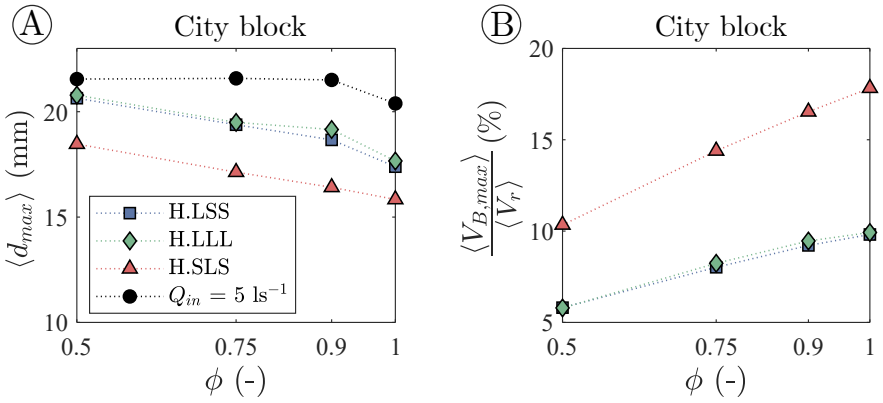

FIGURE 5.8. (A) Maximum flow depth, d_{max}, within the city block (averaged between the two measurement points, P_{BU} and P_{BD}) as a function of the storage capacity, ϕ, for the three inflow hydrographs, and flow depth for the steady-state flow $Q_{in} = 5\ \mathrm{l s^{-1}}$. (B) Maximum floodwater volume stored within the city block, $V_{B_{max}}$, as a function of the storage capacity, ϕ, for the three inflow hydrographs, normalised by the floodwater volume dispatched during the rising stage, V_r

[1]Due to the strong influence of the inflow hydrograph rising stage unsteadiness, α_r on d_{max} within the block, V_r was chosen instead of V to normalize the floodwater volumes stored within the block.

5.4.4 Surface velocities

For the unsteady tests, the evolution of the surface velocity field over time was only measured in the right and left streets[2] (at P_{RS} and P_{LS} locations, respectively, see Figure 3.20) and within the city block, by using the inflow hydrograph H.LSS for all storage capacity values. In the right street, where the flow regime is supercritical in steady flow and during most of the unsteady flow, the maximum surface velocity is about equal in both steady and unsteady flows and hardly varies when the block storage capacity increases (Figure 5.9.A), with a maximum variation of about 2%, compared to the reference case (Figure 5.9.B). For the left street, the flow regime is subcritical and the maximum surface velocity when $\phi = 0$ is very similar for both steady and unsteady flows, 22 cm s^{-1} and 21 cm s^{-1}, respectively (approximately 1/4 of the maximum velocity found on the right street), see Figure 5.9.A. Contrary to the right street, in this street there is a strong variation of $U_{s,max}$ with respect to the reference case when ϕ increases. For steady flow, this variation ranges from -30% to -20%, while for unsteady flow it ranges from -9% to 10% when $\phi = 0.5$ increase to $\phi = 1$ (Figure 5.9.B).

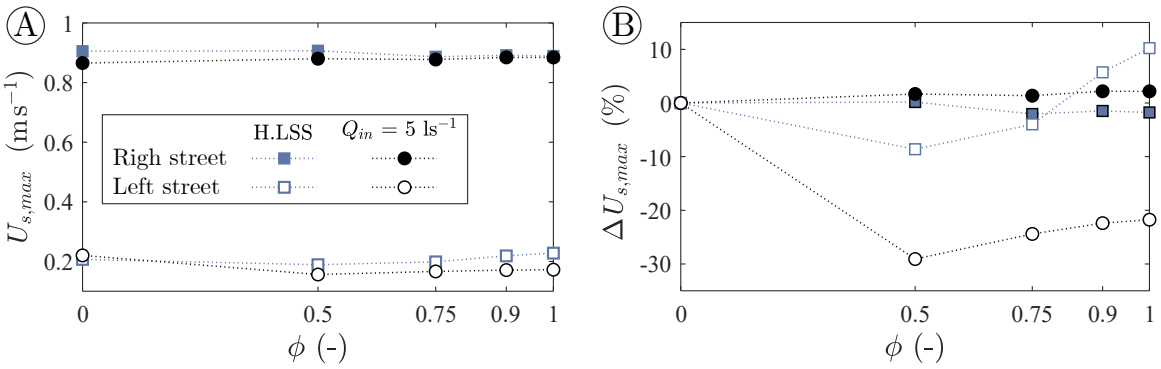

FIGURE 5.9. Maximum surface velocity, $U_{s,max}$ and relative difference in maximum velocity, $\Delta U_{s,max}$, with respect to the reference scenario ($\phi = 0$), as a function of the storage capacity of the city block, in right and left streets, for inflow hydrograph H.LSS and the steady flow case, $Q_{in} = 5$ ls^{-1}.

Within the city block, the unsteady surface velocity magnitude, U_s, ranges from 0 to 33 cm s^{-1}. For each porosity value (when $\phi \neq 0$), five 2D surface velocity maps are plotted in Figure 5.10: two maps during the rising stage (identified by labels R50 and R75), one map

[2]The presence of an oblique hydraulic jump, which moved along the street with the change in discharge, made the use of the LSPIV technique for velocity estimation in the upstream and downstream streets unfeasible.

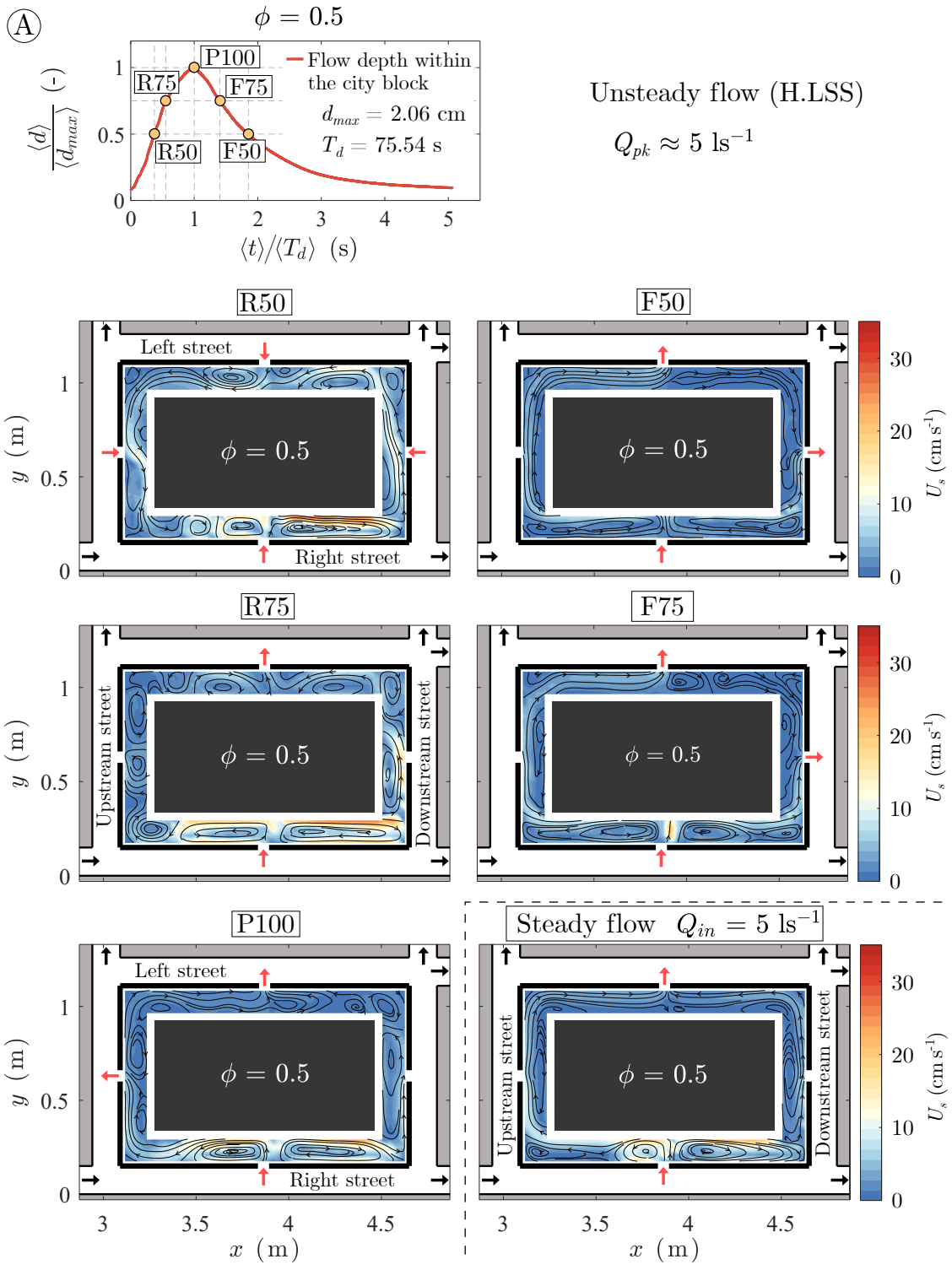

FIGURE 5.10. Surface velocity, U_s, within the city block for cases $\phi = 0.50$ (A), 0.75 (B), 0.9 (C) and 1 (D) for unsteady flow (H.LSS), at five different instants: at 50% and 75% of d_{max}, during the rising stage (R50 and R75) and falling stage (F50 and F75), and at d_{max} (P100). For steady flow with $Q_{in} = 5$ ls^{-1} the velocity map is shown at the bottom. Black arrows indicate the flow direction in the streets and red arrows through the openings in the block walls. At the top is shown the stage hydrograph within the city block, where T_d is the time between the base and maximum flow depths within the city block.

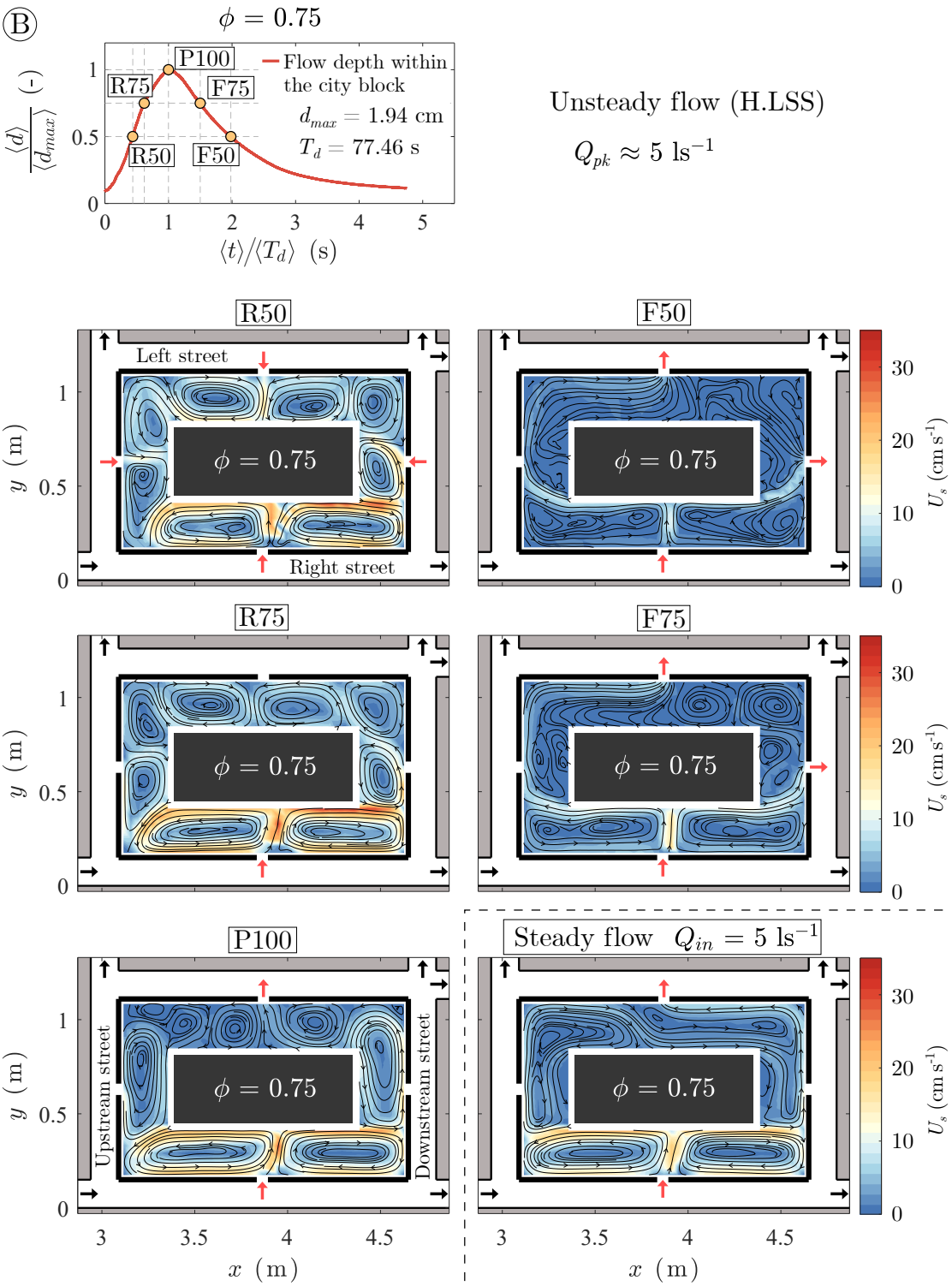

FIGURE 5.10. (Continued).

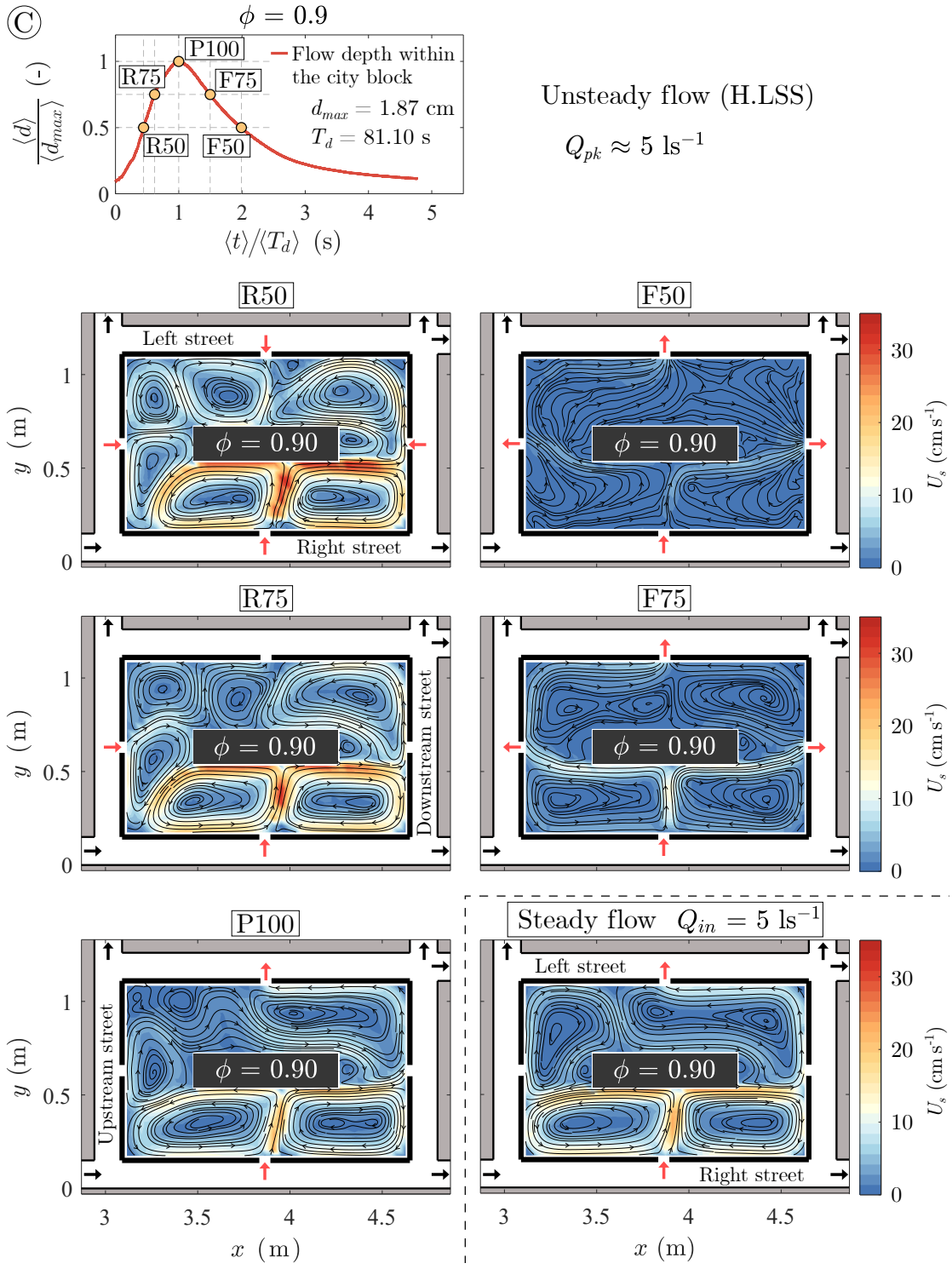

FIGURE 5.10. (Continued).

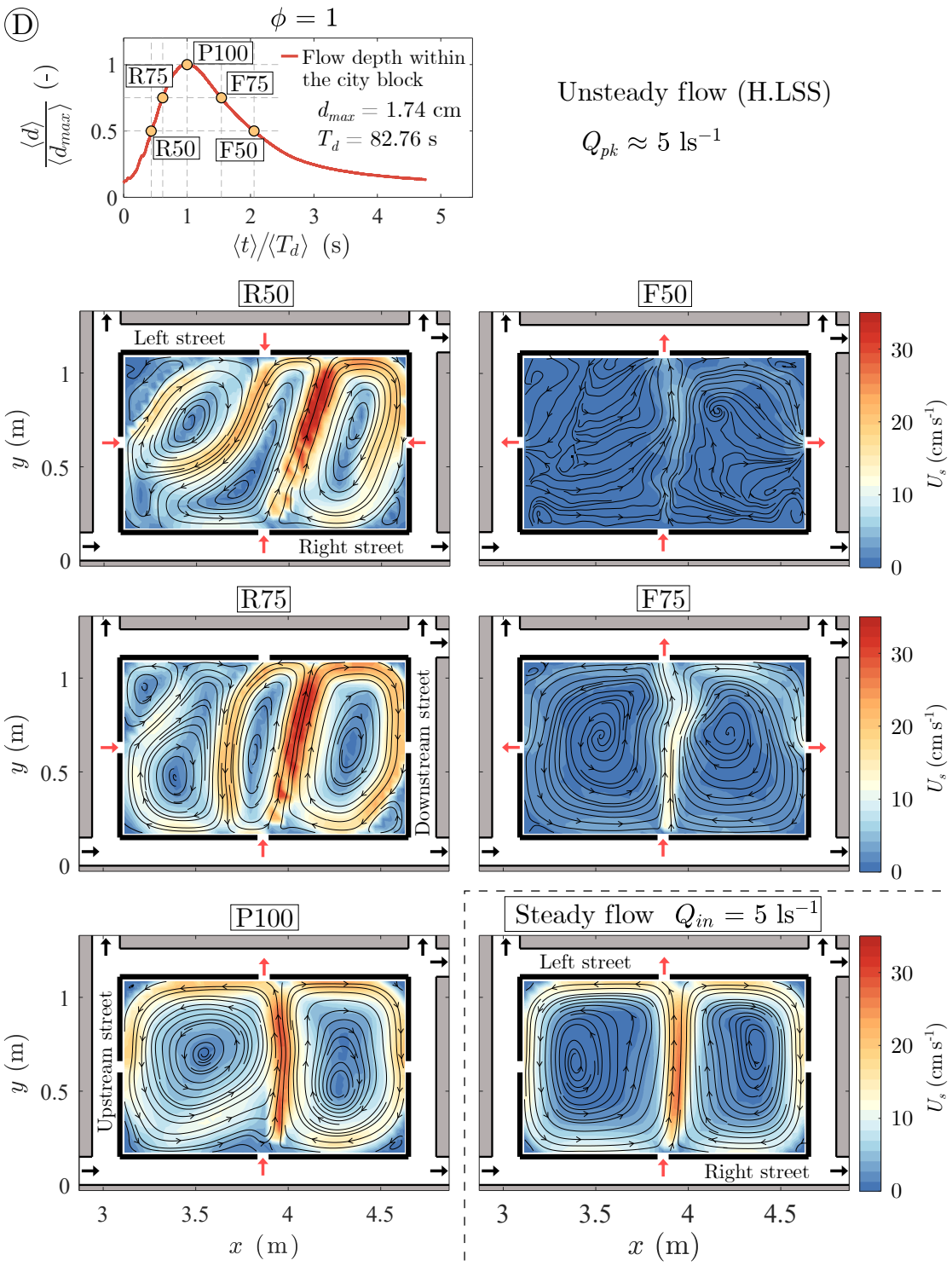

FIGURE 5.10. (Continued).

at maximum flow depth, d_{max}, within the block (identified by the label P100) and two more during the falling stage (identified by labels F50 and F75). The numbers 50 and 75 denote 50% and 75% of d_{max}, respectively. For all ϕ values, the velocities during the rising stage are greater than during the falling stage. Among all cases, the highest maximum velocity is obtained for $\phi = 1$, with a magnitude about 7% higher than in the other scenarios. The main intrusion flow into the block occurs through the right street opening, and thus the greatest velocities take place in this region. The water jet here, together with the clearance between the block walls and the non-porous building walls, have a great influence on the flow pattern and form a complex recirculation pattern. For $\phi = 0.5$, where the clearance is the smallest, up to ten recirculation cells are observed at R75 (Figure 5.10.A). The number of recirculating cells then decreases with the enlargement of the clearance: for $\phi = 0.75$ (Figure 5.10.B), eight cells, $\phi = 0.90$ (Figure 5.10.C), seven cells, and for $\phi = 1$, only five cells, three large and two small (Figure 5.10.D).

For the steady flows, the surface velocity magnitude, ranges from 0 to 28 $\mathrm{cm\,s^{-1}}$, with the maximum velocity recorded when $\phi = 1$. An interesting finding is that for all ϕ values, the maximum velocity in steady flow is lower than in unsteady flow, this difference ranges between 15% and 20%. The number of recirculation cells is also lower in steady flows compared to unsteady flows (at P100), except for $\phi = 1$, where two main cells take place at the flood peak (P100) as in steady flow regime.

5.5 Flood hazard at prototype scale

The Froude similitude detailed in Eqs. 3.13 and 3.14, permits to estimate the velocities and flow depths at the real-world prototype scale. Then, assuming that the surface velocity (measured by the LSPIV technique) equals the depth-averaged velocity, the $U_s - d$ curves in the right and left streets, for steady (indicated with markers in grey tones) and unsteady flows (indicated by coloured dashed lines) for the different ϕ values are integrated in the flood hazard diagram proposed (Section 3.5), see Figure 5.11. In the right street the level of flood hazard evolves from *low* to *high* during the rising stage and opposite during the falling stage. The *high* hazard level occurs during about 60% of the flood duration, mainly due to the elevated velocities measured in this street (Figure 5.9.A). The well known unsteady flow hysteresis, leads to a different level of hazard during the rising and falling stages, mostly for

flow depths below 0.5 m and velocities lower than 3 $\mathrm{m\,s^{-1}}$, always being higher the level of hazard during the rising stage, for a given flow depth and during the falling stage for a given velocity.

The flow depth and particularly the velocities in the left street are lower than in the right street, therefore the hazard evolves only from *low* to *moderate*. The unsteady flow hysteresis produces a more accentuated difference between the rising and falling stages than in the right street. The hysteresis is opposite from the right street: the highest hazard occurs during the falling stage (between $d = 0.5$ m and $d = 0.3$ m), for a given flow depth and during the rising stage for a given velocity. In this street, during the rising stage the flow from the downstream street reaches the crossroad with the left street, a backwater effect is then produced, increasing the flow depth, but not the velocity (Figure 5.11.B). In the rising stage, for $\phi = 0$, the velocity is higher than in all other ϕ cases, however, this does not reflect an increase in the level of hazard, because the velocities and flow depths are hazard low at this stage. In the falling stage, the flow velocity increases when increasing storage capacity, and this increases the level of hazard, from low to moderate.

Something important to note is that for both right and left streets the results for steady flows are closer to the results for unsteady flows during the falling stage of the inflow hydrograph. This might be due to the lower degree of unsteadiness of the inflow hydrograph in this stage (α_f) than in the rising stage (α_r), see Table 5.1.

The hazard criteria was also applied to obtain 2D pedestrian flood hazard maps within the city block for steady and unsteady conditions. For the unsteady flow, five hazard maps are shown for the cases with block storage capacity (from $\phi = 0.5$ to $\phi = 1$) at the same instants as the surface velocity maps shown in section 5.4.4 (at d_{max} and at 50% and 75% of d_{max} in the rising and falling stage), see Figure 5.12. Within the block, the highest velocities were measured during the rising stage, hence for all ϕ values, the level of hazard is also higher during this stage and the hazard is maximum at the maximum flood depth. The level of hazard varies from *low* to *significant*, being always greater in the area near the right street (because of the inflow jet, already mentioned above). A larger area with *significant* hazard level is found when $\phi = 1$, because the jet through the opening in the right street is not dissipated by the interior non-porous building, and thus extends further in the block area.

The hazard maps for steady flow with $Q_{in} = 5$ $\mathrm{l\,s^{-1}}$ (Figure 5.12, bottom) slightly differ

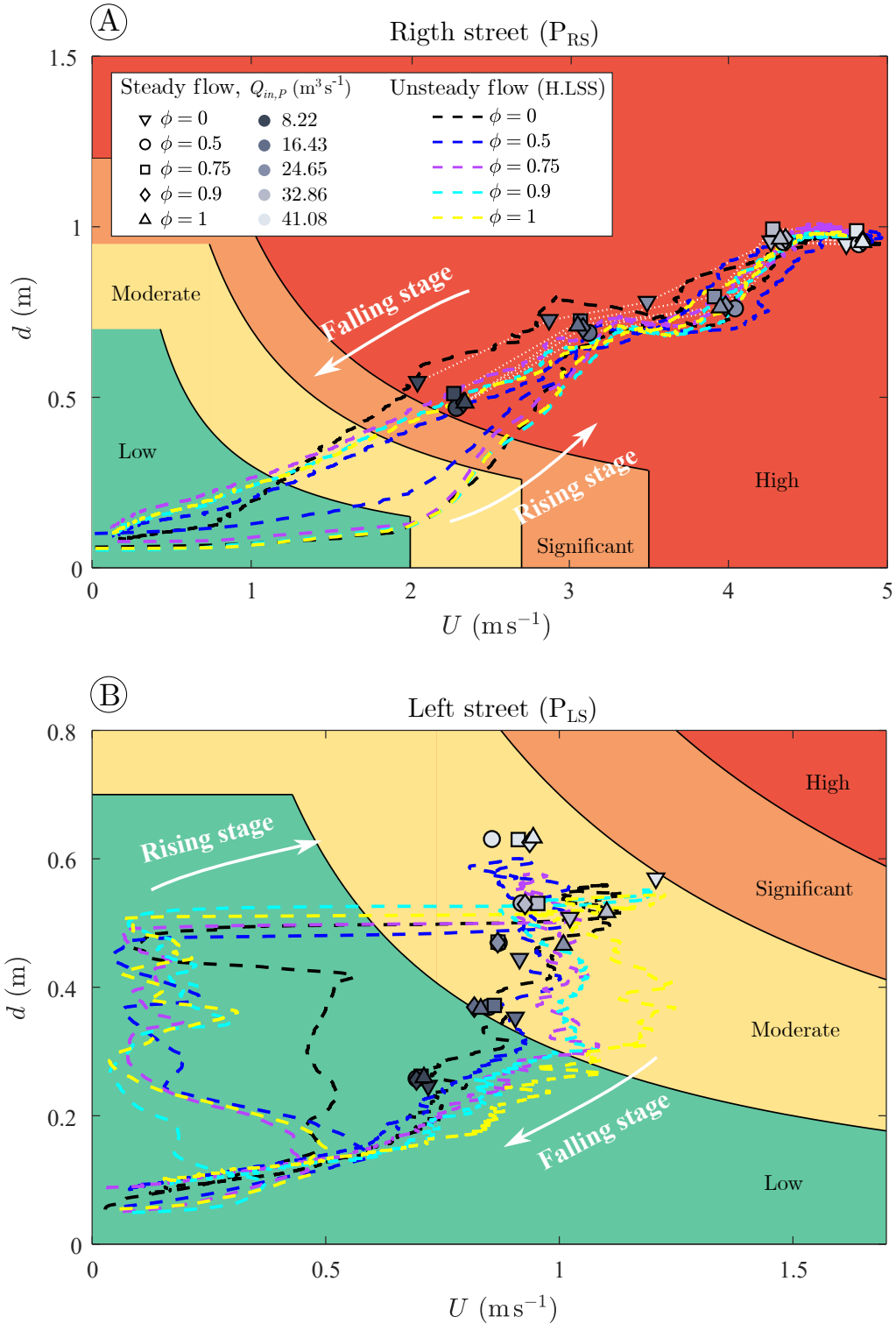

FIGURE 5.11. Curves $U_s - d$ at prototype scale in the right (A) and left (B) streets (at locations P_{RS} and P_{LS}, respectively), for the five storage capacity values, ϕ, plotted over the flood hazard diagram for pedestrians. The dashed coloured lines correspond to the unsteady flow for H.LSS. The markers with grey intensity correspond to steady flows according to the inlet discharge (from $Q_{in} = 1$ to $Q_{in} = 5\,\mathrm{l\,s^{-1}}$ at model scale, here upscaled to the prototype scale).

from those at d_{max} (P100) in unsteady flow. For cases $\phi = 0.5$ and $\phi = 0.75$, the hazard maps for steady flow present a lower levels of hazard than those for unsteady flow, while the opposite stands for case $\phi = 0.9$, and for $\phi = 1$, both hazard maps are very similar for steady and unsteady flows.

5.6 Comparison with other research studies

The results of two inflow hydrographs (H.LSS and H.SLS) with different $V_{B,max}/V_r$ ratios are plotted together on Figure 5.13. Are shown the relative change respect to the reference case (i.e. when $\phi = 0$), in maximum flow depth, Δd_{max}, global peak discharge, ΔQ_{pk} and maximum surface velocity, $\Delta U_{s,max}$ as a function of the $V_{B,max}/V_r$ ratio. Plots in the right street are not included because the impact on flow depth and velocity due to floodwater volume storage within the block is marginal. For the rest of the three streets, the maximum flow depth increases (up to 10%) when a small volume of floodwater is stored in the block (i.e., when $V_{B,max}/V_r < 10\%$). However, when the floodwater volume stored in the block increases ($V_{B,max}/V_r$ increases), the flow depth is reduced, up to -13% for $V_{B,max}/V_r \approx 18\%$, compared to the reference case (Figure 5.13, upper plots). This result is consistent with the decrease in flow depth caused by the floodwater volume storage within buildings, reported by Abdullah et al. (2011) and Huang et al. (2014a), and the limited effect observed also by Paquier et al. (2019), all of them mentioned in Section 5.1.

Regarding the flow velocity in the streets, Paquier et al. (2019) reported an average 5% decrease in velocity by storing floodwater in the city blocks. However, in this study, it was found that flow depths and velocities varies strongly (increasing or decreasing), depending on the floodwater volume stored within the city block. In the left street, the maximum velocity decreases for values $V_{B,max}/V_r < 8.5\%$, with a maximum variation about -9% (Figure 5.13, bottom centre plot). For larger $V_{B,max}/V_r$ values, the maximum velocity increases respect to the reference case, up to 10% when $V_{B,max}/V_r \approx 10\%$.

As expected, the global peak discharge decreased when increasing the maximum volume stored within the block. This attenuation increases from 3% to 10% when the relative volume of floodwater stored within the block ($V_{B,max}/V_r$) increased from 6% to 18% (this is equivalent to 3.5% and 5.5% of the total volume V). These values are much lower than the ones reported by Avila et al. (2016), up to 75% when storing in tanks beneath the city

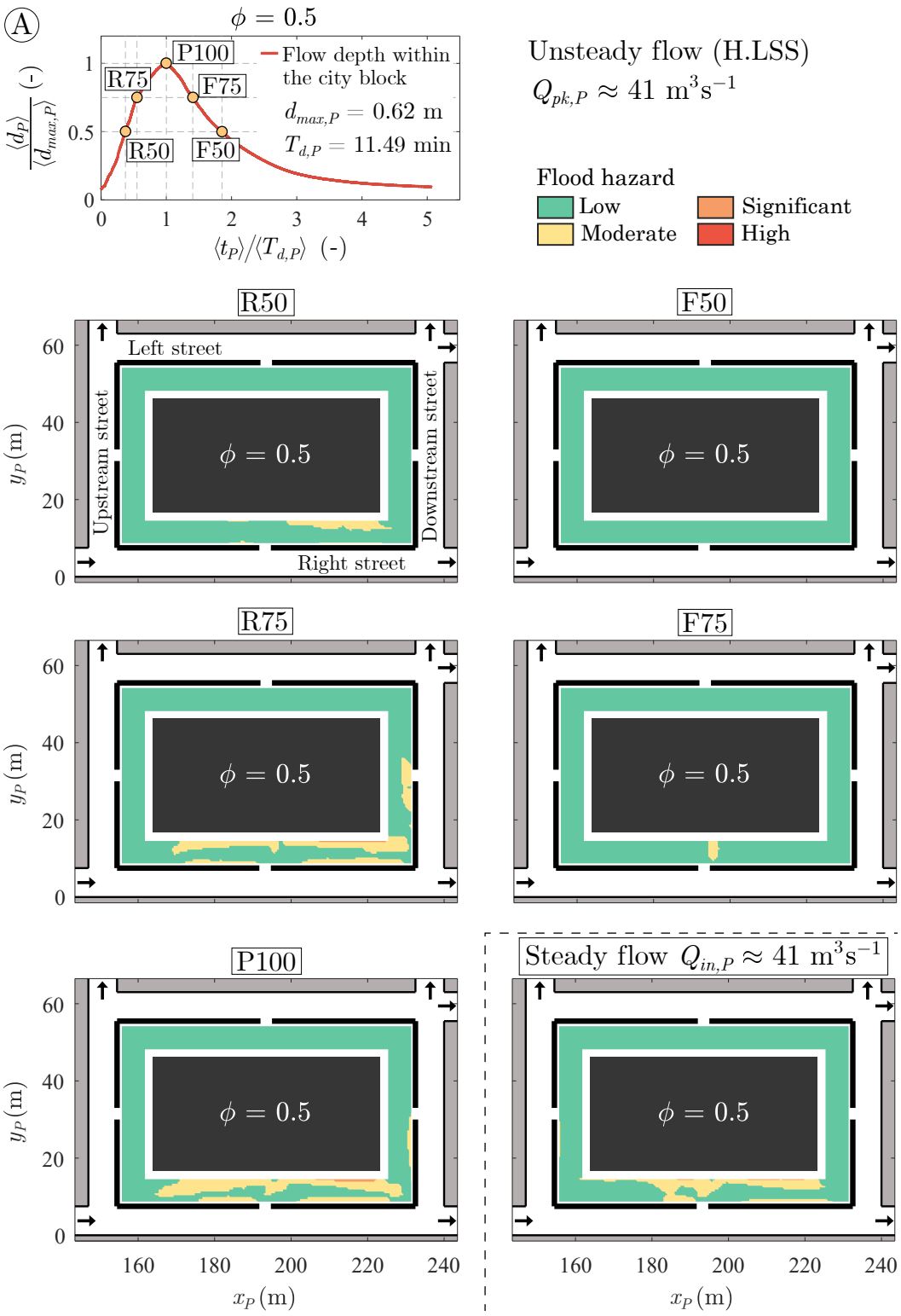

FIGURE 5.12. Flood hazard maps for pedestrians at prototype scale, for cases with $\phi = 0.5$ (A), 0.75 (B), 0.9 (C) and 1 (D) at different instants for the unsteady flow (H.LSS): at d_{max} (P100) and at 50% and 75% of d_{max} on the rising stage (R50 and R75) and falling stage (F50 and F75). Flood hazard maps in steady flow for d_{max}, i.e. with $Q_{in} \approx Q_{pk}$ are also included. At the top is shown the stage hydrograph within the city block, where $T_{d,P}$ is the time between the base and maximum flow depths within the city block, upscaled to the prototype scale.

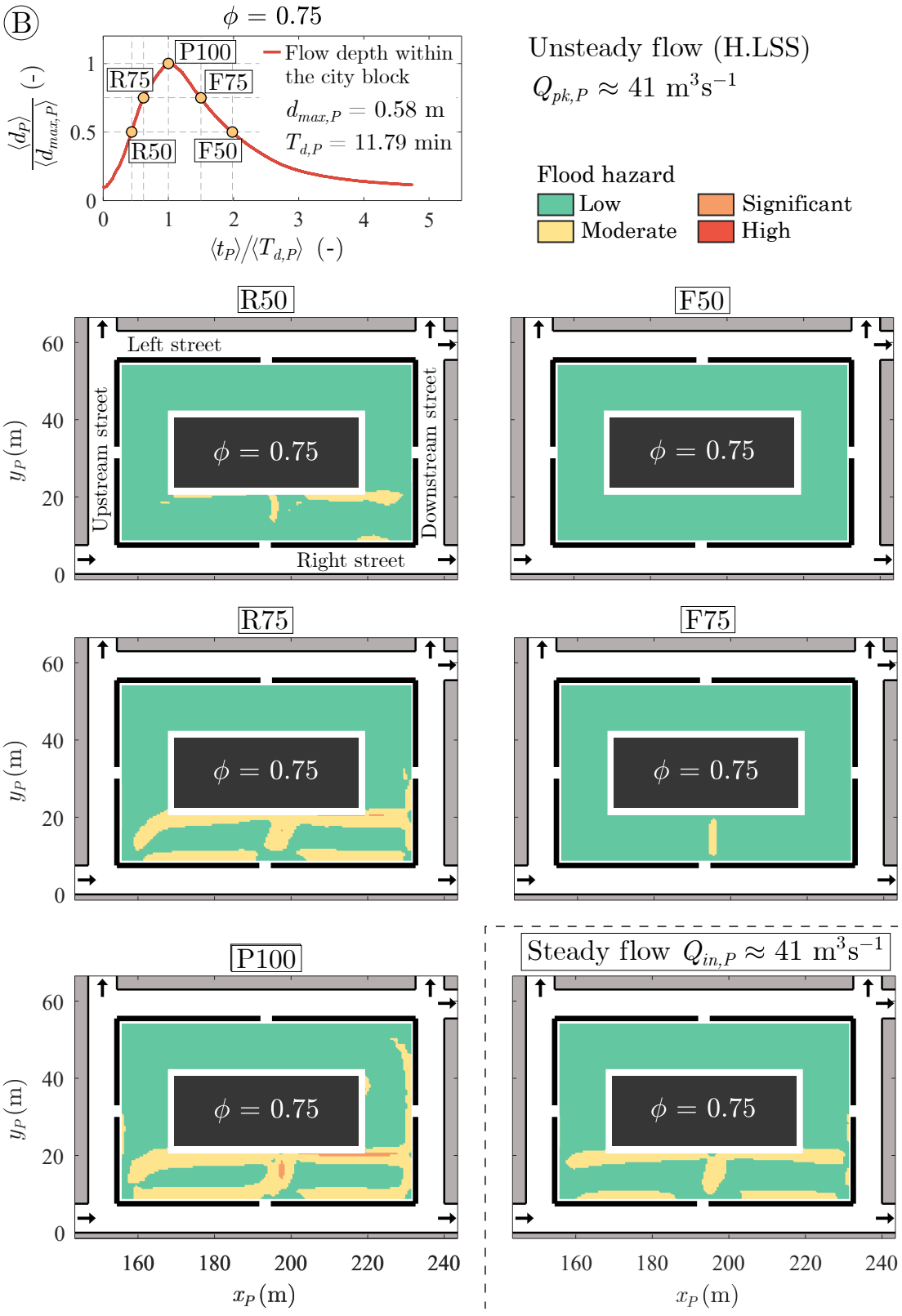

FIGURE 5.12. (Continued).

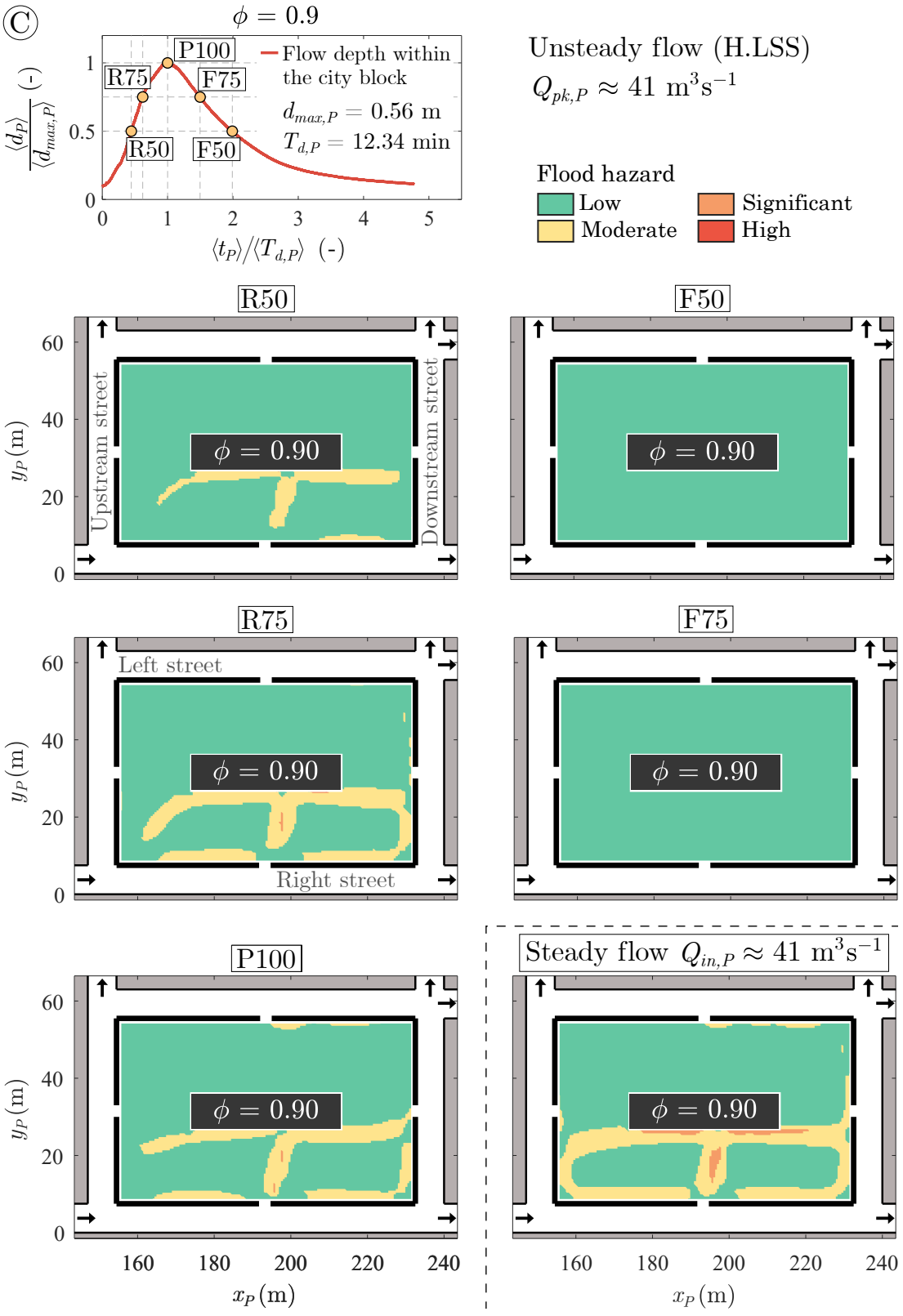

FIGURE 5.12. (Continued).

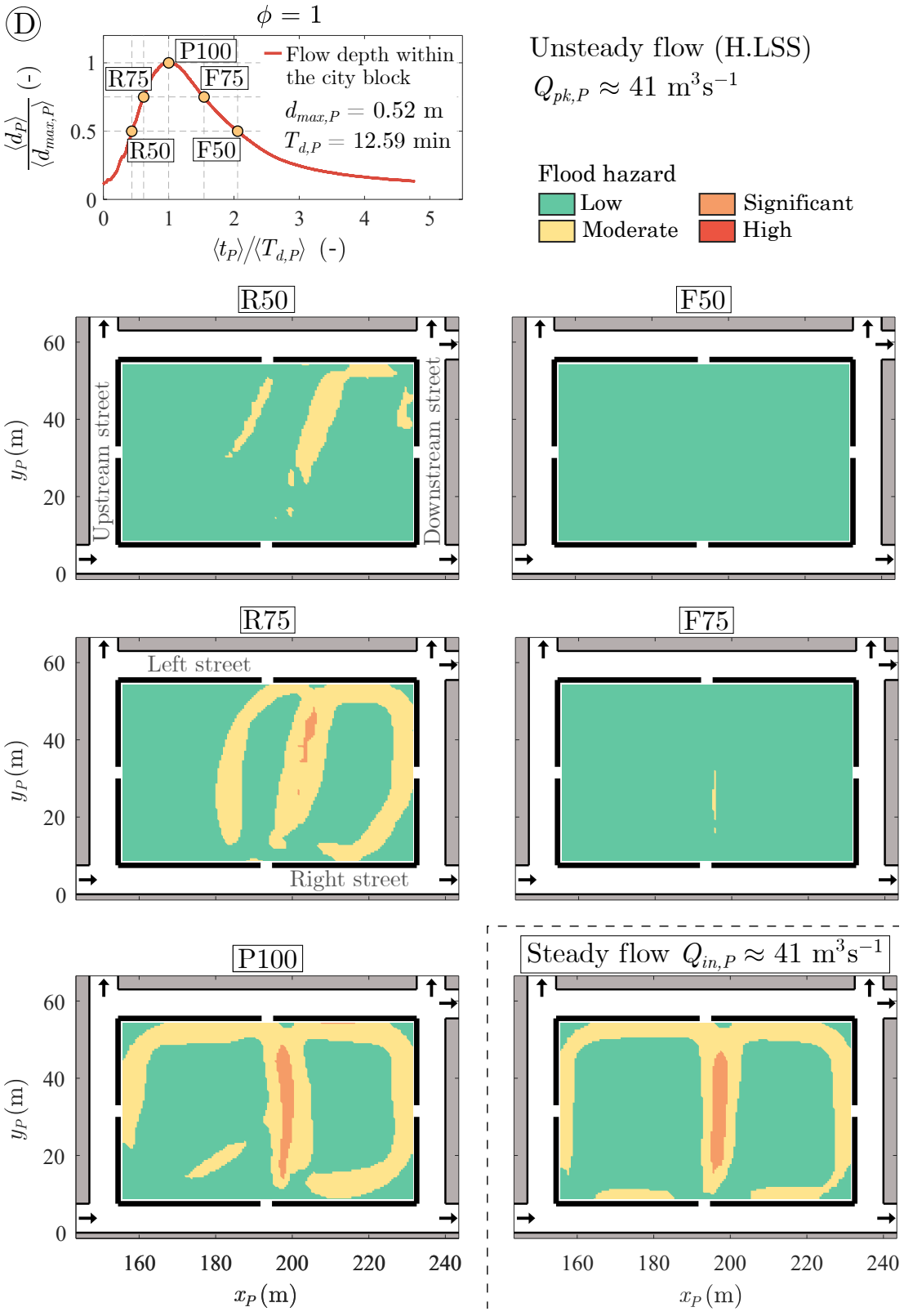

FIGURE 5.12. (Continued).

blocks 17% of the total floodwater. This is mainly due to the difference in methodologies, however, it is still valuable to recognise that the internal spaces in the blocks can strongly modify the flood flow features. Therefore, neglecting these spaces or assuming that they can only mitigate the effect of flooding can lead to an underestimation of parameters such as flow velocity and/or flow depth in some specific streets.

Finally, it should be noted that the intrusion and storage of floodwater into the city block requires porosity trough the block walls, i.e., conveyance porosity, ψ. In this study, ψ was represented by an opening in each of its 4 walls, and it was kept constant for all cases. Therefore, different conveyance porosity (different number or size of openings) and different distribution of this porosity (different location of the openings on the walls) could lead to different results, but this analysis was not undertaken herein.

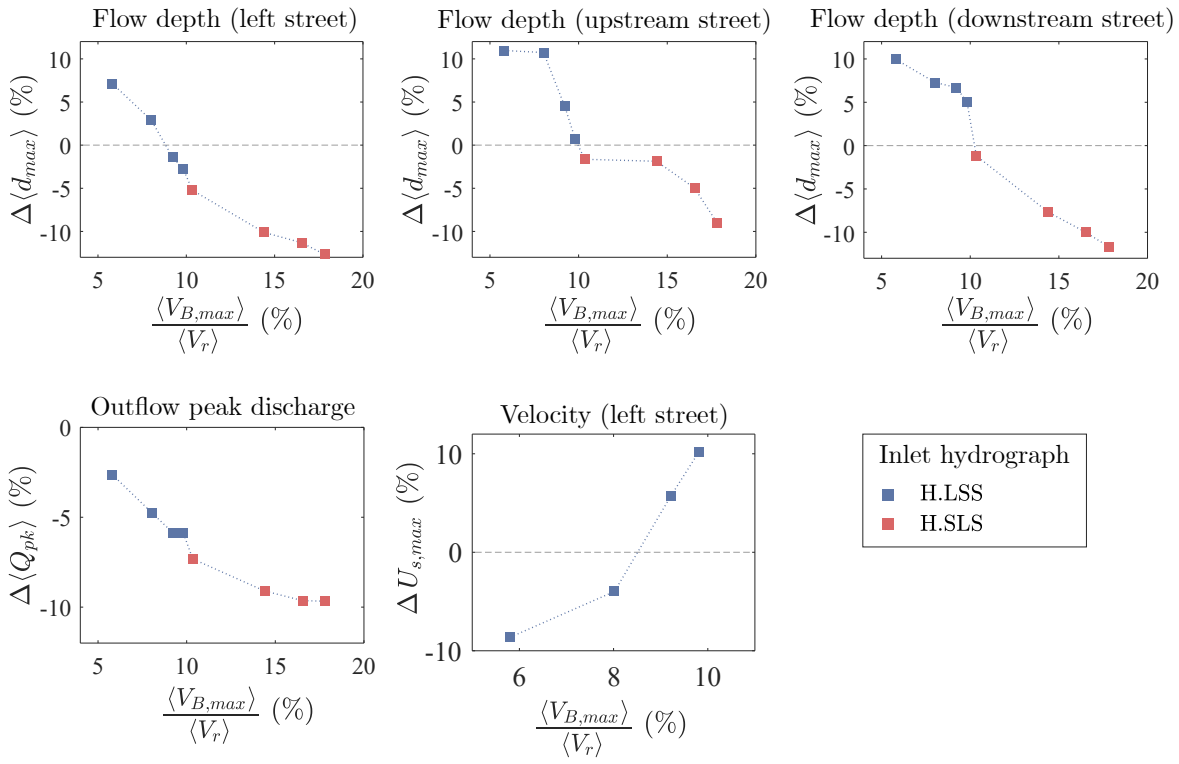

FIGURE 5.13. Relative change in flow depth in left, upstream and downstream streets (top), peak discharge of global outflow hydrograph (bottom left corner) and surface velocity in the left street (bottom centre), respect to the reference case (i.e. when $\phi = 0$), as a function of the ratio between the floodwater volume stored within the city block, $V_{B,max}$, and the volume dispatched by the inflow hydrograph during the rising stage, V_r. Results from inflow hydrographs H.LSS and H.SLS are shown in blue and red markers, respectively.

5.7 Conclusions

By means of laboratory experiments the present work investigated the influence of the internal space within a city block (storage capacity, ϕ) on flood flows. Three different inflow hydrographs were tested, together with steady flows for five storage capacity values ,ϕ. For each case, inflow and outflow discharges together with flow depths and velocities were monitored at specific locations in the urban area.

It was found that increasing the storage capacity of the block, ϕ, attenuates the global peak discharge from upstream to downstream region of the urban area, with a maximum reduced peak discharge of 10%. However, ϕ can also increase the discharge in certain streets, by up to 14% was observed in this study. Oppositely, the time lag between the inflow and global outflow hydrograph peak discharges was not significantly impacted. The storage capacity also reduced the maximum flow depth in most of the streets, by up to 13% for the left and downstream streets and by about 15% within the city block. The impact on surface velocity in the right street remained limited to 4%, however, for the left street, the increase in ϕ increased the maximum surface velocity, by about 20% when ϕ increased from 0.5 to 1. Within the city block, a slight increase in velocity was found (7%) at the highest storage capacity value (i.e., $\phi = 1$). In this zone several recirculating flow cells occur, which number and size are driven by the clearance between the block walls and the non-porous building walls.

With the modifications, mainly on the left street, due to the increased storage capacity, the hazard for pedestrians increases in this area, mainly due to the increase in velocity. Within the block, there is an increase in hazard level in few areas when storage capacity increases. Consequently, neglecting the presence of these interior spaces within city blocks during flood studies could lead to underestimate or overestimate the effects of flooding in certain areas. Therefore, it is highly advisable to take them into account together with the conveyance porosity of city blocks for a proper hazard assessment.

During these tests the incidence of the inflow hydrograph unsteadiness, α_r, was quite noticeable. Among the three inflow hydrographs tested, the results for the two hydrographs with the same α_r value (~ 2.2) were very similar and different from those of the inflow hydrograph with a higher unsteadiness degree (H.SLS, with $\alpha_r = 4.49$). For a higher value of α_r the attenuation of the global peak discharge was higher: from 5% when $\alpha_r = 2.2$ to

10% when $\alpha_r = 4.49$. The variation of the maximum flow depths in the streets surrounding the block with respect to the reference case were greater for the higher α_r value (except on the right street where they were the same) and in different senses, i.e., for $\alpha_r = 2.2$ the maximum flow depths for most cases increased, while for $\alpha_r = 4.49$ in all cases the maximum flow depth decreased.

Finally, the results for unsteady flows differed in some respects from those for steady flows. Flow depths were most of the cases greater for steady flows in the streets and within the block, up to 30%. Maximum surface velocity was lower in most cases for steady flows: in the left street, by up to 25% and within the city block, up to 20%. The assessed flood hazard to pedestrians varied, in some cases the hazard level was higher in unsteady flows ($\phi = 0.5$ and 0.75), in others in steady flow ($\phi = 0.9$) and it was about the same for $\phi = 1$.

CHAPTER 6

GENERAL CONCLUSIONS AND PERSPECTIVES

6.1 General conclusions

The aim of the present PhD thesis work was to investigate the influence of lateral flow exchanges between streets and a city block during an urban flood. The investigation relied on laboratory experiments carried out on the physical model MURI. Two questions prompted this research work: (*i*) what is the influence of a porous city block on flood hazard in a long-duration flood event; and (*ii*) what is the influence of a porous city block on flood hazard in a flash flood event. Two main properties of the city block were considered: the potential to convey flow through the block (quantified by the conveyance porosity, ψ) and the capacity to store part of the floodwater volume (quantified by the storage capacity, ϕ). Steady and unsteady flows accounted for long-duration flooding and flash flooding, respectively. Therefore, to study the influence of the different properties of a porous city block and to answer the initial questions, three key issues were addressed:

- *Key issue 1.* What is the influence of varying the magnitude of the city block conveyance porosity, ψ, on flow depths, velocities and discharges in the streets and within the block under steady flow conditions?

- *Key issue 2.* What is the influence of varying the distribution of the city block conveyance porosity, ψ, on flow depths, velocities and discharges in the streets and within the block under steady flow conditions?

- *Key issue 3.* What is the influence of varying the city block storage capacity, ϕ, on flow depths, velocities and discharges in the streets and within the block under unsteady flow conditions?

To answer key issue 1, the magnitude of the conveyance porosity of the city block was varied along the city block walls by increasing the number of openings along the walls. The increased conveyance porosity of the city block influenced the floodwater features (compared to results obtained considering a non-porous block, i.e., $\psi = 0$) as follows:

- Overall, the flow depths did not show a noticeable variation in the streets around the city block. However, local areas were observed where it decreased or increased significantly as the conveyance porosity increased, up to -6% and 12%, respectively in this investigation. In the street reaches not adjacent to the city block, a marginal variation in flow depths was found. Similarly, within the city block, no major variation of flow depth was observed (2%), in this area the free surface was roughly horizontal. An important finding is that flow depths can vary widely from the inner to the outer side of the city block (i.e., with adjacent streets), up to 14%.

- Flow velocities in the streets varied strongly as the conveyance porosity increased, mainly in the areas where the porosity is located, up to 70% was observed in this study. Moreover, within the city block, the conveyance porosity had a significant influence on the flow patterns (number and size of recirculation cells) and velocity magnitude. Away from the area surrounding the city block no major influence on the flow velocity was observed, 4% maximum.

- The distribution of the flow discharges in the streets were strongly influenced, with variations by up to 70%. The discharge through the block also increased with increasing conveyance porosity, but this also depends on the location of the porosity along the block walls. Oppositely, discharges at the downstream end of the streets varied very little, 4% maximum. Hence, the outflow discharge distribution was barely affected (except for the extreme case, with no city block, i.e, $\psi = 100$).

To answer key issue 2, the conveyance porosity distribution along the walls was varied by changing the openings location. The flood flow features were influenced as follows:

- Only local variations in flow depth were observed in the streets, up to 14%. As these occur in the zones close to the conveyance porosity, the change in its distribution along the block walls can locally influence the flow depths in the streets.
- Flow velocities within the city block were higher when the conveyance porosity was distributed along the walls adjacent to the predominant flow streets (i.e., with the larger discharge), up to 400% higher.
- The discharge through the city block substantially increased when the conveyance porosity was distributed along the walls adjacent to the predominant flow streets, and it was almost nil when distributed along walls adjacent to streets with non-predominant flows.

When assessing the flood hazard to pedestrians, the conveyance porosity led to local modifications (increase or decrease in the level of hazard), both in the streets and within the city block, mainly in the areas close to the walls where the conveyance porosity was located.

For key issue 3, the conveyance porosity remained constant while the storage capacity within the city block was varied by increasing the empty horizontal surface. The increased storage capacity of the city block influenced the flood flow features (compared to results obtained considering a city block with no storage capacity, i.e., $\phi = 0$) as follows:

- The maximum flow depth within the city block and in the streets around it tended to decrease, while the floodwater volume stored within the city block increased.
- The flow velocity in the street with the predominant flow was only slightly influenced (2%), while in the street with the non-predominant flow, the velocity increased significantly, up to 20%. Within the city block, a 7% increase in the maximum velocity was registered, due to the larger space available as the storage capacity increases.
- The peak discharge was globally attenuated, up to 10%, but it was observed that the storage capacity together with the conveyance porosity can also increase the flow discharge in certain streets.

- The level of flood hazard to pedestrians increased slightly within the city block with the increase in storage capacity. Moreover, the level of hazard was always more significant during the rising stage of the inflow hydrograph, with the greatest hazard occurring when the peak discharge was reached.

- Finally, the unsteadiness of the inflow hydrograph highly influenced the flow characteristics, strongly affecting the floodwater volume stored within the city block and consequently, flow depths, velocities and discharges in the streets and within the block.

The present results revealed that a porous city block mainly impact the flood flow features in the vicinity of the block, and then the flood hazard. Moreover, disregarding the flow exchanges between streets and buildings may lead to a misestimation of the flood severity in certain areas. Therefore, taking into account that city blocks are endemic to every urban area, it is highly recommended to consider their effects for a more reliable flood hazard assessment, in numerical simulation or physical modelling on urban floods.

Finally, it should be noted that the large amount of data recorded during this research work (velocities, flow depths and discharges) for various flow conditions, could represent a valuable source of information. These data could be of interest for the calibration and validation of numerical flood models, including 2D and 3D, porosity models, etc. An article comparing experimental measurements with 2D and 3D numerical modelling results is under development with the DEUFI project partners.

6.2 Perspectives

One of the greatest challenges when investigating urban flooding is the level of detail that is assumed to be appropriate when reproducing the various elements that constitute an urban area. As seen in Chapter 2, the investigation of the different processes that take place during urban flooding has been carried out in stages, integrating increasingly complex flows, since the beginning of the 21st century (see Mignot et al., 2019). In this research, the effects of a porous city block in its neighbouring street network was undertake. This represented a step further towards a realistic urban area, compared to what has been done previously, where the built-up areas where considered as impervious areas (see Figure 6.1, pictures A, B and C). In this 1st attempt, the geometry of the city block, as well as its interior arrangement

were represented in a highly simplified manner (Figure 6.1.D). The results can thus be used as reference for further research, with more realistic city block layouts (trying to emulate an urban area during a real flood event, see in Figure 6.1.E).

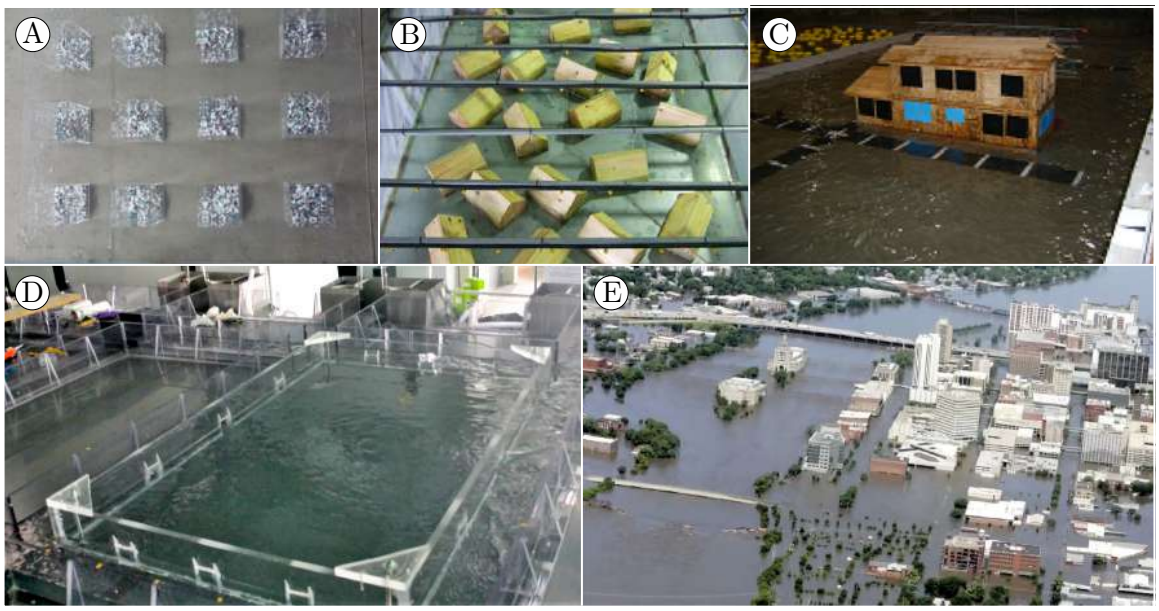

FIGURE 6.1. (A) Fluvial flooding, simulated within a flume, representing built-up areas as aligned non-porous blocks, from Huang et al. (2014b). (B) Pluvial flooding, representing residential buildings as non-porous wooden blocks, from Cea et al. (2010). (C) Coastal flooding, on a detached two-storey residential building with open windows, from van de Lindt et al. (2009). (D) Fluvial flooding, in an idealised urban area, considering the flow exchanges with a porous city block, used in this research work. (E) 2008 flooding in Cedar Rapids, USA (source: University of Iowa YouTube channel, www.youtube.com/watch?v=t58MhL2W-7s)

The next step, could be to incorporate more details within the city block, such as windows and possibly dividing walls (corresponding to buildings within the block). Incorporating these elements in this reduced urban area would be a step forward. Moreover, the research work carried out by Mignot et al. (2020) highlighted that the furniture and vehicles located in the streets on the side of the building openings significantly impact the intrusion of flood flows into buildings. Then, the inclusion of these elements in the present reduced urban area (MURI) in a second step, would provide valuable information.

Another research work in perspective on this same physical model could incorporate the sewage network, together with the porous city block. I consider important to take advantage of the existing results on the vertical flow exchanges between this sewerage network and the streets (see Chibane et al., 2021), as well as on the transversal exchanges between streets

and the city block presented in this PhD thesis. Both studies contain baseline data for a possible comparison with the research that would combine both effects (that from a porous city block and that from the sewerage network).

Finally, the number of flows and scenarios studied here produced a large amount of data, which can be used for the adaptation and improvement of numerical models, such as foreseen in the framework of the DEUFI project. Thus, complementing this study with numerical modelling results, incorporating more values of conveyance porosity and storage capacity, as well as under various flow conditions (mainly unsteady, different duration and unsteadiness degree) would provide relevant information in the study of urban flooding. Moreover, using the results for the development of empirical laws to model the effects of city blocks, without explicitly including them in the 2D computation (similar to what has been proposed by Choley et al., 2021), would be a major advance, and could complement existing models (e.g., porosity models). In addition, it would be particularly interesting to further investigate the effect of the inflow hydrograph unsteadiness, as it was observed here that strongly affects the flood flows features during their interaction with a porous city block.

References

Abdullah, A. F., Vojinovic, Z., Price, R. K., and Aziz, N. A. A. (2011). A methodology for processing raw LiDAR data to support urban flood modelling framework. *Journal of Hydroinformatics*, 14(1):75–92.

Abt, S., Wittier, R., Taylor, A., and Love, D. (1989). Human stability in a high flood hazard zone. *Journal of the American Water Resources Association*, 25(4):881–890.

Araud, Q., Finaud-Guyot, P., Lawniczak, F., François, P., Vazquez, J., and Mosé, R. (2014). Modeling Flood in an Urban Area: Validation of Numerical Tools Against Experimental Data. In Gourbesville, P., Cunge, J., and Caignaert, G., editors, *Advances in Hydroinformatics: SIMHYDRO 2012 – New Frontiers of Simulation*, pages 207–220. Springer Singapore, Singapore.

Aronica, G. T. and Lanza, L. G. (2005). Drainage efficiency in urban areas: a case study. *Hydrological Processes*, 19(5):1105–1119.

Arrault, A., Finaud-Guyot, P., Archambeau, P., Bruwier, M., Erpicum, S., Pirotton, M., and Dewals, B. (2016). Hydrodynamics of long-duration urban floods: experiments and numerical modelling. *Natural Hazards and Earth System Sciences*, 16(6):1413–1429.

Arrighi, C., Huybrechts, N., Ouahsine, A., Chassé, P., Oumeraci, H., and Castelli, F. (2016). Vehicles instability criteria for flood risk assessment of a street network. *Proceedings of the International Association of Hydrological Sciences*, 373:143–146.

Arrighi, C., Oumeraci, H., and Castelli, F. (2017). Hydrodynamics of pedestrians' instability in floodwaters. *Hydrology and Earth System Sciences*, 21(1):515–531.

Avila, H., Avila, L., and Sisa, A. (2016). Dispersed storage as stormwater runoff control in consolidated urban watersheds with flash flood risk. *Journal of Water Resources Planning and Management*, 142(12):04016056.

Baba, Y., Ishigaki, T., and Toda, K. (2017). Experimental studies on safety evacuation from underground spaces under inundated situations. *Journal of JSCE*, 5(1):269–278.

Barkdoll, B. D., Hagen, B. L., and Odgaard, A. J. (1998). Experimental comparison of dividing open-channel with duct flow in t-junction. *Journal of Hydraulic Engineering*, 124(1):92–95.

Bazin, P.-H., Mignot, E., and Paquier, A. (2017). Computing flooding of crossroads with obstacles using a 2d numerical model. *Journal of Hydraulic Research*, 55(1):72–84.

Bazin, P.-H., Nakagawa, H., Kawaike, K., Paquier, A., and Mignot, E. (2014). Modeling flow exchanges between a street and an underground drainage pipe during urban floods. *Journal of Hydraulic Engineering*, 140(10):04014051.

Beg, M. N. A., Carvalho, R. F., and Leandro, J. (2018). Effect of surcharge on gully-manhole flow. *Journal of Hydro-environment Research*, 19:224–236.

Beretta, R., Ravazzani, G., Maiorano, C., and Mancini, M. (2018). Simulating the influence of buildings on flood inundation in urban areas. *Geosciences*, 8(2).

Best, J. L. and Reid, I. (1984). Separation zone at open‐channel junctions. *Journal of Hydraulic Engineering*, 110(11):1588–1594.

Bignami, D. F., Rosso, R., and Sanfilippo, U. (2019a). *Flood Impact on Buildings*, pages 11–24. Springer International Publishing, Cham.

Bignami, D. F., Rosso, R., and Sanfilippo, U. (2019b). *Flood Impact on Human Beings Stability*, pages 25–43. Springer International Publishing, Cham.

Black, R. (1975). Flood proofing rural residences: A 'project agnes' report. *Pennsylvania. New York State College of Agriculture and Life Sciences, Ithaca, Prepared for Economic Development Administration, Washington, DC Office of Technical Assistance.*

Bonham, A. and Hattersley, R. (1967). Low level causeways. technical report 100.

Cançado, V., Nascimento, N., Ruiz, R., Oliveira, L. K., Alcântara, F., Rodrigues, B., and Jung, M. (2010). Economical consequences of floods: modelling impacts in urban areas.

Cea, L. and Costabile, P. (2022). Flood risk in urban areas: Modelling, management and adaptation to climate change. a review. *Hydrology*, 9(3):50.

Cea, L., Garrido, M., and Puertas, J. (2010). Experimental validation of two-dimensional depth-averaged models for forecasting rainfall–runoff from precipitation data in urban areas. *Journal of Hydrology*, 382(1-4):88–102.

Chanson, H. (2004). *Hydraulics of open channel flow.* Elsevier.

Chanson, H., Brown, R., and McIntosh, D. (2014). Human body stability in floodwaters: The 2011 flood in brisbane cbd. In Chanson, H. and Toombes, L., editors, *Hydraulic Structures and Society - Engineering Challenges and Extremes: Proceedings of the 5th IAHR International Symposium on Hydraulic Structures (ISHS2014)*, pages 1–9, Australia. The University of Queensland.

Chibane, T., Paquier, A., and Benmamar, S. (2021). Experimental study of the flow patterns in a street during drainage or overflow to or from drains. *Urban Water Journal*, 18(7):544–557.

Chock, G., Robertson, I., Kriebel, D., Francis, M., and Nistor, I. (2013). *Tohoku, Japan, Earthquake and Tsunami of 2011.* American Society of Civil Engineers.

Choley, C., Finaud-Guyot, P., Garambois, P.-A., and Mosé, R. (2021). An effective urban flood model accounting for street-building exchanges. In *SimHydro 2021: Models for complex and global water issues-Practices and expectations*.

Clausen, L. and Clark, P. (1990). The development of criteria for predicting dambreak flood damages using modelling of historical dam failures. In White, W. R., editor, *International Conference on River Flood Hydraulics, 17-20 Sptember 1990*, pages 369–380. John Wiley & Sons, UK.

Cox, D., Tomita, T., Lynett, P., and Holman, R. (2009). *Tsunami inundation with macro-roughness in the constructed environment*, pages 1421–1432.

Cox, R., Shand, T., and Blacka, M. (2010). Australian rainfall and runoff revision project 10: appropriate safety criteria for people. *Water Research*, 978:085825–9454.

CRED and UNDRR (2020). Human cost of disasters. an overview of the last 20 years: 2000–2019. *CRED, UNDRR, Geneva*.

Dawson, R. J., Speight, L., Hall, J. W., Djordjevic, S., Savic, D., and Leandro, J. (2008). Attribution of flood risk in urban areas. *Journal of Hydroinformatics*, 10(4):275–288.

de Moel, H., van Alphen, J., and Aerts, J. C. J. H. (2009). Flood maps in europe–methods, availability and use. *Natural Hazards and Earth System Sciences*, 9(2):289–301.

Dewals, B., Bruwier, M., Pirotton, M., Erpicum, S., and Archambeau, P. (2021). Porosity models for large-scale urban flood modelling: A review. *Water*, 13(7).

Dewals, B., Kantoush, S., Erpicum, S., Pirotton, M., and Schleiss, A. (2008). Experimental and numerical analysis of flow instabilities in rectangular shallow basins. *Environmental Fluid Mechanics*, 8(1):31–54.

Dijkstra, L., Poelman, H., and Veneri, P. (2019). The eu-oecd definition of a functional urban area. *Editions OCDE*, (11).

Djordjevic, S., Prodanovic, D., Maksimovic, C., Ivetic, M., and Savic, D. (2005). SIPSON – Simulation of Interaction between Pipe flow and Surface Overland flow in Networks. *Water Science and Technology*, 52(5):275–283.

Djordjevic, S., Saul, A. J., Tabor, G. R., Blanksby, J., Galambos, I., Sabtu, N., and Sailor, G. (2013). Experimental and numerical investigation of interactions between above and below ground drainage systems. *Water Science and Technology*, 67(3):535–542.

Dong, B., Xia, J., Zhou, M., Deng, S., Ahmadian, R., and Falconer, R. A. (2021). Experimental and numerical model studies on flash flood inundation processes over a typical urban street. *Advances in Water Resources*, 147:103824.

Dufresne, M., Dewals, B. J., Erpicum, S., Archambeau, P., and Pirotton, M. (2010). Classification of flow patterns in rectangular shallow reservoirs. *Journal of Hydraulic Research*, 48(2):197–204.

El Kadi, K., Paquier, A., Riviere, N., Leblois, E., and Guinot, V. (2007). Rives project: knowledge and management of urban flood risks. In *Aqua terra 2007, Amsterdam, NLD, 07-09 février 2007*, page 18.

El Kadi Abderrezzak, K., Lewicki, L., Paquier, A., Rivière, N., and Travin, G. (2011). Division of critical flow at three-branch open-channel intersection. *Journal of Hydraulic Research*, 49(2):231–238.

Finaud-Guyot, P., Garambois, P.-A., Araud, Q., Lawniczak, F., François, P., Vazquez, J., and Mosé, R. (2018). Experimental insight for flood flow repartition in urban areas. *Urban Water Journal*, 15(3):242–250.

Finaud-Guyot, P., Garambois, P.-A., Dellinger, G., Lawniczak, F., and François, P. (2019). Experimental characterization of various scale hydraulic signatures in a flooded branched street network. *Urban Water Journal*, 16(9):609–624.

Fritsch, K., Assmann, A., and Tyrna, B. (2016). Long-term experiences with pluvial flood risk management. *E3S Web Conf.*, 7:04017.

Fujita, I., Muste, M., and Kruger, A. (1998). Large-scale particle image velocimetry for flow analysis in hydraulic engineering applications. *Journal of Hydraulic Research*, 36(3):397–414.

Gallegos, H. A., Schubert, J. E., and Sanders, B. F. (2009). Two-dimensional, high-resolution modeling of urban dam-break flooding: A case study of baldwin hills, california. *Advances in Water Resources*, 32(8):1323–1335.

Goltsman, A. and Saushin, I. (2019). Flow pattern of double-cavity flow at high reynolds number. *Physics of Fluids*, 31(6):065101.

Gordon, A. and Stone, P. (1973). *Car stability on road floodways*. National Capital Development Commission.

Goring, D. G. and Nikora, V. I. (2002). Despiking acoustic doppler velocimeter data. *Journal of Hydraulic Engineering*, 128(1):117–126.

Guinot, V. (2012). Multiple porosity shallow water models for macroscopic modelling of urban floods. *Advances in Water Resources*, 37:40 – 72.

Guinot, V., Sanders, B. F., and Schubert, J. E. (2017). Dual integral porosity shallow water model for urban flood modelling. *Advances in Water Resources*, 103:16–31.

Gurram, S. K., Karki, K. S., and Hager, W. H. (1997). Subcritical junction flow. *Journal of Hydraulic Engineering*, 123(5):447–455.

Gómez, M. and Russo, B. (2011). Methodology to estimate hydraulic efficiency of drain inlets. *Proceedings of the Institution of Civil Engineers - Water Management*, 164(2):81–90.

Gómez, M., Russo, B., and Tellez-Alvarez, J. (2019). Experimental investigation to estimate the discharge coefficient of a grate inlet under surcharge conditions. *Urban Water Journal*, 16(2):85–91.

Güney, M. S., Tayfur, G., Bombar, G., and Elci, S. (2014). Distorted physical model to study sudden partial dam break flows in an urban area. *Journal of Hydraulic Engineering*, 140(11):05014006.

Hager, W. H. (1989a). Supercritical flow in channel junctions. *Journal of Hydraulic Engineering*, 115(5):595–616.

Hager, W. H. (1989b). Transitional flow in channel junctions. *Journal of Hydraulic Engineering*, 115(2):243–259.

Hsu, C.-C., Lee, W.-J., and Chang, C.-H. (1998a). Subcritical open-channel junction flow. *Journal of Hydraulic Engineering*, 124(8):847–855.

Hsu, C.-C., Tang, C.-J., Lee, W.-J., and Shieh, M.-Y. (2002). Subcritical 90° equal-width open-channel dividing flow. *Journal of Hydraulic Engineering*, 128(7):716–720.

Hsu, C.-C., Wu, F.-S., and Lee, W.-J. (1998b). Flow at 90° equal-width open-channel junction. *Journal of Hydraulic Engineering*, 124(2):186–191.

Huang, C.-J., Hsu, M.-H., Chen, A. S., and Chiu, C.-H. (2014a). Simulating the storage and the blockage effects of buildings in urban flood modeling. *Terrestrial, Atmospheric & Oceanic Sciences*, 25(4).

Huang, C.-J., Hsu, M.-H., Teng, W.-H., and Wang, Y.-H. (2014b). The impact of building coverage in the metropolitan area on the flow calculation. *Water*, 6(8):2449–2466.

Hunter, N. M., Bates, P. D., Neelz, S., Pender, G., Villanueva, I., Wright, N. G., Liang, D., Falconer, R. A., Lin, B., Waller, S., Crossley, A. J., and Mason, D. C. (2008). Benchmarking 2d hydraulic models for urban flooding. *Proceedings of the Institution of Civil Engineers - Water Management*, 161(1):13–30.

Ishigaki, T. (2003). Hydraulic model tests of inundation in urban area with underground space. In *Proc. of 30th IAHR Congress, Greece, 2003*, pages 487–493.

Ishigaki, T., Asai, Y., Nakahata, Y., Shimada, H., Baba, Y., and Toda, K. (2010). Evacuation of aged persons from inundated underground space. *Water science and technology*, 62(8):1807–1812.

Ishigaki, T., Kawanaka, R., Onishi, Y., Shimada, H., Toda, K., and Baba, Y. (2009). Assessment of Safety on Evacuating Route During Underground Flooding. In *Advances in Water Resources and Hydraulic Engineering*, pages 141–146. Springer Berlin Heidelberg, Berlin, Heidelberg.

Isidoro, J. M., de Lima, J. L., and Leandro, J. (2013). The study of rooftop connectivity on the rainfall-runoff process by means of a rainfall simulator and a physical model. *Zeitschrift für Geomorphologie, Supplementary Issues*, pages 177–191.

Jonkman, S., Bočkarjova, M., Kok, M., and Bernardini, P. (2008). Integrated hydrodynamic and economic modelling of flood damage in the netherlands. *Ecological Economics*, 66(1):77–90. Special Section: Integrated Hydro-Economic Modelling for Effective and Sustainable Water Management.

Jonkman, S. and Penning-Rowsell, E. (2008). Human Instability in Flood Flows [1]. *JAWRA Journal of the American Water Resources Association*, 44(5):1208–1218.

Kantoush, S. A., Schleiss, A. J., Sumi, T., and Murasaki, M. (2011). Lspiv implementation for environmental flow in various laboratory and field cases. *Journal of Hydro-environment Research*, 5(4):263 – 276.

Karvonen, T., Hepojoki, A., Kotala, J., and Huhta, H.-K. (2000). The use of physical models in dam-break flood analysis, RESCDAM. final report of helsinki university of technology. Technical report, Helsinki.

Kates, R. W. (1962). Hazard and choice perception in flood plain management. *Department of Geography, University of Chicago*, Research Paper No. 78.

Kemper, S. and Schlenkhoff, A. (2019). Experimental study on the hydraulic capacity of grate inlets with supercritical surface flow conditions. *Water Science and Technology*, 79(9):1717–1726.

Kim, B., Sanders, B. F., Famiglietti, J. S., and Guinot, V. (2015). Urban flood modeling with porous shallow-water equations: A case study of model errors in the presence of anisotropic porosity. *Journal of Hydrology*, 523:680–692.

Konrad, C. P. (2003). Effects of urban development on floods. Technical report, US Department of the Interior, US Geological Survey Tacoma, WA, USA.

Kramer, M., Terheiden, K., and Wieprecht, S. (2016). Safety criteria for the trafficability of inundated roads in urban floodings. *International Journal of Disaster Risk Reduction*, 17:77–84.

Kundzewicz, Z. W., Kanae, S., Seneviratne, S. I., Handmer, J., Nicholls, N., Peduzzi, P., Mechler, R., Bouwer, L. M., Arnell, N., Mach, K., Muir-Wood, R., Brakenridge, G. R., Kron, W., Benito, G., Honda, Y., Takahashi, K., and Sherstyukov, B. (2014). Flood risk and climate change: global and regional perspectives. *Hydrological Sciences Journal*, 59(1):1–28.

Lakshmana-Rao, N., Sridharan, K., and Yahia Ali Baig, M. (1968). Experimental study of the division of flow in an open channel. In *Proc. Conference on Hydraulics and Fluid Mechanics, The Institution of Engineers, Australia*, pages 139–142.

Le Coz, J., Jodeau, M., Hauet, A., Marchand, B., and Le Boursicaud, R. (2014). Image-based velocity and discharge measurements in field and laboratory river engineering studies using the free fudaa-lspiv software. In *Proceedings of the international conference on fluvial hydraulics, River Flow*, volume 3, pages 2014–05.

Leandro, J., Carvalho, R., and Martins, R. (2010). Experimental scaled-model as a benchmark for validation of urban flood models. *Novatech 2010*.

Leandro, J., Lopes, P., Carvalho, R., Páscoa, P., Martins, R., and Romagnoli, M. (2014). Numerical and experimental characterization of the 2d vertical average-velocity plane at the center-profile and qualitative air entrainment inside a gully for drainage and reverse flow. *Computers & Fluids*, 102:52–61.

Lee, S., Nakagawa, H., Kawaike, K., and Zhang, H. (2012). Study on inlet discharge coefficient through the different shapes of storm drains for urban inundation analysis. *Journal of Japan Society of Civil Engineers, Ser. B1 (Hydraulic Engineering)*, 68(4):I_31–I_36.

Lee, S., Nakagawa, H., Kawaike, K., and Zhang, H. (2013). Experimental validation of interaction model at storm drain for development of integrated urban inundation model. *Journal of Japan Society of Civil Engineers, Ser. B1 (Hydraulic Engineering)*, 69(4):I_109–I_114.

Li, X., Erpicum, S., Bruwier, M., Mignot, E., Finaud-Guyot, P., Archambeau, P., Pirotton, M., and Dewals, B. (2019). Technical note: Laboratory modelling of urban flooding: strengths and challenges of distorted scale models. *Hydrology and Earth System Sciences*, 23(3):1567–1580.

Li, X., Erpicum, S., Mignot, E., Archambeau, P., Pirotton, M., and Dewals, B. (2021). Influence of urban forms on long-duration urban flooding: Laboratory experiments and computational analysis. *Journal of Hydrology*, 603:127034.

Liang, D., Falconer, R. A., and Lin, B. (2007). Coupling surface and subsurface flows in a depth averaged flood wave model. *Journal of Hydrology*, 337(1):147–158.

Liu, L., Sun, J., Lin, B., and Lu, L. (2018). Building performance in dam-break flow–an experimental study. *Urban Water Journal*, 15(3):251–258.

Lo, W.-C., Tsao, T.-C., and Hsu, C.-H. (2012). Building vulnerability to debris flows in Taiwan: a preliminary study. *Natural Hazards*, 64(3):2107–2128.

Macchione, F., Costabile, P., Costanzo, C., and Lorenzo, G. D. (2019). Extracting quantitative data from non-conventional information for the hydraulic reconstruction of past urban flood events. a case study. *Journal of Hydrology*, 576:443 – 465.

Martins, R., Kesserwani, G., Rubinato, M., Lee, S., Leandro, J., Djordjević, S., and Shucksmith, J. D. (2017). Validation of 2d shock capturing flood models around a surcharging manhole. *Urban Water Journal*, 14(9):892–899.

Martins, R., Leandro, J., and de Carvalho, R. F. (2014). Characterization of the hydraulic performance of a gully under drainage conditions. *Water Science and Technology*, 69(12):2423–2430.

Martínez-Gomariz, E., Gómez, M., and Russo, B. (2016). Experimental study of the stability of pedestrians exposed to urban pluvial flooding. *Natural Hazards*, 82(2):1259–1278.

Martínez-Gomariz, E., Gómez, M., Russo, B., and Djordjević, S. (2018). Stability criteria for flooded vehicles: a state-of-the-art review. *Journal of Flood Risk Management*, 11(S2):S817–S826.

McGrane, S. J. (2016). Impacts of urbanisation on hydrological and water quality dynamics, and urban water management: a review. *Hydrological Sciences Journal*, 61(13):2295–2311.

Mejía-Morales, M. A., Mignot, E., Paquier, A., Sigaud, D., and Proust, S. (2021). Impact of the porosity of an urban block on the flood risk assessment: A laboratory experiment. *Journal of Hydrology*, 602.

Merz, B., Kreibich, H., Schwarze, R., and Thieken, A. (2010). Review article "assessment of economic flood damage". *Natural Hazards and Earth System Sciences*, 10(8):1697–1724.

Meselhe, E. A., Peeva, T., and Muste, M. (2004). Large scale particle image velocimetry for low velocity and shallow water flows. *Journal of Hydraulic Engineering*, 130(9):937–940.

Mignot, E., Bonakdari, H., Knothe, P., Lipeme Kouyi, G., Bessette, A., Rivière, N., and Bertrand-Krajewski, J.-L. (2012). Experiments and 3D simulations of flow structures in junctions and their influence on location of flowmeters. *Water Science and Technology*, 66(6):1325–1332.

Mignot, E., Camusson, L., and Riviere, N. (2020). Measuring the flow intrusion towards building areas during urban floods: Impact of the obstacles located in the streets and on the facade. *Journal of Hydrology*, 583:124607.

Mignot, E. and Dewals, B. (2022). Hydraulic modelling of inland urban flooding: recent advances. *Journal of Hydrology*, page 127763.

Mignot, E., Li, X., and Dewals, B. (2019). Experimental modelling of urban flooding: A review. *Journal of Hydrology*, 568:334 – 342.

Mignot, E., Paquier, A., and Ishigaki, T. (2006). Comparison of numerical and experimental simulations of a flood in a dense urban area. *Water Science and Technology*, 54(6-7):65–73.

Mignot, E., Rivière, N., Perkins, R., and Paquier, A. (2008). Flow patterns in a four-branch junction with supercritical flow. *Journal of Hydraulic Engineering*, 134(6):701–713.

Mignot, E., Zeng, C., Dominguez, G., Li, C.-W., Rivière, N., and Bazin, P.-H. (2013). Impact of topographic obstacles on the discharge distribution in open-channel bifurcations. *Journal of Hydrology*, 494:10 – 19.

Milanesi, L. and Member, I. (2019). A conceptual model of vehicles stability in flood flows. *Journal of Hydraulic Research*, page 9.

Milanesi, L., Pilotti, M., and Bacchi, B. (2016). Using web-based observations to identify thresholds of a person's stability in a flow. *Water Resources Research*, 52(10):7793–7805.

Milanesi, L., Pilotti, M., and Ranzi, R. (2015). A conceptual model of people's vulnerability to floods. *Water Resources Research*, 51(1):182–197.

Monteil, C., Foulquier, P., Defossez, S., Péroche, M., and Vinet, F. (2022). Rethinking the share of responsibilities in disaster preparedness to encourage individual preparedness for flash floods in urban areas. *International Journal of Disaster Risk Reduction*, 67:102663.

Muste, M., Fujita, I., and Hauet, A. (2008). Large-scale particle image velocimetry for measurements in riverine environments. *Water Resources Research*, 44(4).

Muste, M., Xiong, Z., Bradley, A., and Kruger, A. (2000). Large-scale particle image velocimetry—a reliable tool for physical modeling. In *Building Partnerships*, pages 1–10.

Nania, L. S., Gómez, M., Dolz, J., Comas, P., and Pomares, J. (2011). Experimental study of subcritical dividing flow in an equal-width, four-branch junction. *Journal of Hydraulic Engineering*, 137(10):1298–1305.

Nanía, L. S., Gonzalo, R., and Gómez, M. (2014). Influence of channel width on flow distribution in four-branch junctions with supercritical flow: Experimental approach. *Journal of Hydraulic Engineering*, 140(1):77–88.

Nanía, L. S., Gómez, M., and Dolz, J. (2004). Experimental study of the dividing flow in steep street crossings. *Journal of Hydraulic Research*, 42(4):406–412.

Neary, V., Sotiropoulos, F., and Odgaard, A. (1999). Three-dimensional numerical model of lateral-intake inflows. *Journal of Hydraulic Engineering*, 125(2):126–140.

Neary, V. S. and Odgaard, A. J. (1993). Three-dimensional flow structure at open-channel diversions. *Journal of Hydraulic Engineering*, 119(11):1223–1230.

Nezu, I. and Nakagawa, H. (1993). Basic structure of turbulence in unsteady open channel flows. In *Proc. of 9th Int. Symposium on Turbulent Shear Flows, Kyoto, 1993.*

Nicholls, R., Zanuttigh, B., Vanderlinden, J. P., Weisse, R., Silva, R., Hanson, S., Narayan, S., Hoggart, S., Thompson, R. C., de Vries, W., and Koundouri, P. (2015). Chapter 2 - developing a holistic approach to assessing and managing coastal flood risk. In Zanuttigh, B., Nicholls, R., Vanderlinden, J. P., Burcharth, H. F., and Thompson, R. C., editors,

Coastal Risk Management in a Changing Climate, pages 9–53. Butterworth-Heinemann, Boston.

Noh, S. J., Lee, S., An, H., Kawaike, K., and Nakagawa, H. (2016). Ensemble urban flood simulation in comparison with laboratory-scale experiments: Impact of interaction models for manhole, sewer pipe, and surface flow. *Advances in Water Resources*, 97:25–37.

Oke, T. R. (1982). The energetic basis of the urban heat island. *Quarterly Journal of the Royal Meteorological Society*, 108(455):1–24.

Paquier, A. (2009). Projet RIVES : Risques d'inondation en ville et évaluation de scénarios. Rapport scientifique final. Research report, irstea.

Paquier, A., Bazin, P. H., and Abderrezzak, K. E. K. (2019). Sensitivity of 2d hydrodynamic modelling of urban floods to the forcing inputs: lessons from two field cases. *Urban Water Journal*, 17(5):457–466.

Park, H., Cox, D. T., Lynett, P. J., Wiebe, D. M., and Shin, S. (2013). Tsunami inundation modeling in constructed environments: A physical and numerical comparison of free-surface elevation, velocity, and momentum flux. *Coastal Engineering*, 79:9 – 21.

Paul, B. K. (1984). Perception of and agricultural adjustment to floods in Jamuna floodplain, Bangladesh. *Human Ecology*, 12(1):3–19.

Peltier, Y. (2011). *Physical modelling of overbank flows with a groyne set on the floodplain*. Theses, Université Claude Bernard - Lyon I.

Peltier, Y., Rivière, N., Proust, S., Mignot, E., Paquier, A., and Shiono, K. (2013). Estimation of the error on the mean velocity and on the reynolds stress due to a misoriented adv probe in the horizontal plane: Case of experiments in a compound open-channel. *Flow Measurement and Instrumentation*, 34:34–41.

Postacchini, M., Bernardini, G., D'Orazio, M., and Quagliarini, E. (2021). Human stability during floods: Experimental tests on a physical model simulating human body. *Safety Science*, 137:105153.

Ramamurthy, A. S., Qu, J., and Vo, D. (2007). Numerical and Experimental Study of Dividing Open-Channel Flows. *Journal of Hydraulic Engineering*, 133(10):1135–1144.

Ramamurthy, A. S. and Satish, M. G. (1988). Division of flow in short open channel branches. *Journal of Hydraulic Engineering*, 114(4):428–438.

Ramsbottom, D., Wade, S., Bain, V., Floyd, P., Penning-Rowsell, E., Wilson, T., Fernandez, A., House, M., and Surendran, S. (2006). Flood risks to people: Phase 2. fd2321/tr2. *DEFRA/Environment Agency, Flood and Coastal Defence R&D Programme*.

Rapp, B. E. (2017). Chapter 9 - fluids. In Rapp, B. E., editor, *Microfluidics: Modelling, Mechanics and Mathematics*, Micro and Nano Technologies, pages 243 – 263. Elsevier, Oxford.

Rentschler, J. and Salhab, M. (2020). *People in Harm's Way: Flood Exposure and Poverty in 189 Countries*. The World Bank.

Rivière, N., Perkins, R., Chocat, B., and Lecus, A. (2006). Flooding flows in city crossroads: experiments and 1-D modelling. *Water Science and Technology*, 54(6-7):75–82.

Rivière, N., Travin, G., and Perkins, R. J. (2011). Subcritical open channel flows in four branch intersections. *Water Resources Research*, 47(10).

Rivière, N., Travin, G., and Perkins, R. J. (2014). Transcritical flows in three and four branch open-channel intersections. *Journal of Hydraulic Engineering*, 140(4):04014003.

Romagnoli, M., Carvalho, R., and Leandro, J. (2013). Turbulence characterization in a gully with reverse flow. *Journal of Hydraulic Engineering*, 139(7):736–744.

Rosenzweig, B. R., McPhillips, L., Chang, H., Cheng, C., Welty, C., Matsler, M., Iwaniec, D., and Davidson, C. I. (2018). Pluvial flood risk and opportunities for resilience. *WIREs Water*, 5(6):e1302.

Rudari, R. (2017). Flood hazard and risk assessment. *Words into Action guidelines: National disaster risk assessment*.

Russo, B., Gómez, M., and Macchione, F. (2013a). Pedestrian hazard criteria for flooded urban areas. *Natural Hazards*, 69(1):251–265.

Russo, B., Gómez, M., and Tellez, J. (2013b). Methodology to estimate the hydraulic efficiency of nontested continuous transverse grates. *Journal of Irrigation and Drainage Engineering*, 139(10):864–871.

Sabtu, N., Saul, A. J., Sailor, G., et al. (2016). Hydraulic interaction of a gully system. *American Academic Scientific Research Journal for Engineering, Technology, and Sciences*, 21(1):202–209.

Sanders, B. F., Schubert, J. E., and Gallegos, H. A. (2008). Integral formulation of shallow-water equations with anisotropic porosity for urban flood modeling. *Journal of Hydrology*, 362(1):19–38.

Sattar, A. M., Kassem, A. A., and Chaudhry, M. H. (2008). Case study: 17th street canal breach closure procedures. *Journal of Hydraulic Engineering*, 134(11):1547–1558.

Schindfessel, L., Creëlle, S., and De Mulder, T. (2015). Flow patterns in an open channel confluence with increasingly dominant tributary inflow. *Water*, 7(9):4724–4751.

Schubert, J. E., Sanders, B. F., Smith, M. J., and Wright, N. G. (2008). Unstructured mesh generation and landcover-based resistance for hydrodynamic modeling of urban flooding. *Advances in Water Resources*, 31(12):1603–1621.

Seong, H., Rhee, D. S., and Park, I. (2020). Analysis of urban flood inundation patterns according to rainfall intensity using a rainfall simulator in the sadang area of south korea. *Applied Sciences*, 10(3).

Shand, T., Cox, R., Blacka, M., and Smith, G. (2011). Australian rainfall and runoff, project 10: appropriate safety criteria for vehicles. *Tech. Rep.; Eng.*

Shen, J., Tan, F., and Zhang, Y. (2018). Improved building treatment approach for urban inundation modeling: A case study in wuhan, china. *Water*, 10(12).

Shu, C., Xia, J., Falconer, R. A., and Lin, B. (2011). Incipient velocity for partially submerged vehicles in floodwaters. *Journal of Hydraulic Research*, 49(6):709–717.

Smith, D. (1994). Flood damage estimation - a review of urban stage-damage curves and loss functions. *Water SA*, 20(3):231–238.

Smith, G., Davey, E., and Cox, R. (2014). Flood hazard. wrl technical report 2014/7. *Water Research Laboratory*.

Smith, G. P., Rahman, P. F., and Wasko, C. (2016). A comprehensive urban floodplain dataset for model benchmarking. *International Journal of River Basin Management*, 14(3):345–356.

Soares-Frazão, S. and Zech, Y. (2008). Dam-break flow through an idealised city. *Journal of Hydraulic Research*, 46(5):648–658.

Soares-Frazão, S., Lhomme, J., Guinot, V., and Zech, Y. (2008). Two-dimensional shallow-water model with porosity for urban flood modelling. *Journal of Hydraulic Research*, 46(1):45–64.

Sturm, M., Gems, B., Keller, F., Mazzorana, B., Fuchs, S., Papathoma-Köhle, M., and Aufleger, M. (2018). Experimental analyses of impact forces on buildings exposed to fluvial hazards. *Journal of Hydrology*, 565:1 – 13.

Takahashi, S., Endoh, K., and Muro, Z. (1992). Experimental study on people's safety against overtopping waves on breakwaters. *Report on the Port and Harbour Institute*, 34(4):4–31.

Tang, H., Zhang, H., and Yuan, S. (2018). Response to: "Discussion of: hydrodynamics and contaminant transport on the degraded bed at a 90-degree channel confluence" by Seastien Pouchoulin, Pedro Xavier Ramos, Emmanuel Mignot, et al. *Environmental Fluid Mechanics*, 18(5):1297–1299.

Taylor, E. H. (1944). Flow characteristics at rectangular open-channel junctions. *Transactions of the American Society of Civil Engineers*, 109(1):893–902.

Testa, G., Zuccala, D., Alcrudo, F., Mulet, J., and Soares-Frazão, S. (2007). Flash flood flow experiment in a simplified urban district. *Journal of Hydraulic Research*, 45(sup1):37–44.

Thusyanthan, N. I. and Gopal Madabhushi, S. (2008). Tsunami wave loading on coastal houses: a model approach. In *Proceedings of the institution of civil engineers-civil engineering*, volume 161, pages 77–86. Thomas Telford Ltd.

Tjallingii, S. (2012). *Water Flows and Urban Planning*, pages 91–111. Springer Netherlands, Dordrecht.

Tomiczek, T., Prasetyo, A., Mori, N., Yasuda, T., and Kennedy, A. (2016). Physical modelling of tsunami onshore propagation, peak pressures, and shielding effects in an urban building array. *Coastal Engineering*, 117:97–112.

Triatmadja, R. and Nurhasanah, A. (2012). Tsunami force on buildings with openings and protection. *Journal of Earthquake and Tsunami*, 06(04):1250024.

UNISDR (2009). Terminology on disaster risk reduction. *United Nations Office for Disaster Risk Reduction, Report*.

United Nations, Department of Economic and Social Affairs, and Population Division (2019). *World urbanization prospects: The 2018 Revision*. United Nations, New York.

van de Lindt, J. W., Gupta, R., Garcia, R. A., and Wilson, J. (2009). Tsunami bore forces on a compliant residential building model. *Engineering Structures*, 31(11):2534–2539.

Velickovic, M., Zech, Y., and Soares-Frazão, S. (2017). Steady-flow experiments in urban areas and anisotropic porosity model. *Journal of Hydraulic Research*, 55(1):85–100.

Ward, R. C. (1978). Floods: a geographical perspective. *MacMillan*.

Weber, L. J., Schumate, E. D., and Mawer, N. (2001). Experiments on Flow at a 90° Open-Channel Junction. *Journal of Hydraulic Engineering*, 127(5):340–350.

White, G. F. (1961). Papers on flood problems. *Department of Geography, University of Chicago*, Research Paper No. 29.

Wüthrich, D., Pfister, M., Nistor, I., and Schleiss, A. J. (2018). Experimental study on forces exerted on buildings with openings due to extreme hydrodynamic events. *Coastal Engineering*, 140:72–86.

Xia, J., Falconer, R. A., Wang, Y., and Xiao, X. (2014a). New criterion for the stability of a human body in floodwaters. *Journal of Hydraulic Research*, 52(1):93–104.

Xia, J., Falconer, R. A., Xiao, X., and Wang, Y. (2014b). Criterion of vehicle stability in floodwaters based on theoretical and experimental studies. *Nat Hazards*, 70:1619–1630.

Xia, J., Teo, F. Y., Lin, B., and Falconer, R. A. (2011). Formula of incipient velocity for flooded vehicles. *Nat Hazards*, 58:1–14.

Yasuda, T., Hiraishi, T., et al. (2004). Experimental study of tsunami inundation in coastal urban area. In *The Fourteenth International Offshore and Polar Engineering Conference*. International Society of Offshore and Polar Engineers.

Zhou, Q., Yu, W., Chen, A. S., Jiang, C., and Fu, G. (2016). Experimental assessment of building blockage effects in a simplified urban district. *Procedia Engineering*, 154:844 – 852. 12th International Conference on Hydroinformatics (HIC 2016) - Smart Water for the Future.

Özgen, I., Liang, D., and Hinkelmann, R. (2016). Shallow water equations with depth-dependent anisotropic porosity for subgrid-scale topography. *Applied Mathematical Modelling*, 40(17):7447–7473.

Appendices

APPENDIX A

DETAILS ON VELOCITY MEASUREMENTS

A.1 LSPIV velocity data convergence

The aim of the present section is to have a visual reference of surface velocities averaged over different time durations. Surface velocity magnitude maps are shown in Figures A.1 and A.2, for the porous city block configuration and the configuration without city block (i.e. the town square configuration), respectively. The velocity maps are displayed for different averaging durations, from 10 to 180 s, for visual comparison. The spatial resolution for velocity estimation on streets and within the city block was 2 $\times$ 2 cm.

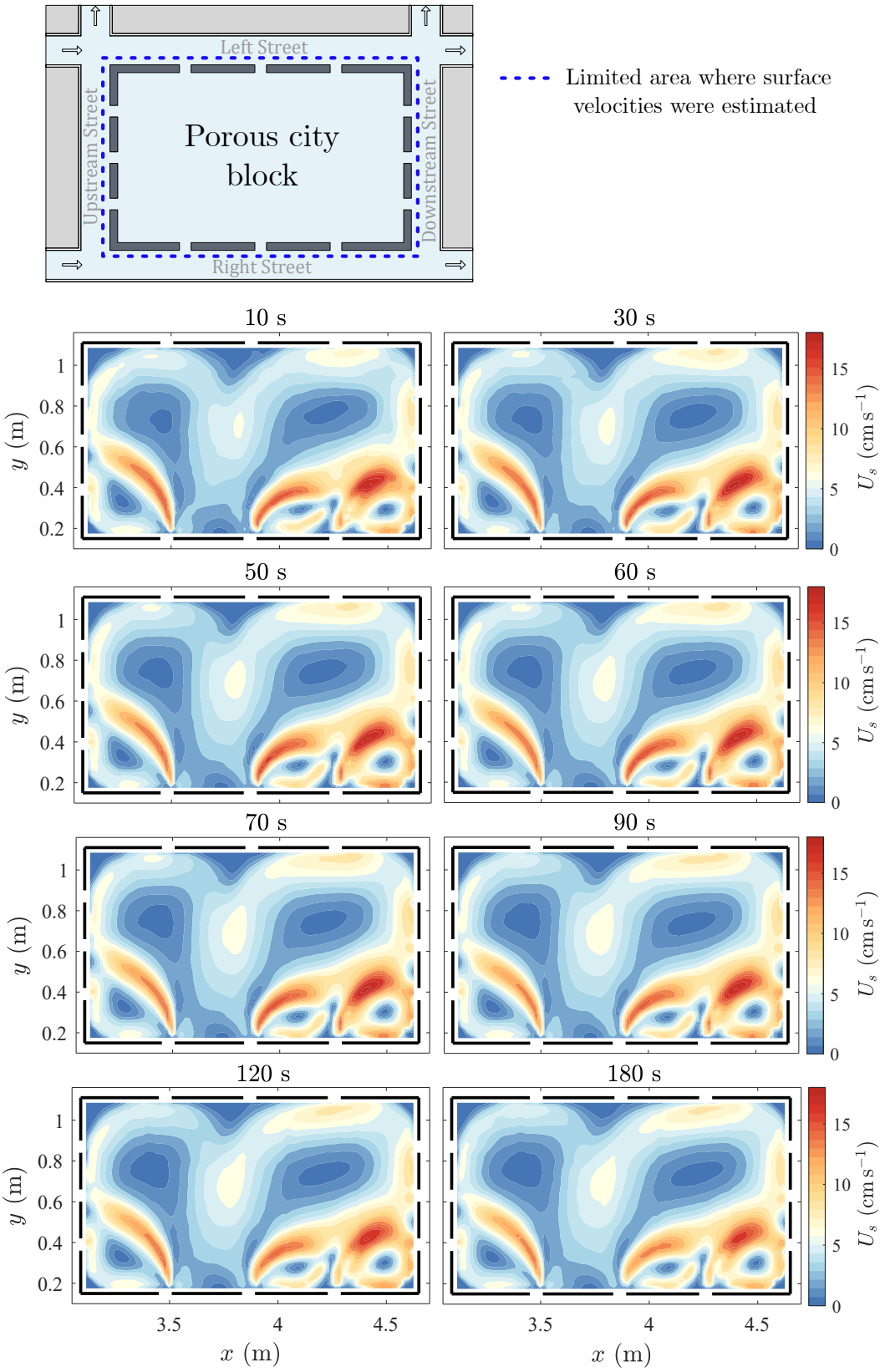

FIGURE A.1. Time-averaged surface velocity magnitude, U_s, within the city porous block (the city block has three openings in each wall), for increasing averaging durations, from 10 to 180 s.

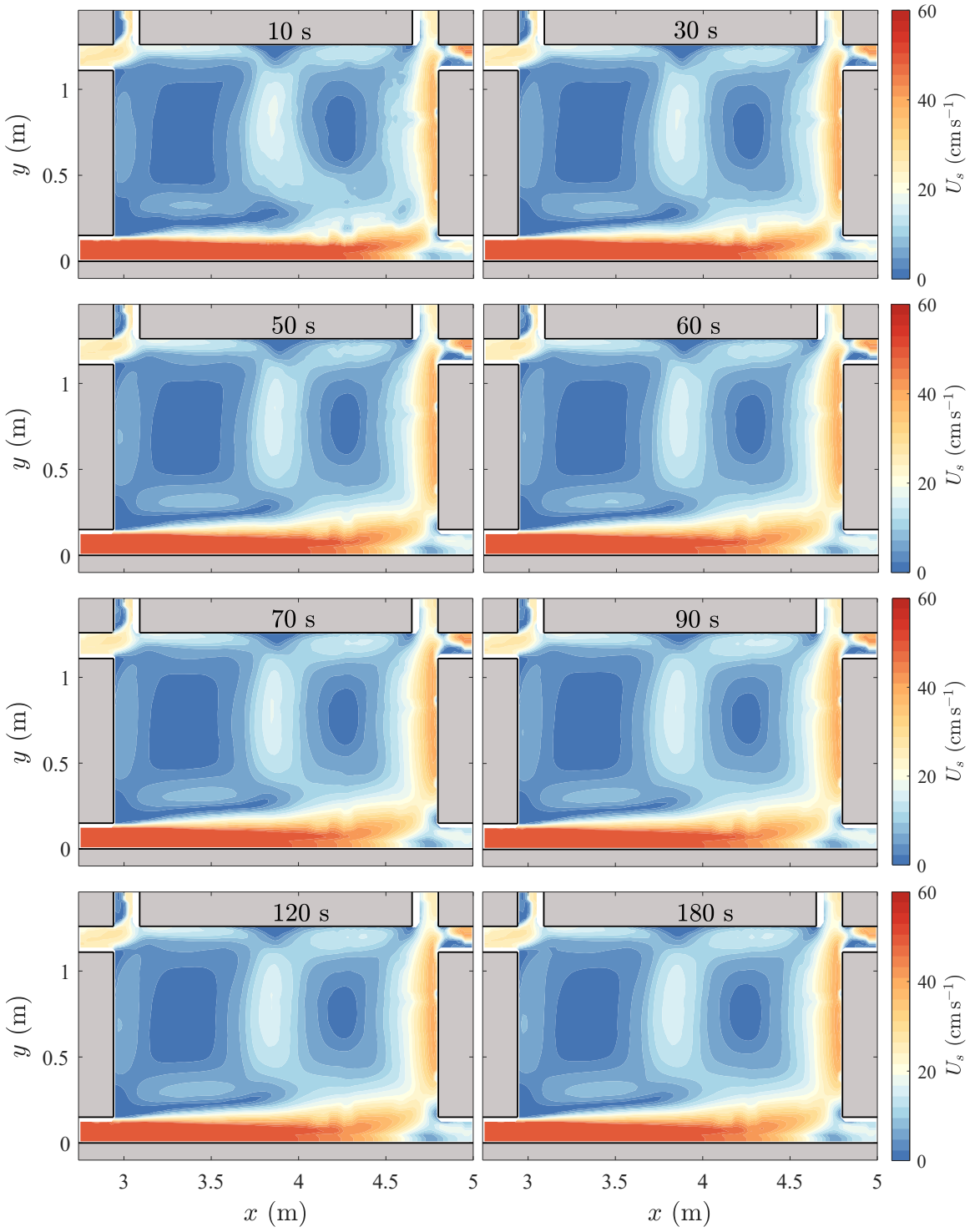

FIGURE A.2. Time-averaged surface velocity magnitude, U_s, for a town square configuration (without the city block), for increasing averaging durations, from 10 to 180 s.

A.2 Comparison between ADV and LSPIV velocity data

The surface velocities estimated with the LSPIV technique are compared with the velocities measured within the water column using the ADV (two types of ADV velocity data are considered, near-surface velocities and depth-averaged velocities). For this purpose, horizontal streamwise velocity (U_x and U_y, depending on the street) profiles are measured with the ADV at various cross sections along the different streets. Within the city block, horizontal profiles, along x-axis, (U_x), are also measured. The tests are carried out under steady flow conditions and subcritical regime using the experimental set-up variant 1 (see Figure 3.4) under various configurations to cover a wide range of flow types: with a non-porous city block, without city block and with porous city block by varying the number of openings. The orientation of the ADV for velocity measurements within the city block is shown in Figure A.3.

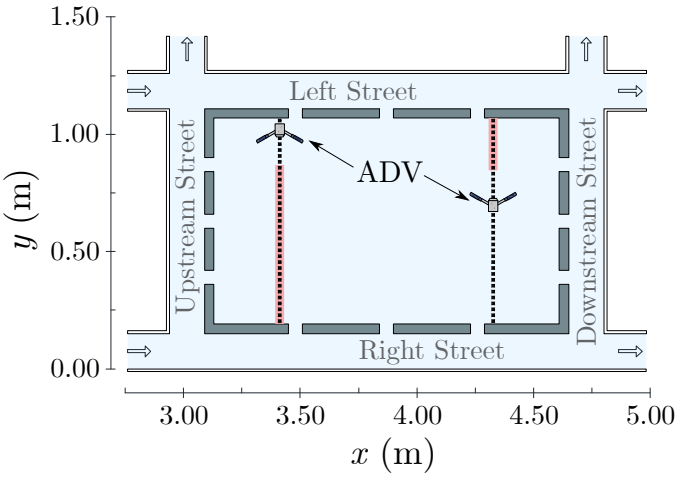

FIGURE A.3. Orientation of the ADV to obtain velocity profiles within the city block. To obtain velocities over the full section between the block walls, the ADV had to be rotated. In this scheme, the ADV is oversized with respect to the block, for better visualisation.

Within the city block, the considered horizontal profiles of ADV velocity, depth-averaged velocities and near-surface velocities are almost identical (see red and green horizontal profiles in the various plots in Figure A.4). This proves that a two-dimensional flow takes place within the block. Indeed, the block can be considered as a shallow water reservoir, where the water body vertical length (VL) is much smaller than its horizontal length (HL), VL/HL $\ll$ 1. Besides the surface velocity profiles obtained with the LSPIV technique are in good agreement with the ADV velocity profiles, mainly in the areas where the flow direction is primarily along the x-axis, see Figure A.4. In areas, located between recirculation cells, the greatest differences are observed. These discrepancies may be linked to a misalignment of the ADV with respect to the stream flow direction. The flow within the block follows spatially different directions, and it is possible that in some areas its location is not ideal and

disturbs the flow. This could be confirmed by observing the great agreement between ADV and LSPIV profiles in areas where none of the above conditions are present, for instance the second graph in Figure A.4 (the velocity profile obtained at position $x = 4.34$ m), as well at the lower plot in Figure 3.19. In both, velocity profiles were obtained along a large recirculation cell, very close to its core, therefore, the flow direction in the left half of these velocity profiles is predominantly along the x-axis, and the right half also, but in the opposite direction.

In the streets, the overall agreement between ADV and LSPIV velocity profiles is fair, but some specific areas exhibit discrepancies. In the right street, the LSPIV velocity magnitude is intermediate between the two ADV velocity profiles, being the near-surface velocity greater than the depth-averaged velocity. Also velocities near the right-hand wall obtained with the LSPIV technique do not show the strong decrease observed in the ADV profiles, see Figure A.5. In the left street, a better agreement between ADV and LSPIV velocity profiles is observed, and both ADV profiles (depth-averaged and near-surface) are very similar to each other, see Figure A.5. For the other streets, upstream and downstream, the agreement between ADV and LSPIV velocity profiles is fair (see Figure A.6), but with a slight underestimation of the velocity with the LSPIV technique in the downstream street.

To conclude, velocities with the LSPIV technique were better estimated within the block than in the streets. I assume this is due to some factors:(i) the free water surface within the block is flat, whereas flow depth fluctuations in the streets, mainly in the right and downstream streets, alter the free surface elevation; (ii) releasing adequate tracer concentration in the streets, to cover their entire cross-section, without causing clogging, is very challenging; and (iii) since the streets are narrow, the side walls, although transparent, created some shade in certain areas, affecting the LSPIV velocities estimation.

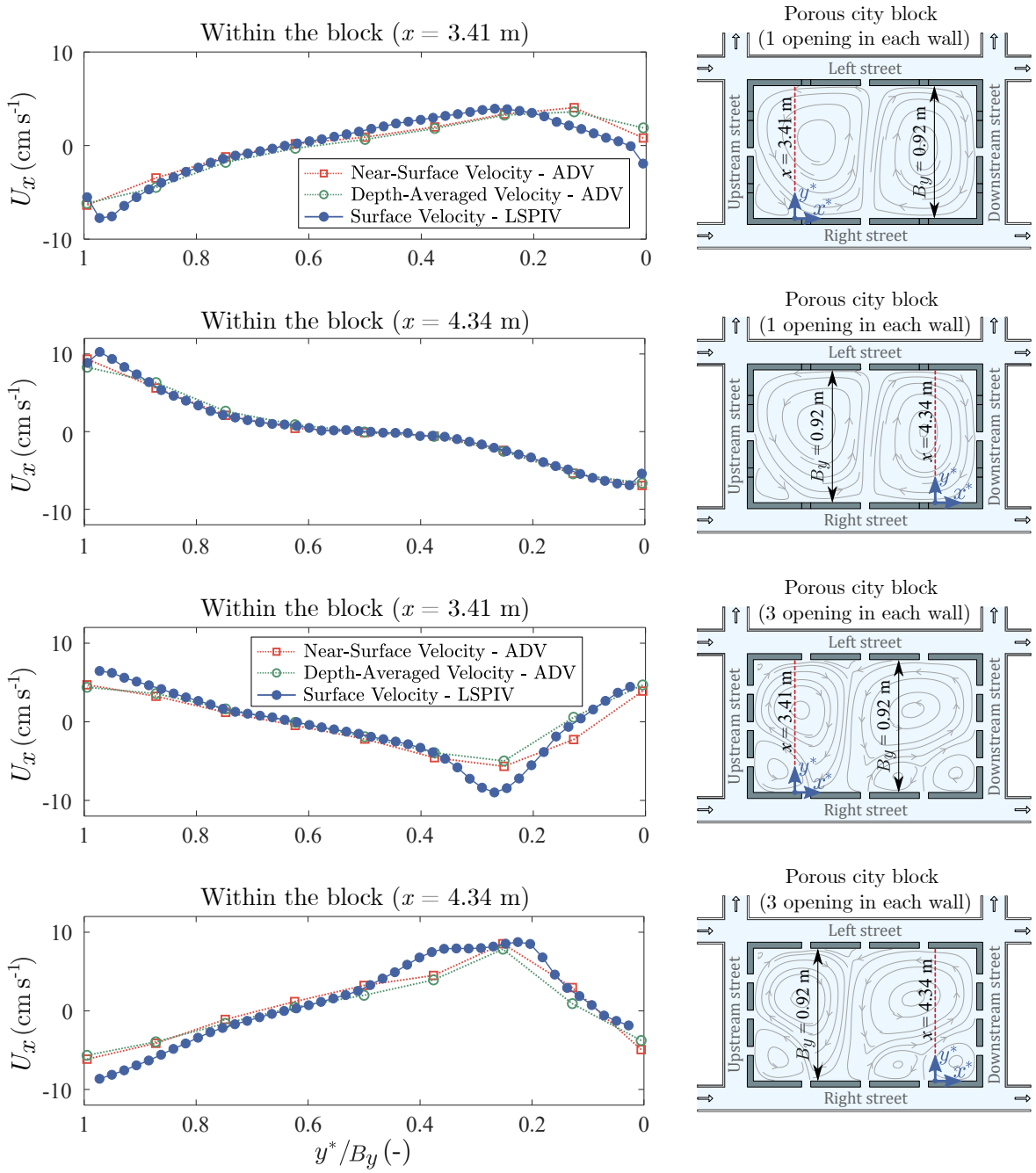

FIGURE A.4. Comparison of horizontal profiles, along x-axis, of time-averaged velocity measured by LSPIV and ADV within the city block for two configurations in the experimental set-up variant 1: First configuration (the two upper plots) with one opening in each block wall, the second one (the two lower plots) with three openings in each block wall. Each set-up schematic shows the measured streamlines within the block. Two ADV velocity profiles are plotted: in green the depth-averaged velocity and in red the velocity measured close to the free-surface. Local coordinates are denoted as $x*$ and $y*$, as indicate in each set-up scheme.

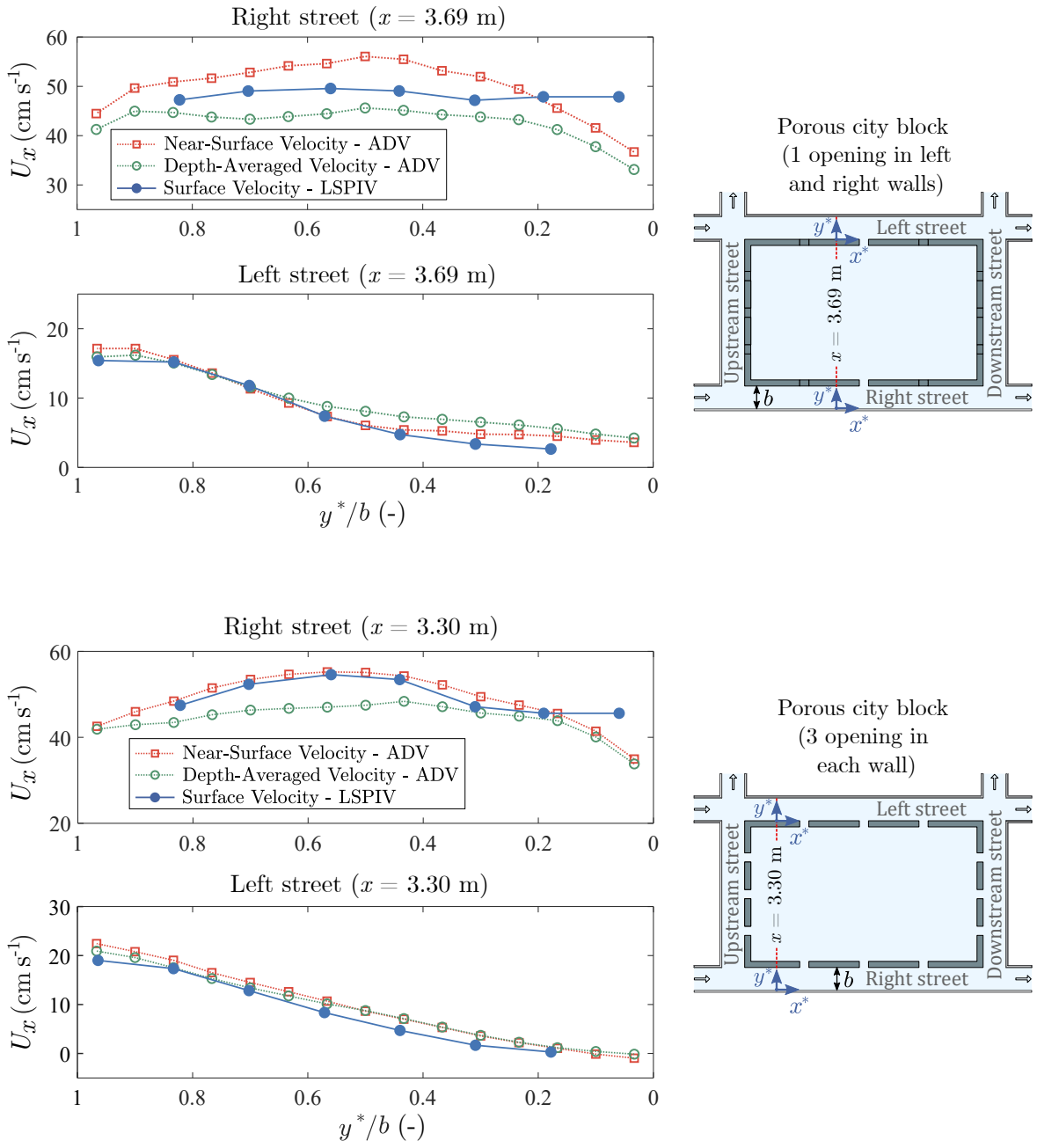

FIGURE A.5. Comparison of horizontal profiles of time-averaged streamwise velocity measured by LSPIV and ADV in the right and left streets for two configurations: First configuration with one opening in left and right block walls (the two upper plots) and a second one with three openings in each block wall (the two lower plots).

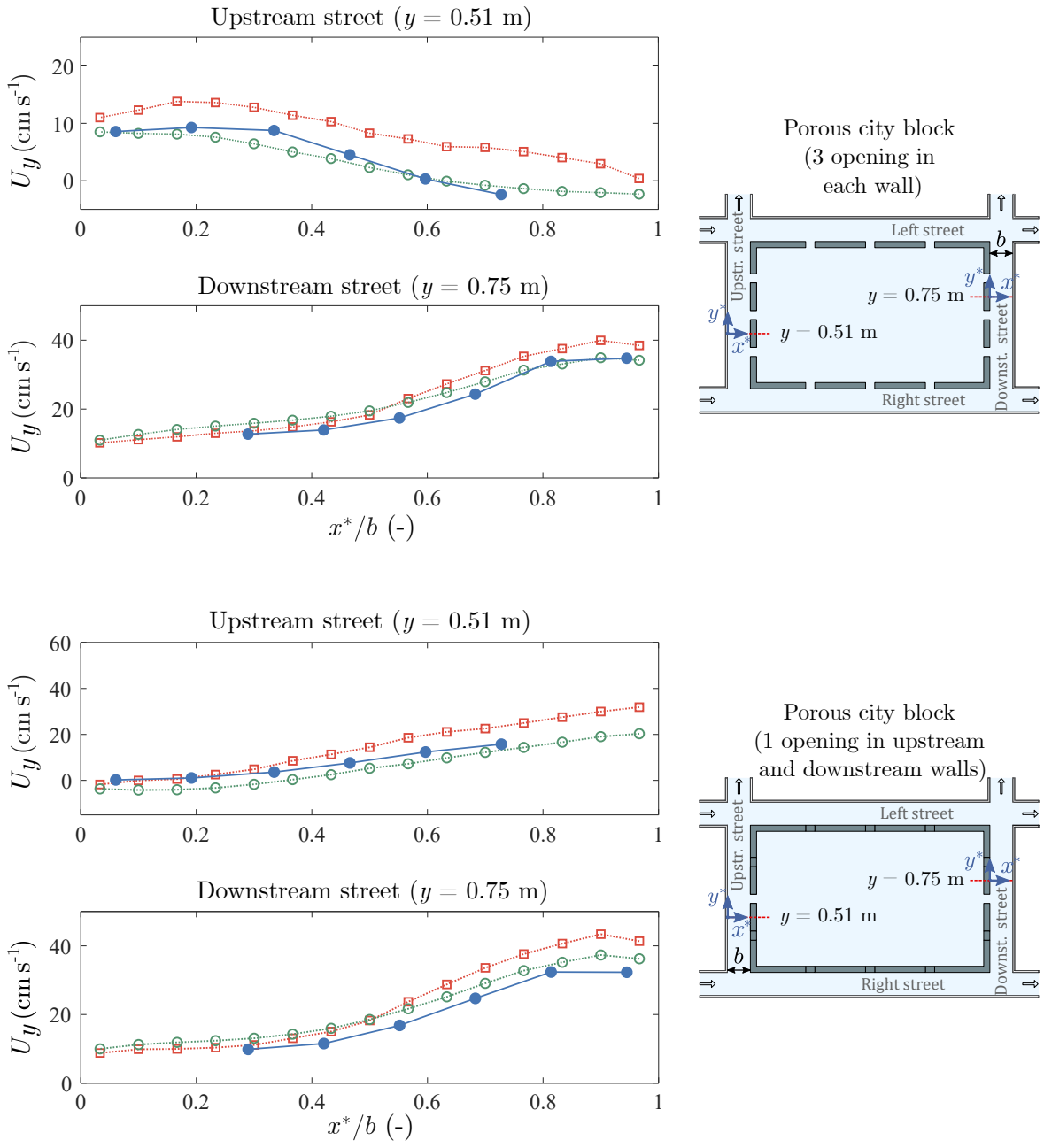

FIGURE A.6. Comparison of horizontal profiles of time-averaged streamwise velocity measured by LSPIV and ADV, in the upstream and downstream streets for two configurations: First configuration with three openings in each block wall (the two upper plots) and a second configuration with one opening in upstream and downstream block walls (the two lower plots).

APPENDIX B

STREET DISCHARGE ESTIMATE BY THE VELOCITY-AREA METHOD: IMPACT OF EXTRAPOLATION METHODS

The discharge estimate in the streets is carried out with the velocity-area method. These velocities are measured with the ADV through the street cross-section, however, due to lack of velocity data in the areas close to the boundaries (sidewalls, free surface and bed), an extrapolation of the measured velocity field is required. Three extrapolation methods are examined: the *no-slip boundary condition*, the *slip boundary condition* (see Figure 3.24) or an *average* between the two aforementioned conditions. While the slip condition is used for the free-surface, for the other boundaries (2 sidewalls and bed) 27 scenarios are evaluated combining the three conditions, see Figure B.1.

This evaluation is performed on fourteen cross-sections, spread over the four streets and under different flow conditions, see Figure B.2. For the two first cross-sections, A and B, in a straight street configuration, the discharge are measured with two flowmeters $Q_{in,1}$ and $Q_{out,1}$. Then, ten cross-sections are considered in a non-porous city block configuration, two in the right street, C and D, two in the left street, E and F, three in the upstream street, G, H and I, and three in the downstream street, J, K and L. The flowmeters at inlets 1 and 2 ($Q_{in,1}$ and $Q_{in,2}$), and those at outlets 1, 2 and 3 ($Q_{out,1}$, $Q_{out,2}$ and $Q_{out,3}$) measure the

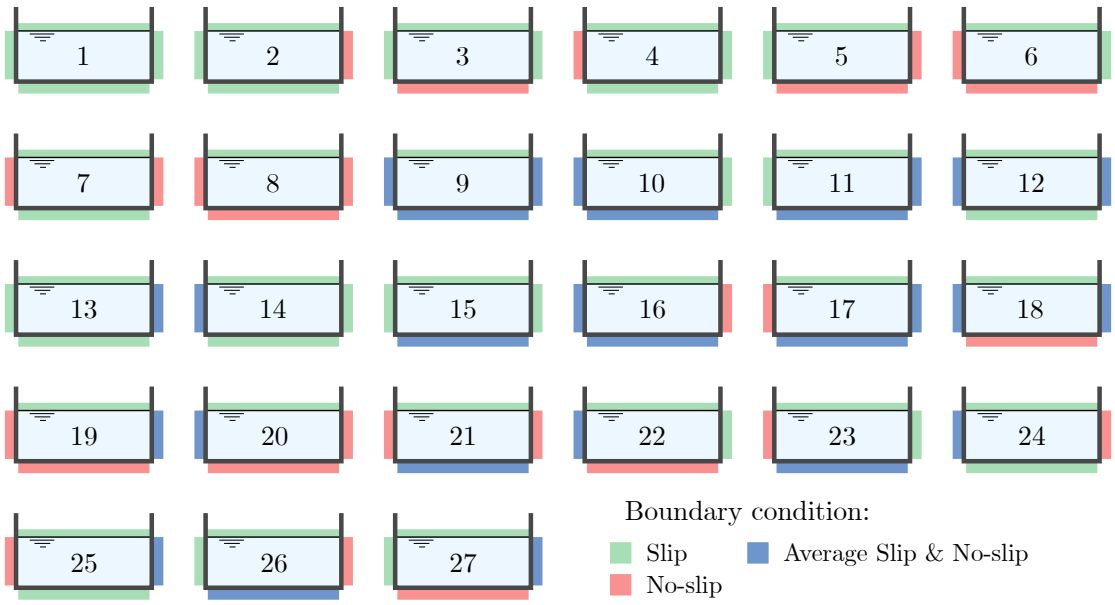

FIGURE B.1. Boundary condition scenarios in the street cross-section, used when extrapolating the measured velocity field near the boundaries. For the street discharge estimation, the slip condition (green) is set at the free-surface boundary, while for the others (sidewalls and bed), a combination of the three proposed conditions is applied.

discharges. Finally, two more cross-sections, M and N, in the right street for a porous city block configuration (an opening in the right and left walls). The flowmeters at outlets 1, 2 and 3 ($Q_{out,1}$, $Q_{out,2}$ and $Q_{out,3}$) measure the discharges. All these tests are performed in subcritical regime.

The estimated discharges in each of these cross-sections, using Eqs. 3.9 and 3.10 with all 27 extrapolation scenarios depicted in Figure B.1, are compared in Figure B.3 with those measured by the electromagnetic flowmeters, thus obtaining the error percentage of each scenario for all the fourteen cross-sections. Due to the varying velocity patterns found in the different cross sections, certain scenarios were better suited for certain streets cross-sections. For instance, scenarios 10 and 11 have the smallest errors when estimating discharges in the right street sections (C, D, M and N), scenarios 9 and 17 when estimating discharges in the left and upstream street sections (E, G, H and I), and scenarios 9 and 14 (J, K, and L) when estimating discharges in the downstream street sections. However, using different extrapolation scenarios as a function of the cross-section location could lead to larger deviations, because these 14 analysed cross-sections represent only a small fraction of all possible velocity patterns and distributions in the different streets, especially when various openings

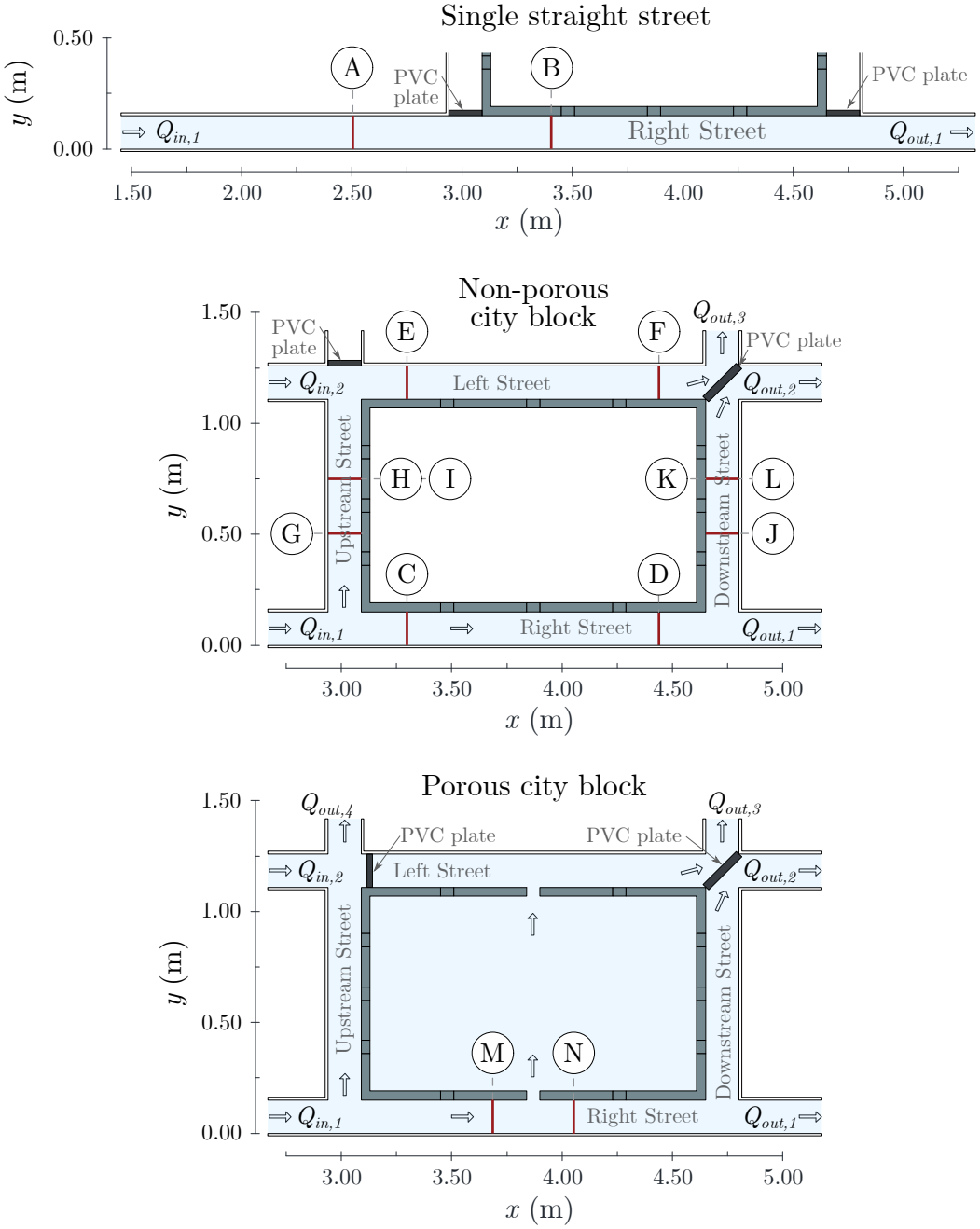

FIGURE B.2. Location of the cross-sections used for the evaluation of the different extrapolation scenarios.

are included in the porous city block.

Therefore, the best-suited extrapolation scenario is identified computing the Mean Absolute Percentage Error (MAPE) for each of the 27 scenarios:

$$MAPE = \frac{1}{n}\sum_{i=1}^{n} \left| \frac{Q_{fl} - Q_{va}}{Q_{fl}} \right| \tag{B.1}$$

where Q_{fl} is the discharge measured by the flowmeter, Q_{va} is the discharge estimated by the Velocity-Area method, and n is the number of cross-sections ($n = 14$). Figure B.3 shows boxplots for the different scenarios together with the values corresponding to the MAPE. Among all scenarios, scenarios 9, 10 and 11 lead to the lowest error (1.47%, 1.49% and 1.48%, respectively), but scenario 9 is chosen because it has the lowest third quartile value. Hence, the boundary conditions for the extrapolation of the velocities near the boundaries are: *slip condition* in the free-surface and the *average* between slip and no-slip conditions in the other three boundaries (sidewalls and bed).

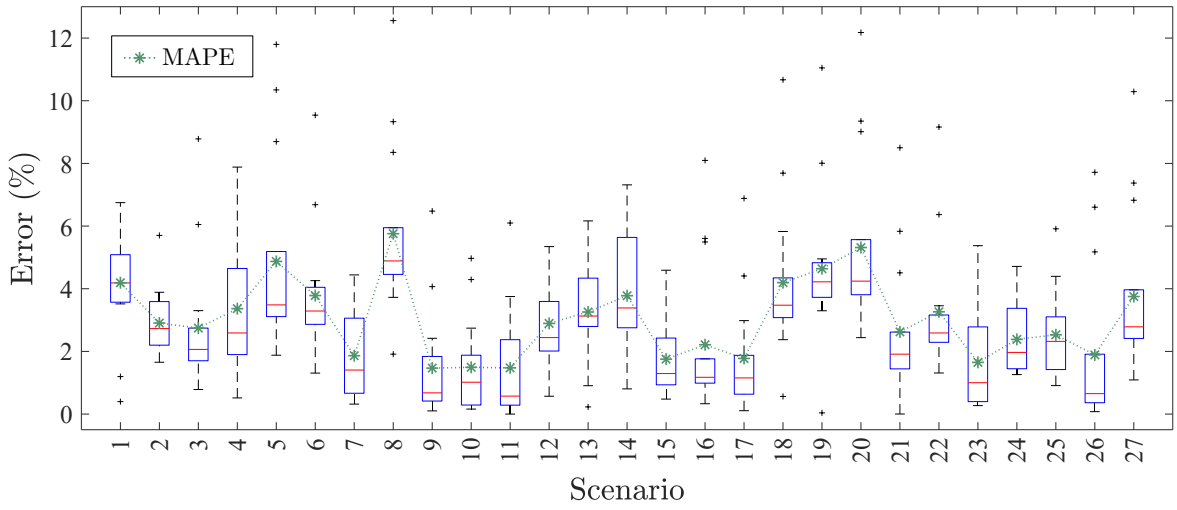

FIGURE B.3. Mean Absolute Percentage Error (MAPE) and distribution of the error percentages for the 27 boundary condition scenarios.

Finally, Figure B.4 shows the time-averaged velocity distributions of all cross-sections analysed, shown in Figure B.2.

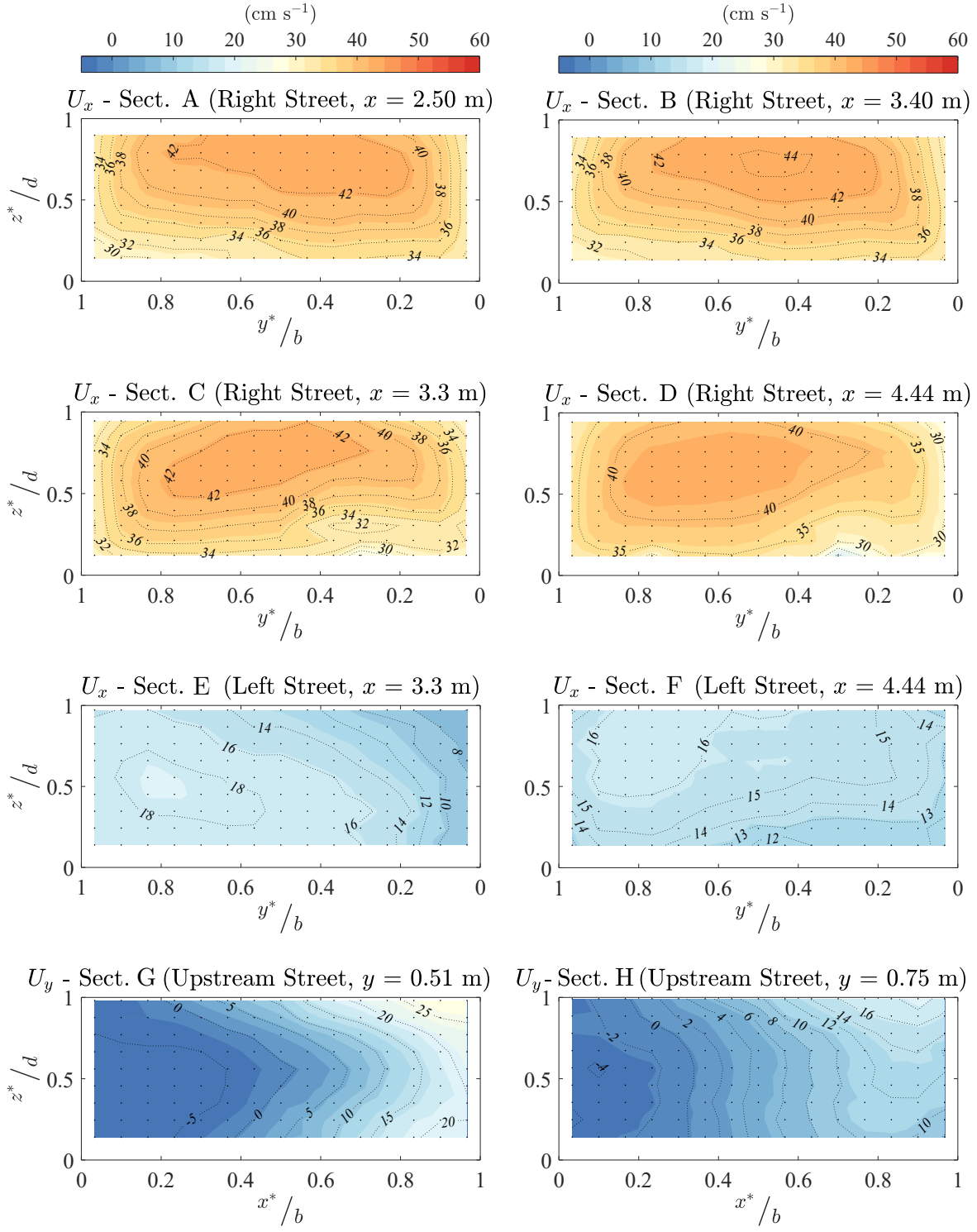

FIGURE B.4. Cross-sectional distributions of the time-averaged velocity of the different cross-sections analysed, shown in Figure B.2.

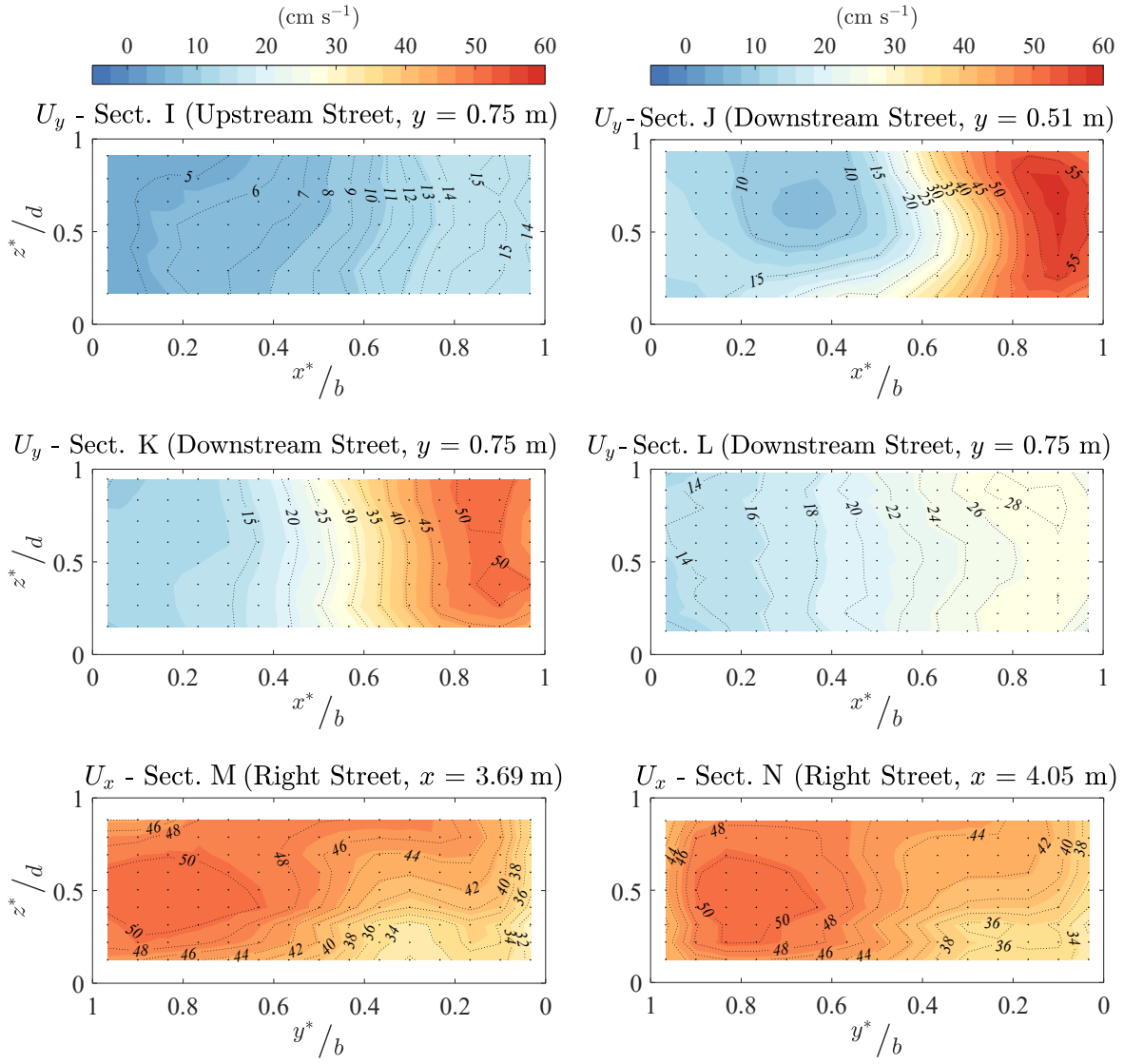

FIGURE B.4. (Continued) Cross-sectional distributions of the time-averaged velocity.

APPENDIX C

EFFECT OF THE ADV INTRUSION ON WATER FLOW THROUGH A NARROW CROSS SECTION.

As shown in Figure 3.22 of Section 3.3.4, to obtain the velocities over a complete street cross-section, the velocity measurements are performed in two stages, in a first stage the velocities of one half cross-section are measured, then in a second stage, after rotating the ADV, the velocities are measured in the remaining half cross-section. Velocity measurements are then performed twice at the centreline of the street cross-section (at x/b = 0.5 in Figure C.1), which is useful for a cross-check of velocities on both sides. However, during different tests it was observed that the ADV shifts the velocity field. When the ADV is located on the right side of the street (oriented to measure the velocities in the left half-section), the flow is shifted towards

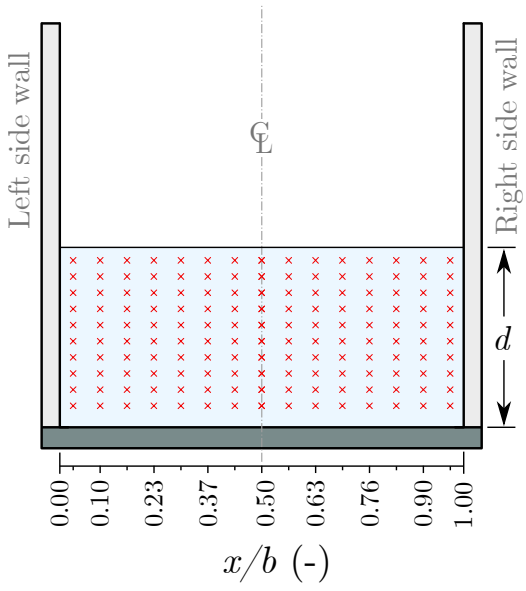

FIGURE C.1. ADV velocity measurement grid in the street cross-section (red markers).

the left wall, then it is placed on the other side to measure velocities in the remaining section, and the same effect occurs in the opposite direction. This was corroborated by placing the ADV frontally to the street cross-section, and measuring the velocities in the central area of the cross-section, see Figure C.2. By comparing in this figure the isovelocity lines of the central cross-section and those corresponding to the left and right half-sections, it is possible to observe the shifting of the velocity field. For instance, the isovelocity line corresponding to $U_y = 15$ cm s^{-1} (shown thickened) is observed shifted to the left in the velocity field of the left half cross-section, compared to the central cross section. The same effect is observed for the other half cross-section, in the opposite direction.

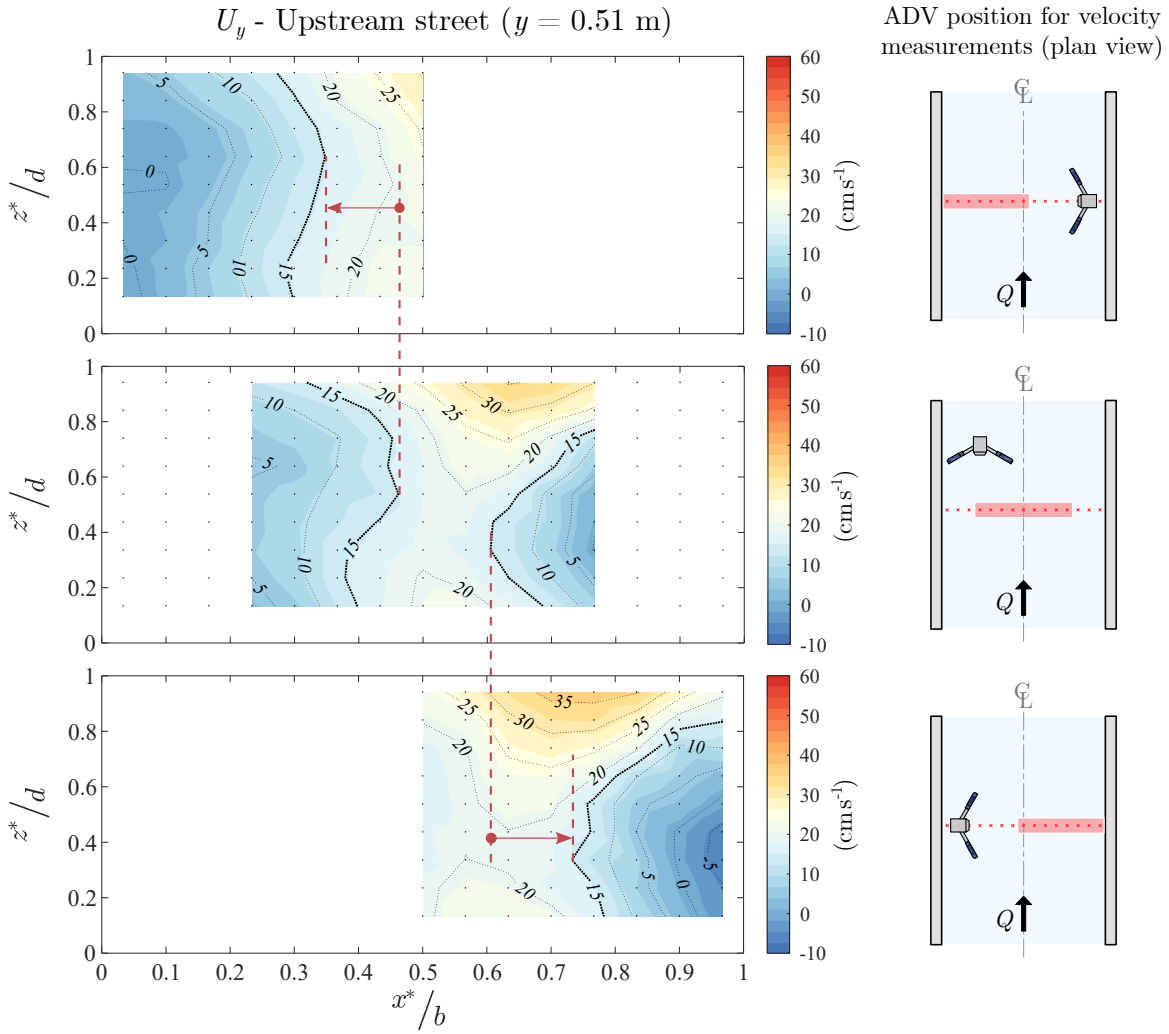

FIGURE C.2. Cross-sectional distributions of the time-averaged velocity in the upstream street. At the top, the left half section, measured with the ADV placed on the right side, in the middle the central section, measured with the ADV placed in front of the flow and at the bottom the right half section measured with the ADV placed on the left side of the street.

Therefore, a method is proposed to correct this velocity field shift caused by the ADV intrusion. This method is based on the following assumptions: (*i*) In a flow undisturbed by the intrusion of the ADV, the velocities corresponding to the street cross-section centreline (i.e. at $x/b = 0.5$ in Figure C.1) should be very similar in both half cross-sectional velocity fields; (*ii*) Due to the intrusion of ADV, the velocities measured at the different x-positions along the street cross-section correspond to a shifted flow; (*iii*) The flow at x-positions close to the sidewalls are shifted less than the flow at x-positions far from the sidewalls (i.e. when the ADV is placed on the left side to measure velocities in the right half cross-section, at $x/b = 0.1$ the flow is less shifted due to the shorter distance to the right wall, while at $x/b = 0.5$ the flow is more shifted due to more space available with the right wall; and (*iv*) The shift magnitude at all flow depths for a given x-position is the same.

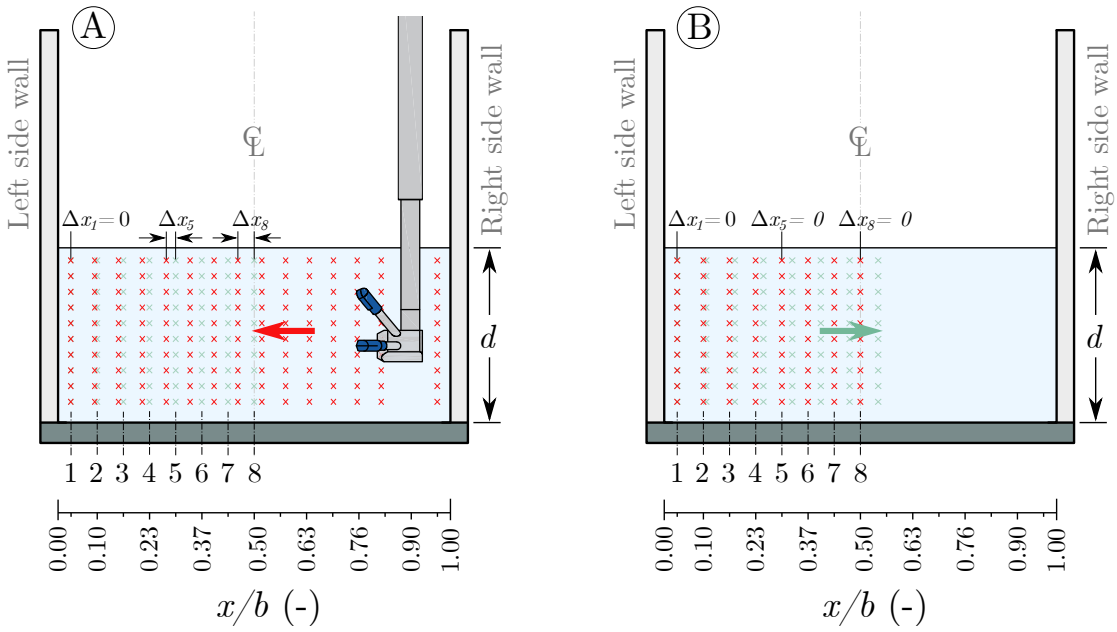

FIGURE C.3. ADV velocity measurements in the left half street cross-section. A) Velocities are measured while the flow is shifted to the left (red markers). Faint markers show the original position of vertical profiles (without the intrusion of the ADV) and where velocity measurements are performed. B) The vertical profiles where the velocities were measured are shifted to the right, interpolating their values at the positions indicated by the red markers.

Each half cross section contains eight vertical profiles where velocities are measured at various flow depths (see scheme A in Figure C.3), then according to assumptions *iii* and *iv*, the shift in profile 1 is very small, set as zero here ($\Delta x_1 = 0$, this is the closest profile to the left wall where the velocity can be measured) and that in profile 8 is the largest

($\Delta x_8 \gg 0$), among all profiles. The method consists of correcting the measured velocities at each half cross-section by reversing the shift caused by the ADV intrusion, with the following procedure:

1. The velocities measured on profile 8 are shifted to the right (opposite direction to the shift caused by the ADV). All profiles from 1 to 8 are evenly distributed along x, between the x-positions of profiles 1 (this one never moves) and profile 8 (see faint marker profiles in scheme B of Figure C.3).

2. New velocities are computed by interpolating the shifted velocities (faint markers profiles in scheme B of Figure C.3) at the original x-positions (red markers profiles in scheme B of Figure C.3).

3. This process is carried out at the same time for both velocity half cross-sections (left and right), until the velocities in profile 8 for both half sections are the same (assumption i).

It is assumed then, that these corrected cross-sectional velocity distributions represent those without the effect of the ADV intrusion and, thus lead to a more reliable computed street discharge. To determine the magnitude of the impact that corrected velocities have on the discharge computation, tests are carried out using the same velocity distributions as in Appendix B, corresponding to the fourteen cross sections shown in Figure B.2, and eleven more cross-sections measured during preliminary tests, spread over the different streets, see Table C.1. The measured velocities of these 25 street cross-sections are corrected by the method described above to compute the discharges, then these discharges are compared with computed discharges from the measured velocities.

Figure C.4 shows the absolute percentage error for each of the 25 cross sections analysed. In general, the error percentages are low, never exceeding 2%, with the highest observed in upstream and downstream streets. The mean absolute error is 0.72% and 75% of the cases have an error below 1.2%. Therefore, despite the disturbance caused by the intrusion of the ADV, velocity correction is no required to compute the street discharge. Moreover, in the required cases and only to display the street cross-sectional velocity distribution adequately, the correction is made, see Figure C.5.

TABLE C.1. Location of the cross-sections in the experimental set-up variant 1 for the analysis of the street discharge estimation.

Cross-section id	City block characteristics	Street	Position
O	1 opening in the middle of each wall	Left	$x = 3.69$ m
P		Left	$x = 4.05$ m
Q		Upstream	$y = 0.75$ m
R		Downstream	$y = 0.51$ m
S		Downstream	$y = 0.75$ m
T	1 opening in the middle of right and left walls	Left	$x = 3.69$ m
U		Left	$x = 4.05$ m
V	1 opening in the middle of upstream and downstream walls	Upstream	$y = 0.51$ m
W		Upstream	$y = 0.75$ m
X		Downstream	$y = 0.51$ m
Y		Downstream	$y = 0.75$ m

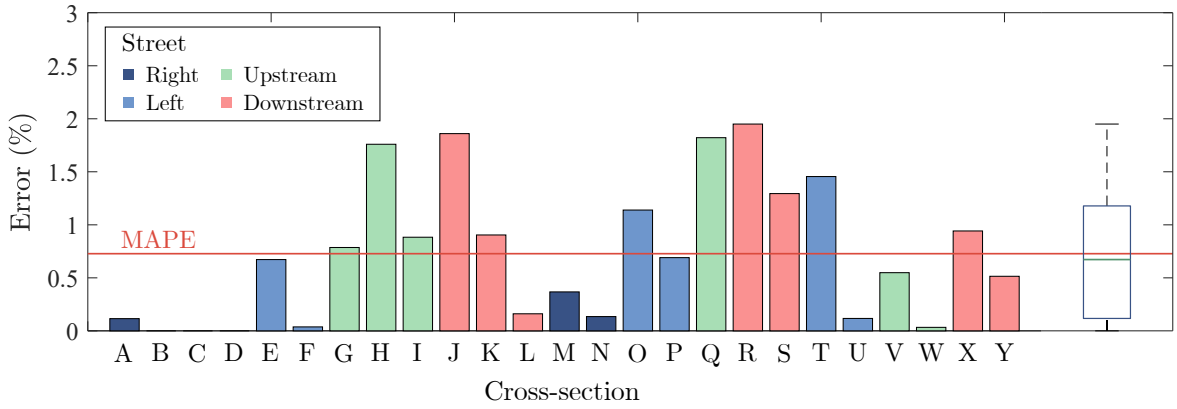

FIGURE C.4. Absolute percentage error between discharges computed with corrected velocities and measured velocities (uncorrected).

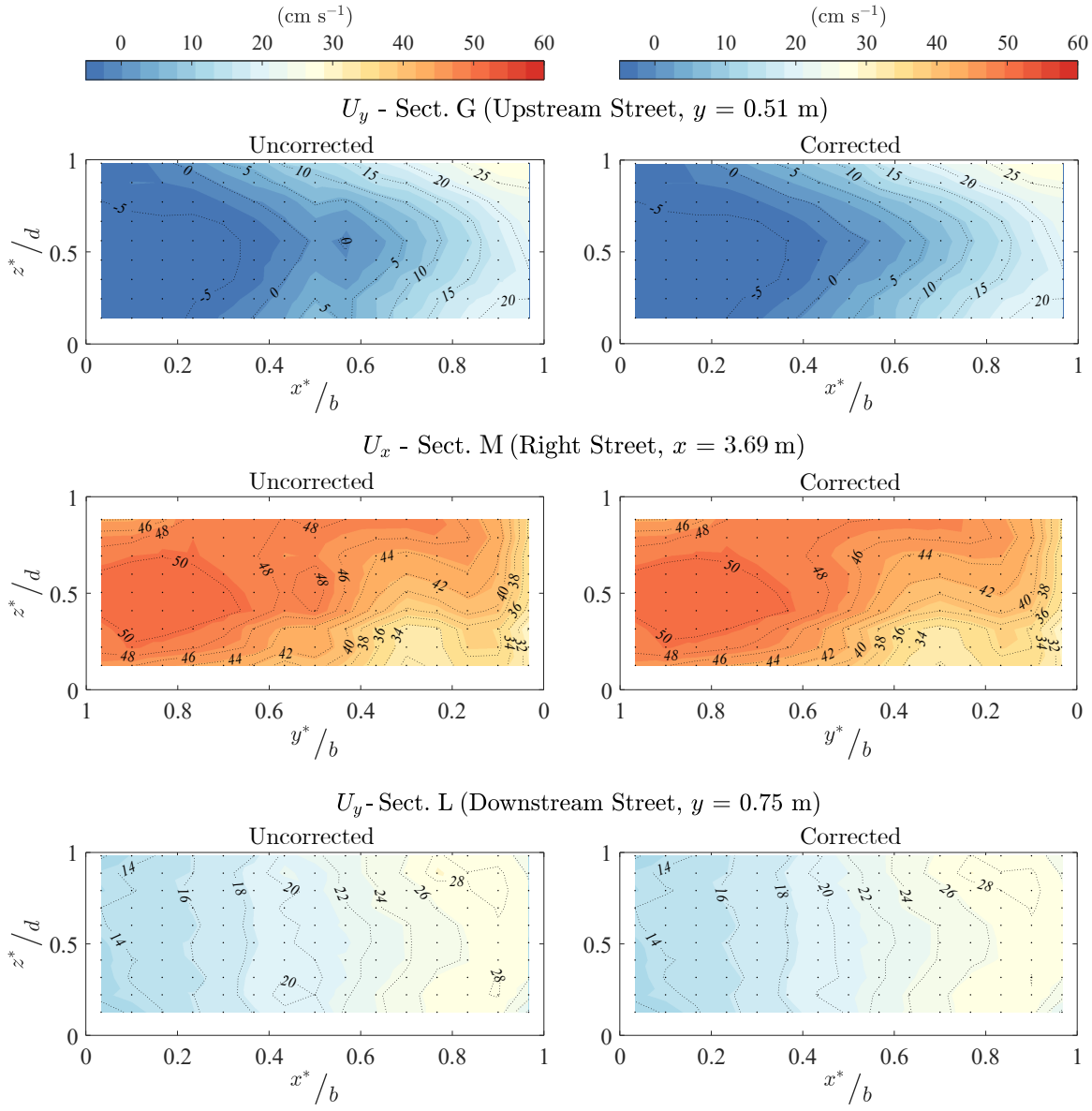

FIGURE C.5. Cross-sectional distributions of the time-averaged velocity, on the left with measured velocities (uncorrected) and on the right with corrected velocities.

APPENDIX D

INFLOW AND OUTFLOW DISCHARGE MEASUREMENTS UNDER STEADY FLOW CONDITIONS

D.1 Inflow and outflow discharges corresponding to key issues 1 and 2

The inflow and outflow discharges for each case are measured each time flow depth measurements and ADV velocity measurements are performed. Therefore, for each case, multiple sets of discharge data are available. The inflow and outflow discharges shown in Figures 4.5 and 4.17 correspond to the average of all these data sets. Statistical data for these discharge data series are shown in Figures D.1 and D.2.

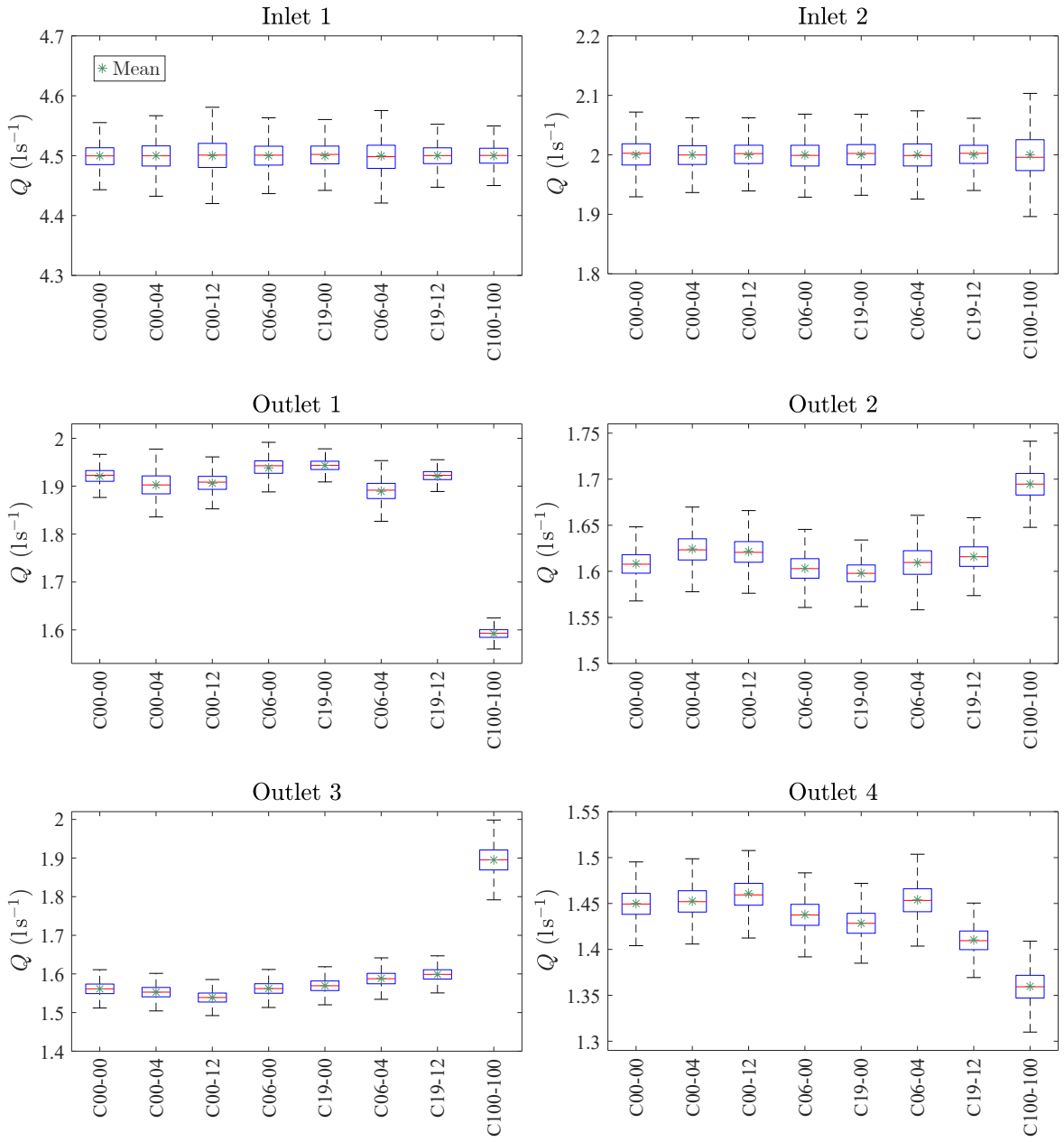

FIGURE D.1. Box plots and mean of outflow and inflow discharges, measured with electromagnetic flowmeters for all experimental cases corresponding to key issue 1.

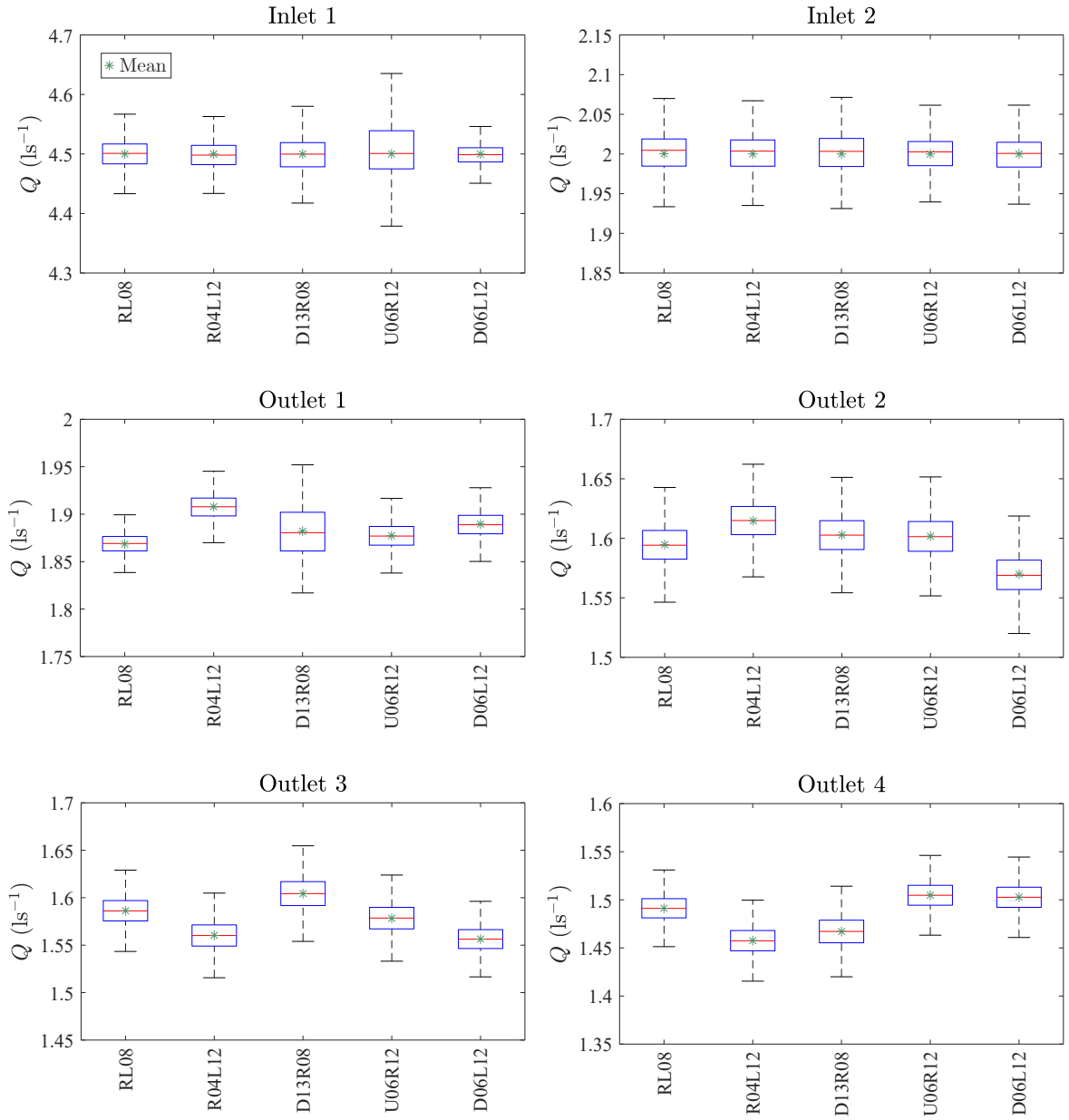

FIGURE D.2. Box plots and mean of outflow and inflow discharges, measured with electromagnetic flowmeters for all experimental cases corresponding to key issue 2.

APPENDIX E

CROSS-SECTIONAL VELOCITY DISTRIBUTIONS

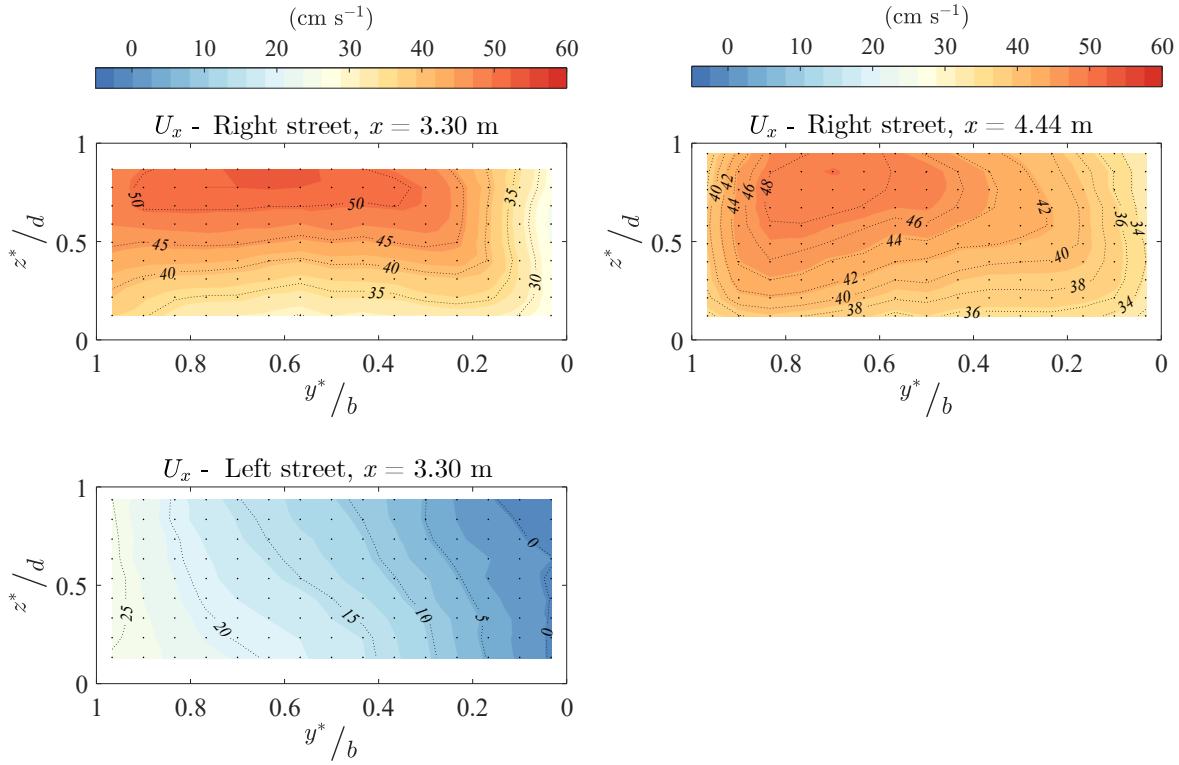

FIGURE E.1. Cross-sectional distribution of the time-averaged streamwise velocity in right and left streets corresponding to case C00-00 (Figure 4.1.A).

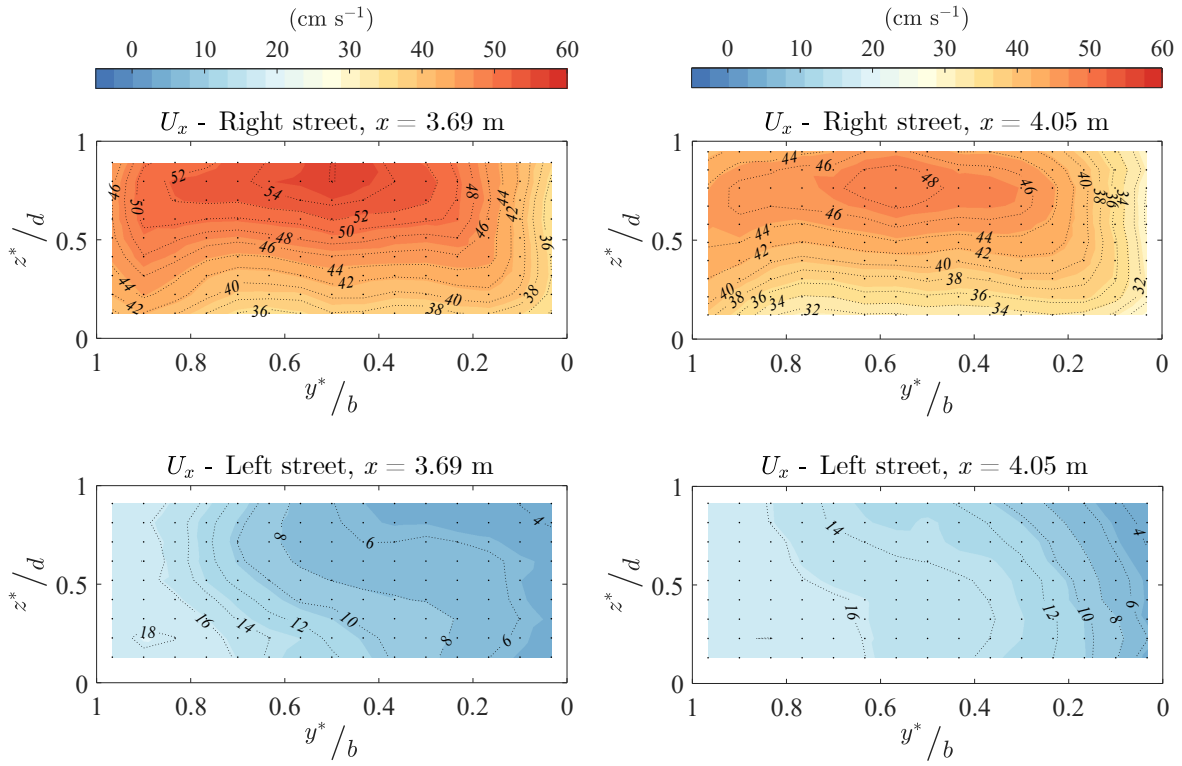

FIGURE E.2. Cross-sectional distribution of the time-averaged streamwise velocity in right and left streets corresponding to case C00-04 (Figure 4.1.C).

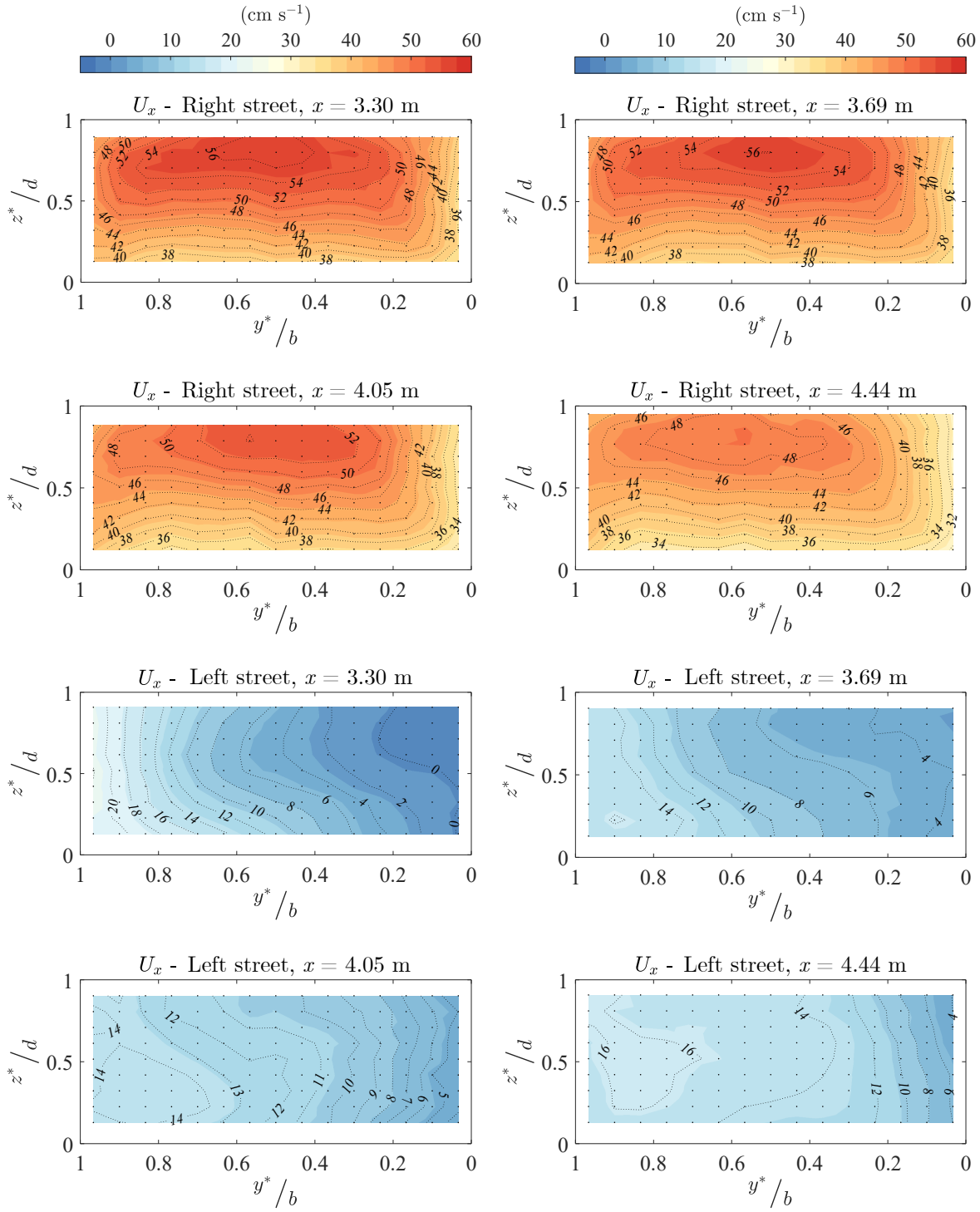

FIGURE E.3. Cross-sectional distribution of the time-averaged streamwise velocity in right and left streets corresponding to case C00-12 (Figure 4.1.D).

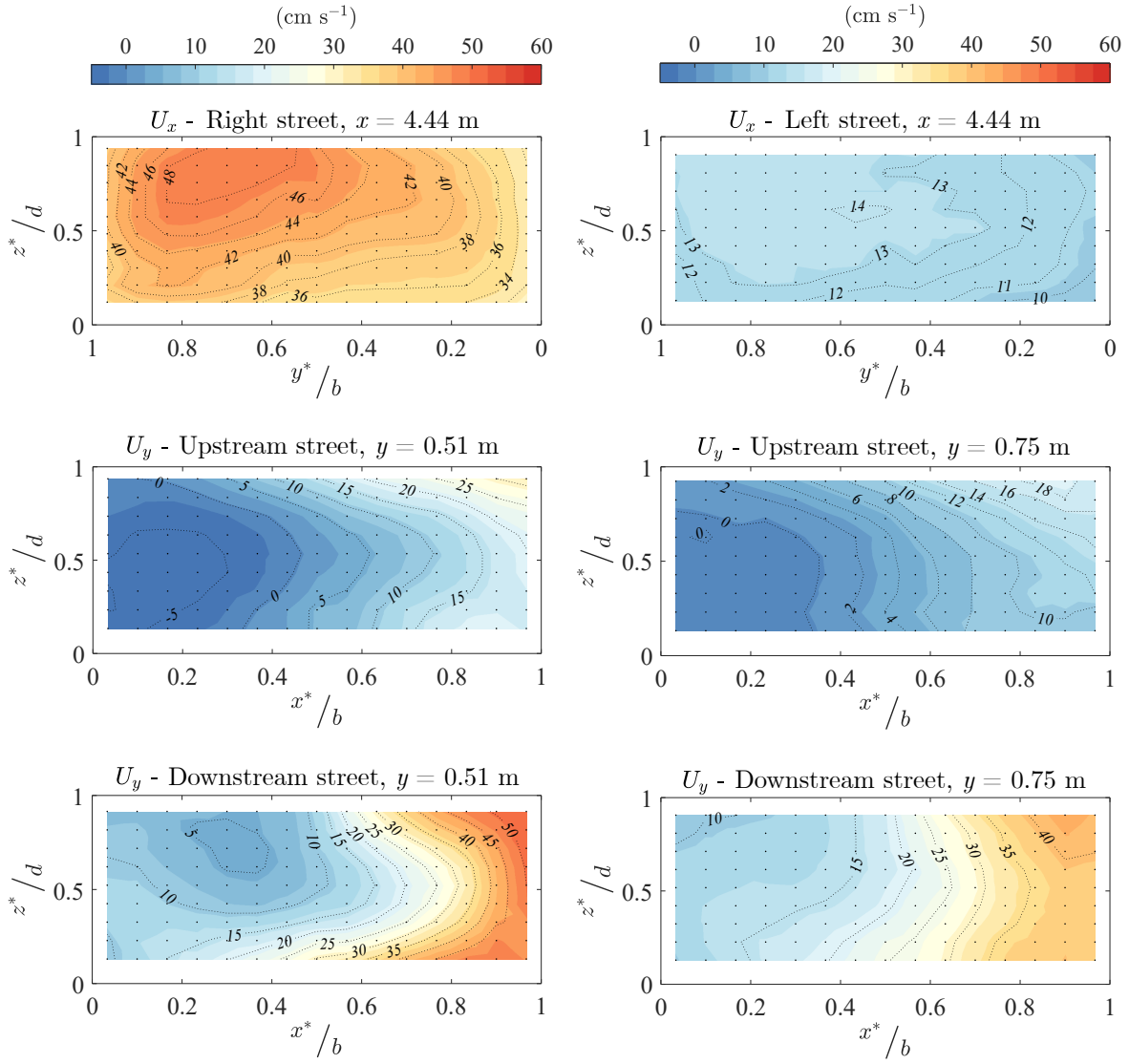

FIGURE E.4. Cross-sectional distribution of the time-averaged streamwise velocity in all streets corresponding to case C06-00 (Figure 4.1.E).

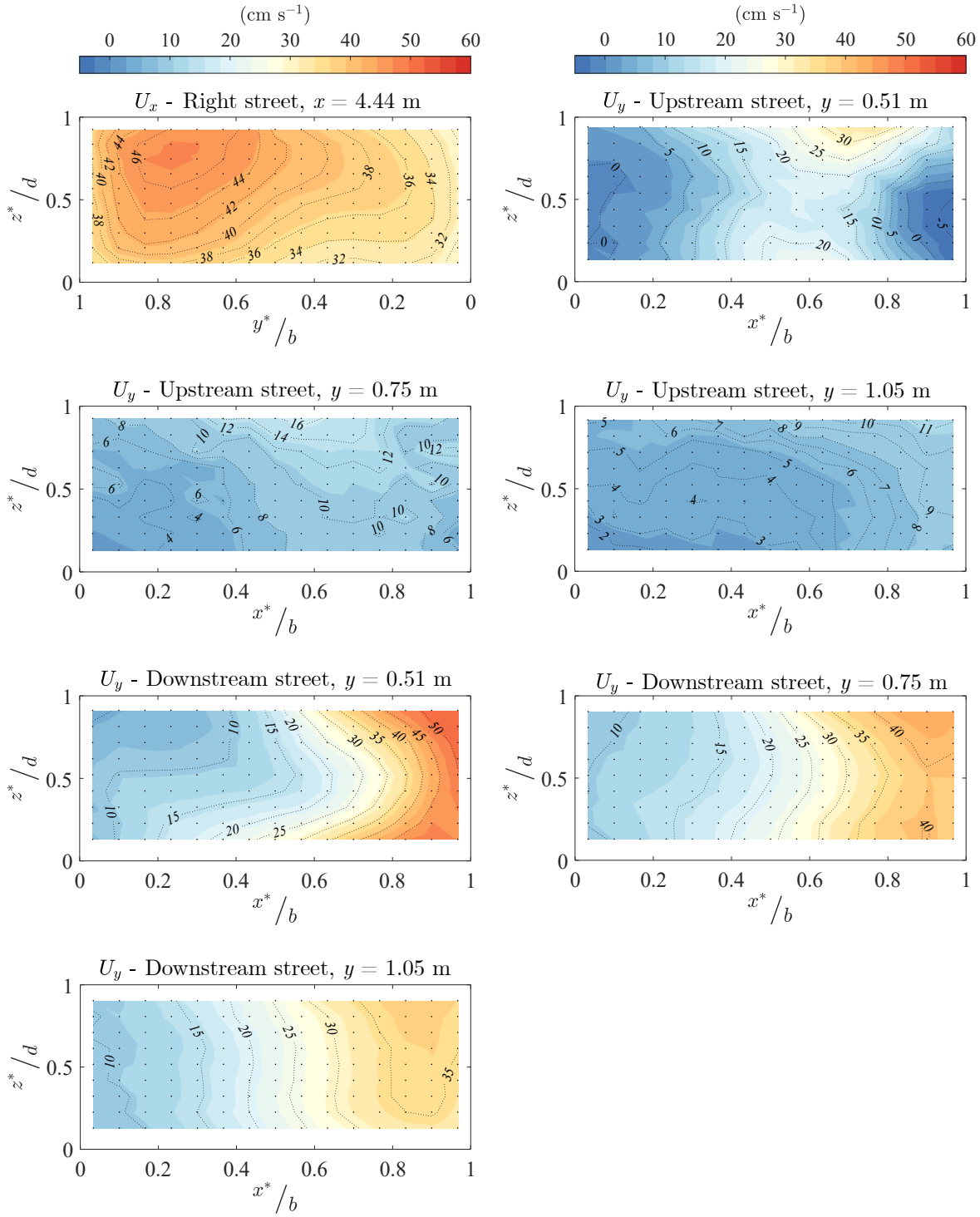

FIGURE E.5. Cross-sectional distribution of the time-averaged streamwise velocity in all streets corresponding to case C19-00 (Figure 4.1.F).

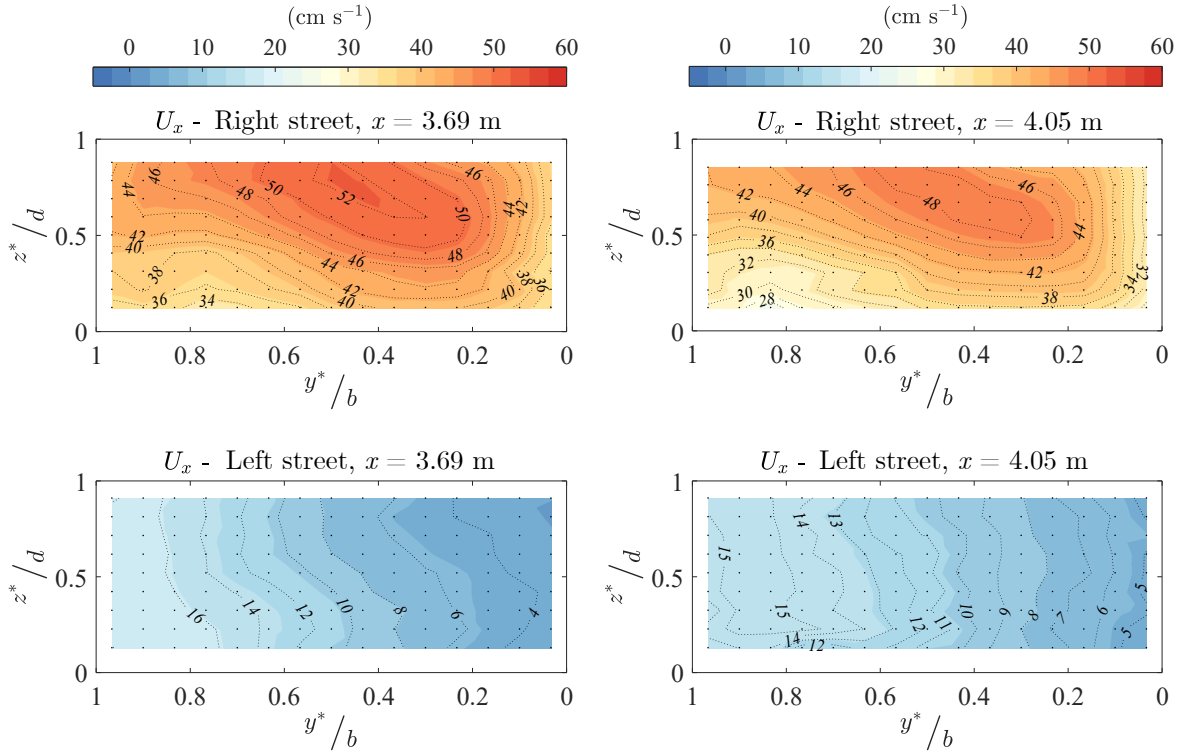

FIGURE E.6. Cross-sectional distribution of the time-averaged streamwise velocity in right and left streets corresponding to case C06-04 (Figure 4.1.G).

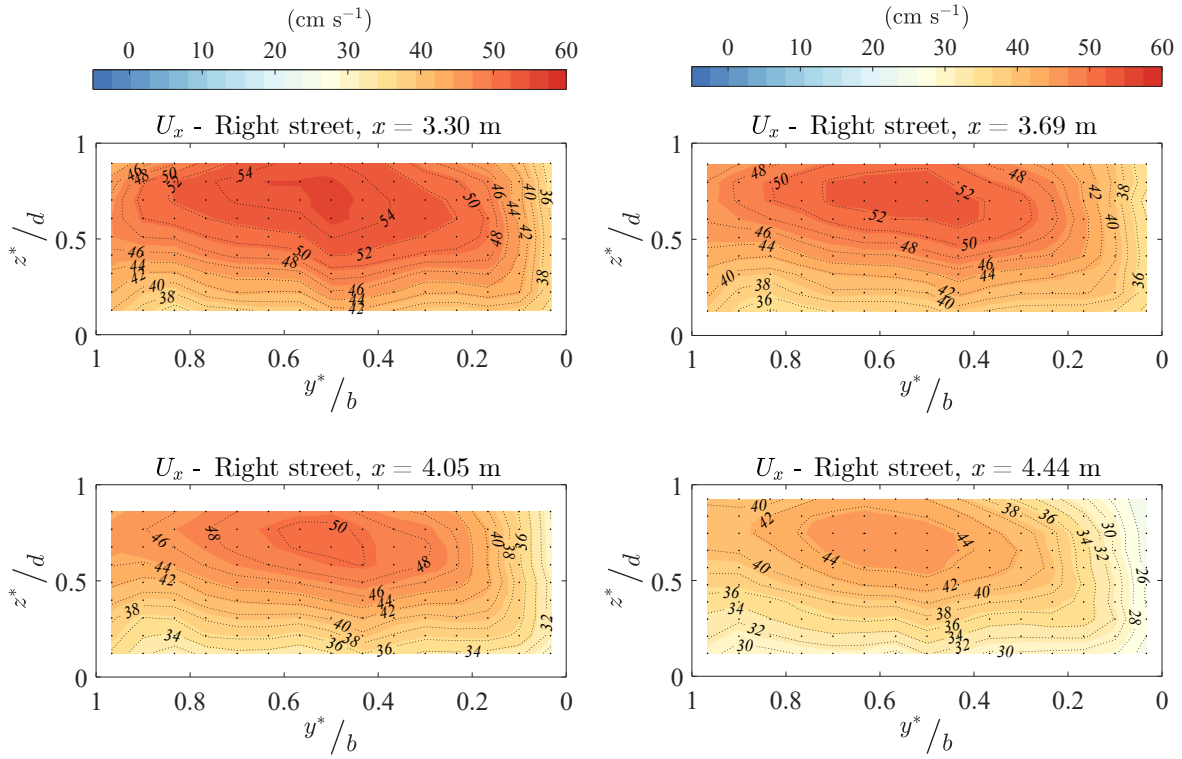

FIGURE E.7. Cross-sectional distribution of the time-averaged streamwise velocity in all streets corresponding to case C19-12 (Figure 4.1.H).

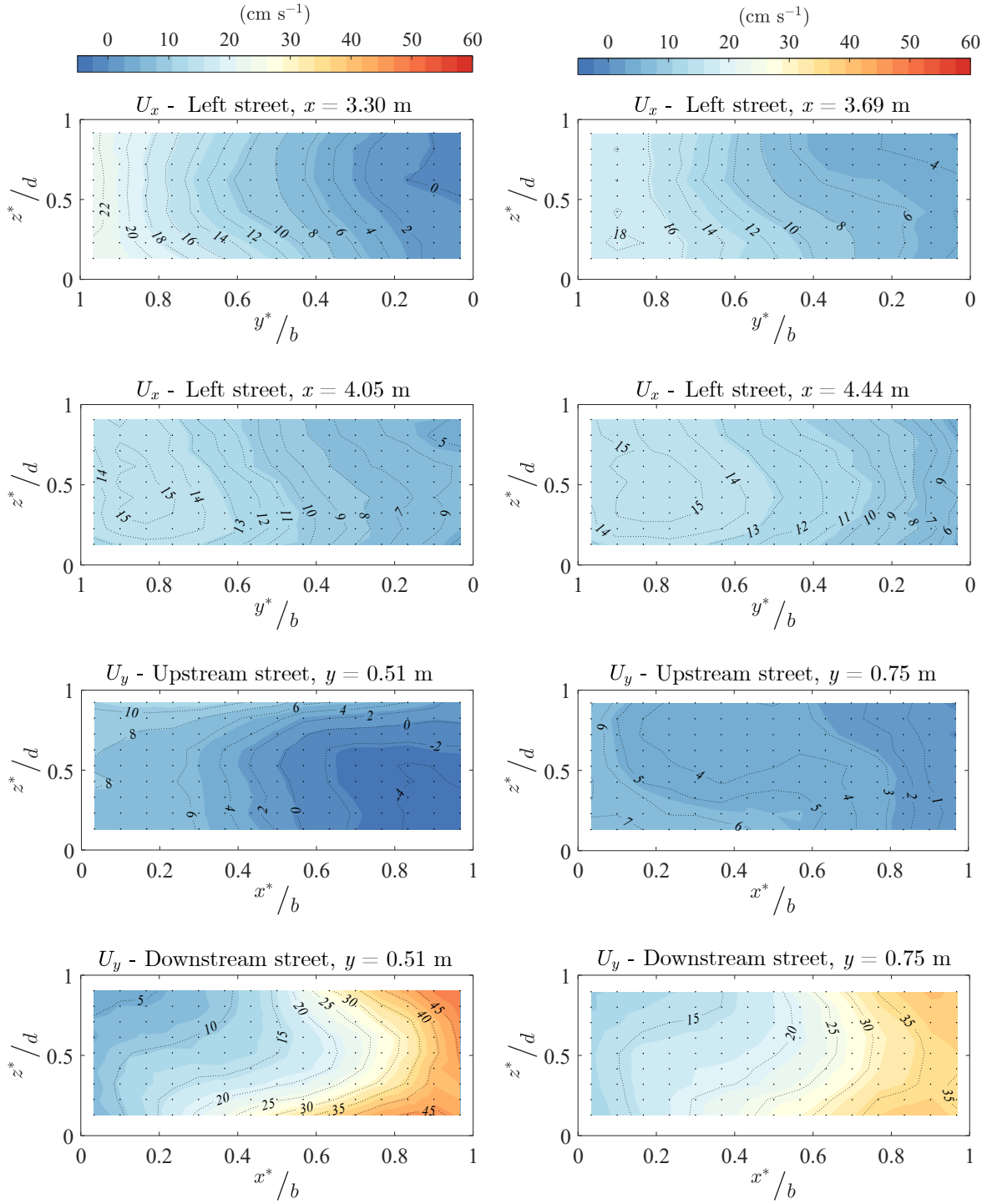

FIGURE E.7. (Continued).

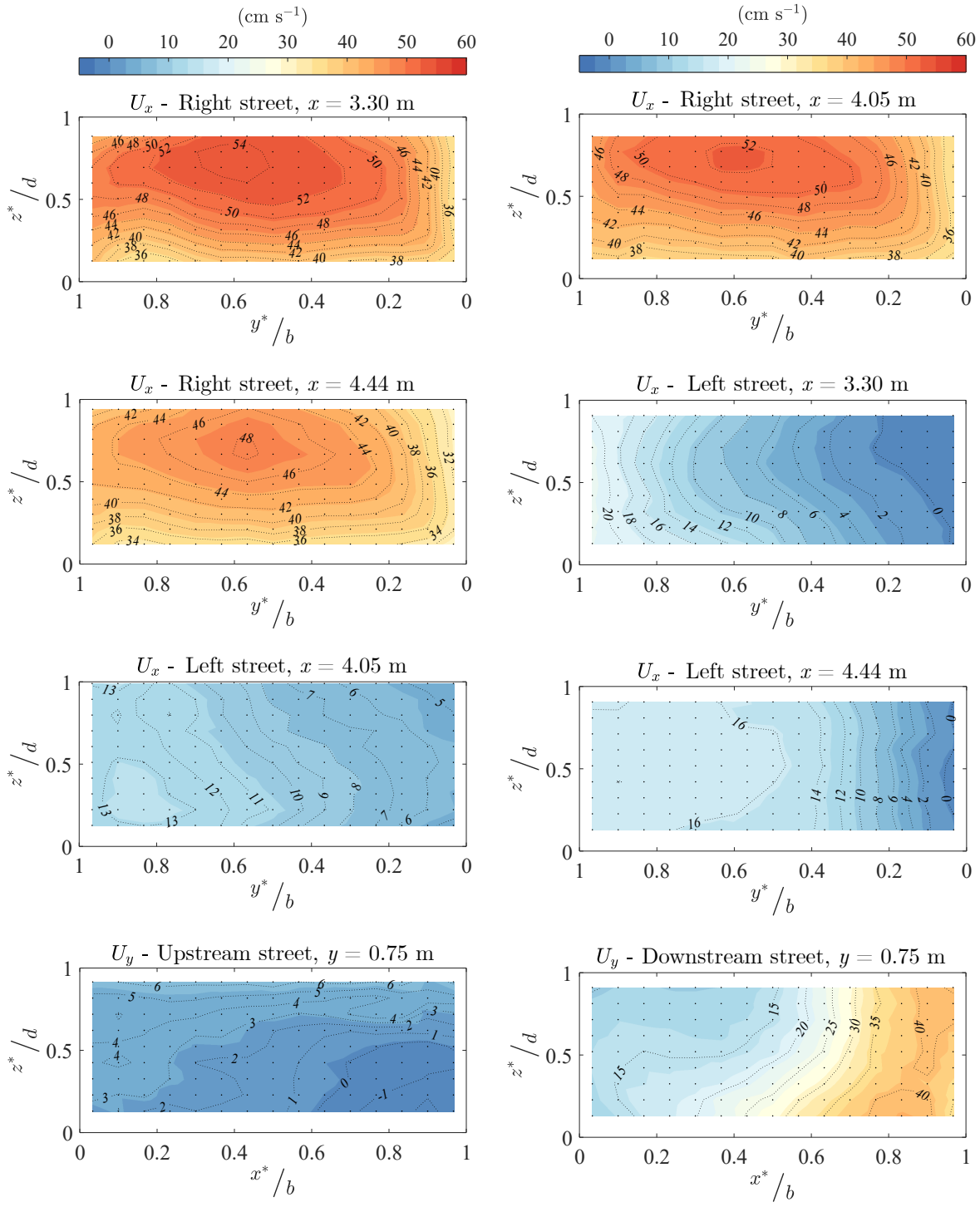

FIGURE E.8. Cross-sectional distribution of the time-averaged streamwise velocity in all streets corresponding to case RL08 (Figure 4.14.A).

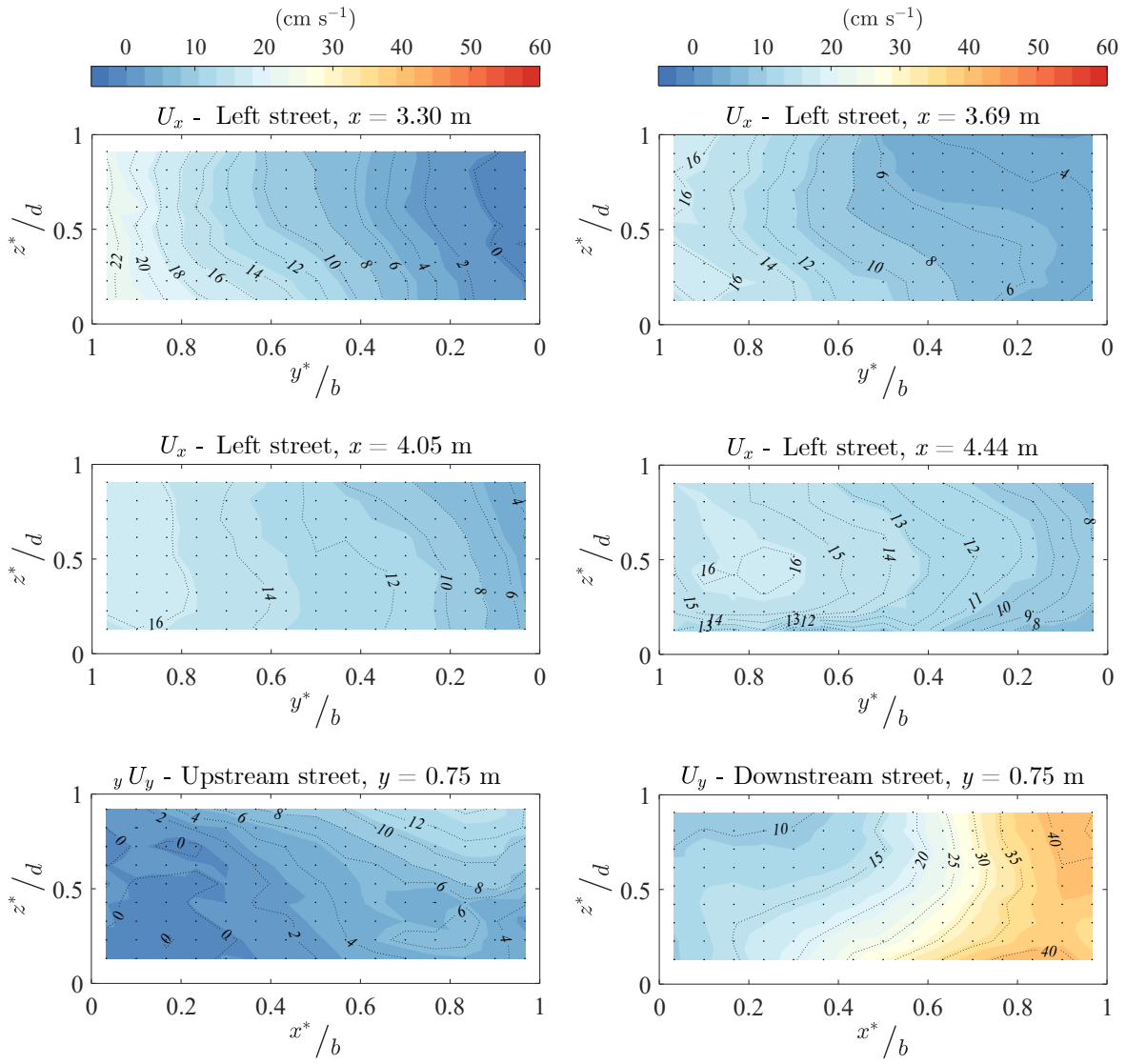

FIGURE E.9. Cross-sectional distribution of the time-averaged streamwise velocity in left, upstream and downstream streets corresponding to case R04L12 (Figure 4.14.B).

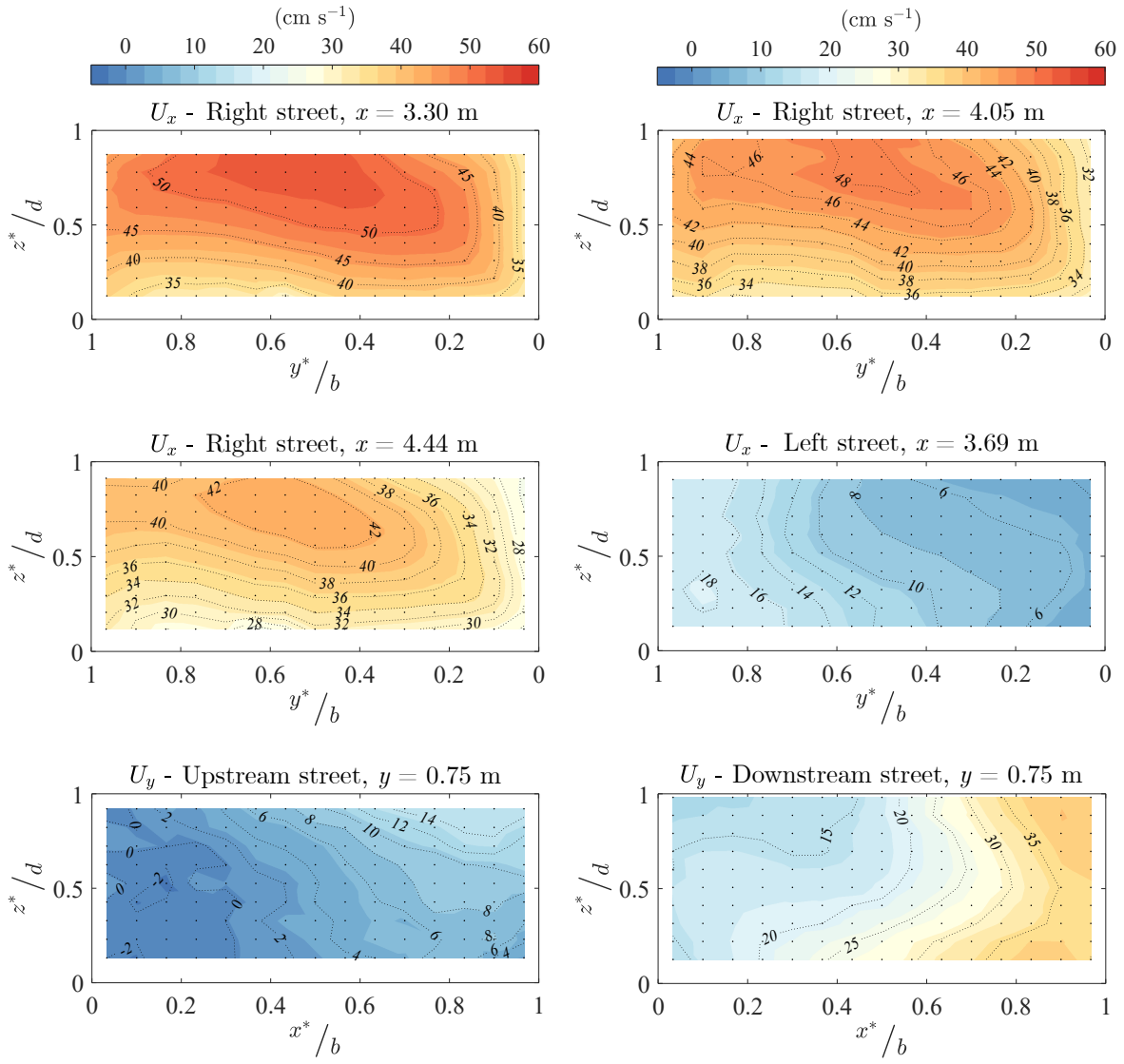

FIGURE E.10. Cross-sectional distribution of the time-averaged streamwise velocity in all streets corresponding to case D13R08 (Figure 4.14.C).

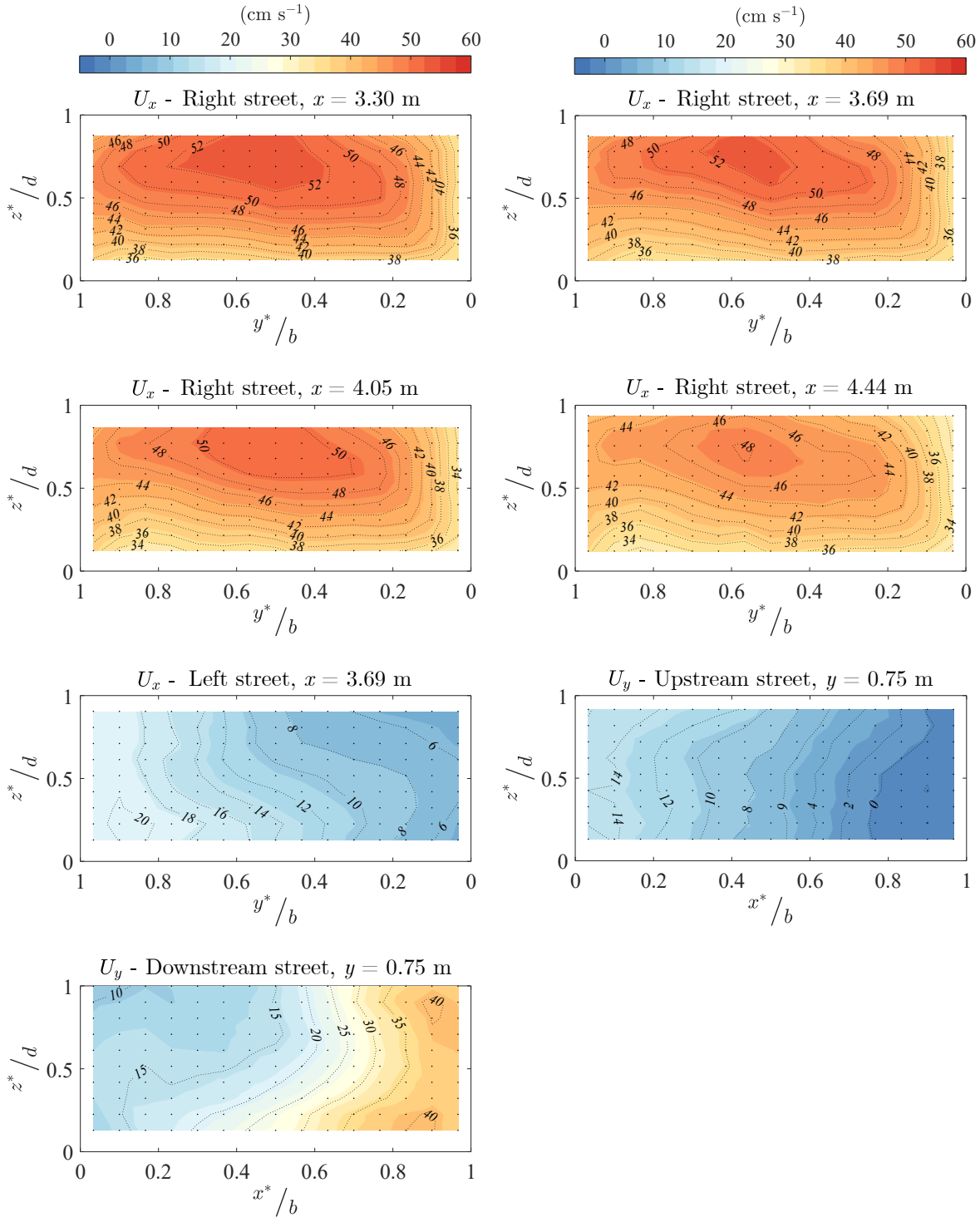

FIGURE E.11. Cross-sectional distribution of the time-averaged streamwise velocity in all streets corresponding to case U06R12 (Figure 4.14.D).

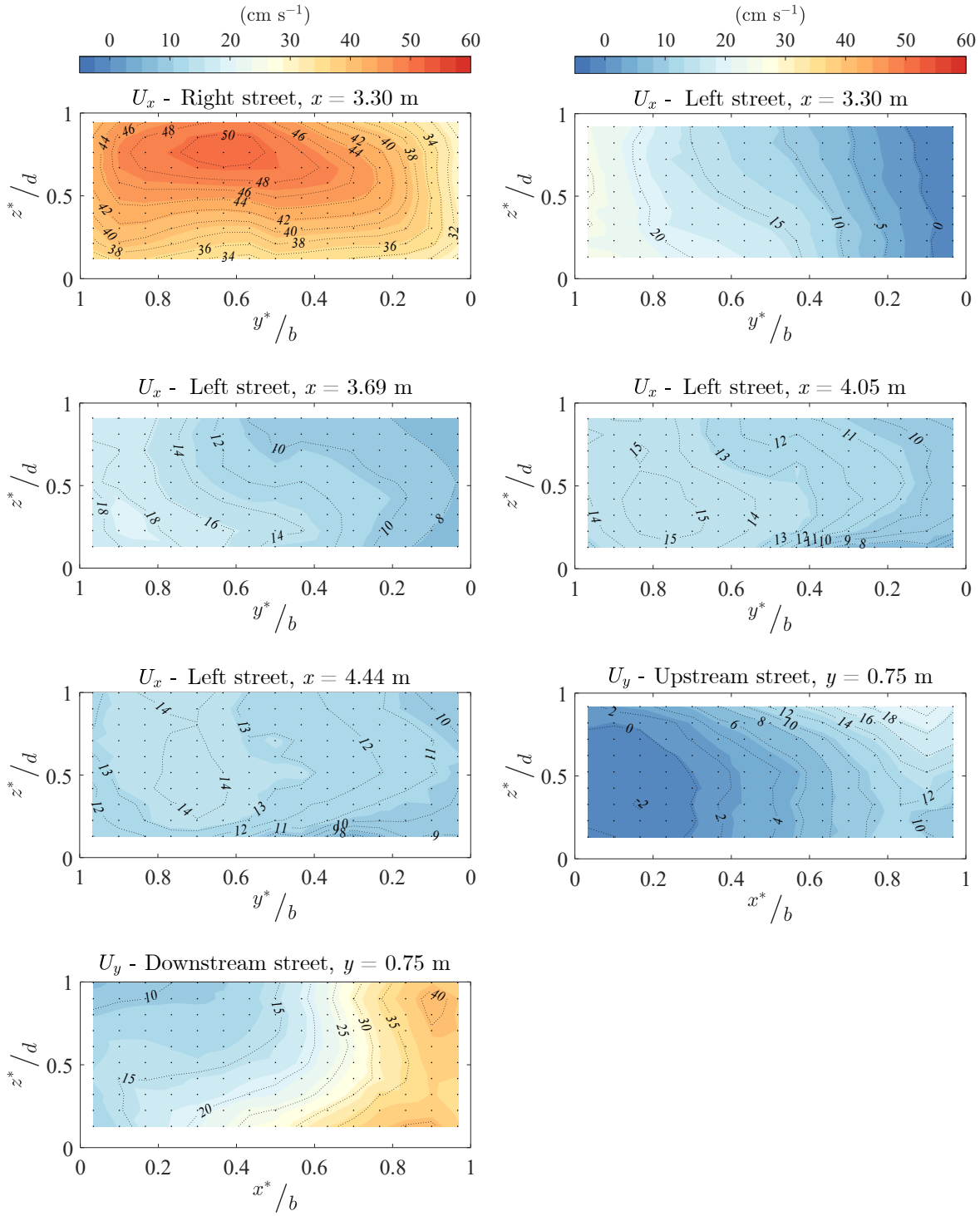

FIGURE E.12. Cross-sectional distribution of the time-averaged streamwise velocity in all streets corresponding to case D06L12 (Figure 4.14.E).

List of Figures

List of Tables

FOLIO ADMINISTRATIF

THESE DE L'UNIVERSITE DE LYON OPEREE AU SEIN DE L'INSA LYON

NOM : Mejía Morales DATE de SOUTENANCE : 23/05/2022

Prénoms : Miguel Angel

TITRE : **Influence of the flow exchanges between streets and a city block during urban floods**

NATURE : Doctorat Numéro d'ordre : 2022LYSEI042

Ecole doctorale : N°162 - MEGA

Spécialité : Mécanique des fluides

RESUME :
L'augmentation du nombre d'inondations urbaines au cours des dernières années incite à évaluer de manière précise l'aléa hydraulique (hauteur et vitesse de l'eau) et le risque associé pour les biens et les personnes. Cette évaluation doit s'appuyer sur une compréhension fine des processus hydrodynamiques en jeu notamment à une échelle locale (celle de la rue ou d'un bloc de bâtiments). Dans ce contexte, le travail de thèse a eu pour but d'étudier les échanges latéraux d'eau entre un bloc de bâtiments et les rues à proximité du bloc lors d'une inondation en ville, en s'appuyant sur des expériences de laboratoire. Ces dernières ont été réalisées dans des conditions d'écoulement stationnaire et instationnaire. La zone d'investigation a été limitée à un seul bloc de bâtiments et à ses rues adjacentes, en considérant les mécanismes qui affectent la capacité du bloc à convoyer et à stocker les flux d'inondation. Trois points clés ont ensuite été abordés pour quantifier l'influence sur la hauteur, la vitesse et le débit d'écoulement dans les rues et à l'intérieur du bloc de bâtiments: (i) en faisant varier la magnitude de la porosité de convoyage du bloc; (ii) en faisant varier la distribution de la porosité de convoyage du bloc; et (iii) en faisant varier la capacité de stockage du bloc. Premièrement, on a constaté que, dans les rues entourant le bloc, la vitesse et la hauteur de l'eau peuvent varier considérablement si l'on tient compte du passage et du stockage des eaux de ruissellement à travers le bloc. À l'intérieur du bloc, le paramètre d'écoulement le plus impacté est le nombre et la taille des cellules d'écoulement secondaires horizontales. Deuxièmement, il a été constaté que l'instationnarité de l'hydrogramme du débit entrant a une forte influence sur les caractéristiques des flux d'inondation, ainsi que sur le volume d'eau stocké dans le bloc. Enfin, le risque d'inondation pour les piétons, qui est à la fois lié à la vitesse et à la hauteur de l'eau, augmente localement en tenant compte du passage et du stockage à l'intérieur du bloc de bâtiments.

MOTS-CLÉS : inondation urbaine, bloc de bâtiments, écoulement instationnaire, capacité de stockage, porosité de convoyage

Laboratoire (s) de recherche : Laboratoire de Mécanique des Fluides et d'Acoustique (LMFA)

Directeur de thèse: Sébastien PROUST

Co-directeur de thèse : Emmanuel MIGNOT

Président de jury : Benjamin DEWALS

Composition du jury : Francesco MACCHIONE, Manuel GOMEZ, Magali JODEAU, Sébastien PROUST, Emmanuel MIGNOT et André PAQUIER (invité).